Yuri Ralchenko Editor

# Modern Methods in Collisional-Radiative Modeling of Plasmas



## Springer Series on Atomic, Optical, and Plasma Physics

Volume 90

#### **Editor-in-chief**

Gordon W.F. Drake, Windsor, Canada

#### Series editors

James Babb, Cambridge, USA
Andre D. Bandrauk, Sherbrooke, Canada
Klaus Bartschat, Des Moines, USA
Philip George Burke, Belfast, UK
Robert N. Compton, Knoxville, USA
Tom Gallagher, Charlottesville, USA
Charles J. Joachain, Bruxelles, Belgium
Peter Lambropoulos, Iraklion, Greece
Gerd Leuchs, Erlangen, Germany
Pierre Meystre, Tucson, USA

The Springer Series on Atomic, Optical, and Plasma Physics covers in a comprehensive manner theory and experiment in the entire field of atoms and molecules and their interaction with electromagnetic radiation. Books in the series provide a rich source of new ideas and techniques with wide applications in fields such as chemistry, materials science, astrophysics, surface science, plasma technology, advanced optics, aeronomy, and engineering. Laser physics is a particular connecting theme that has provided much of the continuing impetus for new developments in the field, such as quantum computation and Bose-Einstein condensation. The purpose of the series is to cover the gap between standard undergraduate textbooks and the research literature with emphasis on the fundamental ideas, methods, techniques, and results in the field.

More information about this series at http://www.springer.com/series/411

Yuri Ralchenko Editor

### Modern Methods in Collisional-Radiative Modeling of Plasmas



Editor Yuri Ralchenko National Institute of Standards and Technology Gaithersburg, MD USA

ISSN 1615-5653 ISSN 2197-6791 (electronic) Springer Series on Atomic, Optical, and Plasma Physics ISBN 978-3-319-27512-3 ISBN 978-3-319-27514-7 (eBook) DOI 10.1007/978-3-319-27514-7

Library of Congress Control Number: 2016930267

#### © Springer International Publishing Switzerland 2016

This work is subject to copyright. All rights are reserved by the Publisher, whether the whole or part of the material is concerned, specifically the rights of translation, reprinting, reuse of illustrations, recitation, broadcasting, reproduction on microfilms or in any other physical way, and transmission or information storage and retrieval, electronic adaptation, computer software, or by similar or dissimilar methodology now known or hereafter developed.

The use of general descriptive names, registered names, trademarks, service marks, etc. in this publication does not imply, even in the absence of a specific statement, that such names are exempt from the relevant protective laws and regulations and therefore free for general use.

The publisher, the authors and the editors are safe to assume that the advice and information in this book are believed to be true and accurate at the date of publication. Neither the publisher nor the authors or the editors give a warranty, express or implied, with respect to the material contained herein or for any errors or omissions that may have been made.

Printed on acid-free paper

This Springer imprint is published by SpringerNature The registered company is Springer International Publishing AG Switzerland

#### **Preface**

The light coming from plasmas has always been one of the primary sources of knowledge on their properties. Be it multi-million-degree magnetic or inertial confinement plasmas, dazzling streamers of the solar corona, photoionized plasmas generated by powerful z-pinches, or industrial plasmas for lithography, their spectra, from hard X-rays to infrared and beyond, can give us a great deal of information about diverse characteristics such as temperature and density, turbulent motions, ionization distributions, and electric and magnetic fields, to name a few. In most cases the measured plasma emission and absorption spectra are quite complex due to a large number of spectral lines with varying intensities and line shapes, as well as the presence of continuum photons. As a result, a reliable interpretation of spectroscopic experiments is mostly achieved with rather sophisticated methods capable of adequately describing the origin, propagation and possible destruction of plasma photons.

One of the most general approaches to calculation of plasma population kinetics and spectra is the collisional-radiative (CR) modeling. First introduced more than 50 years ago in a seminal paper by Bates, Kingston, and McWhirter, it addresses determination of state populations and ensuing spectra from a microscopic picture of interactions between emitters (i.e., atoms and ions in plasma) and other plasma particles. Thus it accounts for the most relevant collisional and radiative processes, hence the name. The variety of terrestrial and astrophysical plasmas results in a considerable diversity of possible interactions and environments, from simple electron-atom (ion) collisions in a stationary optically thin plasma to non-Maxwellian particle distribution functions to relatively weak forbidden radiative transitions to heavy-particle interactions to transient and/or optically thick plasmas, and so on. Unlike equilibrium descriptions of plasma population kinetics, for example, local thermodynamic equilibrium (LTE), a general CR approach calls for a fairly detailed (and of course reasonably accurate!) representation of relevant elementary interactions. This approach connects plasma modeling with the powerful apparatus of contemporary atomic physics, which may require utilization of very extensive sets of atomic data.

vi Preface

The idea for this book originated from invigorating discussions among the participants of the series of non-LTE code comparison workshops. The present collection of chapters is aimed at providing an overview of the modern methods employed in collisional-radiative modeling with emphasis on recent developments. Such a review seems to be long overdue, notwithstanding extensive applications of CR models to various plasmas as witnessed by hundreds, if not thousands, of articles on this subject.

The eight chapters presented here address both general topics, such as the balance between detail and completeness in CR models and self-consistent large-scale CR modeling, and more specific issues, such as simulations with different representations of atomic structure, applications in radiation hydrodynamics and interaction of monochromatic X-rays with matter, astrophysical applications, and validation and verification of CR models. This collection is not an introductory textbook and thus is intended for advanced students and young researchers who already have some knowledge in CR approach. We hope also that it will be useful for scientists and researchers working in general plasma spectroscopy.

When this book was in a final stage of preparation, one of the contributors, Prof. Vladimir G. Novikov of the Keldysh Institute of Applied Mathematics in Moscow, Russia, suddenly passed away. He was an excellent physicist with a wide range of interests and one of the leading specialists in quantum-statistical methods for high-temperature plasmas. We dedicate this book to his memory.

Gaithersburg, MD, USA

Yuri Ralchenko

#### **Contents**

L	Balancing Detail and Completeness in Collisional-Radiative					
	Models					
	3.ep					
			uction			
	1.2		Space Completeness			
1.4 Applica		Degree of State Detail				
			cation-Driven Approaches to Balancing Detail			
			ompleteness			
		1.4.1				
			General Models for Moderate-Density Plasmas			
		1.4.3				
	1.5		usions			
	Refe	erences				
2	Self	Self-consistent Large-Scale Collisional-Radiative Modeling				
	Christopher J. Fontes, James Colgan and Joseph Abdallah Jr					
	2.1	Introd	uction			
	2.2	Large-	Scale Collisional-Radiative Modeling			
		2.2.1	The Los Alamos Suite of Atomic Physics Codes			
		2.2.2	Selecting a List of Configurations			
		2.2.3	Selecting the Level of Refinement			
		2.2.4	Constructing the Rate Matrix			
		2.2.5	Steady-State Solutions Versus Time-Dependent			
			Solutions			
		2.2.6	Boundary Conditions for the Steady-State CR			
			Equations			
		2.2.7	Different Methods of Solving the Steady-State CR			
			Equations			
	2.3	An Ill	ustrative Example			
	2.4		ary and Outlook			
	D.f.					

viii Contents

3	Gen	eralize	d Collisional Radiative Model Using Screened	
	Hyd	rogenio	c Levels	5
	Hk	Chun	g, S.B. Hansen and H.A. Scott	
	3.1	Introd	uction	5
	3.2	Forma	ılism	5.
		3.2.1	Generalized Collisional-Radiative Atomic Levels	5.
		3.2.2	Atomic Transition Rates	5
		3.2.3	Plasma Effects	6
		3.2.4	Spectroscopic Emissivity and Opacity	6
	3.3	Applic	cations	6
		3.3.1	Steady-State Plasmas Generated by Long-Pulse Lasers	6
		3.3.2	Two-Temperature Plasmas Generated by Short-Pulse	
			Lasers	69
		3.3.3	Photoionization Equilibrium Plasmas	7
		3.3.4	Photo-Ionized Plasmas Generated by X-Ray Free	
			Electron Lasers	7
		3.3.5	Radiative Loss Rates of Heavy Elements	7
	3.4	Validi	ties and Limitations	7
		3.4.1	Completeness	7
		3.4.2	Improvement on SH Model Spectra	7.
		3.4.3	Dielectronic Recombination	70
		3.4.4	Radiative Power Losses	70
		3.4.5	Continuum Lowering	7
		3.4.6	CR Models in High-Energy-Density Radiation-	
			Hydrodynamic Simulations	73
	3.5	Summ	nary	7
	Refe	rences		7
4				
4			Radiative Modeling for Radiation Hydrodynamics	0
			C	8
		ard A.		8
	4.1		uction	-
	4.2		ning Equations	8.
	4.3		TE Material Response	8′
	4.4		Density Effects	9
	4.5		ed Balance, Energy Conservation and Discretization	9
	4.6		ervation and Consistency in Non-LTE Thermal	10
	4.7		tion Transport	10
	4.7		nary	10
	Refe	erences		10
5	Ave	rage At	tom Approximation in Non-LTE Level Kinetics	10
			. Novikov	
	5.1		uction	10
	5.2		Kinetics Equations	10

Contents ix

	5.3	The Rates of Collisional and Radiative Processes	108
		5.3.1 Excitation by Electron Impact	108
		5.3.2 Electron-Impact Ionization and Three-Body	
		Recombination	111
		5.3.3 Autoionization and Dielectronic Capture	113
		5.3.4 Rates of Radiative Processes	114
	5.4	Configuration Accounting in the Extended CR-AA Model	116
	5.5	Reducing Detailed Level Kinetics to Extended CR-AA Model	117
	5.6	The Calculation Algorithm	120
	5.7	Results of Calculation for Tin Plasma	121
	Refe	erences	125
_	G 11		
6		isional-Radiative Modeling and Interaction of Monochromatic	107
		ays with Matter	127
		Peyrusse	107
	6.1	Introduction	127
	6.2	Atomic Model Construction for the Modeling of X-Ray	4.00
		Interaction with Matter	128
	6.3	Interaction with Gas	130
	6.4	Interaction with Small Objects	135
	6.5	Interaction with Solids	136
		6.5.1 Population Kinetics and Atomic Structure at Solid	
		Density	137
		6.5.2 Temperature and Population Evolution	139
		6.5.3 Energy Deposition	144
		6.5.4 Modeling of Al, V and Ag Samples Irradiated	
		in the X-UV or X-Ray Range	146
	6.6	Conclusion	150
	Refe	erences	150
7	Snee	ctral Modeling in Astrophysics—The Physics of Non-	
′		librium Clouds	153
		Ferland and R.J.R. Williams	133
	7.1	Introduction	154
	7.2	Working with Real Nebulae: The Observational	154
	1.2	Questions We Are Trying to Answer	155
	7.3	Approaches to Astronomical Spectral Modelling	162
	7.3 7.4	Spectral Calculations	166
	7.4	•	166
	7.5	The females Bulling in the 1911 Emile 111111	
	7.5	The Physics of the Astronomical Problem	173
	7.6	Future Opportunities and Challenges	174
		7.6.1 New Spectroscopic Opportunities	174
	D 6	7.6.2 And the Grand Challenges to Exploiting Them	177
	P oto	prances	1.78

x Contents

3	Validation and Verification of Collisional-Radiative Models			
	Yu. Ralchenko			
	8.1	Introduction		
	8.2	Tests and Uncertainty Analysis of CR Models		
	8.3	Overview of NLTE Code Comparison Workshops		
	8.4	Code Comparison Parameters		
		8.4.1 List of Parameters for Steady-State Cases		
		8.4.2 Global Parameters		
		8.4.3 Ion Parameters		
		8.4.4 Data for Atomic States		
	8.5	Concluding Remarks		
	Ref	erences		

## Chapter 1 Balancing Detail and Completeness in Collisional-Radiative Models

Stephanie B. Hansen

**Abstract** Collisional-radiative models based on highly detailed atomic structure (e.g. fine-structure levels) tend to demonstrate very good agreement with highly resolved experimental data. Such models typically predict X-ray line positions with high accuracy and can faithfully reproduce the intensities of lines from metastable and dielectronic states. Models based on less detailed structure (e.g. configurations) necessarily have lower fidelity at the spectroscopic level. Their key advantage lies in the completeness of their state structure: highly averaged models can capture the population flux through high-*n* and multiply excited states critical for accurate predictions of charge state distributions. For complex multi-electron ions, highly detailed models with extensive structure become intractable. This Chapter explores the tension between detail, completeness, and tractability in collisional-radiative modeling.

#### 1.1 Introduction

Two principal design elements of a collisional-radiative model are the states to be included and the rates that couple them. This chapter focuses on the first design element: the selection of electronic orbitals or states that form the basis of the atomic model. Because state-space design is a critical determinant of the accuracy and applicability of a given model, this Chapter will cover considerations related to the extent of the modeled state space, its degree of detail, and the generation of atomic data. Chapter 3 focuses on the second design element: the spontaneous, collisional, and radiative rates that connect the set of electronic states.

In a collisional-radiative model, "state" (and sometimes "level") is used to denote a particular member of the population vector X that satisfies the rate equation dX/dt = AX, with A the rate matrix. For the screened hydrogenic models (SHM) discussed in Chap.3, the basic states are Layzer complexes of the form

1

S.B. Hansen (\simeq)

Sandia National Laboratories, Albuquerque, NM, USA e-mail: sbhanse@sandia.gov

© Springer International Publishing Switzerland 2016 Yu. Ralchenko (ed.), *Modern Methods in Collisional-Radiative Modeling of Plasmas*, Springer Series on Atomic, Optical, and Plasma Physics 90, DOI 10.1007/978-3-319-27514-7\_1 S.B. Hansen

 $(n_1)^{N_1}(n_2)^{N_2}\dots(n_{max})^{N_{max}}$ , where  $n_m$  are the principal quantum numbers of n-shell orbitals and  $N_m$  are their *populations*. The total number of bound electrons in an ion with charge Z-N is  $N=\sum N_m$  for each Layzer complex. These complexes are sometimes called non-relativistic superconfigurations (SCs). This notation offers a useful and compact representation of the extent of a model's state space and can be used to describe even non-hydrogenic models: for example, the state space of more detailed models based on relativistic unresolved transition arrays (UTAs) or fine structure terms can be compactly described using this n-shell notation as long as each Layzer complex is completely filled by the more detailed states. Even models that are less detailed than the SHM, such as models that combine several high-n orbitals into a single state, can be described by a variation of this notation with  $n_m$  replaced by a range of n.

The ideal state space of a collisional-radiative model is one that is both strictly complete and fully detailed. Strict completeness for an N-electron ion means that all permutations of N electrons in all possible n-shell orbitals are explicitly included in the state space. "Full detail" is a less rigorous concept: for the purposes of this Chapter, fully detailed means that all of the superconfigurations included in the model are split into states with sufficient detail to meet the intended application of the model. For example, the radiative power losses from high-temperature plasmas with negligible emission from  $\Delta n = 0$  transitions can be well described by an SHM model, while high-resolution spectroscopic measurements often require a state space based on fine-structure terms, and collisional-radiative calculations in the presence of strong fields or anisotropic electron distributions might demand further splitting of the state space into magnetic sublevels.

In practice—and even in principle, for isolated ions with unbounded *n*—strictly complete and fully detailed models are computationally intractable. Collisional-radiative models thus fall into a class of computational science where the exact solution can be theoretically but not computationally determined. Balancing the requirements of state-space completeness and degree of state detail is an essential part of the art of collisional-radiative modeling, and this Chapter offers some guidelines for constructing reliable, tractable, and useful collisional-radiative models for a variety of applications.

#### 1.2 State-Space Completeness

State-space completeness is a critically important feature of a reliable collisional-radiative model, but can be difficult or even impossible to achieve. In a completely isolated ion, the maximum principle quantum number is unbounded. Thus, a strictly complete model based on Layzer complexes is not achievable for even one-electron ions. Even effective completeness, by which we mean convergence in the charge state distribution with increasingly extensive structure, is not possible for isolated ions at finite temperature because level populations do not converge with increasing n.

To illustrate this point, consider a one-electron (H-like) ion with nuclear charge Z and SHM state energies defined in reference to the binding energy of the 1s electron: the  $(n)^1$  superconfigurations have energies  $E_n = RyZ^2(1 - 1/n^2)$  and statistical weights  $g_n = 2n^2$ . In the simplest case of local thermodynamic equilibrium (LTE) at a finite temperature T, the populations of the of the  $(n)^1$  superconfigurations follow Boltzmann statistics:  $X_n = g_n \exp[-E_n/T]$ . For low temperatures, the exponential term ensures that  $X_1$  holds the majority of the population among the low-n states. However, because the  $E_n$  and therefore the exponential term asymptote to constant values, while  $g_n$  increases with n, there is for each finite temperature some n such that  $X_n > X_1$ , above which the high-n populations will dominate. Thus the solution to even the simplest (LTE) treatment of the simplest (one-electron) ion is divergent.

In real physical systems, the influence of neighboring particles truncates the high-n state space, lowering the ionization potential by roughly  $\Delta I$  (eV)  $\sim 8 \times (Z^* + 1)^{2/3} (N_e/10^{22})^{1/3}$  in the ion sphere approximation [1], with  $N_e$  the electron density in e/cm³ and  $Z^*$  the ion charge. This ionization potential depression (IPD)—also called pressure ionization or continuum lowering—destroys high-n orbitals with binding energies less than  $\Delta I$ . As a very rough rule of thumb, states with  $n < 2(Z^* + 1)^{1/2}/(N_e/10^{22})^{2/15}$  must be included for strict completeness. For plasmas at near-solid densities, the state-space restriction due to pressure ionization can be significant: at  $N_e = 10^{22}$  e/cm³ one must include only states up to  $n_{max} = 10$  for hydrogen-like ions with Z = 30 and up to  $n_{max} = 3$  for Z = 1. By contrast, strict completeness requires  $n_{max} > 100$  for mid-to high-Z hydrogen-like ions in low-density astrophysical or tokamak plasmas.

For multi-electron ions, strict completeness becomes even more difficult to achieve due to the large number of possible permutations of N electrons into n shells. Even using a relatively undetailed state structure like the superconfigurations of the SHM, the explosion of statistical weight for high-n, multiply excited states very quickly reaches the memory capacity of modern computing facilities. Figure 1.1 illustrates the growth of statistical weight, which is roughly equivalent to the number of highly detailed states, for models with  $n_{max} = 8$  and either single or single and limited double excitation. Collisional-radiative models with  $10^6$  states require TB of computing memory to store the rate matrix, and solving the rate matrix for systems at this scale approaches intractability. Balancing the demands of completeness and tractability thus requires a thoughtful approach to state-space design.

Two general approaches to resolving the tension between completeness and tractability have proven successful. The first approach uses information about the intended model application to generate a fixed state space that does not introduce too much inaccuracy: this is effective completeness by design. For example: hot plasmas at moderate densities driven by collisions with thermal electrons can be reliably modeled using a fairly restricted set of singly and doubly excited states; plasmas driven by intense, high-energy radiation fields require "hollow-ion" states with multiple inner-shell holes, and modeling the emission and relaxation from charge exchange requires multiply excited high-*n* states. Limiting the anticipated plasma conditions can be very effective in restricting the states that must be modeled especially since closed-shell ions have smaller statistical weights (see Fig. 1.1) and can dominate

4 S.B. Hansen

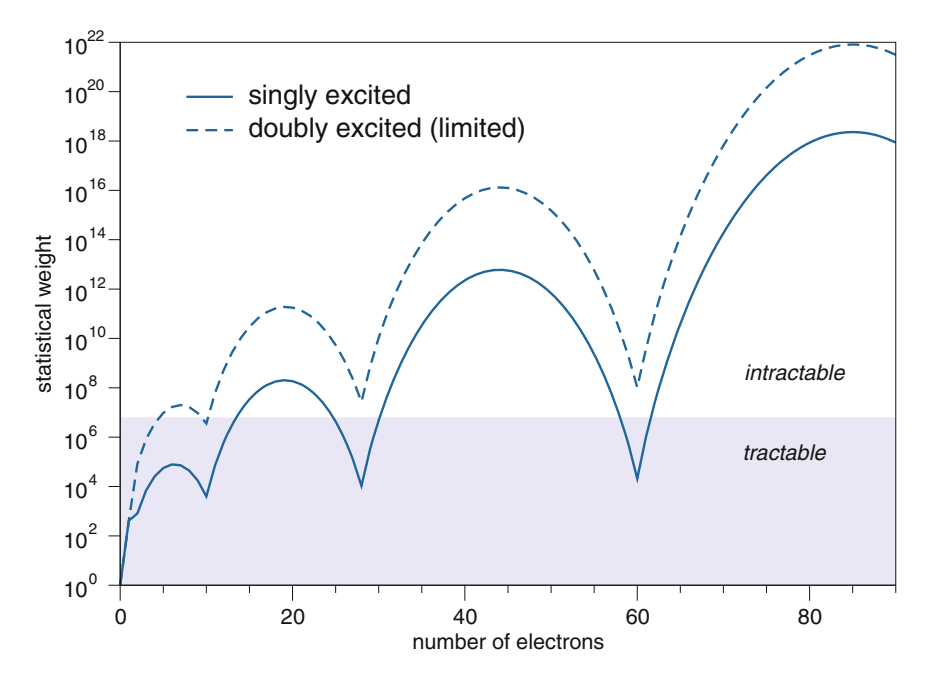


Fig. 1.1 Statistical weight per ion increases dramatically with the number of bound electrons. The statistical weight is an upper limit for the number of states in a highly detailed model; highly averaged models can have many fewer states encompassing the same statistical weight. The state space illustrated by the *solid line* includes all states formed by single excitation (including all innershell excitation) to  $n_{max} = 8$ . The *dashed line* also includes double excitation to  $n_{max} = 8$  from the valence and first inner shells. Computational tractability for highly detailed models is roughly indicated by the *shaded region*. Less detailed models can cover the same configuration space with many fewer state: a superconfiguration model would require only about 100 states per ion for these configurations

the charge state distribution over fairly wide ranges of temperature due to their relatively large ionization potentials. The second approach is to design a model with a dynamic state space that can adapt to different applications: this is explicitly enforced effective completeness. This can be done either by generating states on an as-needed basis within the population solver itself (as in the Monte Carlo approach taken in [2] and discussed further below) or by a methodical stepwise increase in the state space that solves the rate matrix and tests for convergence at each step. While this second approach produces more generally reliable models, it does not guarantee tractability.

State-space completeness impacts the accuracy of collisional-radiative calculations in two ways: First, the enormous statistical weights of high-*n* and multiply excited states can hold a great deal of population, as illustrated by the one-electron example above. The population in such states can directly and significantly affect the charge state distribution (CSD) and the emission or absorption signatures from the plasma. This aspect of completeness is particularly critical for plasma at high density

or under intense external irradiation, where excitation rates are of the same order as spontaneous radiative decay rates and high-lying electronic configurations can maintain near-LTE occupations. It is also critical for ions undergoing charge exchange, where electrons are preferentially (and multiply) captured into high-n orbitals. In high-density plasma, pressure ionization helps to restrict the state space, however in that case, the particular treatment of IPD becomes a critical consideration, which is by no means resolved [3]. And in low-density photoionized or recombining plasmas, there is no such grace.

The second critical aspect of high-*n* multiply excited states is their role as dielectronic recombination channels, which can have a major influence on the CSD even for low-density plasmas without significant radiation fields. In this "coronal limit," spontaneous radiative and Auger decay rates are much more rapid than collisional rates and the vast majority of population resides in the ground states of the ions. But even here, the charge state distribution is highly sensitive to the treatment and completeness of the high-*n* multiply excited states, because these states provide the channels for the critical dielectronic recombination process. The sensitivity of CR calculations to dielectronic recombination is illustrated in Fig. 1.2, which gives the results of a test case from a NLTE code comparison workshop [4]. When dielectronic capture and Auger decay processes are excluded, there is very good agreement among a wide

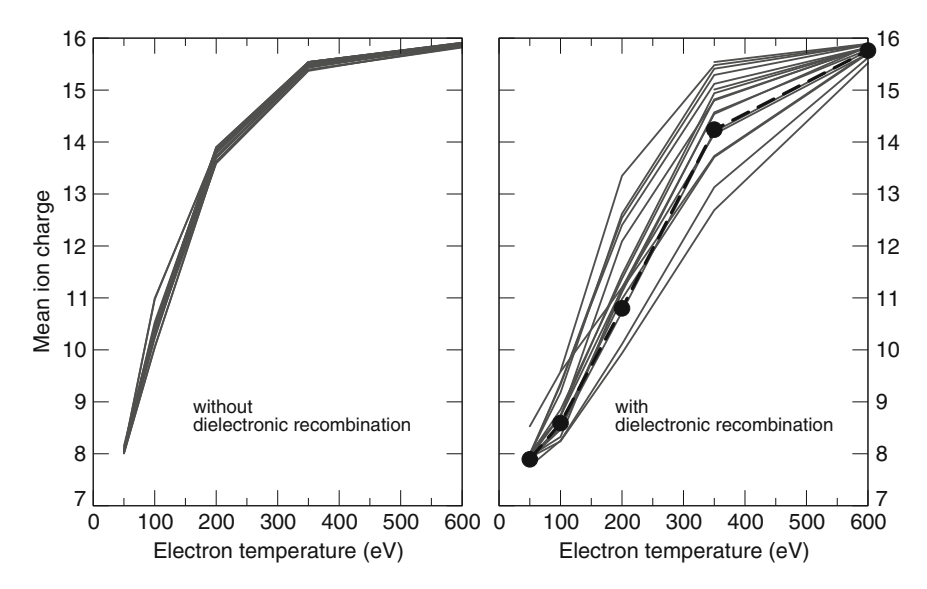


Fig. 1.2 The average ion charge predicted by a variety of collisional-radiative models is highly sensitive to the completeness of dielectronic recombination channels. The plot on the *left* shows good agreement between a wide variety of models with very different degrees of detail and completeness for a coronal argon plasma ( $N_e = 10^{12} \text{ e/cm}^3$ ) when dielectronic processes are excluded. The plot on the *right* shows the significant disagreement that results from including dielectronic processes in models with diverse detail and completeness. The heavy *dashed line* is from an effectively complete coronal model that uses a tabulated dielectronic recombination rate [5]

S.B. Hansen

range of models—but this agreement all but vanishes when DR is included, largely due to the idiosyncratically incomplete state structure in the individual models.

Models with insufficient state-space completeness tend to overpredict ionization. In the low-density coronal limit, incomplete excitation-autoionization (EA) and dielectronic recombination (DR) channels lead to inaccurate rates between charge states. This is illustrated in Fig. 1.2: excluding both EA and DR processes entirely, as is done in the left-hand plot, results in a significant overestimation of the average ion charge. On the right-hand plot, most of the models have limited completeness and thus predict a higher charge state than the effectively complete coronal model shown by the dashed line; the few models that predict lower charge states are screened hydrogenic models that use approximate rates and may exclude  $\Delta n = 0$  EA and DR channels. Models can achieve effective completeness in the coronal regime by treating high-n doubly excited states implicitly, using pre-calculated EA and DR rates summed to convergence in n (e.g. [5]) rather than tracking dielectronic capture and Auger decay through high-n states explicitly included in the population vector. This implicit approximation breaks down at moderate densities, where pressure ionization invalidates the n-summed dielectronic recombination rate and collisions open new DR channels by moving significant population into excited states. Incomplete models also tend to overpredict ionization in the high-density LTE limit, where three-body recombination dominates over dielectronic recombination and excitation rates support near-statistical populations of highly excited states. The reason for this can be seen by again considering the simple one-electron ion, where high-n states can hold significant population due to their high statistical weights. Excluding these high-n states forces population into the continuum and artificially increases the calculated charge state.

#### 1.3 Degree of State Detail

We have seen that the completeness of modeled state space influences the first-order accuracy of the charge state distribution (CSD) in collisional-radiative models, affecting gross predictions like the equation of state, radiative power loss (RPL), and the spectral location of emission features. This Section will show that the detail with which the modeled states are treated influences the finer features of the CSD and spectra. The effects of state detail on emission and absorption spectra are particularly important because detailed spectroscopic data is a primary touchstone between collisional-radiative models and the atomic systems they represent. Plasma diagnostics based on comparisons of model predictions with high-resolution spectroscopic data necessarily require that the model treat both the electronic states and the rates that govern their populations with fairly high fidelity.

To illustrate the importance of detailed state structure on modeled spectra, consider the lowest two superconfigurations of a two-electron (He-like) argon ion:  $(1)^2$  and  $(1)^1(2)^1$ . This superconfiguration includes three configurations:  $1s^2$ , 1s2s, and 1s2p,

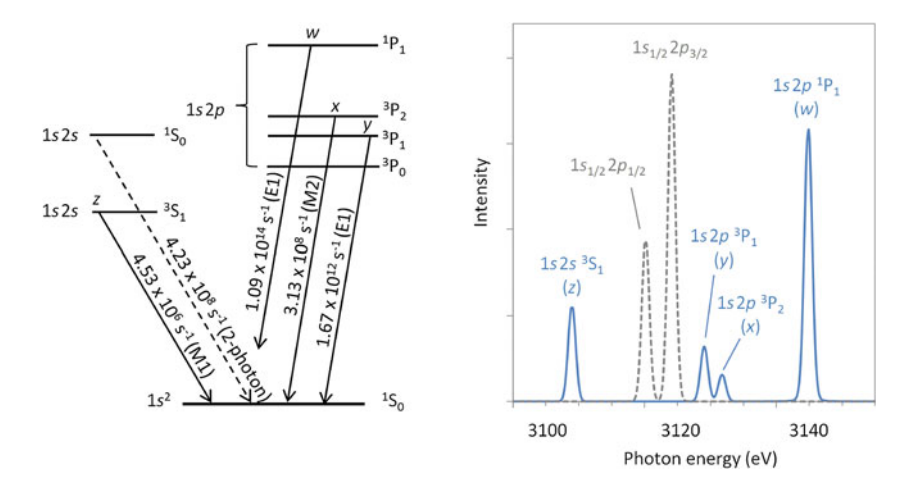


**Fig. 1.3** On the *left* is a level diagram of the fine structure states in the  $1s^2$ , 1s2s, and 1s2p configurations of He-like argon. Transition rates are given for electric dipole (E1), magnetic dipole (M1), magnetic quadrupole (M2), and two-photon decay rates [6]. On the *right* are calculated He-like emission spectra at coronal conditions  $(T_e = 1 \text{ keV}, N_e = 10^{12} \text{ e/cm}^3)$  from both a fine-structure model (solid), which captures the character of the metastable emission, and from a configuration-averaged model (dashed), which produces only a rough representation of the emission

whose seven fine-structure levels are illustrated in Fig. 1.3. The intercombination line (denoted y) arises from a transition from 1s2p  $^3P_1$  to  $1s^2$   $^1S_0$  with a radiative decay rate about 100 times smaller than the decay rate of the 1s2p  $^1P_1$  to  $1s^2$   $^1S_0$  resonance line (w). Other dipole-forbidden lines (x and z) have even smaller decay rates. Yet despite the orders-of-magnitude differences in their radiative decay rates, all four lines are observed with significant intensities in measured emission spectra from low-density plasmas such as tokamaks. This is because emission line intensities depend on the product of upper-level populations and radiative decay rates, and since the upper levels of the x, y, and z transitions are metastable, they can accumulate significant populations in low-density plasmas.

In a low-density plasma, any electron that finds itself in an excited state will undergo radiative (or Auger) stabilization. As this stabilization proceeds via either direct decay to ground or cascading decay into lower excited states, population can accumulate in long-lived, low-lying excited states. These metastable states do not autoionize and have only small radiative decay rates to the ground state. Absent significant collisional depopulation, these states will collect population that can be many times larger than the population of nearby resonance states with stronger decay channels, leading to comparable line intensities. Figure 1.3 illustrates the emission spectrum from He-like argon in a low-density plasma, where all of the metastable states are populated at sufficient levels to produce strong emission.

As electron densities increase, collisional processes depopulate the metastable states, resulting in a disappearance of the associated lines until they reach their statistical limits, where upper level populations follow Boltzmann distributions and

S.B. Hansen

the relative intensities of the lines are proportional to the statistical weights of the upper levels and the radiative decay rates of the transitions. This density dependence makes emission signatures from He-like and other closed-shell ions powerful plasma diagnostics. While the exact density dependence of the line intensities depends on the details of the collisional and radiative rates that govern the populations, intercombination-to-resonance line ratios tend to be sensitive to densities around  $N_e \sim 5 \times 10^9 \Delta E^{7/2} \, \mathrm{cm}^{-3}$ , with  $\Delta E$  the transition energy in eV.

High populations in metastable states can also contribute to a process called ladder ionization, which becomes important when the electron temperature is too small to support significant collisional ionization from the ground state but large enough to support ionization from excited states that lie much closer to the continuum limit. The collisional ionization flux and charge state distribution therefore depend on the degree of state detail. In addition, some mid-shell ions support excitationautoionization processes for states formed by single excitation from inner subshells (e.g. the  $1s^2 2s 2p^6 nl$  states in F-like iron are autoionizing for n > 6). Models that average over subshells do not generally capture the resultant  $\Delta n = 0$  excitationautoionization and dielectronic recombination channels (cf. Fig. 1.2). Thus, models with insufficient detail tend to underpredict ionization around closed shells. Usually, however, this is a smaller effect than the overpredicition of ionization one finds in models with insufficient completeness. And because models with more complete high-*n* structure will more accurately represent the cascades that populate metastable states, completeness remains important even for simple few-electron ions in lowdensity plasmas.

While the degree of detail in the state structure can have a significant impact on population dynamics and line intensities, it plays an even more critical role in the accuracy of line positions. Transition energies between n-shells of even complex ions can be grossly obtained to within about 10 % by very simple screened hydrogenic estimates, which account for shell energies and screening. Transition energies between nl or nlj orbitals can be determined within about 1% using relatively straightforward Hartree- or Dirac-Fock methods, which account for spin-orbit coupling and relativistic effects. However, high-resolution spectrometers can measure line positions to parts per million, and reliable line identification generally requires multiconfiguration calculations that include extensive configuration interaction effects, which influence both transition energies and rates. The poor performance of models with even modest averaging (by relativistic configuration) is illustrated by the dashed-line spectrum in Fig. 1.3, which shows transitions from a Dirac-Fock structure calculation [7] in comparison to the emission predicted by a fine-structure calculation based on atomic data from the Flexible Atomic Code [8]. Not only does the less detailed calculation fail to capture line emission from metastable states at low densities, but its predictions for transition energies are significantly less accurate.

Like completeness, the degree of state detail plays a significant role in model accuracy at all densities. The importance of detailed state structure is most obvious at low densities, where metastable effects are large, collisional broadening is

small, and emission lines can be measured with high precision from long-lived and well-characterized plasmas. At higher densities, collisions move level populations towards LTE, broaden emission lines through collisional and Stark effects, and increase the population in high-n and highly excited states. This population transfer shifts emission from distinct single-line resonance transitions to complex satellite features that can be reasonably well described by unresolved transition arrays (UTAs) [9] or other statistical treatments [10]. But as population moves into these exotic states, the precise treatment of the pressure ionization that truncates the state space begins to play a determining role in model predictions, and the degree of state detail determines how accurate that treatment will be. In aluminum at T = 100 eV and solid density, for example (cf. [3]), the n = 3 M-shell is significantly perturbed by free electrons and neighboring ions. But a 3s orbital has a much different shape and character than a 3d orbital and is affected differently by the dense plasma environment. Such differences cannot be resolved by models that do not account for subshell splitting.

### 1.4 Application-Driven Approaches to Balancing Detail and Completeness

The tension between state-space completeness and the degree of state detail arises because computational resources are finite. In the present computational environment, collisional-radiative calculations with  $\sim 10^3$  states can be done quickly and routinely, and  $\sim 10^6$  states can be calculated with heroic effort. To illustrate this tension between completeness and detail, consider a three-electron Li-like ion with  $n_{max} = 10$ —a relatively simple and restricted system. The number of fine-structure levels scales roughly with statistical weights, which grow factorially as  $g_n!/[N!(g_n-N)!]$  for each  $(n)^N$  complex. A strictly complete fine-structure representation of even this simple three-electron system has more than  $10^6$  states and is approaching intractability. A highly averaged SHM model, which grows roughly as (n + N - 1)!/[N!(n-1)!], is strictly complete with only a few hundred states for the same ion. An effectively complete coronal fine-structure model limited to only the ground and singly excited configurations (reliable only at coronal densities) also has only a few hundred states.

Restricting the state space and reducing the degree of state detail can both increase computational efficiencies in collisional radiative models by orders of magnitude, and both are viable strategies for designing tractable CR models. But each concession, each departure from the ideal, has implications for the model's accuracy and range of applicability. The sections below describe the advantages and limitations of approaches to collisional-radiative modeling that have been developed in response to the tension among state-space completeness, the degree of state detail, and computational tractability.

10 S.B. Hansen

#### 1.4.1 Coronal Fine-Structure Models

In low-density plasmas like those found in tokamaks ( $N_e \sim 10^{14}$  e/cm³), electron beam ion traps (EBITs,  $N_e \sim 10^{12}$  e/cm³), and stellar coronae ( $N_e \sim 10^{10}$  e/cm³), collisional rates are dwarfed by radiative decay rates and the overwhelming majority of population resides in ground states. High-resolution emission spectroscopy of these plasmas produces sharp, well-defined lines that can only be matched by highly detailed and accurate atomic structure calculations. Bright emission lines from metastable states in these plasmas require extensive modeling of collisional, radiative, and cascade processes among the singly excited states. Distinct dielectronic recombination satellite lines formed by radiative stabilization of autoionizing states following dielectronic capture are present but tend not to dominate the emission spectra.

These observations have driven extensive development of highly detailed fine-structure collisional-radiative models. Since only ground states have significant population, most emission can be adequately described by including only states formed by single excitation from the ground configuration. Including a modest number of doubly excited states with  $\Delta n = 1$  or 2 above the valence shell is generally sufficient to account for observed DR satellite emission, and completeness in the DR channels can be ensured by implicit inclusion of doubly excited high-n states through DR rate tables (e.g. [5]).

These coronal CR models can produce very good agreement with high-precision data from low-density plasmas and are used to diagnose temperatures, densities, and velocities (through Doppler shifts of well-resolved lines). They can generally handle non-thermal electron velocity distributions and modest external radiation flux. But as electron densities increase past  $\sim 10^{17}$  e/cm³ or photon fluxes brighten towards  $T_{rad} \sim T_e$ , increasing excitation rates can move significant population into excited configurations, invalidating tabulated ground-state DR rates and opening up population channels into multiply excited states that are not generally included in these models. At high densities, these models tend to be significantly overioinized and produce spectra with profound deficits in both emission and absorption.

#### 1.4.2 General Models for Moderate-Density Plasmas

Laboratory plasmas generated by high-power lasers or high-current discharges through solid, foam, or gas targets produce emission spectra with distinct emission lines and satellite complexes that cannot, in general, be completely described by coronal-style models. At densities of  $10^{18}$ – $10^{22}$  e/cm³, the emission from these plasmas can be measurably influenced by collisional and Stark broadening, and the charge state distribution is governed by a complex interplay of all of the collisional and spontaneous processes that inform the rate matrix. Excited-state populations are high enough to require explicit treatment of dielectronic capture and multiple excitation,

opening up new configuration space that presents a computational challenge for detailed models. Highly averaged general models like the SHM that can more easily handle this required completeness are challenged by the continuing presence of metastable states and produce only rough agreement with high-precision spectroscopic measurements. The tension between model completeness and detail is thus profound in this moderate-density plasma regime, and many different approaches have been taken.

Some models start with an extensive database of fine-structure states and rates calculated using sophisticated multi-configuration atomic structure codes and perform a brute-force averaging of the fine-structure states and rates in order to obtain a tractable collisional-radiative rate matrix (e.g. [11]). After the CR solution is obtained, the fine structure states can be populated according to Boltzmann statistics and used to generate spectra with accurate line positions. Such models typically limit the principal quantum number to  $n_{max} \sim 6$  and the number of allowed excitations to two or three and these excitation are allowed only from near-valence shells. These restrictions help keep the atomic structure and rate calculations tractable, and the CSD and RPL predictions from these models tend to be of very high quality. At low densities, the CSDs from these models will not be quite as accurate as those from coronal models, since they lack both the complete implicit DR channels and ladder ionization from metastable states. At high densities, the models must incorporate ad-hoc continuum lowering effects and, since they exclude extensive multiply excited state structure, may lack the completeness to provide highly accurate charge state distributions and spectra. Finally, although the line positions from these models are as accurate as their underlying atomic data, the intensities of lines arising from states that are not statistically populated (e.g. by cascades into metastable sates or strong dielectronic capture) can be highly inaccurate and would not be suitable for density diagnostics based on line ratios.

Other models start with a database of either relativistic or semi-relativistic configuration-averaged states (e.g. [12]), which can be calculated much more efficiently and permit an extension of the state space to a higher n (typically  $n_{max} \sim 8$ ) and more extensive excitation (for example, multiple excitations from the valence shell or excitation from inner shells). These extensions in state-space completeness improve the performance of these models at both high and low densities, and such models typically produce high-quality CSDs and RPLs over a very wide range of plasma conditions. However, their spectra can be only roughly compared with experimental data, as we have illustrated in Fig. 1.3. While the spectra could not be used for density diagnostics based on metastable line intensities, they can certainly be used to assess temperature based on the observed charge states. This class of model is discussed further in Chap. 2.

A third class of generally applicable model is based on the screened hydrogenic approach described in Chap. 3 (e.g. FLYCHK [13, 14] and DCA [15]). These models can calculate level structure and rates for arbitrary superconfigurations as needed for the calculation at hand; they do not require pre-existing atomic structure or rate databases. They tend to be orders of magnitude faster than either of the model types

described above, while being also significantly more complete. They tend to provide good-quality CSDs over a wide range of densities but only fair estimates for RPLs, since  $\Delta n = 0$  emission for nl - nl' transitions within the superconfigurations has to be added with an ad-hoc representation of the subshell populations. Since the spectra produced from the n-shell state structure of these models bears little resemblance to all but the simplest experimental data, those SHM models that produce spectra generally use external atomic structure data that includes subshell splitting, impose statistical or Boltzmann internal distribution functions to populate subshells within the screened hydrogenic SCs, and are used only for rough estimates of emission or absorption spectra. Although these models are not particularly reliable for plasma diagnostics, they are extremely useful as aids to experimental design, are fast enough to be used inline in radiation-hydrodynamic calculations (see Chap. 4), and are accurate enough to help define the required state space for or bootstrap calculations with more detailed CR models.

A fourth class of general CR model is based on hybrid-structure states. These models attempt to use the highest degree of detail necessary for the desired application, but implement that detail as selectively as possible in order to maintain tractability. One such hybrid-structure model [16] starts with a relatively complete set of highly averaged states and then splits these states on successive iterations of the collisional-radiative solver until convergence is reached in the CSD and RPL. Another model [17] couples a limited fine-structure database of "coronal" states to a more extensive set of configuration-averaged and SHM states. The coronal states ensure good agreement with experimental line positions and intensities at low densities, the configuration-average states provide a reasonable treatment of satellite emission from high-*n* and multiply excited states, and completeness is ensured by the superconfigurations, which are determined by a bootstrap SHM calculation that dynamically extends the state space until the CSD and RPL converge. A third example of the hybrid-structure approach augments the spectrum from a configuration-average calculation with selected strong fine-structure transitions [18].

These hybrid-structure models can efficiently produce both accurate spectra and reliable CSDs and RPLs. But they are more difficult to design and implement than models with uniform state structure because they require combining data structures that can have a quite disparate properties. Fine-structure states typically have relatively small statistical weights, are well represented by a degenerate element in the population matrix without internal energy structure, and include extensive configuration interaction (CI) that ensures high accuracy in line positions. By contrast, configuration-averaged states are typically calculated with only limited CI and can have much larger statistical weights with implicit internal energy structure. Often, the internal partition function of configuration-averaged states is well-represented by simple Boltzmann statistics (low-lying metastable states are a significant exception; these must be treated individually in the rate matrix). Finally, superconfiguration states average over even spin-orbit effects, excluding CI entirely, and can have enormous statistical weights. Worse still, superconfigurations can have significant implicit internal structure, with energy splitting similar to the ionization potential

for complex many-electron ions. Combining such disparate state structures without enforcing consistency among them can lead to unphysical results. For example, satellite emission from configuration-averaged levels that do not include extensive CI can easily fall on the wrong side of fine structure lines that do [19]. And assuming statistical populations within extensively averaged states at low densities, where population is highly concentrated in the low-lying implicit levels, can lead to gross inaccuracies in state populations [20].

#### 1.4.3 Self-consistent Field Models for Dense Plasma

Plasmas near solid density ( $N_e > 10^{23}$  e/cm³) tend to emit and absorb radiation in a broad quasi-continuum, with density-broadened lines and strong satellite features that can be reasonably well described by unresolved transition arrays. Pressure ionization of high-n states plays a major role in determining the state space, as the populated valence wavefunctions are distorted by interactions with free electrons and neighboring ions. Precise measurements are difficult to make in the high-energy-density regime due to the short lifetimes and high gradients of laboratory experiments and the opaque material surrounding astrophysical sources that reach these extreme conditions. Thus model development in this regime is often driven by theoretical constraints rather than experimental data. Theoretical validation is enabled by the highly collisional environment that drives populations towards LTE.

One example of models that perform well at the high density extreme are ion sphere models, which solve for the wavefunctions of nl or nlj orbitals in a selfconsistent field surrounding a fictitious average atom. The average atom is allowed to have non-integer shell occupations and can respond to dense plasma environments in a physically consistent way. Because continuum lowering is natively included and the average atom is fully described by a small set (tens) of fractionally populated orbitals, strict completeness is easy to achieve with these highly averaged models. They thus provide a rigorous standard for more detailed models in the dense plasma regime, at least in LTE. Fractional shell populations  $X_n$  can be computed from detailed models by  $X_n = \sum_i X_i N_n$ , with  $X_i$  the fractional population of the state i and  $N_n$  the nshell occupation in that state, and directly compared with the average-atom shell populations. Any deficit in the detailed model  $X_n$  indicates incompleteness in its state structure. However, average atom models tend to produce very poor spectra, since specific configurations are required to produce distinct transitions. And moving average-atom models comfortably into the non-LTE collisional-radiative regime is difficult [21], since they lack the basic structure of distinct doubly excited states through which the critical dielectronic recombination process occurs.

While the average-atom approach has significant drawbacks, the self-consistent field approach itself provides a strong foundation for collisional-radiative modeling in the high-density regime. A highly successful class of models uses expansions of average-atom wavefunctions to form configurations with integer occupations that

are amenable to standard collisional-radiative modeling treatments. Unlike models based on isolated-ion data, which impose ad hoc external treatments to account for continuum lowering and pressure ionization effects, these self-consistent field models include density effects in a native and self-consistent way. The two major drawbacks to most models of this type are the general lack of extensive configuration interaction and the computational overhead required to generate the state space and rate coefficients from scratch for each specific set of plasma conditions. However, the ability to generate new states can facilitate novel approaches to CR modeling: one appealing approach starts with a state space consisting of a single configuration, then computes final states and rate-based probabilities for all one- and two-electron processes out of that configuration. A Monte Carlo algorithm takes a random walk through the state space, constructing the state space and state populations simultaneously and requiring much less memory than a fixed-state-space model of equivalent size [2]. Another approach uses expansions of average atom orbitals to determine the required state space for particular conditions and then refines the atomic structure to produce reliable emission and absorption data [22].

#### 1.5 Conclusions

Balancing the competing requirements of state detail, state-space completeness, and computational tractability is a key challenge in collisional-radiative modeling. An ideal general model that includes both the highly detailed state structure required for accurate spectroscopic predictions and the strictly complete state space required for accurate charge state distributions would be utterly intractable for all but the simplest ions. Designing a reliable and tractable collisional-radiative model requires understanding the consequences of each departure from the ideal and must be informed by the model's intended application. A model intended for inline use in radiative hydrodynamics codes, where speed and validity over a wide range of conditions are essential, will have a very different character than a model intended for spectroscopic analysis of high-resolution data, where highly accurate state structure and populations are required. This Chapter has explored the impact of limiting state-space completeness and detail on model reliability and has described a variety of model design approaches for diverse applications.

**Acknowledgments** Sandia National Laboratories is a multi-program laboratory managed and operated by Sandia Corporation, a wholly owned subsidiary of Lockheed Martin Corporation, for the U.S. Department of Energy's National Nuclear Security Administration under contract DE-AC04-94AL85000. This work was supported by the U.S. Department of Energy, Office of Science Early Career Research Program, Office of Fusion Energy Sciences under FWP-14-017426.

#### References

- 1. D.A. Libermann, J.R. Albritton, J. Quant. Spectr. Rad. Transfer 51, 197 (1994)
- 2. B.G. Wilson, J.R. Albritton, D.A. Libermann, preprint UCRL-JC-104252 (1990)
- O. Ciricosta, S.M. Vinko, H.-K. Chung, B.-I. Cho, C.R.D. Brown, T. Burian, J. Chalupsky, K. Engelhorn, R.W. Falcone, C. Graves, V. Hajkova, A. Higginbotham, L. Juha, J. Krzywinski, H.J. Lee, M. Messerschmidt, C.D. Murphy, Y. Ping, D.S. Rackstraw, A. Scherz, W. Schlotter, S. Toleikis, J.J. Turner, L. Vysin, T. Wang, B. Wu, U. Zastrau, D. Zhu, R.W. Lee, P. Heimann, B. Nagler, J.S. Wark, Phys. Rev. Lett. 109, 065002 (2012)
- H.-K. Chung, C. Bowen, C.J. Fontes, S.B. Hansen, Y. Ralchenko, High En. Dens. Phys. 9, 645 (2013)
- P. Mazzotta, G. Mazzitelli, S. Colafrancesco, N. Vittorio, Astron. Astrophys. Suppl. Series 133, 403 (1998)
- 6. A. Derevianko, W.R. Johnson, Phys. Rev. A 56, 1288 (1997)
- 7. D.A. Liberman, J.R. Albritton, B.G. Wilson, W.E. Alley, Phys. Rev. A 50, 171 (1994)
- 8. M.F. Gu, Astrophys. J. 582, 1241 (2003)
- 9. A. Bar-Shalom, J. Oreg, W.H. Goldstein, Phys. Rev. A 40, 3183 (1989)
- 10. C.A. Iglesias, High En. Dens. Phys. **8**, 253 (2012)
- 11. S. Mazevet, J. Abdallah Jr., J. Phys. B 39, 3419 (2006)
- C.J. Fontes, H.L. Zhang, J. Abdallah Jr., R.E.H. Clark, D.P. Kilcrease, J. Colgan, R.T. Cunningham, P. Hakel, N.H. Magee, M.E. Sherrill, J. Phys. B, (in press) (2015)
- 13. H.-K. Chung, M.H. Chen, W.L. Morgan, Y. Ralchenko, R.W. Lee, High En. Dens. Phys. 1, 3 (2005)
- 14. H.-K. Chung, M.H. Chen, R.W. Lee, High En. Dens. Phys. 3, 57 (2007)
- 15. H.A. Scott, S.B. Hansen, High En. Dens. Phys. 6, 39 (2010)
- 16. O. Peyrusse, J. Phys. B 33, 4303 (2000)
- 17. S.B. Hansen, J. Bauche, C. Bauche-Arnoult, M.F. Gu, High En. Dens. Phys. 3, 109 (2007)
- 18. O. Porcherot, J.-C. Pain, F. Gilleron, T. Blenski, High En. Dens. Phys. 7, 234 (2011)
- 19. S.B. Hansen, Can. J. Phys. 89, 633 (2011)
- 20. S.B. Hansen, J. Bauche, C. Bauche-Arnoult, High En. Dens. Phys. 7, 27 (2011)
- 21. G. Faussurier, C. Blancard, E. Berthier, Phys. Rev. E 63, 026401 (2001)
- 22. M. Jeffery, L.M. Upcraft, J.W.O. Harris, D.J. Hoarty, High En. Dens. Phys. 9, 642 (2011)

## Chapter 2 Self-consistent Large-Scale Collisional-Radiative Modeling

Christopher J. Fontes, James Colgan and Joseph Abdallah Jr

**Abstract** The ability to accurately model plasmas with the collisional-radiative approach typically depends on a number of factors. For example, the number of bound electrons per ion and the particular quantities to be modeled are two key determinants. When the dominant ion stages of a plasma contain only a few electrons per ion, it is possible to construct models in full fine-structure detail. The underlying list of configurations can be chosen to be sufficiently complete such that all quantities of interest, ranging from aggregate quantities such as the mean ion charge to detailed spectroscopic quantities such as the emission spectrum, can be calculated in a converged manner. For plasmas composed of more complex ions, it is often necessary to construct atomic models using an averaged scheme, such as the average-atom or configuration-average methods. In this case, quantities such as the mean ion charge and radiative power loss may still be accurately determined, but obtaining spectroscopically accurate line features can be computationally challenging or intractable. In this work, we use the Los Alamos suite of codes to illustrate some of the concepts associated with large-scale collisional-radiative modeling. Emphasis is placed on the use of fine-structure and configuration-average models with a significant level of detail in order to generate plasma quantities in an ab-initio, self-consistent fashion, with as little approximation as possible. This approach can be used as a benchmark for comparison with less detailed models or for comparison with experimental data.

C.J. Fontes (⊠) · J. Colgan · J. Abdallah Jr Los Alamos National Laboratory, Los Alamos, NM 87545, USA e-mail: cjf@lanl.gov

J. Colgan

e-mail: jcolgan@lanl.gov

J. Abdallah Jr e-mail: abd@lanl.gov 18 C.J. Fontes et al.

#### 2.1 Introduction

During the early development of the collisional-radiative (CR) modeling of plasmas in the 1960s, e.g. [1, 2], applications were limited to simple H- and He-like ions with a relatively small (<20) number of energy levels. In fact, Bates, Kingston and McWhirter coined the phrase "collisional-radiative recombination" in their early work [1]. Those numerical simulations were made possible due to then-recently available atomic physics data and access to "modern" computers that could be used to solve the relevant system of coupled linear equations. Their use of CR modeling provided insight into the recombination heating of fusion plasmas that was not possible by analytic techniques, providing a pertinent example of the role that numerical analysis could play in understanding complex phenomena.

During the intervening 55 years, CR modeling has expanded in a multitude of directions. State-of-the-art methods regularly include atomic models that explicitly contain thousands of bound-electron energy states in ions and neutral atoms, with maximum values exceeding one million states. Averaging techniques allow for the implicit consideration of models that implicitly describe more than a billion states, albeit in an aggregate sense. These CR methods are fed by an impressive, vast array of fundamental atomic data from which the necessary atomic rates are derived. The generation of such data and the CR modeling itself are, of course, made possible by the steadily advancing power provided by modern computational platforms.

However, the situation has not advanced so far that computers have taken the place of physical insight and intuition when it comes to large-scale CR modeling. The quality of the CR solution is only as good as the atomic physics model that is used as input. Constructing a good model for a particular application requires some experience, which also helps in understanding whether the resulting solution is reasonable, both from a physical and numerical perspective. There are a number of considerations that go into building an atomic physics model. Three of the most basic ingredients are: (1) the states that are included in the model, (2) the fundamental data that describe the states and the processes that connect them, e.g. energies and rate coefficients, and (3) the amount of averaging or expanding that will be applied to these data before the rate matrix is constructed.

In the next section, we will discuss some common methods for choosing the states in a particular model. A proper discussion of the accuracy of the fundamental atomic data has been the subject of intensive research for decades. This topic includes which theories, e.g. Hartree-Fock, Dirac-Fock-Slater, close-coupling, distorted-wave, etc., produce sufficiently accurate atomic structure and cross section data to model a given application. A well-known, general trend in this context is that the more highly charged the ions in a plasma become, the more accurate it is to calculate the atomic data with perturbative methods. This behavior is due to the fact that, as the mean

<sup>&</sup>lt;sup>1</sup>We note the use of the word "states", rather than "levels", in the previous paragraph. We employ "states" in this work as a generic term, which could refer to well-defined concepts such as configurations or fine-structure levels, or some sort of averaged quantity. The word "levels" is reserved for fine-structure levels in this work.

charge of a plasma increases, the number of bound electrons per ion decreases. In this case, the Coulomb interaction between bound and continuum electrons can be more accurately described in a perturbative sense, since the complicated effects due to correlations among the bound and free electrons decrease in relative importance. We will not further discuss this topic here, and the reader is referred to the literature for more details, e.g. [3, 4].

The amount of averaging or expanding that is performed on the chosen set of states dictates the level of refinement of the atomic model. Examples, in order of ascending refinement, are: average-atom, super-configuration, non-relativistic configuration-average, relativistic configuration-average, LS-term, and fine-structure treatments. In addition, hybrid schemes have been developed to combine these treatments in order to keep the number of coupled rate equations to a tractable level, while allowing spectroscopic detail to be applied where it is most needed for a given application. The level of refinement directly impacts the amount of time and computational resources required to calculate the atomic data, as well as to construct and obtain a solution of the CR set of coupled equations. More specifically, if we express the system of coupled CR equations in the standard compact matrix form

$$\frac{d\mathbf{N}}{dt} = R\mathbf{N}\,,\tag{2.1}$$

then the rate matrix, R, will be square with  $N_s$  rows and columns, where  $N_s$  is the number of states for which populations are to be computed and  $\mathbf{N}$  is the population vector of length  $N_s$ . The level of refinement determines the value of  $N_s$ . Since the time to solve the steady-state CR equations typically scales as  $O(N_s^3)$  or  $O(N_s^2)$ , depending on the method of solution, the value of  $N_s$  is a key determinant of whether a particular model will be computationally tractable.

In Sects. 2.2 and 2.3, we will discuss the commonly used configuration-average and fine-structure treatments. While it is desirable to build a very detailed, fine-structure model for every plasma application, it is simply not feasible. The number of fine-structure levels typically grows to an intractable size when the number of bound electrons per ion exceeds  $\sim 10-20$ . Therefore, we will also discuss and demonstrate some methods that are useful to calculate fine-structure models with as much detail as possible, in a computationally tractable manner.

In addition to the above physics considerations, numerical issues inevitably arise in large-scale CR modeling that do not occur when considering smaller-scale cases. For example, we discuss the existence of small cross sections in these large models in Sect. 2.2. There is also the difficult task of convincing oneself that a particular CR calculation generates the correct populations. The detailed solutions that result from such modeling are not verifiable against analytic expressions. Nevertheless, certain limiting behaviors, such as coronal equilibrium and local thermodynamic equilibrium, must be satisfied, which provides some measure of confidence before attempting to model plasmas under true CR conditions. In addition, the use of different levels of refinement in the model and the expected trends in spectral complexity can provide insight into whether the numerical implementation is functioning properly. Therefore, some discussion of large-scale verification is also provided in Sect. 2.3.

C.J. Fontes et al.

In closing this introductory section, we note that there is no formal definition of the term "large-scale" when discussing CR modeling. It is not unreasonable, at the present time in history, to apply this phrase to models with more than  $N_s \sim 10^4$  explicit states. The CR rate matrix for such a system will necessarily contain  $N_s^2 \sim 10^8$  elements (many of which are likely to be zero), which requires almost 1 GB of random access memory (RAM). When this 1 GB value is combined with the amount of additional RAM that is required to store all of the data and ancillary information to construct the rate matrix, the total needed RAM approaches 2 GB, which requires a 64-bit operating system in order to handle the addressing for such large computer programs. Admittedly, the choice of  $N_s \sim 10^4$  is a somewhat arbitrary distinction, but models of this size and beyond possess characteristics that are relevant to the discussions provided in this chapter.

#### 2.2 Large-Scale Collisional-Radiative Modeling

In order to provide a definite context for discussing various concepts associated with large-scale collisional-radiative modeling, we consider the Los Alamos suite of modeling codes. There are a number of such codes that have been developed in the CR modeling community, some of which are discussed elsewhere in this book. We focus on the Los Alamos codes here because, besides our familiarity with them, they are capable of calculating very large atomic physics models ( $>10^6$  states) in a self-consistent manner. Much of the material presented in this section is also valid for small-scale CR modeling.

The intended meaning of the term "self-consistent" in the previous paragraph is two-fold. First, it indicates that the atomic physics data are all computed within the same framework, i.e. a model is composed of data obtained from a consistent theoretical and numerical approach. The data are not assembled from different sources, which is sometimes required when a full set of self-consistent data can not be generated for various reasons. Second, it indicates that all of the states in a model are of the same type, e.g. only configurations, or only fine-structure levels of the same level of refinement (see below) are considered. This approach is in contrast to hybrid schemes, which can employ a mixture of different types of states in constructing the CR equations and/or in generating spectral quantities from the solution of those equations.

#### 2.2.1 The Los Alamos Suite of Atomic Physics Codes

The Los Alamos suite of atomic physics codes has been under development for more than 25 years. It is designed for applications to both the population kinetic modeling of plasmas and the generation of atomic structure and cross sections calculations to compare with measurements of a fundamental nature. The suite has both

semi-relativistic [5–7] and fully relativistic capabilities [8], which can be used to model plasmas under either local thermodynamic equilibrium (LTE) or non-LTE (NLTE) conditions. These codes have been applied to a diverse set of problems [5–134], some of which concern the large-scale CR modeling of present interest. Applications include: the diagnosis of plasma conditions of high energy density physics experiments, usually density and temperature, by comparison of measured emission spectra with simulations; providing estimates of radiation losses in magnetic fusion devices; modeling astrophysical systems, including the emission from solar corona and supernovae, as well as the opacity at the base of the solar convection zone and in stellar envelopes; and commercial applications, such as lighting systems and lithography.

A schematic diagram of the suite is displayed in Fig. 2.1. We provide only a brief overview of the suite here, as it has been described in some detail in previous publications [5–8]. The fundamental atomic physics codes, CATS, RATS, ACE and GIPPER, generate data associated with the commonly considered processes of electron-impact excitation and de-excitation, photo-excitation, spontaneous and stimulated radiative decay, electron-impact ionization, three-body recombination, photo-ionization, radiative recombination, autoionization, and dielectronic capture. More exotic processes, such as collisional double ionization and its inverse, four-

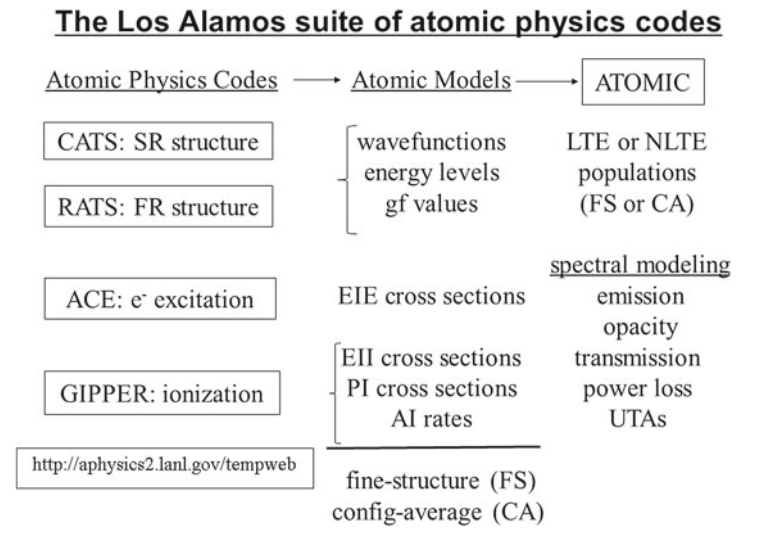


**Fig. 2.1** A schematic diagram of the Los Alamos suite of atomic physics codes: CATS, RATS, ACE, GIPPER and ATOMIC. The first four codes produce fundamental atomic physics data that are processed by ATOMIC, which calculates populations for plasmas under local thermodynamic equilibrium (LTE) or non-LTE (NLTE) conditions, as well as a variety of spectral quantities. Abbreviations are as follows: *SR* semi-relativistic, *FR* fully relativistic, *EIE* electron-impact excitation, *EII* electron-impact ionization, *PI* photoionization, *AI* autoionization, and *UTA* unresolved transition array

body-recombination, can also be considered [98] when the appropriate plasma conditions are encountered. CATS, based on Cowan's Hartree-Fock atomic structure codes [3] and RATS, based on the Dirac-Fock-Slater atomic structure code of Sampson and coworkers [4], are used for atomic structure and plane-wave-Born electron-impact excitation (PWB) cross sections for semi-relativistic and relativistic configurations, respectively. ACE is the associated code for computing distortedwave (DW) electron-impact excitation cross sections and GIPPER calculates cross sections and rates for ionization processes. The semi-relativistic capabilities in CATS, ACE, and GIPPER can be accessed through the internet [135]. These data-generating codes write atomic physics data files in a consistent, random-access binary format called IPCRESS, which stands for Independent of Platform and Can be Read by Existing Software Subroutines. The choice of an efficient, binary file format is crucial for handling the large amounts of data that are generated for large-scale CR modeling. The ATOMIC code processes these binary files as input in a general and convenient way to construct and solve the CR equations. The size of ATOMIC can expand to many hundreds of gigabytes to accommodate the atomic model.

#### 2.2.2 Selecting a List of Configurations

Every model that is calculated with the Los Alamos suite of codes starts by choosing a list of bound-electron configurations. The list is specified in non-relativistic (nl) notation, regardless of whether the model will be generated in semi-relativistic (SR) mode or fully relativistic (FR) mode. The SR mode produces energies and wavefunctions for each nl-type configuration, while the FR mode produces the same quantities, but for all possible relativistic  $(nl_i)$  configurations (sometimes referred to as "subconfigurations") that can arise from the specified list of *nl* configurations. Due to the extra quantum number *j* in the relativistic case, the number of subconfigurations will always be equal to or greater than the number of nl configurations. For complicated models, a given set of nl configurations can expand to a corresponding set of nlj subconfigurations that is a factor of 10–100 larger in size. This expansion factor can be an important determinant of whether a particular relativistic configuration-average model will be numerically tractable due to computer memory restrictions when trying to solve the CR equations. Of course, allowing an expansion to fine-structure mode can result in a model that has several orders of magnitude more levels than the number of underlying configurations, depending on the number of open shells in the ion stages of interest.

A proper choice of configurations depends on the type of plasma to be modeled, so that the desired spectral quantities will be calculated in an accurate, converged manner. It is not feasible to describe all possible configuration-generation algorithms here. Instead, we provide some basic concepts that have proved useful in modeling a wide range of applications with the Los Alamos suite of codes, including calculations of the numerous test cases prescribed for the series of NLTE Code Comparison Workshops [136–143] that have been held approximately ever other year since 1997.

One starts by identifying the relevant ion stages for the plasma conditions of interest. A simple estimate can be obtained from basic energy considerations, such as comparing the value of the plasma electron temperature to the ionization energies of the various ion stages for the element of interest. The NIST database [144] can be a useful tool in this regard. Another efficient method is to use a fast, hydrogenic-type code, such as FLYCHK [145], that can provide a reasonably accurate estimate of the charge state distribution for a wide range of plasmas. Sometimes the relevant ion stages can be determined by identifying spectral lines when comparing to an experiment.

Once the relevant ion stages have been identified, a list of configurations for each stage needs to be generated for each stage. In general, for the self-consistent approach that is being considered here, one typically starts with the ground configuration of a given ion stage and then creates excited-state configurations via one-electron promotions from each nl subshell, up to some maximum shell denoted by the principal quantum number  $n_{\rm max}$ . Such a simple, one-electron-promotion scheme is sufficient for modeling low-density, coronal plasmas.

As the density of the plasma increases and true CR conditions are achieved, excited states will contain a non-negligible amount of population and configurations that are connected to the ground configuration via multi-electron promotions must be included in the model. The number and type of such promotions to obtain converged populations and spectra can be very problem-specific. These promotions should typically be applied in a consistent manner across all ion stages. For example, if two-electron promotions are considered from the L shell of the ground configuration in one ion stage, then such promotions should be considered in all other ion stages. Without such consistency of promotions, there is a risk of artificially restricting the flow of population into certain states, which could result in an inaccurate set of populations and missing radiative features. The situation is analogous to the steadystate flow of water through a coupled system of connected pipes. If a particular pipe is suddenly closed off, the rate of flow in the other pipes will self-correct to different steady-state values. Of course, computational limitations sometimes make it impossible to consistently implement the same type of promotions across all ion stages. In that case, it is sometimes sufficient to implement such promotions in only the most dominant ion stages of the charge state distribution, but it is difficult to ascertain whether such a model will produce a converged set of populations because a sensitivity study with respect to model size can not be performed.

A typically important concept for collisionally dominated plasmas is to promote several electrons *within* the valence shell of the ground configuration. The maximum number of electrons involved in these intra-shell promotions should be determined such that the resulting excited configurations are reasonably close in energy. This set forms a kind of collective ground configuration on which additional single- or multi-electron promotions should be applied in a uniform manner. In this way, a reasonably complete set of energetically consistent configurations can be generated. In order to express the list of configurations that can arise from these, and other, multi-electron promotions, in a compact form, it is convenient to introduce the supershell notation. A supershell is indicated by the symbol  $[n]^w$ , which represents all permitted sets of orbital combinations that can arise from permuting w electrons within the shell

C.J. Fontes et al.

denoted by principal quantum number n. For example,  $[2]^3$  is a shorthand notation for the following three nl configurations:  $2s^2 2p$ ,  $2s 2p^2$ , and  $2p^3$ . If, instead, nlj configurations are considered, the same  $[2]^3$  symbol represents the following seven configurations:  $2s_{1/2}^2 2p_{1/2}$ ,  $2s_{1/2} 2p_{1/2}^2$ ,  $2s_{1/2} 2p_{3/2}$ ,  $2s_{1/2} 2p_{3/2}^2$ ,  $2s_{1/2} 2p_{3/2}^2$ ,  $2s_{1/2} 2p_{3/2}^2$ ,  $2s_{1/2} 2p_{3/2}^2$ ,  $2p_{1/2}^2 2p_{3/2}^2$ , and  $2p_{3/2}^3$ . More complicated lists of configurations can be easily specified by appending additional supershells to form superconfigurations, e.g.  $[2]^3 [3]^5$  represents a particular set of 45 nl configurations in the O-like ion stage. The notation  $[n-n']^w$  indicates that w electrons are to be permuted within a range of shells, from n to n'. The modified supershell notation,  $[n]_y^w$ , provides more control in specifying a list of configurations by limiting the number of permuted electrons within the n shell to be the integer  $y \le w$ . Thus,  $[1]^2 [2]^8 [3]_2^{13}$  represents all configurations that arise from two-electron promotions within the n=3 shell of the ground configuration of V-like ions, i.e. from  $1s^2 2s^2 2p^6 3s^2 3p^6 3d^5$  in nl notation. (In this example, no promotions are allowed within the K and L shells because they are full.)

The recommendation to apply a consistent set of electron promotions within the valence shell across all ion stages is, of course, not always possible because the number of valence-shell electrons is not the same in every ion stage. For example, a particular ion stage may contain only a single valence electron, in which case it is impossible to perform, for example, the 3-electron permutations that are allowed just two ion stages away. In this case, only 1-electron permutations should be performed. This situation becomes more sensitive when a closed-shell ion stage is at, or near, the center of the charge state distribution of the plasma. As a simple illustration, the statistical weights of the ground configurations for highly charged ions surrounding the Ni-like  $(3d^{10})$  ion stage are presented in Fig. 2.2. The Ni- and Zn-like stages both have the minimum statistical weight of one, indicating that Nature provides a barrier to the amount of population that might flow into these stages compared to the neighboring ones, at least as far as this metric is concerned. On the other hand, this paucity of statistical weight in the Ni-like stage is accompanied by the wellknown stability of its ground state from an energy-minimization perspective. Thus, population naturally tends to concentrate in the Ni-like ground state for a wider range of temperatures compared to nearby ion stages.

It can be challenging to determine how to apply a consistent set of electron promotions across these ion stages such that an accurate set of populations will result from solving the CR equations in this case. The application of a consistent set of electron promotions across all ion stages naturally leads to a model with a smaller number of configurations (and total statistical weight) in the Ni- and Zn-like stages compared to the other stages, based on simple combinatoric considerations, i.e. the ground-configuration pattern that is displayed in Fig. 2.2 is imprinted on the entire model if consistent electron promotions are applied. If the number of promotions is not sufficiently high, then the resulting charge state distribution obtained from a solution of the CR equations can exhibit an unphysical double-maximum or result in a particular ion stage not achieving dominance. This is an example of artificially limiting the flow of population into certain states. Thus, when closed-shell ion stages are relevant, care should be exercised in choosing the list of configurations. It is

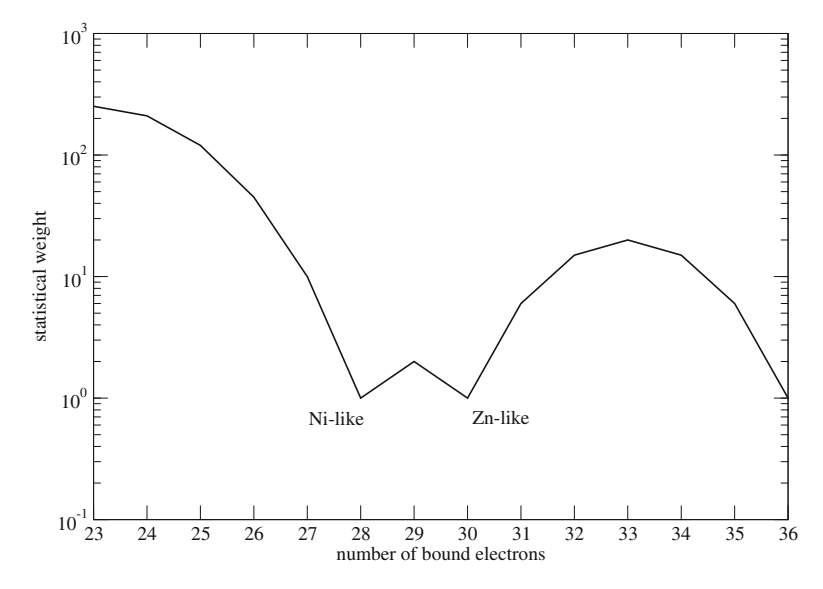


**Fig. 2.2** A plot of the statistical weight versus number of bound electrons for the ground configurations of the ion stages surrounding the closed-shell Ni-like stage. The Ni- and Zn-like stages are explicitly labeled

recommended that 3-, or more, electron promotions be considered from the Ni-like M shell to higher lying shells, and that these promotions be uniformly applied to the adjacent ion stages. In addition, up to 3-electron promotions from, and within, the N shell of the ground configurations of stages with less charge than Ni-like should also be considered. 1- or 2-electron promotions from the L shell may also be important. This approach can generate a large number of configurations, but still may not be sufficient to produce an accurate set of populations in this particular case. Sensitivity studies with respect to varying model size are highly recommended to assess the stability (and, hence, convergence) of the solution to the CR equations.

The physical state of the plasma may also impose additional requirements when generating the list of configurations. For example, for photo-driven and laser-produced plasmas, the radiation drive or presence of hot electrons might produce emission features that are associated with transitions to a final state that contain one or more innershell vacancies with respect to the ground state. In order to model such features, electron promotions must be included that encompass the appropriate radiative transitions in the model, even if the resulting states are not expected to contain a significant amount of population for the conditions of interest. These states will necessarily increase the order of the rate matrix, thereby increasing the time required to solve the CR equations. Furthermore, any state that is connected to such a radiating state via a strong rate is also potentially important and should be included in the model. Thus, when modeling plasmas that produce complicated emission features from ions with many bound electrons, the task of choosing a list of configurations

26 C.J. Fontes et al.

can be quite challenging, particularly when limited by computational resources, such as CPU time and RAM, when constructing and solving the CR equations.

#### 2.2.3 Selecting the Level of Refinement

After the list of configurations has been generated, a decision must be made about the level of refinement of the model. The two most commonly used levels of refinement in the Los Alamos suite of codes are the configuration-average (CA) and fine-structure (FS) modes. Within the CA mode, there exist the two additional two options of using non-relativistic (nl-type) configurations or relativistic (nl-type) configurations. Within the FS mode there exist four additional options that will be discussed below.

The generation of nl-type CA models starts with the CATS code and is labeled NRCA or, more commonly, SRCA when the semi-relativistic approximation is employed. The generation of nlj-type CA models is initiated with the RATS code and is labeled FRCA to indicate a fully relativistic calculation. In each case, the atomic structure calculations produce appropriately averaged energies, weighted oscillator strengths (gf values), and PWB EIE cross sections. (See, for example, [4] for a list of FRCA expressions for the various physical quantities.) The model generation continues through the ACE code to calculate more accurate DW EIE cross sections for those transitions deemed most important, based on the plasma conditions. This choice typically includes all possible excitation transitions from the ground and lowest lying configurations because they often contain the most population, which is determined by EIE for collisionally dominated plasmas. The number of DW transitions is restricted according to this prescription because DW EIE cross sections can be significantly more expensive to calculate than PWB data. After the ACE code, ionization data are generated with the GIPPER code for the three basic ionization processes and the model is complete. The ATOMIC code is then used to construct and solve the CR equations for the SRCA or FRCA model. In this case, the number of states in the model, which is also the order of the rate matrix, is simply the number of *nl*- or *nlj*-type configurations in the model.

For FS models, the level of refinement can be further broken down by the amount of configuration interaction that is included in the model. A detailed description of the four basic options (referred to as SCR, SCNR, CPLX and FULL CI) is provided in [8]. They are summarized here in Table 2.1, along with the two types of configuration-average modes described above.

The levels of refinement are listed in the table in ascending order, ranked according to the number of lines, or gf values, that can be generated from a fixed list of nl configurations. Both "single configuration" (SCR and SCNR) options are possible in RATS since it employs nlj configurations, which can be combined to obtain the more averaged nl-configuration data. On the other hand, CATS employs nl configurations and so only the SCNR option is available. In this case, the SCNR appellation is typically shortened to SC. The two single-configuration options offer a fast alternative

Level of refinement	Description				
SRCA	Semi-relativistic configuration-average model based on non-relativistic (nl) configurations				
FRCA	Fully relativistic configuration-average model based on relativistic (nlj) configurations				
SCR	Fine-structure model with configuration interaction limited to basis states arising from a single relativistic configuration				
SCNR (or SC <sup>a</sup> )	Fine-structure model with configuration interaction limited to basis states arising from a single non-relativistic configuration				
CPLX	Fine-structure model with configuration interaction limited to basis states arising from all non-relativistic configurations within a Layzer complex				
FULL CI	Fine-structure model with all possible configuration interaction				

**Table 2.1** A list of the different levels of refinement that are possible when generating an atomic physics model with the Los Alamos suite of codes

to the FULL CI option, which can be very expensive to run due to the inclusion of all possible configuration interaction when diagonalizing the Hamiltonian to obtain FS levels and energies. The SCR and SCNR options can be useful to do scoping calculations in order to get some idea of how sensitive is a particular spectrum to a FS treatment, or when a FULL CI calculation is simply not feasible. (For complicated ions, even the SCR and SCNR options may not be feasible.) The CPLX option offers a compromise between the single-configuration and FULL CI limits by limiting configuration interaction to those basis states that arise from all non-relativistic configurations within a Layzer complex [146]. This option becomes more accurate as the ion charge increases and the FS level energies tend to become grouped according to Layzer complex.

As in the case of the two types of CA calculations, the choice of which FS option to use is made before running CATS or RATS. When the atomic structure calculations are finished, those data are used in ACE and GIPPER to generate the remainder of the atomic physics model. The resulting model is fully self-consistent for a prescribed level of refinement, with the same amount of configuration interaction throughout. The choice of FS option can significantly affect the required computer time for both the atomic structure and subsequent cross section calculations. The four types of calculations can be ordered from fastest to slowest according to their level of refinement: SCR < SCNR < CPLX < FULL CI. For the complicated models indicative of large-scale CR modeling, the time required to generate the atomic model can differ by one or more orders of magnitude when comparing adjacent options in the stated hierarchy. A similar statement holds for the time required to solve the CR equations, as illustrated in Sect. 2.3.

The various levels are listed in ascending order, based on the number of lines, or gf values that can be generated from a given list of nl configurations

<sup>&</sup>lt;sup>a</sup>The SC label is typically used in place of SCNR for calculations performed with the CATS atomic structure code

28 C.J. Fontes et al.

### 2.2.4 Constructing the Rate Matrix

The construction of the CR matrix takes place after all possible collisional and radiative processes are computed for the relevant ions of interest. The competition between the rates associated with each of the fundamental atomic processes determines the ion populations within the plasma. The rates are determined from the cross sections for these processes and the plasma conditions, such as the electron-energy distribution, photon-energy distribution, and ion or electron density. Of course, one must also know the details of the atomic structure of the configurations or levels under consideration, since energy levels, occupation numbers, and statistical weights are all required to compute rate coefficients. Usually one only computes the cross sections for the five forward-going processes, (electron-impact excitation, photo-excitation, electron-impact ionization, photo-ionization, and autoionization), since the cross sections for the corresponding inverse processes can be determined from the appropriate micro-reversibility relations [147]. Such an approach guarantees internal consistency, which can be absent if atomic data are obtained from multiple sources that employ different theoretical and computational methods.

The calculation of the rate coefficients for each collisional and radiative process involves an integration over the appropriate cross section and electron or radiation distribution. If the electron distribution is Maxwellian, or if the photon distribution is Planckian, the rate coefficient for an inverse process is found quickly from the principle of detailed balance [148]. However, if the electron distribution is non-Maxwellian (for example, if the plasma in question contains hot electrons) or if the radiation distribution is non-Planckian (for example, if the plasma is under the influence of a short-pulse laser), then the rate coefficient of the inverse process in question must be found by numerical integration. Such distributions require that the calculation of three-body recombination rates involve a double integration, which can be time-consuming, depending on the specifics of the problem.

An issue that is more likely to occur when dealing with large-scale models than with small models is that cross sections with negative or oscillatory behavior can be generated by the fundamental data codes for a very small number of transitions. While such behavior is precluded based on theoretical considerations, it does occur due to the implementation of various numerical approximations. For example, when computing distorted-wave EII cross sections, it is expensive to calculate explicit values at a large number of incident energies. Instead, only a few energies are chosen and the resulting values are fit with a formula that produces the correct physical behavior. This type of fitting procedure can result in negative cross sections at high incident energies.

While these cross sections are often relatively small in magnitude, and therefore unimportant for the CR modeling to be performed, the resulting rate coefficients can be represented by indeterminate values, which will cause the solver to crash. If the model is large, it can be very difficult to debug this problem. A simple option for dealing with negative cross sections is to test for negative values and to remove those particular transitions from consideration. If it is desirable to retain these transitions, it is sometimes possible to salvage a particular cross section by finding the highest

incident energy for which a positive value was calculated and then extrapolating to higher energies with an appropriate limiting formula. The high-energy values of the cross section often do not contribute significantly to the rate coefficient for Maxwellian and Planckian distributions, and so it is not necessary to calculate that portion very accurately. In such cases one can use, for example, the well-known (non-relativistic) Bethe high-energy expression of  $\ln(E_i)/E_i$  [149] for the extrapolation of EII cross sections, where  $E_i$  is the incident electron energy. Similarly, Kramers' high-energy limit of  $E_p^{-3}$  [150], where  $E_p$  is the photon energy, can be used to extrapolate when dealing with negative PI cross sections. If oscillatory behavior is detected at high energies, then the same type of extrapolation procedure can sometimes be used in an automated way to salvage such cross sections.

Once the rate coefficients for all processes are in hand, then the *rates* for each process are determined in a straightforward manner. These rates are inserted into the CR equations, which are solved to obtain the ion state populations.

## 2.2.5 Steady-State Solutions Versus Time-Dependent Solutions

For some transient plasmas, for example those found in intense short-pulse laser-matter interactions, it may be necessary to solve the full time-dependent collisional-radiative equations given by (2.1). Often, the time-dependent equations are solved until the system has reached steady-state, and the time taken to reach such a state will vary with the problem. The ordinary differential equations represented by (2.1) can be solved such that the solution for one time step represents the initial condition for the subsequent time step. One must also then specify an initial condition for the plasma at time t=0. This system of ordinary differential equations may be stiff, especially if the material starts in a neutral state, in which few free electrons are present to initiate collisions. Various routines exist to treat such systems of equations; an efficient algorithm has been given by Gear [151]. This method contains various options to treat stiff or non-stiff differential equations.

For many problems atomic processes are much faster than hydrodynamic evolution. In that case, the plasma reaches steady-state so quickly that one only need consider the steady-state solution to the collisional-radiative equations, i.e. when the left-hand-side of (2.1) is set equal to zero. In this case, (2.1) reduces to a set of coupled algebraic equations, which is considered in the following subsection.

# 2.2.6 Boundary Conditions for the Steady-State CR Equations

In order to obtain a unique solution of the rate equations described in the previous subsections, one must also specify a boundary condition for the system. Usually, either the total atom number density,  $N_a$ , or the electron density,  $N_e$ , is known for the

30 C.J. Fontes et al.

problem at hand. Although the atom number density can often be determined more readily by experiment, finding the solution to the rate equations is actually more straightforward if the electron density is known. This is because the electron density must be known to construct the rates that make up the rate equation. In the cases where the atom number density is given, one must estimate the electron density, use it to construct and solve the rate equations, and then compare the resulting atom number density to the specified value. An iterative scheme can then be employed to converge on the electron density that produces an atom number density in agreement with the specified value within a prescribed tolerance.

Due to the fact that the system of steady-state CR equations is constructed in such a way that the following condition is satisfied for each row i of the rate matrix:

$$R_{ii} = -\sum_{j \neq i} R_{ji}, \tag{2.2}$$

the system of equations is not linearly independent. This condition arises from the requirement that each rate for a given atomic process (associated with a transition from state i to j) appear exactly twice in the rate matrix: once as a positive contribution to the (off-diagonal)  $R_{ji}$  element as a populating term for state j, at the expense of state i, and once as the equivalent negative contribution to the (diagonal) element  $R_{ii}$  as a depopulating term of state i, in favor of state j. Thus, a boundary condition must be chosen to close the system of equations, resulting in a unique set of state populations.

There are several options for the boundary condition. One possible option is that charge neutrality be enforced, i.e.

$$\sum_{is} (i-1)N_{is} = N_e , \qquad (2.3)$$

where s is the index of a particular state of ion stage i, with i=1 for the neutral stage, i=2 for the singly ionized stage, etc. So,  $N_{is}$  represents a particular element of the solution vector  $\mathbf{N}$  that appears in (2.1). The charge neutrality condition is used in place of one of the CR equations and that new system of equations is actually solved. If the electron density,  $N_e$ , is known, the new system of equations is solved directly to obtain the corresponding ion state populations. If the atom number density is specified, the system of equations is solved by varying  $N_e$  until particle conservation is satisfied, i.e.

$$\sum_{ia} N_{is} = N_a. \tag{2.4}$$

For systems where the neutral stage is included, use of the charge neutrality condition results in a number of zeros being inserted into the rate matrix, with one zero being added for each state in the neutral stage. This insertion can sometimes be problematic as it may increase the condition number of the matrix, making it harder for standard

numerical techniques to produce an accurate solution. One can also test the stability of a given solution obtained from this approach by replacing different equations with the charge neutrality condition, in order to gauge the sensitivity for a particular problem of interest.

Alternatively, one can obtain a solution of population ratios from the reduced system of equations that results from removing a single row and column that corresponds to a particular state from the rate matrix. A unique set of absolute populations can then be obtained from these ratios by using the charge neutrality condition defined in (2.1). This approach can sometimes produce a new matrix that is better-conditioned and hence easier to solve since no boundary condition explicitly appears, potentially avoiding some of the problems previously discussed.

It is often worthwhile to solve the steady-state CR equations using several of the methods described above, within available resource limitations, as this can allow some assessment of the accuracy of the population vector. This is particularly true for large-scale modeling, for which the dynamic range of the state populations can be quite large and calculating accurate values for the smallest populations can be numerically challenging.

# 2.2.7 Different Methods of Solving the Steady-State CR Equations

After choosing a particular method for including the boundary condition per the previous section, we recast the resulting set of coupled algebraic equations into the generic matrix equation of the form  $A\mathbf{x} = \mathbf{b}$ . There are several different options available to solve this generic problem inherent in finding the ion state populations from the system of CR equations for the steady-state case. Choosing the best option for obtaining a solution usually depends on the properties of the matrix A.

The most reliable way to solve such a linear algebraic system is usually a direct approach, which is most often done through LU decomposition, or some variant thereof. Highly optimized numerical libraries, such as LAPACK [152], contain efficient routines for such treatments. However, the time to obtain a solution with such methods typically scales as  $O(N_s^2)$  or  $O(N_s^3)$ , where, again,  $N_s$  is the order of the matrix given by the number of states in the model. For larger problems, this scaling can require CPU times that are prohibitive. Also, since this method stores every element of the matrix, the storage requirements can also become problematic as the size of the matrix increases.

When the option described in the previous subsection is chosen to remove a single row and column from the rate matrix, rather than to explicitly include the boundary condition, it is possible to take advantage of the block tri-diagonal (BTD) structure of the resulting matrix A. BTD methods, e.g. [153], require less memory than direct solvers since they do not consider the zero elements that reside outside of the blocks. The time scaling of BTD solvers can be better than more generic direct solvers, but is

dependent on the number and size of the blocks. In the limit that each block contains only a single element, i.e. a simple tri-diagonal system, the scaling is linear,  $O(N_s)$ . The time scaling of BTD solvers on actual CR problems of interest typically falls between linear and quadratic.

A convenient method for large-scale systems can often take the form of an iterative approach. A commonly used method is known as the Generalized Minimum Residual (GMR) method [154, 155]. This approach generates a sequence of approximations to the true solution and has a convergence criterion based on the size of the scaled norm of the residual of the matrix (where the residual is defined as  $RES = ||\mathbf{b} - A\mathbf{x}||$ ). A key advantage of such an approach is that, given a good initial estimate of the solution vector  $\mathbf{x}$ , the GMR method can quickly converge on the correct answer, often to within a very tight tolerance criteria. The CPU time required to obtain such a solution can often be much smaller than for direct methods. Another advantage of this approach is that one need only store the non-zero elements of the matrix, as well as two corresponding one-dimensional arrays containing the indices of the non-zero elements. Thus, the storage requirements can be much smaller than a direct approach, especially when the matrix in question is sparse.

However, some caution is advised when using such iterative methods: for ill-conditioned systems, which often occur when the neutral stage is included within the model, the GMR approach as implemented via the SSLUGM program [156] may not converge or may sometimes converge to an incorrect solution. Furthermore, when the GMR method (again, as implemented via SSLUGM) is applied to problems characterized by a dense matrix, its performance may become seriously degraded. This behavior is due, in part, to the internal requirements of methods such as SSLUGM to sort various arrays in the appropriate order, which may take significant time for arrays with millions of elements.

For many plasmas of interest that are at relatively high temperatures, the dominant ion stages are well away from the neutral stage, and the number of interactions included between the states is relatively few, making the resulting collisionalradiative matrix quite sparse. The sparsity of such matrices can often be 1% or less, where sparsity is defined as the ratio of the number of non-zero matrix elements to the number of total matrix elements expressed as a percentage. A high level of sparsity typically also occurs under general conditions for models that are computed in configuration-average mode. When the configuration-average mode is considered, the fraction of allowed transitions between states compared to the theoretical limit of  $N_s^2$  is significantly less than what typically occurs in a fine-structure model due to configuration interaction. When a condition of high sparsity is achieved, iterative sparse solvers are a very efficient method by which state populations can be obtained from the rate equations. As noted above, fine-structure calculations that include all possible configuration interaction between the interacting levels in the atomic structure and atomic collision stages of the calculation often produce a rate matrix that is non-sparse. Such complex cases may then require direct solvers to obtain the state populations.

When one wishes to find the solution of CR equations that contain on the order of  $10^5$ , or more, number of states, it can also be advantageous to use parallel computing

to efficiently find the solution to the rate matrix. Several packages now exist to solve matrices using parallel architectures. For example, the ScaLAPACK package is a recent parallel adaptation of the LAPACK software [157]. We have found that routines from this package scale quite well with the number of processors used, but still perform poorly with respect to CPU time when compared to iterative techniques. However, this approach should be valuable if one has a large, dense rate matrix, or one containing the neutral stage. For example, for such cases in which the memory required is too large to fit on a single processor, ScaLAPACK could prove extremely useful. There also exist parallel adaptations of iterative solvers. One which we have found to be quite efficient is the LAMG (Los Alamos Multi Grid) solver [158]. This solver has been demonstrated to produce solutions for models containing on the order of 1.2 million configurations [86], and has been shown to scale well for use with over 100 processors. The results from this approach also agreed well with results from the GMR solver, with both approaches requiring similar amounts of CPU time. Other parallel linear algebra packages that could be useful in finding the solution to the CR equations include the SuperLU package [159], which is a sparse direct solver, and the PESSL library, which is the parallel version of the Engineering and Scientific Subroutine Library from IBM [160].

It is likely that the full potential of these parallel methods of solving the rate equations will only be realized when models containing tens of millions of levels (or configurations) are constructed. In such cases, the time and memory requirements will make parallel solutions indispensable. However, for such extremely large calculations, other run-time and memory requirements must also be considered when solving a kinetics problem. In particular, issues such as constructing and storing the vast amounts of atomic data required, reading these data into a code designed to construct and solve the rate matrix, efficiently managing these data across potentially many processors of a supercomputer and parallel I/O methods must all be carefully considered when contemplating such calculations.

## 2.3 An Illustrative Example

A significant number of CR-modeling applications that were carried out with the Los Alamos suite of codes are provided in the reference list. Scattered throughout those references is additional useful information about large-scale CR modeling, including overlap with the discussion provided in this section. Noteworthy examples include [53, 86, 91, 115, 134].

In this section, we provide a steady-state example of large-scale CR modeling for the case of highly charged iron. This example does not have a particular application, but was chosen in order to conveniently illustrate a number of the issues discussed above. The model includes the seven highest charged ion stages, including the bare nucleus. A list of configurations for the H- through C-like stages is provided in supershell notation in Table 2.2. Only electric dipole allowed gf values are considered in this example, but higher-order multipole transitions [8] could have been included if

**Table 2.2** List of configurations expressed in supershell notation for H- through C-like ions of Fe

Ion stage	Superconfigurations	Ion stage	Superconfigurations
H-like	[1–10] <sup>1</sup>	He-like	[1] <sup>2</sup> [1] <sup>1</sup> [2–10] <sup>1</sup> [1] <sup>0</sup> [2] <sup>2</sup> [1] <sup>0</sup> [2] <sup>1</sup> [3–10] <sup>1</sup>
Li-like	$[1]^{2} [2-10]^{1}$ $[1]^{1} [2]^{2}$ $[1]^{1} [2]^{1} [3-10]^{1}$ $[1]^{1} [3]^{2}$ $[1]^{1} [3]^{1} [3-10]^{1}$ $[1]^{0} [2]^{3}$	Be-like	[1] <sup>2</sup> [2] <sup>2</sup> [1] <sup>2</sup> [2] <sup>1</sup> [3–10] <sup>1</sup> [1] <sup>2</sup> [3] <sup>2</sup> [1] <sup>2</sup> [3] <sup>1</sup> [4–10] <sup>1</sup> [1] <sup>1</sup> [2] <sup>3</sup> [1] <sup>1</sup> [2] <sup>2</sup> [3–10] <sup>1</sup>
B-like	[1] <sup>2</sup> [2] <sup>3</sup> [1] <sup>2</sup> [2] <sup>2</sup> [3–10] <sup>1</sup> [1] <sup>2</sup> [2] <sup>1</sup> [3] <sup>2</sup> [1] <sup>2</sup> [2] <sup>1</sup> [3] <sup>1</sup> [4–10] <sup>1</sup> [1] <sup>1</sup> [2] <sup>4</sup> [1] <sup>1</sup> [2] <sup>3</sup> [3–4] <sup>1</sup>	C-like	[1] <sup>2</sup> [2] <sup>4</sup> [1] <sup>2</sup> [2] <sup>3</sup> [3–10] <sup>1</sup> [1] <sup>2</sup> [2] <sup>2</sup> [3] <sup>2</sup> [1] <sup>1</sup> [2] <sup>5</sup> [1] <sup>1</sup> [2] <sup>4</sup> [3–4] <sup>1</sup>

desired. This particular model employs a value of  $n_{\rm max}=10$ . It contains the simplest one-electron promotions from the valence shell of the ground configuration to the n=10 shell for each ion stage There are also a number of multi-electron promotions that allow for more complicated transitions. These include a variety of single vacancies in the K-shell for all stages and double vacancies in the K shell for the He- and Li-like stages. The latter are formed by promoting both 1s electrons only to the n=2 shell. Note that similar two-electron promotions have been omitted from the lower stages, which violates the recommendation to include electron promotions across all ion stages in a uniform manner. This omission represents a possible risk of artificially restricting the flow of population into certain states and should be tested with convergence studies that include larger models and a more consistent treatment of the electron promotions. Note that a similar inconsistency exists in the B- and C-like stages for the  $[1]^1[2]^3$   $[3-4]^1$  and  $[1]^1[2]^4$   $[3-4]^1$  superconfigurations, respectively. In order to be consistent with the higher stages, the  $[3-4]^1$  notation should be replaced with  $[3-10]^1$  in these two cases.

As mentioned in the introduction, it is not possible to verify the state populations obtained from numerical solution of the CR equations against an analytic result. However, it useful to at least demonstrate that the CR solutions reproduce the expected low- and high-density limits of coronal equilibrium (CEQ) and LTE, respectively. As an illustration of such testing, the mean charge,  $\overline{Z}$ , of an iron plasma with an electron temperature of  $T_e = 2$  keV is plotted in Fig. 2.3 as a function of electron density. In this case CR, CEQ and LTE calculations were performed with the CATS code at the lowest level of refinement in Table 2.1, SRCA. The CR calculation was performed

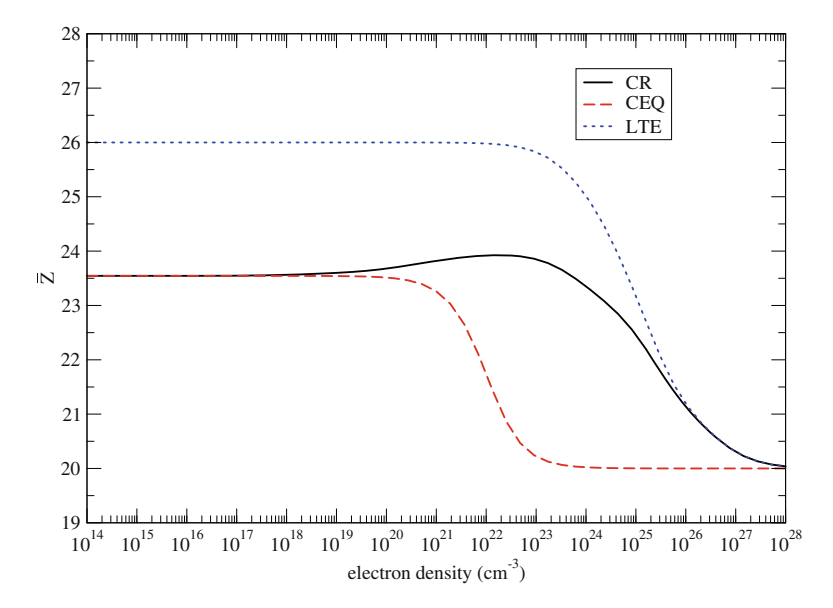


Fig. 2.3 Calculations of the mean charge as a function of electron density for an iron plasma with an electron temperature of  $T_e=2~\rm keV$ . These calculations were performed with the CATS code using the SRCA level of refinement for the model described in Table 2.2. The *solid black curve* represents a collisional-radiative (CR) calculation with a radiation temperature of  $T_r=0$ . The *dashed red curve* represents the calculation performed in the coronal equilibrium (CEQ) approximation. The *dotted blue curve* represents the calculation performed in the local thermodynamic equilibrium (LTE) approximation. The CR curve exhibits the expected limiting behaviors of CEQ at low densities and LTE at high densities

with a radiation temperature of  $T_r = 0$ . The CEQ calculation was performed under the assumption that all of the population resides in the ground configuration of each ion stage and  $T_r = 0$ , with effective ionization and recombination rates connecting each ion stage. The LTE calculation was performed with simple Saha-Boltzmann statistics at  $T_e = 2$  keV. As expected, the CR curve reproduces the limiting behavior of CEQ at low densities, transitioning from CEQ to CR conditions at an electron density of  $N_e \sim 10^{19} \, \mathrm{cm}^{-3}$ . As the electron density increases to  $\sim 10^{26} \, \mathrm{cm}^{-3}$ , the CR curve merges with the LTE result, reproducing the expected high-density behavior. The flattening out of all three curves to a constant value of 20 at the highest densities is artificial and is caused by the truncation of the model at the C-like stage. Very similar verification  $\overline{Z}$  plots can be generated for the higher levels of refinement listed in Table 2.1. More stringent tests could be performed by comparing the spectra, or even individual state populations, obtained for these three types of calculations. We emphasize that this type of verification is only a type of self-consistency check. It does not provide any information about the accuracy of the model for a particular plasma application.

Level of refinement	# of states	# of gf values	# of non-zero matrix elements	Sparsity	CPU time	$\overline{Z}$	RPL			
SRCA	1644	46550	109289	4.04	1	23.5	7.00			
FRCA	5796	299661	665881	1.98	4	23.5	5.55			
SCR	35039	1685698	26095875	2.12	251	23.6	4.55			
SCNR	35039	5079867	68769031	5.60	1428	23.6	4.46			
CPLX	35039	17382675	203443348	16.6	7237	23.6	4.31			
FULL CI	35039	28747284	326245363	26.6	22694	23.6	4.40			

**Table 2.3** Summary of information for CR calculations with different levels of refinement for the iron model described in the text

These calculations were carried out at  $T_e = 2$  keV,  $T_r = 0$  and  $N_e = 10^{14}$  cm<sup>-3</sup>. A GMR solver [156] was used to obtain the populations in all cases. The sparsity of the rate matrix is given in the form of a percentage, the CPU time required to solve the CR equations is given in seconds, and the radiated power loss (RPL) is given in W/cm<sup>3</sup>

Next, we consider the different levels of refinement for this iron model. CR calculations were performed at  $T_e = 2$  keV,  $T_r = 0$  and the specific electron density  $N_e = 10^{14}$  cm<sup>-3</sup>, which is in the CEQ region. A summary of information for the six levels of refinement is provided in Table 2.3.

The SRCA data were calculated with CATS atomic structure data and the semirelativistic approach throughout, while the remaining five levels of refinement were calculated with RATS atomic structure data and the fully relativistic treatment. The GMR approach was used in the ATOMIC code for each case to obtain population solutions of the CR equations and to generate emissivity spectra.

An inspection of Table 2.3 confirms a number of expected trends. For example, the number of states increases in going from the CA to FS modes. The SRCA calculation has the smallest number of states (nl configurations), and the FRCA calculation has the next smallest number of states (nlj) configurations). The increase in the number of states when passing from SRCA to FRCA mode is about a factor of 3.5, which is typical for a model of this size, but can reach a factor of 50 or more for very complicated models. The number of states (fine-structure levels) is identical in all four FS modes. The number of gf values increases monotonically as the level of refinement increases. The largest (FULL CI) and smallest (SRCA) values differ by a significant factor of 617. The number of non-zero matrix elements in the rate matrix and time required to solve the CR equations also increase monotonically with the level of refinement. Note the impressive factor of 22,694 increase in time required to obtain a solution when comparing the two extreme cases. The sparsity increases monotonically with the level of refinement if the simplest SRCA is excluded from consideration. The SRCA calculation possesses a higher sparsity than the FRCA one due to the differing number of transitions that are allowed for the fundamental atomic processes when taking into account *nl* versus *nlj* configurations.

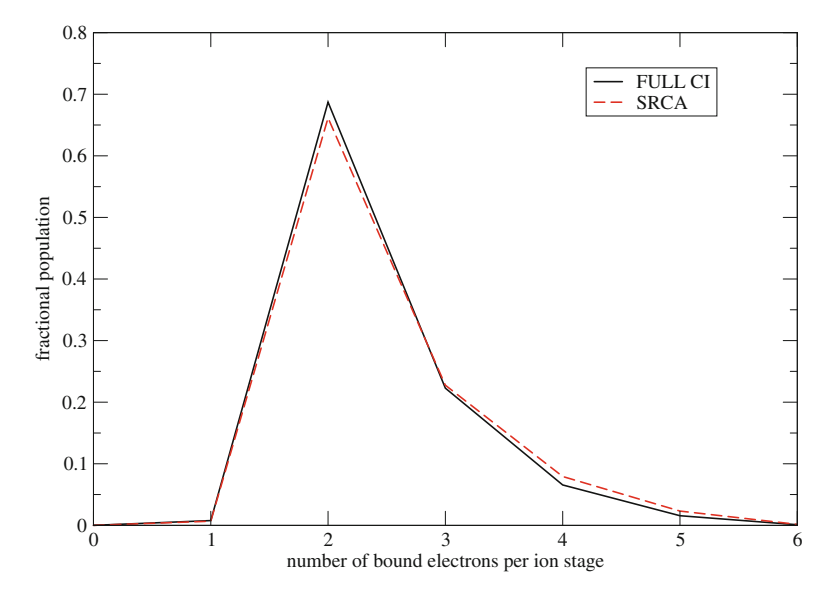


**Fig. 2.4** Calculated values of the charge state distribution for an iron plasma with  $T_e = 2$  keV,  $T_r = 0$  and  $N_e = 10^{14}$  cm<sup>-3</sup>. The FULL CI calculation is represented by the *solid black curve* and the SRCA calculation by the *dashed red curve* 

The six values of  $\overline{Z}$  are very similar, with a maximum discrepancy of 0.43 %, which is often the case when comparing this highly averaged quantity across different levels of refinement. The next-most averaged quantity to consider is the underlying charge state distribution, from which  $\overline{Z}$  can be derived. These data are displayed in Fig. 2.4 for the least and most refined calculations. The SRCA and FULL CI curves are very similar, with the peak He-like populations differing by  $\sim$ 3.9 %.

The radiated power loss (RPL) is also presented in Table 2.3. The RPL is another averaged quantity, obtained by integrating the frequency-dependent emissivity, which is examined below. In this case, some significant differences start to emerge when comparing the different levels of refinement. The two CA values of the RPL are higher than the four FS values by 25–60%. This pattern is typical and underscores the inability of CA models to properly account for the population in metastable versus dipole-radiating excited states. In FS models, the population is allowed to flow between metastable and dipole-radiating excited levels that arise from the same configuration. In CA models, the population for a configuration is essentially the sum of that contained in those two types of FS levels. The configuration will be dipole-radiating with an appropriately averaged gf value, but the population will be too high compared to the FS value, and hence the CA calculation will produce more radiation. On the other hand, the four FS RPL values are tightly grouped, differing by a maximum amount of 5.6%.

38 C.J. Fontes et al.

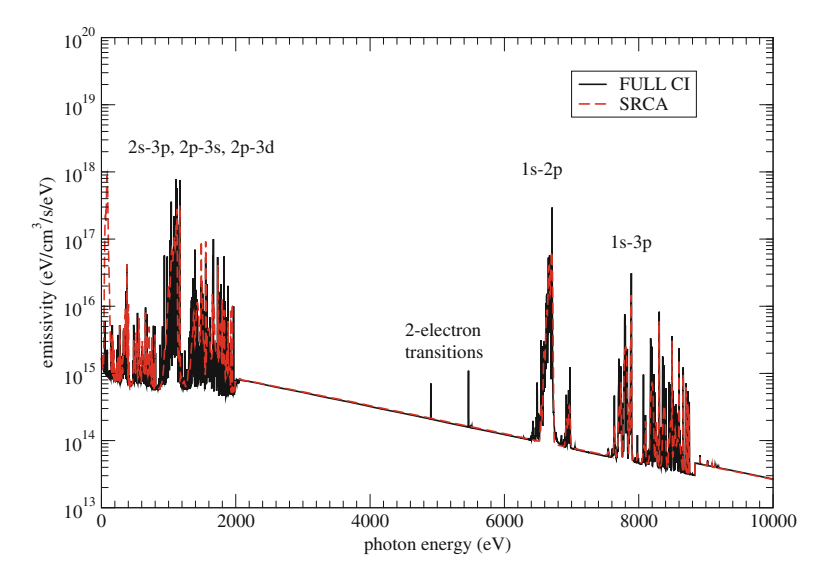


**Fig. 2.5** Emissivity versus for photon energy for an iron plasma with  $T_e=2$  keV,  $T_r=0$  and  $N_e=10^{14}$  cm<sup>-3</sup>. The FULL CI calculation is represented by the *solid black curve* and the SRCA calculation by the *dashed red curve*. Several K- and L-shell features are labeled, along with the location of two 2-electron transitions near the center of the energy range

The final analysis presented here is for the energy-dependent emission. In Fig. 2.5, we present the emissivity for the least (SRCA) and most (FULL CI) refined cases. The SRCA spectrum was calculated with the non-relativistic unresolved transition array (UTA) approach [18, 161], which was developed to broaden the CA lines in such a way that they reproduce the integrated emission obtained from a SCNR calculation. The FULL CI spectrum was calculated with basic Doppler and natural broadening using a Voigt profile. The overall qualitative agreement between the two spectra is reasonably good. The two calculations have emission features for the indicated K- and L-shell transitions in the same basic locations, but, as expected, the heights and energy positions of various lines are visibly different. In addition, the FULL CI spectrum contains features that do not exist in the SRCA spectrum. For example, the two weak, narrow lines near the center of the figure at energies of  $\sim$ 4905 and ~5465 eV correspond to exotic 2-electron transitions in the Li-like stage that can occur only when configuration interaction is included in the model. The lower energy line belongs to the  $1s 2s 2p - 1s^2 5d$  transition array, and the higher energy line to the  $1s \ 2s \ 2p - 1s^2 \ 3d$  transition array.

The complete set of six emissivities is presented in Fig. 2.6, one panel for each level of refinement in Table 2.1. The FRCA spectrum was generated with the relativistic UTA approach [162, 163] and the FS spectra were all generated with Doppler and natural broadening using a Voigt profile. At a glance, the qualitative agreement is reasonably good when comparing the six panels, The four FS calculations exhibit very similar features, but differ in the details. The  $\Delta n = 0$  features that occur at

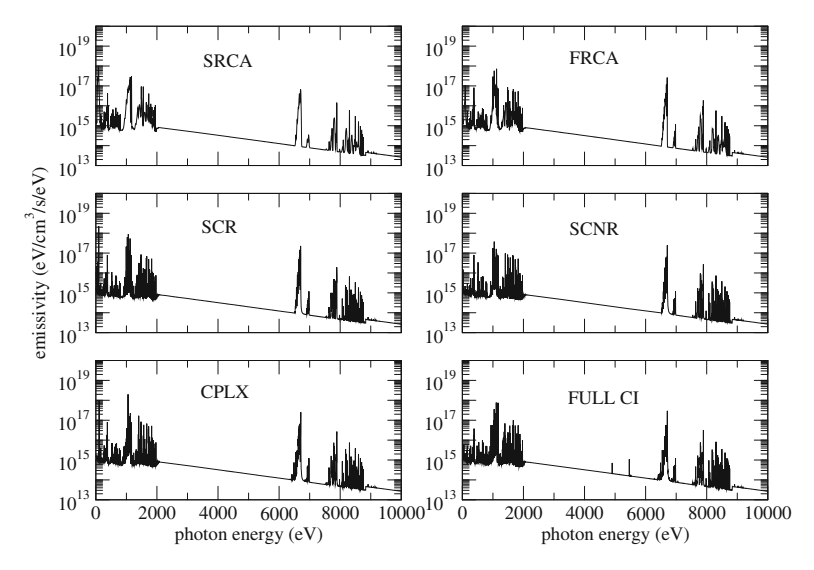


**Fig. 2.6** Emissivity versus for photon energy for an iron plasma with  $T_e = 2$  keV,  $T_r = 0$  and  $N_e = 10^{14}$  cm<sup>-3</sup>. Each panel includes a label to indicate which level of refinement was used to generate the spectrum

low energies, i.e. at the far left in each panel, are typically the most sensitive to configuration interaction, while the sensitivity of the  $\Delta n>0$  transitions occurs only for certain features in specific energy ranges. The FULL CI calculation is the only one to display the 2-electron transitions near the middle of the energy range.

The above analysis was for the coronal density of  $N_e = 10^{14} \text{ cm}^{-3}$ . According to Table 2.3, a higher density, such as  $N_e = 10^{22}$  cm<sup>-3</sup>, would place the plasma firmly within the CR region. An analysis of this higher density displays very similar patterns. For example, the number of non-zero matrix elements is the same as those reported in Table 2.3 for each level of refinement and the times to solve the CR equations are also very similar. The mean ion charge increases slightly by about 0.3. The RPL data become confined to a much tighter range, with a spread of only 5% among the six levels of refinement. The increase in density provides more collisions that reduce the metastable state populations in favor of the dipole-radiating state populations, which results in a similar RPL value for the CA and FS methods. To illustrate this point, the six emissivities for  $N_e = 10^{22}$  cm<sup>-3</sup> are presented in Fig. 2.7. The quantitative agreement between the various spectra is much improved for this higher density, but differences remain for certain lines in particular energy bands. In general, for a particular application, the physical conditions and the spectral range of interest ultimately determine whether it is worth performing a CR calculation at the highest level of refinement, or whether it is sufficient to use a more approximate, but faster, approach.

40 C.J. Fontes et al.

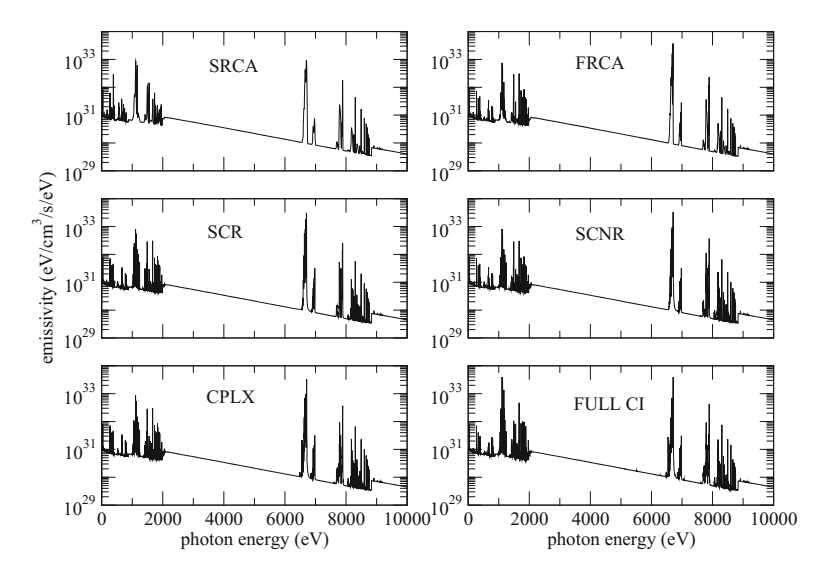


**Fig. 2.7** Emissivity versus for photon energy for an iron plasma with  $T_e=2$  keV,  $T_r=0$  and  $N_e=10^{22}$  cm<sup>-3</sup>. Each panel includes a label to indicate which level of refinement was used to generate the spectrum

## 2.4 Summary and Outlook

Steady progress has been made in the development of various aspects of CR modeling since the seminal work of Bates, Kingston and McWhirter in the early 1960s. In this chapter, the narrative focused on state-of-the-art, large-scale CR modeling, using the Los Alamos suite of atomic physics codes as a particular example. The discussion was limited to self-consistent models, which consider a single type of state, e.g. configurations or fine-structure levels. Such an approach has the desirable feature of internal consistency and uniformity across all ion stages. However, a disadvantage is that full configuration interaction calculations can not be extended to ions with an arbitrarily large number of bound electrons. Computational resources have not evolved to the point of allowing such calculations, nor are they likely to do so any time soon. Such limitations mean that the self-consistent approach must employ a lower level of refinement when modeling complicated systems. Even with a lower level of refinement, the model size may not be complete enough to obtain a converged set of populations for a given application.

In order to provide more accurate FS modeling in this case, hybrid methods are a possible option. Within the context of the Los Alamos suite of codes, the simplest type of hybrid method for FS models would be to include full configuration interaction only between configurations of spectroscopic importance. Combinations of the lower levels of refinement, SCR, SCNR and CPLX, or even no configuration interaction, could be used in calculating the atomic structure for the remaining configurations. The next level of hybridity involves the solution of the CR equations

in SRCA mode and then statistically distributing the resulting populations into the more numerous relativistic nlj configurations for the same model. Such an approach was demonstrated in [65]. This approach allows the populations to still be calculated in a fully self-consistent, albeit configuration-average approximate, manner. The use of non-relativistic configurations to solve the CR equations greatly reduces the size of the rate matrix and the time to obtain a set of populations. The splitting of the populations into more refined relativistic configurations results in many more lines, in more accurate energy positions, which would not have been possible if a self-consistent FRCA calculation had been attempted. However, a disadvantage of this approach is that statistical distribution may not produce accurate populations, particularly for metastable states, which can be very sensitive to true CR conditions.

Along the same line of reasoning, a more refined hybrid method involves the solution of the CR equations in configuration-average mode, and then those populations are statistically distributed into fine-structure levels. Such an approach was implemented in [86]. More recently [134], the same type of hybrid approach was combined with the mixed UTA (or MUTA) technique [90] to simulate tungsten emission spectra of interest to magnetic fusion research in fine-structure detail. Again, these hybrid methods allow for spectra with a significant level of refinement, but the level populations may not be adequate due to the choice of statistical distribution of configuration-average populations.

The above methods are referred to as "dual" methods because they use one type of state to obtain a self-consistent solution of the CR equations and then distribute those populations to the states of a more refined model. True hybrid methods, beyond the dual ones described above, simultaneously employ different types of states within the CR equations. These states can include superconfigurations, configurations, finestructure levels, or arbitrarily averaged states. An example of the latter type is the reduced detailed configuration accounting (RDCA) approach, which has been implemented in the Los Alamos suite of codes [103, 109]. This approach allows the states contained within a large-scale self-consistent model, and their corresponding atomic data, to be averaged in a significant way. The resulting small-scale model can be used to obtain averaged plasma quantities in a relatively fast, accurate manner. Another hybrid scheme has been implemented in the SCRAM code [164], which can simultaneously include states such as superconfigurations, configurations and fine-structure levels in the same model. This approach has the advantage of being able to attain a high level of completeness, even for plasmas composed of complicated ions. In general, a disadvantage of these hybrid methods is a potential lack of self-consistency in the underlying atomic physics data. Further development of such true hybrid schemes offers a possible way forward to solve currently intractable problems in large-scale CR modeling.

**Acknowledgments** Helpful conversations with Yu. Ralchenko, D.P. Kilcrease and P. Hakel are gratefully acknowledged. This work was carried out under the auspices of the National Nuclear Security Administration of the US Department of Energy at Los Alamos National Laboratory and supported by contract no DE-AC52-06NA25396.

### References

- D.R. Bates, A.E. Kingston, R.W.P. McWhirter, Recombination between electrons and atomic ions. I. Optically thin plasmas. Proc. R. Soc. (Lond.) A267, 297 (1962)
- D.R. Bates, A.E. Kingston, R.W.P. McWhirter, Recombination between electrons and atomic ions. II. Optically thick plasmas. Proc. R. Soc. (Lond.) A270, 155 (1962)
- 3. R.D. Cowan, *The Theory of Atomic Structure and Spectra* (University of California Press, Berkeley, 1981)
- D.H. Sampson, H.L. Zhang, C.J. Fontes, A fully relativistic approach for calculating atomic data for highly charged ions. Phys. Rep. 477, 111 (2009)
- 5. R.E.H. Clark, J. Abdallah Jr., Atomic data for titanium. Phys. Scr. **T37**, 28 (1991)
- J. Abdallah Jr., R.E.H. Clark, J.M. Peek, C.J. Fontes, Kinetics calculations for near Ne-like ions. J. Quant. Spec. Rad. Trans. 51, 1 (1994)
- N.H. Magee, J. Abdallah Jr., R.E.H. Clark, J.S. Cohen, L.A. Collins, G. Csanak, C.J. Fontes, A. Gauger, J.J. Keady, D.P. Kilcrease, A.L. Merts, in *Astronomical Society of the Pacific Conference Proceedings* ed. by S.J. Adelman, W.L Wiese, vol. 78, pp. 51–55. ASP, New York (1995)
- 8. C.J. Fontes, H.L. Zhang, J. Abdallah Jr., R.E.H. Clark, D.P. Kilcrease, J. Colgan, R.T. Cunningham, P. Hakel, N.H. Magee, M.E. Sherrill, The Los Alamos suite of relativistic atomic physics codes. J. Phys. B: At. Mol. Opt. Phys. 48, 144014 (2015)
- 9. R.E.H. Clark, J. Abdallah Jr., G. Csanak, S.P. Kramer, Electron-impact cross sections and coherence parameters for the  $6s^{21}S 6s6p^{1}P$  transition in neutral barium. Phys. Rev. A **40**, 2935 (1989)
- J. Abdallah Jr., R.E.H. Clark, X-ray transmission calculations for an aluminum plasma. J. Appl. Phys. 69, 23 (1991)
- 11. J. Abdallah Jr., R.E.H. Clark, J.M. Peek, Excited-state 1s 2p absorption by aluminum ions with partially filled L shells. Phys. Rev. A **44**, 4072 (1991)
- T.S. Perry, S.J. Davidson, F.J.D. Serduke, D.R. Bach, C.C. Smith, J.M. Foster, R.J. Doyas, R.A. Ward, C.A. Iglesias, F.J. Rogers, J. Abdallah Jr., R.E. Steward, J.D. Kilkenny, R.W. Lee, Opacity measurements in hot dense medium. Phys. Rev. Lett. 67, 3784 (1991)
- R.E.H. Clark, G. Csanak, J. Abdallah Jr., Theoretical studies on the electron-impact excitation of neutral magnesium. Phys. Rev. A 44, 2874 (1991)
- R.E.H. Clark, J. Abdallah Jr., J.B. Mann, Integral and differential cross sections for electron impact ionization. Ap. J. 381, 597 (1991)
- J. Abdallah Jr., R.E.H. Clark, J.M. Peek, Steady-state ionization balance calculations for a selenium plasma. Phys. Rev. A 45, 3980 (1992)
- R.E.H. Clark, G. Csanak, J. Abdallah Jr, S. Trajmar, Differential cross sections for electron scattering by excited Ba (... 6s6p <sup>1</sup>P<sub>1</sub>) atoms. J. Phys. B: At. Mol. Opt. Phys. 25, 5233 (1992)
- 17. J.J. Keady, J. Abdallah Jr., R.E.H. Clark, Accurate methods for calculating atomic processes in high temperature plasmas. Plasma Phys. Controll. Nuclear Fusion Res. 3, 205 (1993)
- D.P. Kilcrease, J. Abdallah Jr., J.J. Keady, R.E.H. Clark, Atomic configuration average simulations for plasma spectroscopy. J. Phys. B: At. Mol. Opt. Phys. 26, L717 (1993)
- J. Abdallah Jr., B.A. Bryunetkin, M.P. Kalashnikov, R.E.H. Clark, P. Nickels, S.A. Pikuz, I.Yu. Skobelev, A.Ya. Faenov, M. Shnurer, Identification of transitions from self-ionized levels of a beryllium-like Mg IX ion in a plasma heated by picosecond laser pulses. Quant. Electron. (Russian) 20, 1159 (1993)
- J. Abdallah Jr., R.E.H. Clark, C.J. Keane, T.D. Shepard, L.J. Suter, Radiation field effects on the spectroscopic properties of seeded plasmas. J. Quant. Spec. Rad. Trans. 50, 91 (1993)
- H.J. Beyer, H. Hamdy, E.I.M. Zohny, K.R. Mahmoud, M.A.K. El-Fayoumi, H. Kleinpoppen, J. Abdallah Jr., R.E.H. Clark, G. Csanak, Electron-impact coherence parameters for the excitation of the 5 <sup>1</sup>P State of Sr. Z. Phys. D 30, 91 (1994)
- 22. J. Abdallah Jr., R.E.H. Clark, Comparison of explicit and effective models for calculating ionic populations in argon plasmas. J. Phys. B: At. Mol. Opt. Phys. 27, 3589 (1994)

- B.A. Bryunetkin, A.Ya. Faneov, M. Kalashnikov, P. Nickles, M. Schnuerer, I.Yu. Skobelev,
   J. Abdallah Jr., X-ray spectral investigations of a high irradiance picosecond laser produced plasma. J. Quant. Spect. Radiat. Transfer. 53, 45 (1995)
- D. Post, J. Abdallah Jr., R.E.H. Clark, N. Putvinskaya, Calculations of energy losses due to atomic processes in tokamaks with applications to the International Thermonuclear Experimental Reactor divertor. Phys. Plasmas 2, 2328 (1995)
- R.E.H. Clark, J. Abdallah Jr., D. Post, Radiation rates for low Z impurities in edge plasmas.
   J. Nuclear Mater. 220–222, 1028 (1995)
- A. Ya. Faenov, I. Yu. Skobelev, S.A. Pikuz, G.A. Kyrala, R.D. Fulton, J. Abdallah Jr., D.P. Kilcrease, High-resolution X-ray spectroscopy of a subpicosecond-laser-produced silcon plasma. Phys. Rev. A 51, 3529 (1995)
- J. Abdallah Jr., L.A. Collins, G. Csanak, A.G. Petschek, G.T. Schappert, Two-photon ionization of an inner shell electron of the Cl atom. Z. Phys. D 34, 233 (1995)
- J. Abdallah Jr., A.Ya. Faenov, D. Hammer, S.A. Pikuz, G. Csanak, Electron beam effects on the spectroscopy of satellite lines in aluminum x-pinch experiments. Phys. Scripta 53, 705 (1996)
- R.E.H. Clark, J. Abdallah Jr., Electron impact cross sections for beryllium and boron. Phys. Scripta T62, 7 (1996)
- M.A. Khakoo, S. Trajmar, L.R. LeClair, I. Kanik, G. Csanak, C.J. Fontes, Differential cross sections for electron impact excitation of Xe: I. Excitation of the five lowest levels; experiment and theory. J. Phys. B: At. Mol. Opt. Phys. 29, 3455 (1996)
- M.A. Khakoo, S. Trajmar, S. Wang, I. Kanik, A. Aguirre, C.J. Fontes, R.E.H. Clark, J. Abdallah Jr., Differential cross sections for electron impact excitation of Xe: II. Excitation of the sixth to twentieth lowest levels; experiment and theory. J. Phys. B: At. Mol. Opt. Phys. 29, 3477 (1996)
- P.W. Zetner, S. Trajmar, S. Wang, I. Kanik, G. Csanak, R.E.H. Clark, J. Abdallah Jr., J.C. Nickel, Inelastic electron scattering by laser-excited barium atoms. J. Phys. B: At. Mol. Opt. Phys. 30, 5317 (1997)
- A.W. Baerveldt, W.B. Westveld, J. van Eck, H.G.M. Heideman, G.D. Meneses, G. Csanak, R.E.H. Clark, J. Abdallah Jr., Cross sections, polarization and orientation in electron impact excitation to Ne\* (2p<sup>5</sup>3p) States. J. Phys. B: At. Mol. Opt. Phys. 31, 573 (1998)
- J. Abdallah Jr., R.E.H. Clark, D.P. Kilcrease, G. Csanak, C.J. Fontes, in AIP Conference Proceedings Vol. 381, 10th APS Topical Conference on Atomic Processes in Plasmas, ed. by A.L. Osterheld, W.H. Goldstein, pp. 131–142 (AIP, New York, 1996)
- A.Ya. Faenov, J. Abdallah Jr., R.E.H. Clark, J. Cohen, R.P. Johnson, G.A. Kyrala, A.I. Magunov, T.A. Pikuz, I.Yu. Skobelev, M.D. Wilke, High-resolution X-ray spectroscopy of hollow atoms created in plasma heated by subpicosecond laser radiation. Proc. SPIE 3157, 10 (1997)
- J. Abdallah Jr., A. Ya. Faenov, T.A. Pikuz, M.D. Wilke, G.A. Kyrala, R.E.H. Clark, Hot electron effects on the satellite spectrum of laser produced plasmas. J. Quant. Spec. Rad. Trans. 62, 1 (1999)
- S.A. Pikuz, T.A. Shelkovenko, V.M. Romanova, J. Abdallah Jr., G. Csanak, R.E.H. Clark, A.Ya. Faenov, I.Yu. Skobelev, D.A. Hammer, Effect of an electron beam generated in an xpinch plasma on the structure of the *K* spectra of multiply charged ions. J. Exp. Theor. Phys. 85, 484 (1997)
- A.M Urnov, J. Dubau, A.Ya. Faenov, T.A. Pikuz, I.Yu. Skobelev, J. Abdallah Jr., R.E.H. Clark, J.S. Cohen, R.P. Johnson, G.A. Kyrala, M.D. Wilke, A.L. Osterheld, X-ray spectra of multiply-charged hollow ions in the emission from a femtosecond laser plasma. J. Exp. Theor. Phys. Lett. 67, 489 (1998)
- 39. F.B. Rosmej, J. Abdallah Jr., Blue satellite structure near He  $\alpha$  and He  $\beta$  and redistribution of level populations. Phys. Lett. A **245**, 548 (1998)
- 40. C.J. Fontes, The role of the  $5p^55d$  configuration and spin-orbit coupling in the electron impact excitation of the lowest lying J=0 and J=2 levels of xenon and krypton. J. Phys. B: At. Mol. Opt. Phys. **31**, 175 (1998)

41. P.V. Johnson, Y. Li, P.W. Zetner, G. Csanak, R.E.H. Clark, J. Abdallah Jr., Electron-impact excitation of the (... 6s6p <sup>1</sup>P<sub>1</sub>) level in ytterbium. J. Phys. B: At. Mol. Opt. Phys. **31**, 3027 (1998)

- J. Abdallah Jr., A.Ya. Faenov, M. Scholz, L. Karpinski, S.A. Pikuz, V.M. Romanova, M. Sadowski, A. Szydlowski, Electron beam effects on the spectroscopy of satellite lines in plasma focus experiments. J. Quant. Spec. Rad. Trans. 62, 85 (1999)
- 43. J. Abdallah Jr., N. Palmer, W. Gekelman, J. Maggs, R.E.H. Clark, Time dependent kinetics model for a helium discharge plasma. J. Phys. B: At. Mol. Opt. Phys. 32, 1001 (1999)
- P.W. Zetner, S. Trajmar, S. Wang, I. Kanik, G. Csanak, R.E.H. Clark, J. Abdallah Jr., D. Fursa,
   I. Bray, Differential cross sections for electron-impact excitation out of the metastable levels of the barium atom. J. Phys. B: At. Mol. Opt. Phys. 32, 5123 (1999)
- D. Fursa, I. Bray, S. Trajmar, I. Kanik, G. Csanak, R.E.H. Clark, J. Abdallah Jr., Integral cross sections for electron scattering by ground-state Ba atoms. Phys. Rev. A 60, 4590 (1999)
- A. Ya. Faenov, A.I. Magunov, T.A. Pikuz, I. Yu. Skobelev, S.A. Pikuz, A.M. Urnov, J. Abdallah Jr, R.E.H. Clark, J. Cohen, R.P. Johnson, G.A. Kyrala, M.D. Wilke, A. Maksimchuk, D. Umstadter, N. Nantel, R. Doron, E. Behar, P. Mandelbaum, J.J. Schwob, J. Dubau, F.B. Rosmej, A. Osterheld, High-resolved X-ray spectra of hollow atoms in a femtosecond laser-produced solid plasma. Phys. Scripta T80, 536 (1999)
- 47. X. Guo, M.A. Khakoo, D.F. Mathews, G. Mikaelian, A. Crowe, I. Kanik, S. Trajmar, V. Zeman, K. Bartschat, C.J. Fontes, Differential cross section ratios for low-energy electron-impact excitation of the 4p<sup>5</sup>5s levels of krypton–sensitive tests of relativistic effects for heavy noble gases. J. Phys. B: At. Mol. Opt. Phys. 32, L155 (1999)
- J. Abdallah Jr., I.Yu. Skobelev, A.Ya. Faenov, A.I. Magunov, T.A. Pikuz, F. Flora, S. Bollanti,
   P. Di Lazzaro, T. Letardi, E. Burattini, A. Grilli, A. Reale, L. Palladino, G. Tomasetti, A. Scafati, L. Reale, Spectra of multicharged hollow ions in plasma created by the shortwavelength laser. Quant. Electron. 30, 694 (2000)
- 49. T. Auguste, P. D'Oliveira, S. Hulin, P. Monot, J. Abdallah Jr., A.Ya. Faenov, I.Yu. Skobelev, A.I. Magunov, T.A. Pikuz, About the role of prepulse in the heating of clusters by high intensive femtosecond laser pulse. J. Exp. Theor. Phys. Lett. 72, 55 (2000)
- J. Abdallah Jr., A.Ya. Faenov, I.Yu. Skobelev, A.I. Magunov, T.A. Pikuz, T. Auguste,
   P. D'Oliveira, S. Hulin, P. Monot, Hot electron influence on the X-ray emission spectra of Ar clusters heated by a high intensity 60 fs laser pulse. Phys. Rev. A 63, 032706 (2001)
- T.S. Perry, S.J. Davidson, F.J.D. Serduke, D.R. Bach, C.C. Smith, J.M. Foster, R.J. Doyas, R.A. Ward, C.A. Iglesias, F.J. Rogers, J. Abdallah Jr., R.E. Stewart, R.J. Wallace, J.D. Kilkenny, R.W. Lee, Opacity measurements in hot dense medium. Astrophys. J. Suppl. Ser. 127, 433 (2000)
- L. Karpinski, M. Paduch, M. Scholz, K. Tomaszewski, A. Szydlowski, S. Pikuz, V. Romanova, A. Ya. Faenov, J. Abdallah Jr., R.E.H. Clark, "Hot electrons" influence on argon K-spectrum emitted from plasma focus discharges. Czech. J. Phys. 50, 113 (2000)
- C.J. Fontes, J. Abdallah Jr., R.E.H. Clark, D.P. Kilcrease, Non-LTE modeling of gold plasmas.
   J. Quant. Spec. Rad. Trans. 65, 223 (2000)
- X. Guo, D.F. Mathews, G. Mikaelian, M.A. Khakoo, A. Crowe, I. Kanik, S. Trajmar, V. Zeman, K. Bartschat, C.J. Fontes, Differential cross sections for electron-impact excitation of krypton at low incident energies: I. Excitation of the 4p<sup>5</sup>5s configuration. J. Phys. B: At. Mol. Opt. Phys. 33, 1895 (2000)
- 55. X. Guo, D.F. Mathews, G. Mikaelian, M.A. Khakoo, A. Crowe, I. Kanik, S. Trajmar, V. Zeman, K. Bartschat, C.J. Fontes, Differential cross sections for electron-impact excitation of krypton at Low incident energies: II. Excitation of the 4p<sup>5</sup>5p, 4p<sup>5</sup>4d and 4p<sup>5</sup>6s configurations. J. Phys. B: At. Mol. Opt. Phys. 33, 1921 (2000)
- 56. G.C. Junkel-Vives, J. Abdallah Jr., F. Blasco, C. Stenz, F. Salin, A.Ya. Faenov, A.I. Magunov, T.A. Pikuz, I.Yu. Skobelev, T. Auguste, P. D'Oliveira, S. Hulin, P. Monot, S. Dobosz, High-resolution X-ray spectroscopy investigations of fs laser irradiated Ar clusters by varying cluster size and laser flux density. J. Quant. Spec. Rad. Trans. 71, 417 (2001)

- 57. G.C. Junkel-Vives, J. Abdallah Jr., F. Blasco, C. Stenz, F. Salin, A.Ya. Faenov, A.I. Magunov, T.A. Pikuz, I.Yu. Skobelev, Observation of H-like ions within Ar clusters irradiated by 35-fs laser via high-resolution X-ray spectroscopy. Phys. Rev. A 64, 021201(R) (2001)
- M.E. Sherrill, R.C. Mancini, J.E. Bailey, A. Filuk, B. Clark, P. Lake, J. Abdallah Jr., Spectroscopy diagnostics of a low temperature laser ablated LiAg plasma plume. Rev. Sci. Inst. 72, 957 (2001)
- D. Fursa, I. Bray, G. Csanak, R.E.H. Clark, J. Abdallah Jr., I. Kanik, S. Trajmar, Electron impact excitation of excited barium. Phys. Rev. A 65, 032723 (2002)
- G.C. Junkel-Vives, J. Abdallah Jr., T. Auguste, P. D'Oliveira, S. Hulin, P. Monot, S. Dobosz, A.Ya. Faenov, A.I. Magunov, T.A. Pikuz, I.Yu. Skobelev, A.S. Boldarev, V.A. Gasilov, Spatially resolved X-ray spectroscopy investigations of femtosecond laser irradiated Ar clusters. Phys. Rev. E 65, 036410 (2002)
- G.C. Junkel-Vives, J. Abdallah Jr., F. Blasco, C. Stenz, F. Salin, A.Ya. Faenov, A.I. Magunov, T.A. Pikuz, I.Yu. Skobelev, Evidence of supercritical density in 45-fs-laser-irradiated Arcluster plasmas. Phys. Rev. A 66, 033204 (2002)
- 62. P.W. Zetner, P.V. Johnson, Y. Li, G. Csanak, R.E.H. Clark, J. Abdallah Jr., Electron-impact excitation of the  $(...6s6p^3P_J)$  levels in ytterbium. J. Phys. B: At. Mol. Opt. Phys. **34**, 1619 (2001)
- 63. A.I. Magunov, T.A. Pikuz, I.Yu. Skobelev, A.Ya. Faenov, F. Blasco, F. Dorchies, T. Caillaud, C. Bonte, F. Salin, C. Stenz, P.A. Loboda, I.A. Litvinenko, V.V. Popova, G.V. Baidin, G.C. Junkel-Vives, J. Abdallah Jr., Influence of ultrashort laser pulse duration on the X-ray emission spectrum of plasma produced in cluster target. J. Exp. Theor. Phys. Lett. 74, 375 (2001)
- 64. A.Ya. Faenov, I.Yu. Skobelev, A.I. Magunov, T.A. Pikuz, J. Abdallah Jr., G.C. Junkel-Vives, F. Blasco, F. Dorchies, C. Stenz, F. Salin, T. Auguste, S. Dobosz, P. Monot, P. D'Oliveira, S. Hulin, A. Boldurev, V.A. Gasilov, X-ray radiation properties of clusters heated by fs laser pulses. Proc. SPIE 4504, 121 (2001)
- J. Abdallah Jr., H.L. Zhang, C.J. Fontes, D.P. Kilcrease, B.J. Archer, Model comparisons for high-Z non-LTE steady-state calculations. J. Quant. Spec. Rad. Trans. 71, 107 (2001)
- S.A. Pikuz, T.A. Shelkovenko, D.B. Sinars, D.A. Hammer, S.V. Lebedev, S.N. Bland, I.Yu. Skobelev, J. Abdallah Jr., C.J. Fontes, H.L. Zhang, Space, time and spectral characteristics of an x-pinch. J. Quant. Spec. Rad. Trans. 71, 581 (2001)
- 67. I.Yu. Skobelev, A.Ya. Faenov, A.I. Magunov, T.A. Pikuz, A.S. Boldarev, V.A. Gasilov, J. Abdallah Jr., G.C. Junkel-Vives, T. Auguste, P. D'Oliveira, S. Hulin, P. Monot, F. Blasco, F. Dorchies, T. Caillaud, C. Bonte, C. Stenz, F. Salin, B.Yu. Sharkov, On the interaction of femtosecond laser pulses with cluster targets. J. Exp. Theor. Phys. 94, 73 (2002)
- 68. I.Yu. Skobelev, A.Ya. Faenov, A.I. Magunov, T.A. Pikuz, A.S. Boldarev, V.A. Gasilov, J. Abdallah Jr., G.C. Junkel-Vives, T. Auguste, S. Dobosz, P. D'Oliveira, S. Hulin, P. Monot, F. Blasco, F. Dorchies, T. Caillaud, C. Bonte, C. Stenz, F. Salin, P.A. Loboda, I.A. Litvinko, V.V. Popova, G.V. Baidin, B.Yu. Sharkov, X-ray spectroscopy diagnostic of a plasma produced by femtosecond laser pulses Irradiating a Cluster Target. J. Exp. Theor. Phys. 94, 966 (2002)
- M.E. Sherrill, R.C. Mancini, J.E. Baily, A. Filuk, B. Clark, P. Lake, J. Abdallah Jr., in AIP Conference Proceedings 13th APS Topical Conference on Atomic Processes in Plasmas, ed. by D.R. Schultz, F.W. Meyer, F. Ownby, vol. 635, pp. 32–41 (AIP, New York, 2002)
- G.C. Junkel-Vives, J. Abdallah Jr., F. Blasco, F. Dorchies, C. Stenz, F. Salin, A.Ya. Faenov,
   A.I. Magunov, T.A. Pikuz, I.Yu. Skobelev, T. Auguste, S. Dobosz, P. D'Oliveira, S. Hulin,
   P. Monot, in AIP Conference Proceedings, 13th APS Topical Conference on Atomic Processes in Plasmas, D.R. Schultz, F.W. Meyer, F. Ownby, vol. 635, pp. 82–91 (AIP, New York, 2002)
- 71. G.D. Meneses, R.E.H. Clark, J. Abdallah Jr., G. Csanak, Cross sections for the excitation of 3s, 3p, 3d, 4s and 4p manifolds in e-Ne collisional. J. Phys. B: At. Mol. Opt. Phys. 35, 3119 (2002)
- U. Andiel, K. Eidmann, P. Hakel, R.C. Mancini, G.C. Junkel-Vives, J. Abdallah Jr., K. Witte, Demonstration of aluminum K-shell line shifts in isochorically heated targets driven by ultrashort laser pulses. Europhys. Lett. 60, 861 (2002)

73. M.A. Khakoo, J. Wrkich, M. Larsen, G. Kleiban, I. Kanik, S. Trajmar, M.J. Brunger, P.J.O. Teubner, A. Crowe, C.J. Fontes, R.E.H. Clark, V. Zeman, K. Bartschat, D.H. Madison, R. Srivastava, A.D. Stauffer, Differential cross sections and cross-section ratios for the electron-impact excitation of the neon 2 p<sup>5</sup>3s configuration. Phys. Rev. A 65, 062711 (2002)

- 74. J. Abdallah Jr., G.C. Junkel-Vives, A.Ya. Faenov, I.Yu. Skobelev, T.A. Pikuz, A.I. Magunov, F. Blasco, C. Bonte, F. Dorchies, T. Caillaud, F. Salin, C. Stenz, Time-dependent study of *K*-shell satellite line structure from L-shell ions in ultra-short laser argon cluster experiments. J. Quant. Spec. Rad. Trans. 81, 3 (2003)
- Y. Fukuda, Y. Akahane, M. Aoyama, N. Inoue, H. Ueda, K. Yamakawa, J. Abdallah Jr., G. Csanak, A.Ya. Faenov, A.I. Magunov, T.A. Pikuz, I.Yu. Skobelev, A.S. Boldarev, V.A. Gasilov, X-ray observations of microdroplet plasma formation under super-intense laser radiation. J. Exp. Theor. Phys. Lett. 78, 146 (2003)
- J. Abdallah Jr., G. Csanak, Y. Fukuda, Y. Akahane, M. Aoyama, N. Inoue, H. Ueda, K. Yamakawa, A.Ya. Faenov, A.I. Magunov, T.A. Pikuz, I.Yu. Skobelev, Time-dependent Boltzmann kinetic model of X-rays produced by the ultrashort-pulse laser irradiation of argon clusters. Phys. Rev. A 68, 063201 (2003)
- R.E.H. Clark, J. Abdallah Jr., Comparison calculations of radiated power loss for silicon and iron. At. Plasma-Mater. Interact. Data Fusion 11, 1 (2003)
- J. Abdallah Jr., R.E.H. Clark, Calculated radiated power loss for neon, silicon, argon, titanium, and iron. At. Plasma-Mater. Interact. Data Fusion 11, 21 (2003)
- R.E.H. Clark, J. Abdallah Jr., C.J. Fontes, Effective rates for calculation of steady-state and time dependent plasmas. At. Plasma-Mater. Interact. Data Fusion 11, 49 (2003)
- Y. Fukuda, Y. Akahane, M. Aoyama, N. Inoue, H. Ueda, Y. Kishimoto, K. Yamakawa, A.Ya. Faenov, A.I. Magunov, T.A. Pikuz, I.Yu. Skobelev, J. Abdallah Jr., G. Csanak, A.S. Boldarev, V.A. Gasilov, X-ray radiation of clusters irradiated by ultrafast, high intensity laser pulses. Proc. SPIE 5196, 234 (2003)
- 81. C.J. Fontes, H.L. Zhang, J. Abdallah Jr., in *AIP Conference Proceeding, 14th APS Topical Conference on Atomic Processes in Plasmas*, ed. by J.S. Cohen, S. Mazevet, D.P. Kilcrease, vol. 730, pp. 41–49 (AIP, New York, 2004)
- K. Eidmann, U. Andiel, F. Pisani, P. Hakel, R.C. Mancini, J. Abdallah Jr., G.C. Junkel-Vives, K. Witte, in AIP Conference Proceeding, 14th APS Topical Conference on Atomic Processes in Plasmas, ed. by J.S. Cohen, S. Mazevet, D.P. Kilcrease, vol. 730, pp. 81–93 (AIP, New York, 2004)
- N.H. Magee, J. Abdallah Jr., J. Colgan, P. Hakel, D.P. Kilcrease, S. Mazevet, M.E. Sherrill,
   C.J. Fontes, H.L. Zhang, in AIP Conference Proceeding, 14th APS Topical Conference on Atomic Processes in Plasmas, ed. by J.S. Cohen, S. Mazevet, D.P. Kilcrease, vol. 730, pp. 168–179 (AIP, New York, 2004)
- 84. M.A. Khakoo, P. Vandeventer, J.G. Childers, I. Kanik, C.J. Fontes, K. Bartschat, V. Zeman, D.H. Madison, S. Saxena, R. Srivastava, A.D. Stauffer, Electron impact excitation of the argon 3p<sup>5</sup>4s configuration: differential cross-sections and cross-section ratios. J. Phys. B: At. Mol. Opt. Phys. 37, 247 (2004)
- S.D. Loch, C.J. Fontes, J. Colgan, M.S. Pindzola, C.P. Ballance, D.C. Griffin, M.G. O'Mullane,
   H.P. Summers, Collisional-radiative study of lithium plasmas. Phys. Rev. E 69, 066405 (2004)
- C.J. Fontes, J. Colgan, H.L. Zhang, J. Abdallah Jr., Large-scale kinetics modeling of non-LTE plasmas. J. Quant. Spec. Rad. Trans. 99, 175 (2006)
- P. Hakel, M.E. Sherrill, S. Mazevet, J. Abdallah Jr., J. Colgan, D.P. Kilcrease, N.H. Magee, C.J. Fontes, H.L. Zhang, The new Los Alamos opacity code ATOMIC. J. Quant. Spec. Rad. Trans. 99, 265 (2006)
- 88. M.E. Sherrill, J. Abdallah Jr., G. Csanak, D.P. Kilcrease, Y. Fukuda, Y. Akahane, M. Aoyama, N. Inoue, H. Ueda, K. Yamakawa, A.Ya. Faenov, A.I. Magunov, T.A. Pikuz, I.Yu. Skobelev, Coupled electron and atomic kinetics through the solution of the Boltzmann equation for generating time dependent X-ray spectra. J. Quant. Spec. Rad. Trans. 99, 584 (2006)
- M.E. Sherrill, J. Abdallah Jr., G. Csanak, E.S. Dodd, Y. Fukuda, Y. Akahane, M. Aoyama,
   N. Inoue, H. Ueda, K. Yamakawa, A.Ya. Faenov, A.I. Magunov, T.A. Pikuz, I.Yu. Skobelev,

- Spectroscopic characterization of an ultrashort laser driven Ar cluster target incorporating both Boltzmann and particle in cell models. Phys. Rev. E **73**, 066404 (2006)
- S. Mazevet, J. Abdallah Jr., Mixed UTA and detailed line treatment for mid-Z opacity and spectral calculations. J. Phys. B: At. Mol. Opt. Phys. 39, 3419 (2006)
- 91. J. Colgan, C.J. Fontes, J. Abdallah Jr., Collisional-radiative studies of carbon plasmas. High Energy Density Phys. **2**, 90 (2006)
- 92. J. Colgan, C.J. Fontes, H.L. Zhang, Inner-shell electron-impact ionization of neutral atoms. Phys. Rev. A 73, 062711 (2006)
- 93. J.A. Cobble, T.E. Tierney, J. Abdallah Jr., Kilovolt radiation from a laser-produced Al plasma. J. Appl. Phys. **102**, 023303 (2007)
- J. Abdallah Jr., D. Batani, T. Desai, G. Lucchini, A. Faenov, T. Pikuz, A. Maganov, V. Narayanan, High resolution X-ray emission spectra from picosecond laser irradiated Ge targets. Laser Part. Beams 25, 245 (2007)
- 95. J. Abdallah Jr., D.P. Kilcrease, N.H. Magee, S. Mazevet, P. Hakel, M.E. Sherrill, Spectral line strength binning method for opacity calculations. High Energy Density Phys. 3, 1 (2007)
- M.E. Sherrill, R.C. Mancini, J. Bailey, A. Filuk, B. Clark, P. Lake, J. Abdallah Jr., Spectroscopic modeling and characterization of a collisionally confined laser-ablated plasma plume. Phys. Rev. E 76, 056401 (2007)
- J.E. Bailey, G.A. Rochau, C.A. Iglesias, J. Abdallah Jr., J.J. MacFarlane, I. Golovkin,
   P. Wang, R.C. Mancini, P.W. Lake, T.C. Moore, M. Bump, O. Garcia, S. Mazevet, Iron opacity measurements at temperatures above 150 eV. Phys. Rev. Lett. 99, 265002 (2007)
- J. Colgan, C.J. Fontes, J. Abdallah Jr., B. Streufert, in AIP Conference Proceeding, 15th International Conference on Atomic Processes in Plasmas, ed. by J.D. Gillaspy, J.J. Curry, W.L. Wiese, vol. 926, pp. 180–189 (AIP, New York, 2007)
- 99. J. Oelgoetz, C.J. Fontes, H.L. Zhang, M. Montenegro, S.N. Nahar, A.K. Pradhan, High-temperature behavior of the helium-like  $K\alpha$  G ratio: the effect of improved recombination rate coefficients for calcium, iron and nickel. Mon. Not. R. Astron. Soc. **382**, 761 (2007)
- 100. J. Oelgoetz, C.J. Fontes, H.L. Zhang, A.K. Pradhan, A study of the breakdown of the quasistatic approximation at high densities and its effect on the helium-like Kα complex of nickel, iron, and calcium. Phys. Rev. A 76, 062504 (2007)
- 101. J. Colgan, J. Abdallah Jr., A. Ya. Faenov, A.I. Magunov, T.A. Pikuz, I. Yu. Skobelev, Y. Fukuda, Y. Akahane, M. Aoyama, N. Inoue, H. Ueda, K. Yamakawa, The role of hollow atoms in the spectra of an ultrashort-pulse-laser-driven Ar cluster target. Laser Part. Beams 26, 83 (2008)
- J. Colgan, J. Abdallah Jr., A. Faenov, T.A. Pikuz, I.Yu. Skobelev, MUTA calculations of a laser produced Mg hollow atom spectrum. Phys. Scripta 78, 015302 (2008)
- J. Abdallah Jr., M.E. Sherrill, The reduced detailed configuration accounting (RDCA) model for NLTE plasma calculations. High Energy Density Phys. 4, 124 (2008)
- J. Colgan, H.L. Zhang, C.J. Fontes, Electron-impact excitation and ionization cross sections for the Si, Cl and Ar isonuclear sequences. Phys. Rev. A 77, 062704 (2008)
- J. Colgan, J. Abdallah Jr., M.E. Sherrill, J. Foster, C.J. Fontes, U. Feldman, Radiative losses of solar coronal plasmas. Astrophys. J. 689, 585 (2008)
- 106. T.C. Berkelbach, J. Colgan, J. Abdallah Jr., A.Ya. Faenov, T.A. Pikuz, Y. Fukuda, K. Yamakawa, Modeling energy dependence of the inner-shell X-ray emission produced by femtosecond-pulse laser irradiation of xenon clusters. Phys. Rev. E 79, 016407 (2009)
- P. Hakel, R.C. Mancini, J. Abdallah Jr., M.E. Sherrill, H.L. Zhang, X-ray line polarization spectroscopy of Li-like Si satellite line spectra. J. Phys. B: At. Mol. Opt. Phys. 42, 085701 (2009)
- 108. J. Oelgoetz, C.J. Fontes, H.L. Zhang, S.N. Nahar, A.K. Pradhan, On the importance of satellite lines to the He-like Kα complex and the G ratio for calcium, iron, and nickel. Mon. Not. R. Astron. Soc. 394, 742 (2009)
- J. Abdallah Jr., M.E. Sherrill, D.P. Kilcrease, C.J. Fontes, H.L. Zhang, J. Oelgoetz, The reduced detailed configuration accounting (RDCA) model for NLTE plasma spectral calculations. High Energy Density Phys. 5, 204 (2009)

48

 P. Hakel, R.C. Mancini, U. Andiel, K. Eidmann, F. Pisani, G. Junkel-Vives, J. Abdallah Jr.,
 X-ray line emissions from tamped thin aluminum targets driven by subpicosecond-duration laser pulses. High Energy Density Phys. 5, 35 (2009)

- 111. Yu. Ralchenko, J. Abdallah Jr., A. Bar-Shalom, J. Bauche, C. Bauche-Arnoult, C. Bowen, M. Busquet, H.-K. Chung, J. Colgan, G. Faussurier, C.J. Fontes, M. Foster, F. de Dortan, I. Golovkin, S.B. Hansen, M. Klapsich, R.W. Lee, V. Novikov, J. Oreg, O. Peyrusse, M. Poirier, A. Sasaki, H. Scott, H.L. Zhang, in AIP Conference Proceeding, 16th International Conference on Atomic Processes in Plasmas, ed. by K.B. Fournier, vol. 1161, pp. 242–250 (AIP, New York, 2009)
- 112. J. Colgan, J. Abdallah Jr., C.J. Fontes, R.E.H. Clark, Non-LTE studies of boron plasma. J. Phys. B: At. Mol. Opt. Phys. 43, 144021 (2010)
- 113. J. Colgan, J. Abdallah Jr., C.J. Fontes, D.P. Kilcrease, J. Dunn, R.W. Lee, Non-LTE and gradient effects in *K*-shell oxygen emission laser-produced plasma. High Energy Density Phys. **6**, 295 (2010)
- 114. J. Colgan, J. Abdallah Jr., A.Ya. Faenov, T.A. Pikuz, I.Yu. Skobelev, F. Flora, M. Francucci, S. Martellucci, Model calculations of the emission of barium plasma in the spectral range of high-n Rydberg levels in a near Ni-like state. J. Phys. B: At. Mol. Opt. Phys. 43, 175701 (2010)
- 115. J. Abdallah Jr., J. Colgan, R.E.H. Clark, C.J. Fontes, H.L. Zhang, A collisional-radiative study of low temperature tungsten plasma. J. Phys. B: At. Mol. Opt. Phys. 44, 075701 (2011)
- 116. J. Colgan, J. Abdallah Jr., A.Ya. Faenov, T.A. Pikuz, I.Yu. Skobelev, Y. Fukuda, Y. Hayashi, A. Pirozhkov, K. Kawase, Y. Kato, S.V. Bulanov, M. Kando, Observation and modeling of high resolution spectral features of the inner-shell X-ray emission produced by 10<sup>-10</sup> contrast femtosecond-pulse laser irradiation of argon clusters. High Energy Density Phys. 7, 77 (2011)
- 117. C.J. Fontes, J. Colgan, H.L. Zhang, J. Abdallah Jr., A.L. Hungerford, C.L. Fryer, D.P. Kilcrease, Atomic data and the modeling of supernova light curves. J. Phys.: Conf. Ser. 388, 012022 (2012)
- J. Abdallah Jr., J. Colgan, Time dependent calculations of electron energy distribution functions for cold argon gas in the presence of intense black body radiation. J. Phys. B: At. Mol. Opt. Phys. 45, 035701 (2012)
- 119. L.H. Frey, W. Even, D.J. Whelan, C.L. Fryer, A.L. Hungerford, C.J. Fontes, J. Colgan, The Los Alamos supernova light-curve project: computational methods. Astrophys. J. Suppl. Ser. **204**, 16 (2013)
- J. Colgan, D.P. Kilcrease, N.H. Magee Jr, G.S.J. Armstrong, J. Abdallah Jr, M.E. Sherrill,
   C.J. Fontes, H.L. Zhang, P. Hakel, Light element opacities from ATOMIC. High Energy
   Density Phys. 9, 369 (2013)
- 121. S. Turck-Chièze, D. Gilles, M. Le Pennec, T. Blenski, F. Thais, S. Bastiani-Ceccotti, C. Blancard, M. Busquet, T. Caillaud, J. Colgan, P. Cossé, F. Delahaye, J.E. Ducret, G. Faussurier, C.J. Fontes, F. Gilleron, J. Guzik, J.W. Harris, D.P. Kilcrease, G. Loisel, N.H. Magee, J.C. Pain, C. Reverdin, V. Silvert, B. Villette, C.J. Zeippen, Radiative properties of stellar envelopes: comparison of asteroseismic results to opacity calculations and measurements for iron and nickel. High Energy Density Phys. 9, 473 (2013)
- 122. J. Colgan, J. Abdallah Jr., A.Ya. Faenov, S.A. Pikuz, N. Booth, O. Culfa, R.J. Dance, R.G. Evans, R.J. Gray, T. Kaempfer, K.L. Lancaster, P. McKenna, A.L. Rossall, I.Yu. Skobelev, K.S. Schulze, I. Uschmann, A.G. Zhidkov, N.C. Woolsey, Exotic dense matter states pumped by relativistic laser plasma in the radiation dominant regime. Phys. Rev. Lett. 110, 125001 (2013)
- 123. S.A. Pikuz, A.Ya. Faenov, J. Colgan, R.J. Dance, J. Abdallah Jr., E. Wagenaars, N. Booth, O. Culfa, R.G. Evans, R.J. Gray, T. Kaempfer, K.L. Lancaster, P. McKenna, A.L. Rossall, I.Yu. Skobelev, K.S. Schulze, I. Uschmann, A.G. Zhidkov, N.C. Woolsey, Measurement and simulations of hollow atom X-ray spectra of solid-density relativistic plasma created by high-contrast PW optical laser pulses. High Energy Density Phys. 9, 560 (2013)
- 124. J. Colgan, D.P. Kilcrease, N.H. Magee Jr., G.S.J. Armstrong, J. Abdallah Jr., M.E. Sherrill, C.J. Fontes, H.L. Zhang, P. Hakel, in AIP Conference Proceeding, Eighth International Con-

- ference on Atomic and Molecular Data and their Applications, ed. by J.D. Gillaspy, W.L. Wiese, Y.A. Podpaly, vol. 1545, pp. 17–26 (AIP, New York, 2013)
- 125. S. Hansen, G.S.J. Armstrong, S. Bastiani-Ceccotti, C. Bowen, H.-K. Chung, J.P. Colgan, F. de Dortan, C.J. Fontes, F. Gilleron, J.-R. Marquès, R. Piron, O. Peyrusse, M. Poirier, Yu. Ralchenko, A. Sasaki, E. Stambulchik, F. Thais, Testing the reliability of non-LTE spectroscopic models for complex ions. High Energy Density Phys. 9, 523 (2013)
- J. Abdallah Jr., J. Colgan, N. Rohringer, Time-dependent calculations of electron energy distribution functions for neon gas in the presence of intense XFEL radiation. J. Phys B 46, 235004 (2013)
- G.S.J. Armstrong, J. Colgan, D.P. Kilcrease, N.H. Magee Jr., Ab initio calculation of the non-relativistic free-free Gaunt factor incorporating plasma screening. High Energy Density Phys. 10, 61 (2014)
- 128. C.J. Fontes, K.A. Eriksen, J. Colgan, H.L. Zhang, J.P. Hughes, Spectral modeling of supernova remnants. High Energy Density Phys. **10**, 43 (2013)
- 129. P. Hakel, G.A. Kyrala, P.A. Bradley, N.S. Krasheninnikova, T.J. Murphy, M.J. Schmitt, I.L. Tregillis, R.J. Kanzleieter, S.H. Batha, C.J. Fontes, M.E. Sherrill, D.P. Kilcrease, S.P. Regan, X-ray spectroscopic diagnostics and modeling of polar-drive implosion experiments on national ignition facility. Phys. Plasmas 21, 063306 (2014)
- 130. S.B. Hansen, J. Colgan, A. Ya. Faenov, J. Abdallah Jr., S.A. Pikuz Jr., I. Yu. Skobelev, E. Wagenaars, N. Booth, O. Culfa, R.J. Dance, G.J. Tallents, R.G. Evans, R.J. Gray, T. Kaempfer, K.L. Lancaster, P. McKenna, A.L. Rossall, K.S. Schulze, I. Uschmann, A.G. Zhidkov, N.C. Woolsey, Detailed analysis of hollow ions spectra from dense matter pumped by X-ray emission of relativistic laser plasma. Phys. Plasmas 21, 031213 (2014)
- J. Colgan, E.J. Judge, D.P. Kilcrease, J.E. Barefield, Ab-initio modeling of an iron laserinduced plasma: comparison between theoretical and experimental atomic emission spectra. Spectrochimica Acta B 97, 65 (2014)
- 132. J.E. Bailey, T. Nagayama, G.P. Loisel, G.A. Rochau, C. Blancard, J. Colgan, Ph Cosse, G. Faussurier, C.J. Fontes, F. Gilleron, I. Golovkin, S.B. Hansen, C.A. Iglesias, D.P. Kilcrease, J.J. MacFarlane, R.C. Mancini, C. Orban, J.-C. Pain, A.K. Pradhan, M. Sherrill, B.G. Wilson, A higher-than-predicted measurement of iron opacity at solar interior temperatures. Nature 517, 56 (2015)
- J. Colgan, D.P. Kilcrease, N.H. Magee Jr., J. Abdallah Jr, M.E. Sherrill, C.J. Fontes, P. Hakel,
   H.L. Zhang, Light element opacities of astrophysical interest from ATOMIC. High Energy
   Density Phys. 14, 33 (2015)
- J. Colgan, C.J. Fontes, H.L. Zhang, J. Abdallah Jr., Collisional-radiative modeling of tungsten at temperatures of 1200–2400 eV. Atoms 3, 76 (2015)
- 135. http://aphysics2.lanl.gov/tempweb/
- 136. R.W. Lee, J.K. Nash, Y. Ralchenko, J. Quant. Spec. Rad. Trans. 58, 737 (1997)
- C. Bowen, A. Decoster, C.J. Fontes, C.J. Fournier, O. Peyrusse, Yu. Ralchenko, J. Quant. Spec. Rad. Trans. 81, 71 (2003)
- 138. C. Bowen, R.W. Lee, YuJ Ralchenko, Quant. Spec. Rad. Trans. 99, 102 (2006)
- J.G. Rubiano, R. Florido, C. Bowen, R.W. Lee, Yu. Ralchenko, High Energy Density Phys.
   3, 225 (2007)
- C.J. Fontes, J. Abdallah Jr., C. Bowen, R.W. Lee, Yu. Ralchenko, High Energy Density Phys. 5, 15 (2009)
- 141. The NLTE-6 Code Comparison Workshop http://nlte.nist.gov/NLTE6/ (unpublished)
- H.-K. Chung, C. Bowen, C.J. Fontes, S.B. Hansen, Yu. Ralchenko, High Energy Density Phys. 9, 645 (2013)
- 143. The NLTE-8 Code Comparison Workshop http://nlte.nist.gov/NLTE8/ (unpublished)
- 144. A. Kramida, Yu. Ralchenko, J. Reader, NIST ASD Team: NIST Atomic Spectra Database (ver. 5.2) (National Institute of Standards and Technology, Gaithersburg, MD, 2015). http://physics.nist.gov/asd
- 145. H.-K. Chung, M.H. Chen, W.L. Morgan, Y. Ralchenko, R.W. Lee, FLYCHK: generalized population kinetics and spectral model for rapid spectroscopic analysis for all elements. High Energy Density Phys. 1, 3 (2005)

50 C.J. Fontes et al.

- 146. D. Layzer, Ann. Phys. (New York) 8, 271 (1959)
- 147. J.M. Blatt, V.F. Weisskopf, *Theoretical Nuclear Physics* (Dover Publications, New York, 1991)
- 148. R.H. Fowler, Statistical Mechanics (Cambridge University Press, Cambridge, 1936)
- H. Bethe, Zur Theorie des Durchgangs schneller Korpuskularstrahlen durch Materie. Ann. Phys. 397, 325 (1930)
- H.A. Kramers, On the theory of X-ray absorption and of the continuous X-ray spectrum. Philos. Mag. 46, 836 (1923)
- C.W. Gear, Numerical initial value problems in ordinary differential equations (Prentice Hall, New Jersey, 1971)
- 152. http://www.netlib.org/lapack/
- E. Isaacson, H.B. Keller, Analysis of Numerical Methods (Chapter 2.3) (Wiley, New York, 1966)
- 154. Y. Saad, M.H. Schultz, SIAM J. Sci. Stat. Comput. 7, 856 (1986)
- 155. Y. Saad, *Iterative methods for sparse linear systems*, 2nd edn. (Society for Industrial and Applied Mathematics, Philadelphia, 2003)
- 156. http://www.netlib.org/slatec/lin/sslugm.f
- 157. http://www.netlib.org/scalapack/
- 158. W.D. Joubert, LAMG: Los Alamos multigrid code reference manual. Los Alamos National Laboratory Report LA-UR-03-6183, Dec 2003 (unpublished)
- 159. X.S. Li, J.W. Demmel, ACM Trans. Math. Softw. 29, 110 (2003)
- 160. http://www-01.ibm.com/support/knowledgecenter/SSFHY8/essl\_welcome.html
- J. Bauche, C. Bauche-Arnoult, M. Klapisch, Transition arrays in the spectra of ionized atoms. Adv. At. Mol. Phys. 23, 131 (1988)
- C. Bauche-Arnoult, J. Bauche, M. Klapisch, Variance of the distributions of energy levels and of the transition arrays in atomic spectra. III. Case of spin-orbit-split arrays. Phys. Rev. A 31, 2248 (1985)
- 163. J. Bauche, C. Bauche-Arnoult, M. Klapisch, Breakdown of *jj* coupling in spinorbit-split atomic transition arrays. J. Phys. B: At. Mol. Opt. Phys. **24**, 1 (1991)
- S.B. Hansen, J. Bauche, C. Bauche-Arnoult, M.F. Gu, Hybrid atomic models for spectroscopic plasma diagnostics. High Energy Density Phys. 3, 109 (2007)

# Chapter 3 Generalized Collisional Radiative Model Using Screened Hydrogenic Levels

H.-K. Chung, S.B. Hansen and H.A. Scott

**Abstract** Collisional-radiative (CR) models are used to obtain atomic level population distributions and radiative properties in plasmas. These quantities are used to help design experiments, to provide data for radiative energy transport in radiationhydrodynamic simulations, and to diagnose laboratory and astrophysical plasmas whose conditions are difficult to or impossible to directly measure. CR models are constructed by coupling a set of electronic energy levels with spontaneous, collisional, and radiation-driven transitions. Since the number of atomic levels and transitions necessary to build a CR model can be prohibitively high, especially for many-electron ions, models are often customized for specific applications by tailoring the structure based on expected plasma conditions. On the other hand, there remains a need for models that are general enough to predict charge state distributions and radiative properties with reasonable accuracy for plasmas over a wide range of plasma conditions. Such generalized models are especially useful for design simulations, which access a wide range of conditions, and for preliminary analysis of spectroscopic data. This chapter describes a class of generalized CR models based on screened-hydrogenic atomic levels and rates. These models have been applied to a wide variety of applications and have demonstrated reliable performance over a wide range of plasma conditions, from the low-density coronal limit to local thermodynamic equilibrium.

H.-K. Chung (⋈)

International Atomic Energy Agency, 1400 Vienna, Austria e-mail: h.chung@iaea.org

S.B. Hansen

Sandia National Laboratories, Albuquerque, NM 87185, USA e-mail: sbhanse@sandia.gov

H.A. Scott

Lawrence Livermore National Laboratory, Livermore, CA 94550, USA e-mail: hascott@llnl.gov

© Springer International Publishing Switzerland 2016 Yu. Ralchenko (ed.), *Modern Methods in Collisional-Radiative Modeling of Plasmas*, Springer Series on Atomic, Optical, and Plasma Physics 90, DOI 10.1007/978-3-319-27514-7\_3 52 H.-K. Chung et al.

### 3.1 Introduction

A collisional-radiative (CR) model describes the atomic processes that couple an ensemble of electronic states in atoms and ions in terms of state populations and transition rates connecting those states. Ultimately these models provide information on plasma properties such as charge state distributions and radiative emissivity and opacity. A set of rate equations is used to calculate the number density of the ith atomic state  $n_i$  as a function of rates  $R_{j\rightarrow i}$  from the jth atomic state to the ith atomic state where  $1 \le i$ ,  $j \le m$  (the maximum number of atomic states) and the loss rate of the ith atomic state  $R_i$ .

$$\frac{dn_i}{dt} = \sum_{j=1}^{j=i-1} R_{j\to i} n_j + \sum_{j=i+1}^{m} R_{j\to i} n_j - R_i n_i \quad \text{and} \quad R_i = \sum_{j\neq i}^{m} R_{i\to j}$$

The set of rate equations can be represented in a matrix form as follows:

$$\frac{d\tilde{n}}{dt} = \bar{R} \cdot \tilde{n}$$

where  $\tilde{n}$  is the population vector and  $\bar{R}$  is the rate matrix. Since many of the transition rates are very fast on timescales of interest, the numerical solution of this equation requires an implicit (or at least semi-implicit) treatment, but in most cases, the solution can be achieved with standard methods. For atomic systems with transitions mediated by electrons and photons, the rates themselves do not explicitly depend on the state populations, although they often have a weak indirect dependence on the populations, and the rate equations are formally linear. Transitions induced by atomic collisions introduce an explicit non-linearity, but usually do not change the quasi-linear nature of the equations. For the steady-state/long timescale case, the rate equations become

$$\frac{d\tilde{n}}{dt} = 0$$

and the solution is only defined up to a multiplicative constant (including the trivial solution  $\tilde{\mathbf{n}}=0$ ). For well-defined solutions, a conservation condition is used, for example conservation of total number density  $N_T$ , or a charge neutrality condition for plasma with total electron density  $N_e$  such as:

$$\sum_{i=0}^{Z} f_i = N_T \text{ and } \sum_{i=0}^{Z} z_i f_i = N_e$$

where Z is the atomic number and  $z_i$  is the charge associated with the *i*th charge state with charge state density  $f_i$ .

If all the necessary atomic parameters, i.e. energy levels and transition rates, are available, it is relatively straightforward in principle to build the rate matrix and obtain the number densities by solving the rate equations. In practice, building a CR model is often quite difficult. Leaving aside the question of atomic data quality, a complete data set of atomic parameters is rarely available and, in addition, the available computational resources often limit the model size. A reliable collisional radiative model must satisfy three constraints: the model should include all atomic processes and states relevant to applications of interest (completeness), the model should be numerically and computationally manageable (tractability) and the model should be able to predict observables that represent physical reality (accuracy).

The main idea of a "generalized" collisional-radiative (GCR) model is to provide reasonable but fast estimates of  $\bar{Z}$  or charge state distributions of plasmas under a wide range of conditions for diverse applications: laser-produced plasmas, beamproduced plasmas, astrophysical plasmas, magnetic fusion plasmas, photoionized plasmas, coronal plasmas, and dense plasmas. An established method of constructing a CR model which is both simple and general while fulfilling the requirements of completeness, tractability and accuracy, is to construct a set of atomic parameters by employing a screened-hydrogenic (SH) formalism. Over the last decade, CR models using screened-hydrogenic parameters have proven to provide a simple and yet reasonable description of atomic processes of plasmas for a variety of applications [1–8]. They have successfully provided estimates of charge state distributions and low-resolution spectra needed to design plasma experiments and have provided a basic understanding of atomic processes required to analyze measured spectra.

The term "screened-hydrogenic" indicates the use of hydrogenic expressions evaluated with screened nuclear charges and screened nuclear charges [9, 10]. Methods for calculating plasma properties that fall under this description have been used for decades and encompass a wide range of techniques, degree of detail and accuracy. The specific formalism that has proved useful in constructing a GCR model is presented in the following section, along with a discussion of the underlying assumptions and associated uncertainties.

### 3.2 Formalism

### 3.2.1 Generalized Collisional-Radiative Atomic Levels

The first step in building a CR model is the choice of atomic states, which is usually based on a specific application and quantities of interest (QOI) such as average charge state  $(\bar{Z})$ , charge state distributions (CSD), spectroscopic emissivity or opacity. If the main QOI is an averaged quantity such as  $\bar{Z}$ , less descriptive atomic states can be used without much loss of accuracy. A more descriptive representation is required to provide accurate results for spectroscopic calculations. Figure 3.1 illustrates various descriptions of atomic states of helium (or helium-like ions) of term-split levels,

54 H.-K. Chung et al.

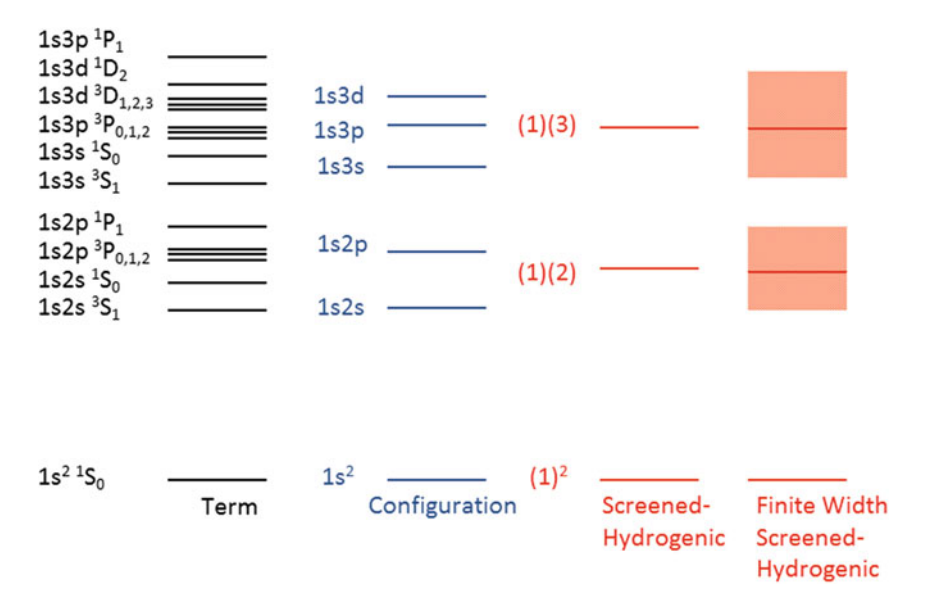


Fig. 3.1 Terms, configurations and screened-hydrogenic levels used in a collisional-radiative model are illustrated

(non-relativistic) configuration levels and SH levels based on principal quantum numbers. A model of 17 term-split levels can be reduced to a model of 6 non-relativistic configurations or to a model of 3 levels. A SH level can be represented by the "average" energy and, optionally, a "width" representing a distribution of individual energy levels. If necessary, levels can be averaged even further.

As defined here, a GCR is a super-configuration model [11–14] using SH levels defined by principal quantum numbers. The atomic levels are labeled by the principal quantum numbers  $\mathbf{n}$  and electron occupation numbers  $\mathbf{i}$  as  $(\mathbf{n})^i$ .

There are two ways of obtaining atomic level energies of the GCR. One method is to average level energies obtained from more detailed atomic states (e.g. term-split levels or configurations). In practice, this method is difficult because one must first obtain the atomic parameters of detailed atomic states, which, for complex many-electron ions, can be extremely challenging. Different averaging methods are possible. The simplest method is to average level energies over the statistical weights  $g_i$ .

$$E_{(1)(2)} = \frac{\sum_{i} g_{i} E_{i}}{\sum_{i} g_{i}} \quad \text{where} \quad i \in 1\text{s2s} \, {}^{3}S_{1}, \, 1\text{s2s} \, {}^{1}S_{0}, \, 1\text{s2p} \, {}^{3}P_{0,1,2}, \, 1\text{s2p} \, {}^{1}P_{1}$$

However, when temperatures are of the same order or smaller than the energy splitting between  $E_i$  levels, this can result in significant error. One can include temperature effects by averaging using Boltzmann statistics:

$$E_{(1)(2)} = \frac{\sum_{i} g_{i} E_{i} e^{-(E_{i} - E_{0})/kT_{e}}}{\sum_{i} g_{i} e^{-(E_{i} - E_{0})/kT_{e}}} \quad \text{where} \quad i \in 1\text{s2s}^{3} S_{1}, \ 1\text{s2s}^{1} S_{0}, \ 1\text{s2p}^{3} P_{0,1,2}, \ 1\text{s2p}^{1} P_{1}$$

Essentially, averaging over statistical weights gives the same result as using Boltzmann statistics with an infinite temperature. Statistical averaging is a reasonable treatment for high-lying Rydberg states where individual states belonging to a SH level tend to be populated statistically. For low-lying SH levels or under coronal conditions where the dominant population is in the lowest energy states, statistical averaging tends to overestimate the excited populations within a SH level.

An "effective temperature" model [15] has been developed to provide more realistic averaging method as a function of plasma conditions and ionization energies. As plasma conditions approach the coronal limit, that is, high temperature and low density, the effective temperature approaches zero and the weight factor for the highlying states also approaches zero. As the density increases, or if the level is close to the ionization limit (e.g. Rydberg states), the effective temperature approaches the plasma temperature and the weight factors become Boltzmann factors.

The temperature- and density-dependent energy levels produced by these averaging techniques can be effective under tightly defined conditions, but they are difficult to use in a GCR model. In some cases, averaged energy levels of bound states exceed the first continuum limit or the order of two averaged levels is reversed resulting in a negative transition energy. Therefore, when GCR levels are produced by averaging, straightforward statistical averaging is preferred, but because of the difficulties in providing a complete model in this manner, screened-hydrogenic levels based on principal quantum numbers are preferred to generate for generating a GCR model.

The second method of constructing level energies is to use the SH formalism. The screened nuclear charges experienced by electrons in each shell are calculated as a linear function of the shell occupations using a set of screening coefficients and are then used to construct the energy of that level. Multiple sets of screening coefficients are available, based upon one or more quantum numbers, i.e. (n, l) or (n, l, j) [16]. The use of more than one quantum number leads to very large numbers of states, so to maintain tractability we restrict SH levels to those based upon principal quantum numbers only.

Energies are computed by applying ionization potentials sequentially from the bare nuclei as illustrated in Fig. 3.2. The ionization potential of a SH level with an outermost bound electron of the principal quantum number n is obtained from the hydrogenic expression (with relativistic corrections)

$$I_{n} = \frac{Q_{n}^{2}}{n^{2}} \frac{e^{2}}{2a_{0}} \left( 1 + \left\lceil \frac{\alpha Q_{n}}{n} \right\rceil \left\lceil \frac{2n}{n+1} - \frac{3}{4} \right\rceil \right)$$

where  $Q_n$  is the screened charge,  $a_0$  Bohr radius and  $e^2/2a_0$  is the Rydberg energy. The screened charge is computed as a function of the screening constants  $\sigma(n, m)$  [17, 18] of the *n*th and *m*th hydrogenic shells and the occupation numbers of the *n*th and *m*th hydrogenic shells,  $N_n$  and  $N_m$  where  $Z_n$  is the charge of the ion;

56 H.-K. Chung et al.

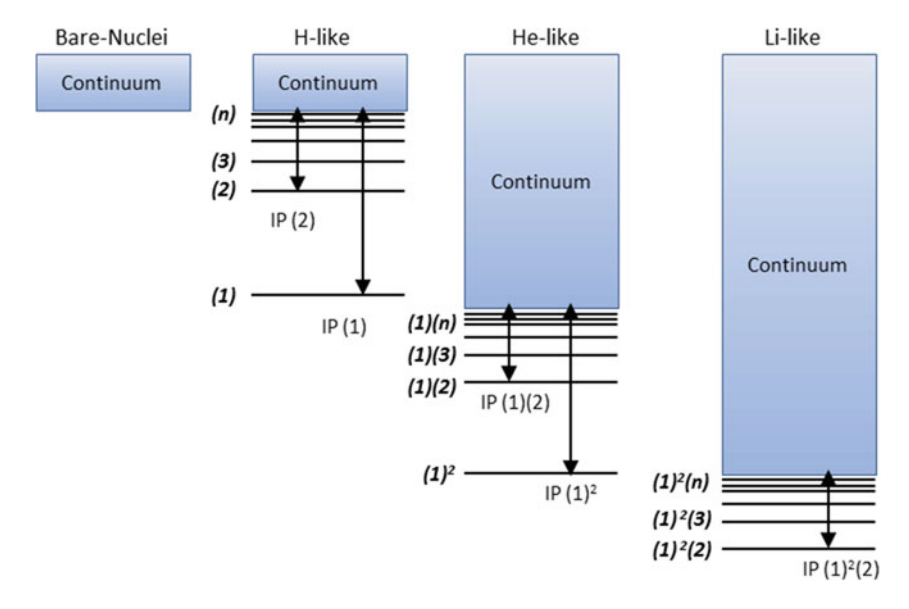


Fig. 3.2 SH level energies are constructed by subtracting the ionization potential of the outermost electron in the valence shell from the continuum limit

$$Q_n = Z_n - \sum_{m < n} \sigma(n, m) N_m - 0.5\sigma(n, n) (N_n - 1)$$

The statistical weight of the SH level denoted by  $(1)^{N_1}(2)^{N_2}...(m)^{N_m}(n)^{N_n}$  is given by binomial coefficients  $C(2m^2, N_m)$  where  $2m^2$  is the maximum occupation number of the mth hydrogenic shell;

$$g = \prod_{m=1}^{n} C(2m^2, N_m)$$

The advantage of generating levels in this manner is the flexibility. The energy level can be computed for any configuration with an arbitrary number of shells and occupation numbers. It is straightforward to calculate energy levels of exotic configurations with many vacant shells. By contrast, energy levels of a configuration with more than 2 vacant shells are extremely time consuming to generate with detailed atomic physics codes. An example of exotic configurations is given by hollow ions with no electrons in the K-shell. As illustrated in Fig. 3.3, SH configuration energies of hollow ions can be easily obtained from the continuum state with calculated ionization potentials. As depicted in the diagram, energy levels of (2)(n) are calculated as the energy of (2) subtracted by the valence shell (n) ionization potential of  $(2)^2(n)$  as the energy of  $(2)^2$  subtracted by the valence shell (n) ionization potential of  $(2)^2(n)$ .

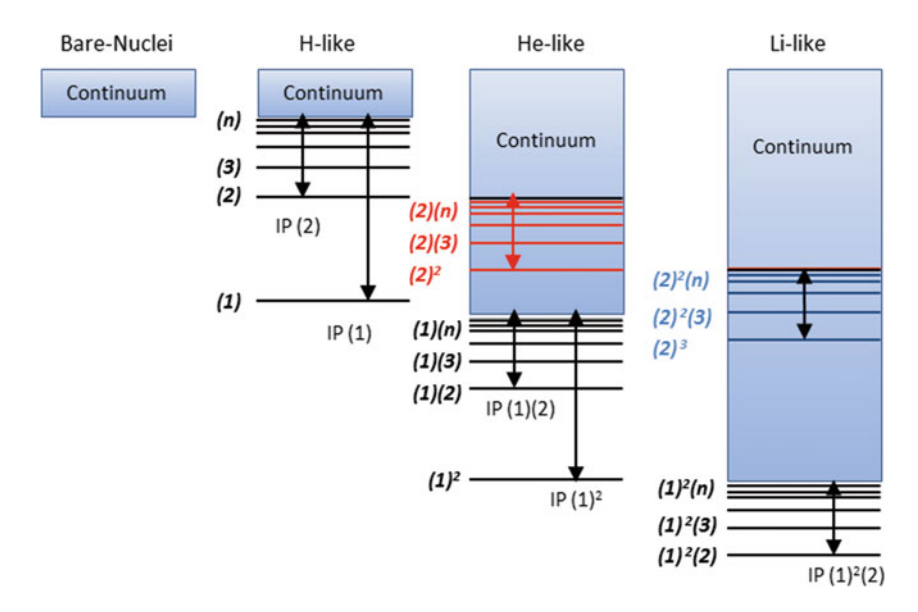


Fig. 3.3 A schematic way of producing energy levels of hollow atom states in He-like ions and Li-like ions is illustrated

SH energy levels are not spectroscopically accurate, not only because each level represents numerous detailed levels, but because of the approximate nature of the formalism. In particular, the ionization energies obtained from the screening constants become noticeably inaccurate near closed shells. Substituting ionization energies from accurate atomic physics calculations, and scaling the SH excitation energies accordingly, removes some of the systematic inaccuracies in the energy levels. The resulting models have been found to produce charge state distributions comparable to results from a variety of codes for a wide range of plasma conditions in the NLTE (non-local thermodynamic equilibrium) kinetics workshops [19–24].

There are more elaborate approaches to improve the accuracy of SH models by employing a "width" to a SH level, which describes the spread and distribution of detailed atomic level energies belonging to one schematic SH level as shown in Fig. 3.1. Using imposed internal partition functions, these models can more accurately model processes between overlapping SH levels and effectively vary the statistical weights of the SH states according to the plasma conditions [25]. Including SH widths also enables finer coupling between SH states and more detailed state structure in hybrid-structure models [26].

This simple and flexible way to construct an arbitrary set of energy levels provides the capability to produce a required "complete" set of (super-) configurations and is a key ingredient of the GCR model. Completeness is required to include all important population channels for atomic processes occurring in an atom surrounded by other atoms, electrons and photons. Even so, a model of complex many-electron ions can easily become intractable; hence care is needed in determining a comprehensive set of

58 H.-K. Chung et al.

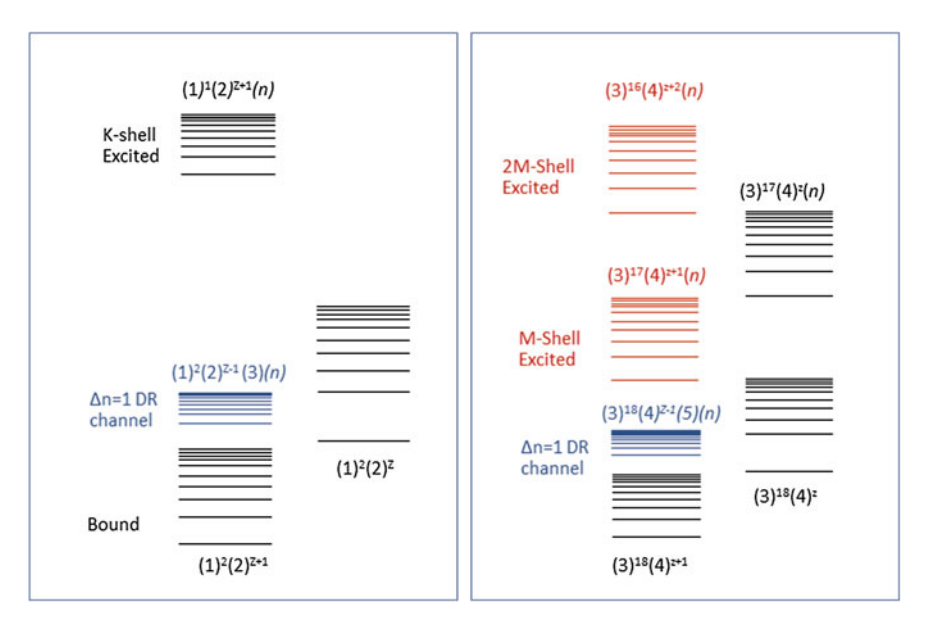


**Fig. 3.4** A schematic diagram of SH levels contained in a GCR model is presented for L-shell (*left*,  $(1)^2(2)^{z+1}$ ) and N-shell (*right*,  $(3)^{18}(4)^{z+1}$ ) ions

configurations that are most relevant to the application of interest. As a rule of thumb, levels involved in dielectronic recombination (DR) processes should be extensively included in a model to ensure a reasonable estimate of charge state distributions. For K- and L-shell ions, levels with doubly excited electrons from the valence shell of the ground configuration are the dominant DR population channels. For M-shell and more electron ions, levels with inner-shell excited electrons play an important role in DR processes. Basic levels in a GCR model are shown in Fig. 3.4 for the two cases of L-shell ions and N-shell ions.

### 3.2.2 Atomic Transition Rates

The transition rates required for most plasma applications are those for electron excitation and ionization, photon excitation and ionization and autoionization. A schematic diagram of atomic processes required for a CR model is illustrated in Fig. 3.5.

The rates of inverse processes, electron de-excitation, recombination, radiative recombination and electron capture, can be obtained by the principle of detailed balance, which states that under conditions of thermal equilibrium, each rate is exactly balanced by its inverse rate. Since this holds between any pair of states, with each state defined by the atomic level and phase space element of each particle, it can

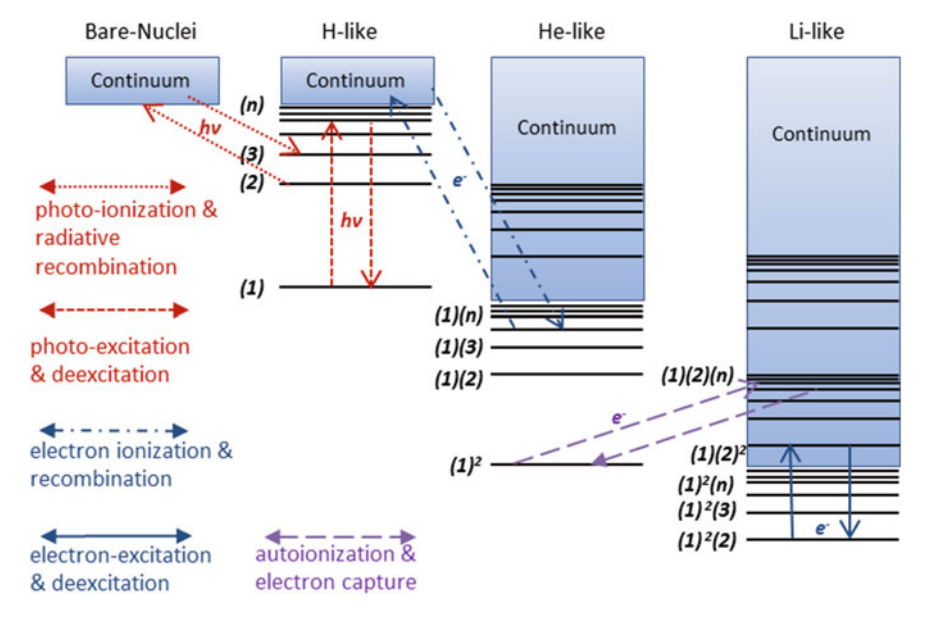


Fig. 3.5 Atomic processes required for a CR model

be applied to energy-dependent differential cross sections as well as transition rates integrated over thermal particle distributions [27].

If transition rates are available between detailed levels (term levels or configuration average levels), transition rates between averaged levels can be obtained by averaging the transition rates  $R_{if}$  over a weight factor  $w_i$ , the statistical weight or Boltzmann factor of an initial state i of each transition connecting the initial state i of the initial averaged level I to the final state f of the final averaged level F.

$$R_{IF} = \frac{\sum_{f \in F} \sum_{i \in I} w_i R_{if}}{\sum_{i \in I} w_i}$$

If detailed level transitions are unavailable for certain levels, schematic rates can be used. Schematic transition rates are obtained from formulas based on transition rates in hydrogenic ions with a minimum set of parameters derived from atomic physics.

### 3.2.2.1 Radiative Processes

Rates of radiative processes between bound states (bound-bound), and between bound and free states (bound-free) are required. Bound-bound transitions are photoexcitation by absorption and deexcitation by spontaneous or stimulated emission of the radiation field. An absorption oscillator strength of a transition from an initial SH level i to a final SH level f may be defined as  $f_{osc}(i \rightarrow f) = f_H(i \rightarrow f)$ 

60 H.-K. Chung et al.

 $P_i(1-P_i/2n_f^2)$  where  $f_H(i \to f)$  is the oscillator strength of hydrogenic ions,  $P_i$  is the occupation number of equivalent electrons in the shell making the transition of the level i and  $2n_f^2$  is the maximum occupation of level f. However,  $f_H(i \to f)$  defined in this manner overestimates, by a factor of a few, compared with averaged values derived from a relativistic Hartree-Fock-Slater atomic physics code. Scaling the oscillator strengths by a factor accounting for screening effects improves the accuracy considerably [9].

By detailed balance, the emission and absorption oscillator strengths are related by

$$g(i \rightarrow f) f_{osc}(i \rightarrow f) = g(f \rightarrow i) f_{osc}(f \rightarrow i)$$

The spontaneous emission rate  $A(f \to i)$  and absorption cross-section  $\alpha(i \to f)$  between two bound levels i and f are directly related to the absorption oscillator strength,  $f_{osc}(i \to f)$  of the photo excitation (PE) transition as

$$A(f \to i) = \frac{8\pi^2 e^2 \nu (i \to f)^2}{mc^3} \frac{g_i}{g_f} f_{osc}(i \to f) \quad \text{and}$$

$$\alpha^{PE}(i \to f) = \frac{\pi e^2}{mc} f_{osc}(i \to f) \varphi(\nu)$$

where the  $g_i$  and  $g_f$  are the statistical weights of the states,  $\nu(i \to f)$  is the photon frequency corresponding to the transition energy, e and m are the electron charge and mass, and c is the speed of light. In general, the transition has a spread in frequency described by the line profile function  $\phi$ , which represents the relative probability of absorbing a photon of frequency  $\nu$ .  $\phi$  is usually a narrow function centered at  $\nu(i \to f)$  and is normalized by

$$\int_{-\infty}^{\infty} \varphi(\nu) \, d\nu = 1$$

The transition rate in units of s<sup>-1</sup> for photo-excitation processes is

$$R^{PE} (i \to f) = 4\pi \int \alpha^{PE} (i \to f) J(\nu) \frac{d\nu}{h\nu}$$
 where 
$$J(\nu) = \frac{1}{4\pi} \int I(\nu, \Omega) d\Omega$$

where  $J(\nu)$  is the angle-averaged intensity and  $I(\nu, \Omega)$  is the specific intensity as a function of frequency  $\nu$  and direction.

A photoionization (PI) rate from an initial SH level i of a charge state  $X^{Z+}$  to a final SH level of another charge state  $X^{(z+1)+}$  is given the same way as

$$R^{PI}(i \to f) = 4\pi \int \alpha^{PI}(i \to f) J(\nu) \frac{d\nu}{h\nu}$$

A scaled photoionization cross-section provided by Kramer [28] as a function of incoming photon energy  $h\nu$ , the screened charge and ionization potential of the ionized n-shell electron  $Q_n$  and  $I_n$ , and Rydberg constant  $I_H$  is widely used.

$$\alpha^{PI} \left( i \to f \right) \left( h \nu \right) = \frac{64 \pi \alpha a_0^2}{3^{1.5}} \frac{I_n^{2.5} I_H^{0.5}}{Q_n \left( h \nu \right)^3}$$

where  $a_0$  is the Bohr radius and  $\alpha$  is the fine structure constant. The inverse process is radiative recombination (RR) where a free electron recombines with an ion, emitting a photon in the process. For a given electron distribution  $f_e(E)$ , the recombination rate is obtained by integrating the cross-section  $\sigma^{RR}(f \to i)(E)$  over the electron and photon distributions, with electron and photon energies related by  $h\nu = I_n + E$ ,

$$R^{RR}(f \to i) = N_e \int_0^\infty \left(\frac{2E}{m_e}\right)^{\frac{1}{2}} \sigma^{RR}(f \to i) (E) f_e(E) dE$$

where the cross-section  $\sigma^{RR}(f \to i)(E)$  is written as

$$\begin{split} \sigma^{RR}(f \to i)(E) &= \sigma^{RR}_{st} \left( f \to i \right) (E) \, J(\nu) + \sigma^{RR}_{sp} (f \to i)(E) \\ &= \left( J(\nu) + \frac{2 \mathrm{h} \nu^3}{c^2} \right) \sigma^{RR}_{st} (f \to i)(E) \end{split}$$

Stimulated and spontaneous radiative recombination cross-sections are written in terms of photoionization cross-section  $\alpha^{PI}(i \to f)(E)$  using the Einstein-Milne relation [27]

$$\sigma_{st}^{RR}(f \to i) (E) = \frac{g_i}{g_f} \frac{h^2}{4m_e E} \frac{\alpha^{PI}(i \to f) (E)}{h\nu} \text{ and}$$

$$\sigma_{sp}^{RR}(f \to i) (E) = \frac{g_i}{g_f} \frac{(h\nu)^3}{2m_e E c^2} \frac{\alpha^{PI}(i \to f) (E)}{h\nu}$$

#### 3.2.2.2 Collisional Processes

The rate of a collisional transition with cross-section  $\sigma(E)$  as a function of incoming electron energy E is obtained by integrating over the electron energy distribution function  $f_e(E)$  as

$$R^{COL}(i \to f) = N_e \int_{\Delta E}^{\infty} v \sigma^{COL}(i \to f) (E) f_e(E) dE$$

where  $\Delta E$  is the threshold energy and v is the electron velocity for an electron of energy E. A scaled collisional excitation (EX) cross-section from an initial level i to a final level f based on oscillator strength  $f(i \to f)$  for the allowed transitions

62 H.-K. Chung et al.

[29, 30] is commonly used

$$\sigma^{EX}\left(i \to f\right)\left(E\right) = \frac{8\pi^{2}a_{0}^{2}}{\sqrt{3}} \left(\frac{I_{H}}{\Delta E}\right)^{2} \frac{f(i \to f)g(U)}{U}$$

where  $U = E/\Delta E$  and g(U) is the Gaunt factor. The collisional de-excitation (DE) cross-section is obtained from detailed balance as

$$\sigma^{DX}(f \to i)(E) = \frac{g_i}{g_f} \frac{E + \Delta E}{E} \sigma^{EX}(i \to f)(E + \Delta E)$$

For a Maxwellian electron distribution, this reduces to a simple relationship between the excitation and de-excitation rates:

$$\frac{R^{DX}(f \to i)}{R^{EX}(i \to f)} = \frac{g_i}{g_f} e^{\Delta E/kT_e}$$

Simple semi-empirical formula of collisional ionization (CI) cross-sections [31, 32] can be used for collisional ionization from an initial level i for electron with energy  $E > \text{ionization potential } \Delta I$ ;

$$\sigma^{CI}\left(i \to f\right)\left(E\right) = \pi a_0^2 C \xi \left(\frac{I_H}{\Delta I}\right)^2 \left(\frac{\Delta I}{E}\right) log\left(\frac{E}{\Delta I}\right) w\left(\frac{E}{\Delta I}\right)$$

where

$$\mathbf{w}\left(\frac{E}{\Delta I}\right) = \left[\log\left(\frac{E}{\Delta I}\right)\right]^{\frac{\beta \Delta I}{E}} \text{ and } \quad \beta = 0.25 \left(\left[\frac{100z + 91}{4z + 3}\right]^{\frac{1}{2}} - 5\right)$$

and z is the charge of the ion and  $\xi$  is the effective number of equivalent electrons in shell. The suggested value of 2 is often used for the constant C.

For a Maxwellian electron distribution, the three-body, or collisional recombination rate coefficient  $R(f \to i)$  is easily obtained from the ionization rate coefficient  $R(i \to f)$  by detailed balance as

$$\begin{split} \frac{R^{CR}(f \to i)}{R^{CI}(i \to f)} &= \frac{g_i}{g_f} \frac{N_e}{2} \left( \frac{h^2}{2\pi m_e k_B T_e} \right)^{3/2} e^{-(E_i - E_f)/k_B T_e} \\ &= 1.66 \times 10^{-22} \frac{g_i}{g_f} \frac{N_e}{T_e^{3/2}} e^{-\Delta I/k_B T_e} \end{split}$$

For an arbitrary electron distribution, the rate coefficient is obtained by integrating over the differential collisional ionization (DCI) cross-section  $\sigma(i \to f)(E \to E', E'')$  for incoming electron energy E and ejected and outgoing electrons of energy E' and E''. This is related to the total cross-section  $\sigma(i \to f)(E)$  through the relation

[27, 33],

$$\sigma^{CI}(i \to f)(E) = \iint \sigma^{DCI}(i \to f)(E \to E', E'')dE'dE''$$
$$= \frac{1}{2} \int_0^{E-I_n} \sigma^{DCI}(i \to f)(E, E_b)dE_b$$

where  $I_n$  is the threshold energy for the ionization process and  $E_b$  is the energy of the ejected energy. Applying detailed balance leads to the Fowler relation for differential collisional recombination cross-section (DCR)  $\sigma(f \to i)(E', E'' \to E)$  [27]

$$\sigma^{DCR}(f \to i)(E', E'' \to E) = \frac{h^3}{16\pi m_e} \frac{g_i}{g_f} \frac{E}{E'E''} \sigma^{DCI}(i \to f)(E \to E', E'')$$

The three-body recombination rate coefficient is then given as

$$\begin{split} \mathbf{R} &= N_e^2 \iiint \left(\frac{2E'}{m_e}\right)^{\frac{1}{2}} \left(\frac{2E''}{m_e}\right)^{\frac{1}{2}} f_e(E') f_e(E'') \sigma(f \to i) (E', E'' \to E) dE' dE'' dE \\ &= N_e^2 \frac{h^3}{2^{5/2} \pi m_e^{3/2}} \frac{g_i}{2g_f} \iiint \left(\frac{2E}{m_e}\right)^{\frac{1}{2}} \left(\frac{E}{E'E''}\right)^{\frac{1}{2}} f_e(E') f_e(E'') \sigma(i \to f) (E \to E', E'') dE dE' dE'' \end{split}$$

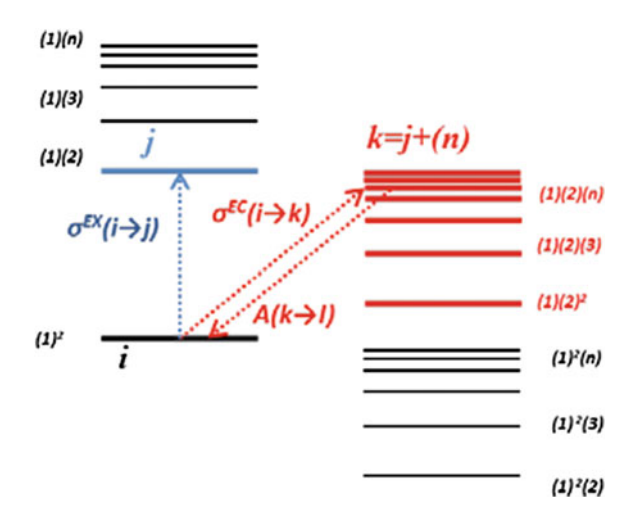
### 3.2.2.3 Autoionization and Electron Capture

There exist numerous autoionizing states acting as the dielectronic recombination and indirect ionization channels. Calculating accurate autoionization rates can be difficult due to the presence of multiple open shells. An approximate rate has been obtained [34] as follows: The autoionization rate  $A(k \to i)$  from state k of an ion (consisting of the excited state f of the next ion plus the outer most excited electron) to a bound state i of the next ion is obtained by detailed balance from the corresponding electron capture cross-section  $\sigma(i \to k)$  from the state i to k.

$$\frac{N_e \int \sigma^{EC} (i \to k) \, v f_e^M (E) \, dE}{A(k \to i)} = \frac{g_k}{g_i} \frac{N_e}{2} \left( \frac{h^2}{2\pi m_e k_B T_e} \right)^{3/2} e^{-(E_k - E_i)/k_B T_e}$$
$$f_e^M (E) = \frac{2}{\sqrt{\pi}} \frac{E^{1/2}}{T_e^{3/2}} e^{-E/k_B T_e}$$

Assuming that the electron capture cross-section averaged over the resonances can be obtained by extrapolating below the threshold of electron excitation cross-section  $\sigma(i \to j)$  as

Fig. 3.6 An illustration of the relationship among autoionization rate, electron capture and electron excitation transitions



$$\overline{\sigma^{EC}(i \to k) v f_e^M(E) dE} = \sigma^{EX}(i \to j) v(i \to j) f_e^M(E(i \to j)) \frac{2Z^2 Ry}{n^3}$$

$$\frac{dE}{dn} = \frac{d}{dn} \left(\frac{Z^2 Ry}{n^2}\right) = -\frac{2Z^2 Ry}{n^3} \quad \text{and} \quad \text{Ry} = \frac{\hbar^2}{2m_e a_0^2}$$

the following relationship is obtained between electron excitation cross-section  $\sigma^{EX}(i \to j)$  and autoionization rate  $A(k \to i)$ ;

$$\frac{\sigma^{EX}(i \to j)}{A(k \to i)} = \frac{g_k}{g_i} \frac{\pi^2 n^3 a_0^2 \hbar}{2z^2 E(i \to j)}$$

This provides a method of approximating autoionization rates from a collisional excitation cross-section evaluated at the threshold energy  $E(i \rightarrow j)$  as illustrated in Fig. 3.6.

# 3.2.3 Plasma Effects

A GCR model is developed using data from isolated atoms but is applied to atoms embedded in plasma. Atoms and ions interact with particles and fields in plasma and the interaction influences atomic parameters such as energy levels, transition probabilities [35–37]. As ion and electron densities increase, atomic levels broaden, shift and disappear due to the interaction with surrounding ions and electrons and atomic transition rates change accordingly as shown in Fig. 3.7. The most prominent effect is the reduction of ionization potentials, which in extreme cases results in a significant change in charge state distributions. Due to the interaction with surrounding ions

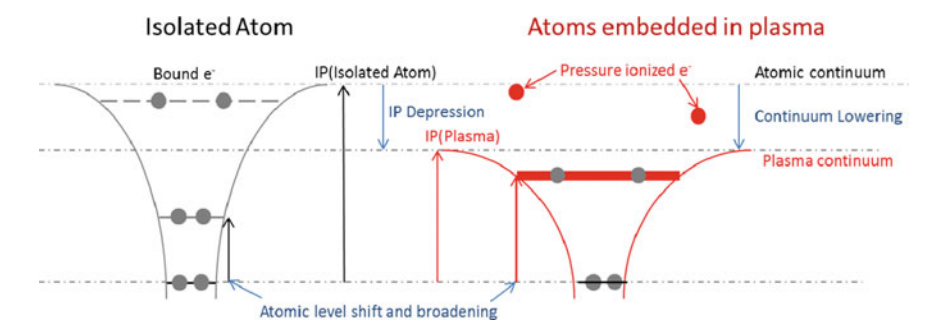


Fig. 3.7 Conceptual illustration of ionization depression/continuum lowering

and electrons, atomic potential changes accordingly. Higher-lying states may not be bound in the new atomic potential and the energy required to ionize the remaining bound electrons is reduced. This phenomenon is called as ionization potential depression (IPD) or continuum lowering. Since this results in enhanced ionization it is sometimes called pressure ionization.

A simple method to include this effect in a CR model is to apply an IPD model to determine the depressed ionization potential. Then two adjustments should be made for the CR model: (1) states identified as being no longer bound are excluded from the rate equations and (2) ionization and recombination rates of remaining states in the model are modified according to the depressed ionization potential. There exist other methods such as the occupation probability method [37] where a statistical weight of state changes as a function of plasma conditions or a level broadening method where a density and width of state is applied as a function of plasma conditions. Recent experiments with x-ray free electron lasers (XFEL) interacting with dense plasmas have sparked numerous discussions on how to treat IPD in plasmas [38–42].

The IPD model of Stewart and Pyatt [36] is widely used. This model uses a finite temperature Thomas-Fermi treatment for bound electrons to evaluate the effect of free electrons and neighboring ions on the ionization potential depression. An ion with a nucleus Z and a net charge z (z=1 for a neutral atom) occupying a sphere (of a radius a) of the ion and free electrons to maintain a neutral charge at the boundary is considered. Stewart and Pyatt obtained a full solution by solving the Poisson equation numerically with a potential due to free electrons and ions, and an approximate analytical solution by placing all the bound electrons at the origin and assuming a uniform free-electron density:

$$\Delta E = \frac{\left\{ \left[ 3\left(z^* + 1\right) \frac{ze^2}{DkT} + 1 \right]^{2/3} - 1 \right\}}{2(z^* + 1)} = \frac{\left\{ \left[ \left( \frac{a}{D} \right)^3 + 1 \right]^{2/3} - 1 \right\}}{2(z^* + 1)}$$

where the Debye length D and the sphere radius a are defined with the free-electron density and ion density far from the ion  $n_e(\infty)$  and  $n_i(\infty)$  and electron temperature

of T;

$$\frac{1}{D^2} = \frac{4\pi e^2}{kT} \left(z^* + 1\right) n_e \left(\infty\right) \qquad \text{where } z^* = \frac{z^2}{z} = \frac{\sum_i z_i^2 n_i(\infty)}{z}$$

$$a^3 = \frac{3z}{4\pi n_e(\infty)}$$

The analytical solution approaches the limiting cases of the Debye-Hückel (DH) model for low density and high temperature and the ion-sphere (IS) models for high density and low temperature.

$$\Delta E^{DH} = \frac{ze^2}{DkT}$$
 for  $\frac{a}{D} \ll 1$ 

$$\Delta E^{IS} = \frac{3}{2} \frac{ze^2}{akT} \quad \text{for } \frac{a}{D} \gg 1$$

Comparisons with numerical solutions show that the analytical expression for the depressed ionization potential approximates the true values reasonably well, particularly for cases with large  $z^*$  and small (a/D) values, and it is the analytical expression which is widely used in CR models.

A treatment of high-lying Rydberg states is critical in obtaining a correct charge state balance for both low and high densities. Due to the  $n^3$  dependency of collisional recombination rate coefficients, excited states with high principal quantum number n act as fast recombination channels and the treatment of these states and the IPD effect are very important in determining population distributions for recombining plasmas or high densities. On the other hand, very high Rydberg orbitals can exist at low density and the autoionization states with high principal quantum number contribute significantly to the dielectronic recombination (DR) processes and hence they play a major role in charge state distributions as well. Discussions on the model completeness can be found in the chapter on model completeness.

# 3.2.4 Spectroscopic Emissivity and Opacity

A SH model has been widely used in obtaining not only charge state distributions but also spectroscopic properties of plasmas under certain conditions, for example, the K-shell spectroscopy of one (H-like) or two electron (He-like) ions or of the K-shell vacant ions ( $K_{\alpha,\beta,\gamma}$  lines) where levels are well characterized by a hydrogen-like level. However, more detailed level structures are generally needed to provide a realistic spectroscopic prediction as shown in the Fig. 3.8 where spectra of term-based model and SH model are compared for the He-like ions of Ge atoms at 10 keV even for K-shell ions.

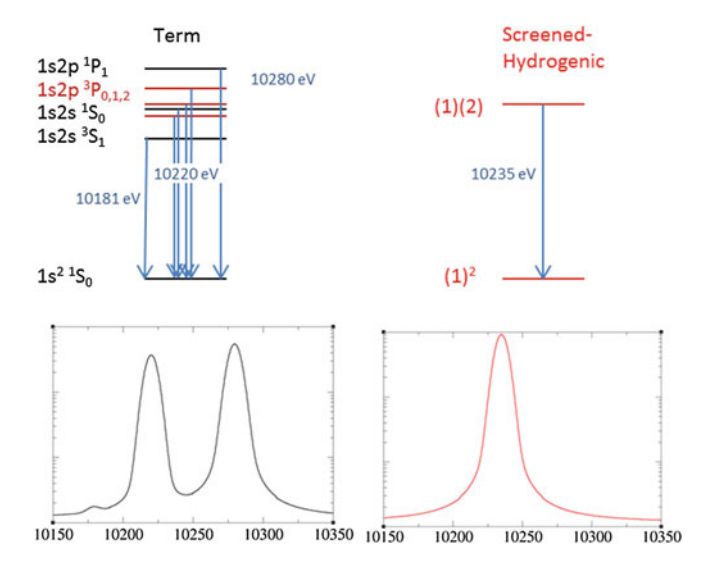


Fig. 3.8 Spectra of term-based model and SH model are compared for the He-like ions of Ge atoms at 10 keV

The procedure to generate a spectroscopic parameter such as emissivity and opacity from a SH model is to generate energy levels and transition probabilities of all the term-split levels [43, 44] or relativistic (or non-relativistic) configurations relevant [45, 46] to the screened-hydrogenic levels and then assign population densities for each term level or each configuration with a weight factor. As in the Sect. 3.2.1, a weight factor could be a statistical weight or a Boltzmann statistics based electron temperature or effective temperature. The population density  $P_j$  of each detailed level j with statistical weight  $g_j$  and energy  $E_j$  is computed by Boltzmann statistics among all the detailed levels belonging to their SH level A as following.

$$P_{\rm j} = \frac{g_j e^{-(E_j - E_0)/kT_e}}{\sum_{i \in A} g_i e^{-(E_i - E_0)/kT_e}} \quad \text{where } E_0 \text{ is the energy of the lowest level belonging to } A$$

The population distribution is used to compute the emissivity and opacity of bound-bound radiation and bound-free radiation for all possible radiative transitions.

A SH model is often applied for the spectroscopy of many electron shells (M or N shell) where numerous lines exist as unresolved lines and it is impractical to compute emissivity and opacity for individual transitions because of the huge number of transitions. The most widely used method in this regard is to use the supertransition-array (STA) model [11–14]. In this method, the STA transition energy, transition probability and the STA width for the line radiation are defined with atomic parameters of more detailed configurations such as relativistic configurations or term-dependent levels. The STA transition energy  $E_{AB}$  from the super configuration (or a SH level) **A** to the super configuration (or a SH level) **B** is defined as follows:

$$E_{AB} = \frac{\sum_{i \in A, j \in B} g_i A (i \to j) E(i \to j) e^{-(E_i - E_0)/kT_e}}{\sum_{i \in A, j \in B} g_i A (i \to j) e^{-(E_i - E_0)/kT_e}}$$

where  $g_i$  and  $g_j$  are the statistical weights of levels i and j belonging to A and B and  $E(i \rightarrow j)$  and  $A(i \rightarrow j)$  are the level energy and spontaneous emission probability of the transition from the detailed level i to the detailed level j. The transition probability  $A_{AB}$  and the STA width  $\mu_{AB}$  are defined as:

$$A_{AB} = \frac{\sum_{i \in A, j \in B} g_i A(i \to j) e^{-(E_i - E_0)/kT_e}}{\sum_{i \in A, j \in B} g_i e^{-(E_i - E_0)/kT_e}}$$

$$\mu_{AB}^2 = \left[\frac{\sum_{i \in A, j \in B} g_i A(i \to j) E(i \to j)^2 e^{-(E_i - E_0)/kT_e}}{\sum_{i \in A, j \in B} g_i A(i \to j) e^{-(E_i - E_0)/kT_e}}\right]^2 - E_{AB}^2$$

With  $E_{AB}$ ,  $A_{AB}$  and  $\mu_{AB}$ , the computation time in solving radiation transfer equations is tremendously saved by reducing the numbers of radiation transitions. However one should store the level and transition probability information and deal with the large number of atomic parameters at each electron temperature.

## 3.3 Applications

A GCR model is constructed to be valid both at the coronal limit and at the local thermodynamic equilibrium (LTE) limit so that it can provide a reasonable prediction for a wide range of plasma conditions. In this section, applications of a GCR model are introduced.

# 3.3.1 Steady-State Plasmas Generated by Long-Pulse Lasers

Plasmas generated by a few nano-second long-pulse lasers are often found to have a large volume of weakly space-dependent plasma conditions at steady-state after the initial hydrodynamic expansion and heating of the plasma, for which emission and absorption spectroscopy are used for the determination of single thermal temperature and density. A GCR model is useful to estimate charge state distributions (CSD) and the average charge state <Z> over a wide range of plasma conditions before designing spectroscopic experiments and/or analysing a time-integrated, space-integrated emission/absorption spectra. Particularly for high Z elements, a CR model using detailed atomic structures is very large and often unavailable.

An example of the predicted average charge states and L-shell spectra for electron temperatures of 4–10 keV and electron density of  $10^{21}$ – $10^{22}$  cm<sup>-3</sup> using a SH model, FLYCHK code [1] is compared with measured gold L-band spectra from the high

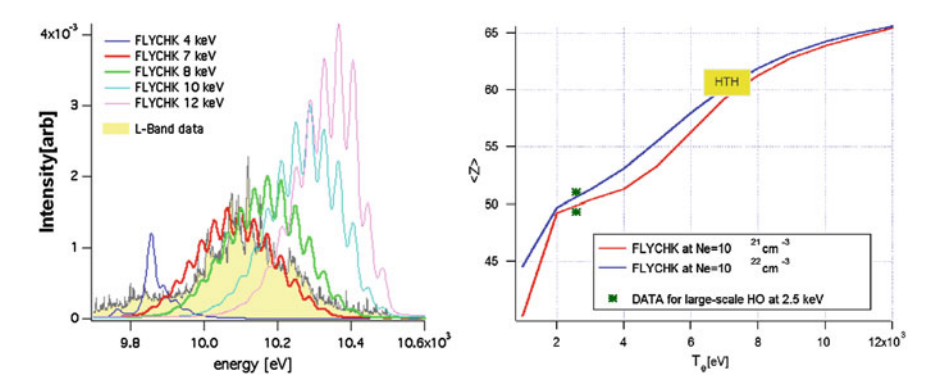


**Fig. 3.9** A SH model predicts spectra and charge state distribution from gold ions over a wide range of plasma conditions. Measured L-band spectra from HTH (High temperature hohlraum) and <Z> from two Hohlraum data are compared with results (Figure is taken from [6])

**Table 3.1** Charge state distribution of gold ions at 8 keV and  $1E21 \text{ cm}^{-3}$ 

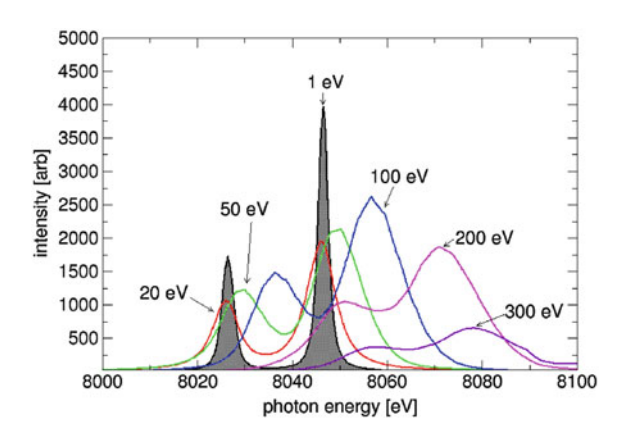
Ion	49	50	51	52	53	54	55	56	57	58	59	60	61
Fraction	0.027	0.071	0.081	0.103	0.119	0.126	0.123	0.109	0.088	0.062	0.040	0.023	0.012

temperature hohlraum (HTH) [3, 6] in Fig. 3.9. Temperatures of HTH are determined to be in the range of 7–8 keV based on the comparison with measured spectra. Ionization distributions of many-electron charge states of high Z elements are often broad as shown in Table 3.1. The calculated maximum relative ion population is only 0.126 for  $Au^{54+}$  at 8 keV and more than 10 charge states from  $Au^{49+}$  to  $Au^{61+}$  are substantially populated (a fraction > 0.01) at this temperature. Consequently, the spectra is broad due to contributions from a range of charge states and it is important to include as many charge states and configurations as possible in the CR model to explain the broad spectral features.

# 3.3.2 Two-Temperature Plasmas Generated by Short-Pulse Lasers

Ultra-short-pulse lasers create plasmas with fast proton beam, x-rays and relativistic electrons which consist of cold, thermal electrons and hot, non-thermal electrons. Relativistic electrons readily ionize K-shell of target atoms and  $K_{\alpha,\beta}$  lines from 2p-1s and 3p-1s transitions are frequently used for plasma diagnostics. Since the density of cold and thermal electrons is usually a few orders of magnitude higher than the density of hot electrons, charge state distributions from the measured K-shell spectra reflect the cold electron characteristics. As a result, observed K-shell spectra have

Fig. 3.10  $K_{\alpha}$  spectra are broadened and shifted from the cold  $K_{\alpha}$  lines with plasma heating as a function of electron temperature



little information on the hot electron characteristics except that energetic electrons do exist to ionize K-shell electrons.

An example of Cu emission spectra [4] in Fig. 3.10 shows  $K_{\alpha}$  spectra changing with cold electron temperatures from 1 to 300 eV (at solid density) and shifting away from the cold  $K_{\alpha}$  position at 8047.78 eV. The hot electron fraction of 0.001 and energy of 3 MeV were used for this example. The broadening and shift of  $K_{\alpha}$  lines is attributed to the heating of cold electrons which leads to ionization of plasmas. When valence electrons are ionized by thermal electrons, the screening from outer electrons is reduced and electrons are more tightly bound for higher charge states.  $K_{\alpha}$  transition energies from 2p-1s transition increase as ionization increases and hence the  $K_{\alpha}$  spectra shift to the higher energies (blue side). In addition,  $K_{\alpha}$  spectral lines broaden as more charge states and atomic levels are populated to emit the K-shell transitions over a wider spectral range than the cold spectra. The shift and broadening of  $K_{\alpha}$  emission spectra is a good diagnostic of thermal electron temperatures.

# 3.3.3 Photoionization Equilibrium Plasmas

Pulsed-power machines such as Sandia Z machines produce astronomical x-rays in the laboratory and generate plasmas at astrophysics relevant conditions. At photoionization equilibrium such as found in gaseous nebulae and active galactic nuclei (AGN), a charge state balance is characterized by the ionization parameter  $\xi$ , a ratio of photoionizing radiation flux and electron density. It is independent of electron temperature. X-ray power from Sandia Z-machine fits in the range of ionization parameters found in X-ray binaries and AGN and the laboratory plasmas created by Sandia Z-machine can be used to study charge state balances of astrophysical plasmas [5].

Examples of Iron charge state distributions with and without radiation field are shown in Fig.3.11 over a temperature range from 30 to 210 eV at the electron

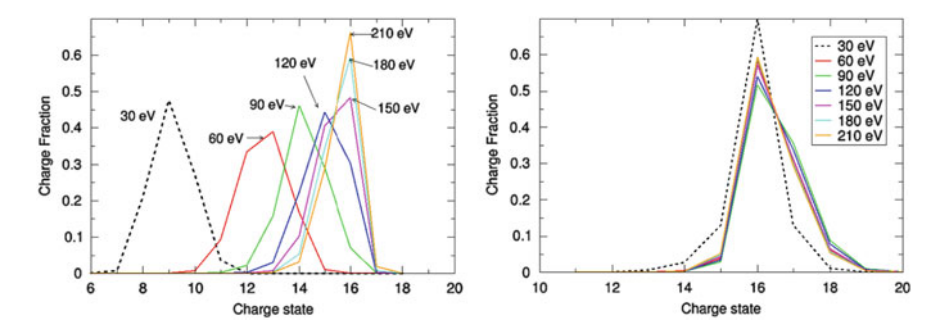


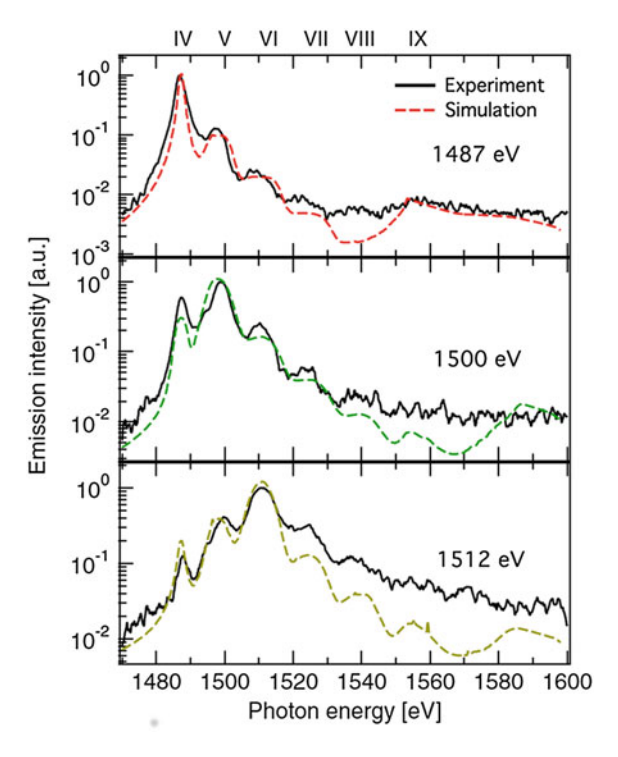
**Fig. 3.11** Charge state distributions of Iron ions at electron temperatures from 30 to 210 eV and electron density of  $1.95 \times 10^{19}$  cm<sup>-3</sup> without (*left*) and with (*right*) radiation field of 165 eV and 0.01 dilution factor

density of  $1.95 \times 10^{19}~{\rm cm^{-3}}$  expected to be valid for an experiment performed in the Z machine. Results show charge state distributions (CSD) increase as a function of temperature without radiation field while the CSD become comparable over a wide temperature range by adding 165 eV Blackbody radiation field (and 0.01 dilution factor). Atomic processes are dominated by photo-ionization process and dielectronic and radiative recombination processes and the ionization distribution is a function of radiation field strength and electron density in photoionization equilibrium plasmas. At the perfect photoionization equilibrium state found in astrophysical plasmas (with very low electron density), the CSD should be same for all temperature cases. The higher densities of the Sandia Z experiment result in non-negligible 3-body recombination that accounts for the small CSD differences over a range of temperatures.

# 3.3.4 Photo-Ionized Plasmas Generated by X-Ray Free Electron Lasers

X-ray free electron lasers (XFEL) create an exotic state of matter such as finite-temperature (warm or hot) dense matter, hollow atoms with 2 vacancies in the K-shell and highly non-equilibrium plasmas [8, 47]. XFEL at the Linear Coherent Light Sources (LCLS) provides a photon source of ultrashort pulses (10–340 fs), high photon energy (800-20 keV) and high photon number (10<sup>12</sup> photons or 10<sup>5</sup> x-rays/Å<sup>2</sup>). Plasmas generated by XFEL undergo time-dependent population cascades from the inner-shell vacant states initiated by XFEL photoionization. The inner-shell vacant states such as K-shell or L-shell vacant states decay rapidly by radiative emission or Auger decay and XFEL-driven plasmas emit strong radiation in the K-shell or L-shell spectral range when the XFEL pulse is on. The XFEL photon energies are transferred to electrons and ions by producing photo electrons and Auger electrons. As the electron density increases with time, collisional processes by elec-

Fig. 3.12 Calculated emission spectra are compared with observed emission from plasmas ionized by XFEL of photon energies 1487, 1500 and 1512 eV (Figure is taken from [8])



trons become significant and ionization processes depend both electron and photon collisions. The absorption process of XFEL is critically tied to the evolution of plasma conditions and a CR model is used to explain the initial photo-absorption processes and the time evolution of ionization processes and related plasma conditions.

In Fig. 3.12, emission spectra are compared between simulations and experiments where a solid target is ionized by XFEL with the photon energy lower than the cold K-edge energy and yet at  $K_{\alpha}$  resonances of L-shell Al ions. Since x-ray photon energy is not high enough to ionize K-shell electrons, there is no K-shell vacant state or K-shell emission initially. Instead x-ray photons ionize L-shell electrons leaving holes in the L-shell. As more and more L-shell electrons are ionized leaving holes in the L-shell, eventually the  $K_{\alpha}$  transition energy of the L-shell hole states is in resonance with the incoming XFEL photon energy and then photo-excitation process of XFEL photons will excite K-shell electrons to L-shell electrons. The K-shell vacant states can decay either by radiative decay emitting  $K_{\alpha}$  radiation or by Auger decay. The resulting emission is highest at the photon energy of  $K_{\alpha}$  resonances of L-shell ion and hence the emission spectra peak at the incoming XFEL photon energies [8].

## 3.3.5 Radiative Loss Rates of Heavy Elements

Radiative loss is an important energy loss mechanism of plasmas containing midto-high Z elements and it is critical to quantify the total energy balance of plasma and consequently temperature predictions. For plasmas in pulsed-power machines or high-Z impurity ions (W, Kr, Mo etc.) in magnetic confined fusion devices, radiative loss rates are needed for a wide range of temperatures and densities as one of the key physical input parameters of hydrodynamic simulations. A SH model provides a quick and reasonable estimate for radiative loss rates when a model of detailed atomic structures is difficult to build. Kr radiative loss rates over a temperature range of 1–5 keV and electron density from 10<sup>16</sup> to 10<sup>24</sup> cm<sup>-3</sup> are compared for a CR model with SH levels (FLYCHK) and a CR model with fine structure levels (HULLAC) and configuration average levels (DHS) [7]. <Z> stays similar for electron densities from 10<sup>16</sup> to 10<sup>18</sup> cm<sup>-3</sup>, which is a characteristic of coronal equilibrium. As N<sub>e</sub> increases, <Z> increases by stepwise ionization via excited states acting as ionization channel at intermediate densities and decreases with Ne as those excited states act as 3-body recombination channel at higher densities. Radiative loss rates are linearly proportional to Ne at coronal equilibrium, which is demonstrated in the right plot over  $N_e$  of  $10^{16}$ – $10^{18}$  cm<sup>-3</sup> in the left plot of the Fig. 3.13.

As a SH model does not include  $\Delta n=0$  transitions, the errors are great when radiative loss is dominated by radiation from levels excited by  $\Delta n=0$  from the ground state. In general, a SH model underestimates radiative loss rates for near coronal and/or near neutral plasmas. On the other hand, when  $\Delta n>0$  transition dominates the radiative loss, the errors are within 30 % for L-shell radiative loss rates of Kr ions. Shown in the right plot of the Fig. 3.13 is the comparison of the number of radiative transitions included in the CR model with detailed levels (HULLAC+DHS) and that of a SH model (FLYCHK).

### 3.4 Validities and Limitations

Comparisons between CR models using a variety of assumptions and different levels of details for atomic structures have been performed at a series of the non-local thermodynamic equilibrium (NLTE) code comparison workshops since 1996 [19–24]. If constructed correctly, SH models have been found to give reasonable estimates of charge state distributions compared with CR models with detailed atomic levels, at maximum within one or two charge states for plasmas with K, L-shell ions, and within a bit more uncertainties for M-shell ions. However, because SH levels use averaged states, calculated line positions are very different from measured lines. Therefore, one should take caution in applying a SH model for spectroscopic analysis. In this section, validity and limitations of SH models are discussed.

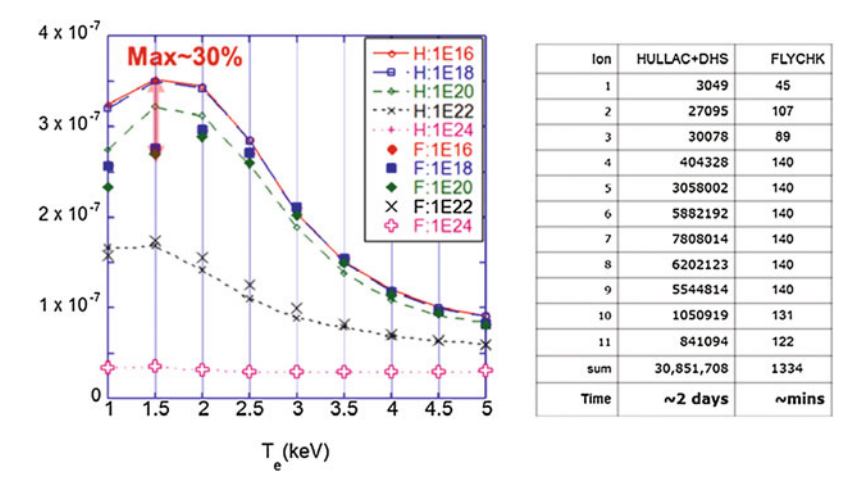


**Fig. 3.13** Radiative loss rates of Kr ions at electron densities from  $10^{16}$  to  $10^{24}$  cm<sup>-3</sup> and electron temperatures from 1 to 5 keV compared between a SH model (F) and a detailed model (H). Please note that the number of radiative transitions in the right table contained in a SH model (FLYCHK) and a detailed model (HULLAC+DHS)

# 3.4.1 Completeness

At the local thermodynamic equilibrium (LTE) limit, population distribution is given by Boltzmann statistics and Saha equations and the completeness of a model is a key ingredient for dense plasmas. Some high-lying levels can be significantly populated if the statistical weight is large. Therefore, an extensive set of levels should be included in a model, only bounded by continuum lowering model. For thermal plasmas, it is

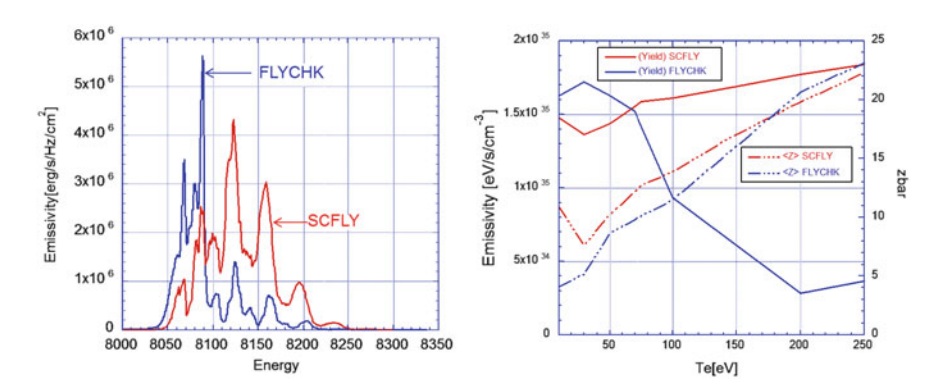


**Fig. 3.14** Cu spectra (*left*) at 300 eV and solid density are compared with (SCFLY) and without (FLYCHK) extensive configurations and Ag emissivity and <Z> (*right*) are compared with and without super configurations (SC)

straightforward to select levels in a model since very high-lying states with high statistical weight are either removed by continuum lowering or rarely populated due to the Boltzmann factor. However, the situation is completely different if those highlying states are substantially populated by non-thermal particles such as relativistic electrons or high energy photons and a model without these levels will provide an erroneous result.

Figure 3.14 shows examples on how results depend on the completeness of models. Cu spectra of two models using SH levels, FLYCHK [1] and SCFLY [48] are compared at thermal electron temperature of 300 eV and solid density with a small fraction of hot electrons to create K-shell holes. FLYCHK uses commonly included levels illustrated in the Fig. 3.4 and SCFLY adds more inner-shell levels that are often neglected in a CR model. For example, FLYCHK includes K<sub>α</sub> spectra of a transition from  $(1)^{1}(2)^{6}$  level to  $(1)^{2}(2)^{5}$  level of N-like ions while SCFLY includes satellite transitions from  $(1)^1(2)^6(3)^i(4)^j$  level to  $(1)^2(2)^5(3)^i(4)^j$  level where the  $(3)^i(4)^j$  electrons are spectators. Therefore the resulting  $K_{\alpha}$  spectra of a transition from  $(1)^{1}(2)^{6}$ level to  $(1)^2(2)^5$  is augmented, broadened and shifted by the contributions of the satellite lines as shown in the left plot of the Fig. 3.14. Without hot electrons,  $(1)^{I}(2)^{6}(3)^{i}$ levels are not populated and there is no difference between FLYCHK and SCFLY results. This example illustrates that a SH model should include a wide range of configurations that may be substantially populated with non-thermal interactions. It is noted that the size of a CR model will be prohibitively large if detailed atomic levels are used for the high-lying levels. Similarly, the  $K_{\alpha}$  emissivity of solid density Ag plasma due to the existence of 1 MeV electrons is constant over a wide range of electron temperatures ( $T_e = 10-250 \text{ eV}$ ) for SCFLY while FLYCHK results gives decreasing emissivity with T<sub>e</sub>, which is not correct. More discussion on the completeness of a CR model is discussed in the chapter on the model completeness.

# 3.4.2 Improvement on SH Model Spectra

A SH model often adopts hybrid structure by complementing SH levels with detailed levels in order to resolve  $\Delta n = 0$  transitions and there are various schemes for this [1, 2, 26]. A truly hybrid CR model is based on detailed atomic structures for bound levels while including SH levels for high lying states and autoionization states [26]. A CR model uses SH levels for many electron ions (more than 3 electrons) and detailed atomic levels for K-shell (H and He) and Li-like ions [1, 2]. In order to improve spectroscopic predictions, a model to use SH levels for population kinetics calculations and more detailed atomic structures for spectral calculations is commonly used as mentioned in the Sect. 3.2.

A SH model is often used for problems of many electron ions where detailed atomic structure models are not available. Charge state distributions of many electron ions are in many cases reasonable compared with more detailed atomic structure models if the SH model is built with necessary configurations. Spectra, on the other hand, needs much care even though detailed atomic structures are adopted for spectral

predictions. The best way is to build a mini CR model using fine-structure levels, for example, within one charge state or, in a lesser accuracy, to use fine-structure levels assuming statistical equilibrium. For most cases, the mini model of fine structure levels may not be of small size as many electron ions are involved. The simpler choice is a configuration average model, which resolves  $\Delta n=0$  transitions. This approximation works reasonably well for intermediate and high density cases by assuming that fine-structure states are in statistical equilibrium. In some cases for high Z elements, spectral lines are heavily influenced by configuration interaction (CI) effects and devise a way to find a global shift of line positions.

### 3.4.3 Dielectronic Recombination

Dielectronic recombination (DR) and excitation autoionization (EA) processes play a critical role in determining charge state distribution at low to intermediate electron densities [7, 23, 24]. Most SH models include these processes by explicitly including autoionizing states involved in DR and EA process. DR rate coefficients of Mo ions are compared between a SH model and a model using fine-structure atomic structures [49] in Fig. 3.15. If DR channels in the model are placed with level energies comparable to true DR resonance energies, the agreement of DR rate coefficients of a SH model is good within a factor of 2 in high temperature ranges where  $\Delta n = 1$ DR processes are dominant. However, at low temperatures where  $\Delta n = 0$  transitions is dominant, the detailed DR rate coefficients increases as T<sub>e</sub> decreases in the fine structure model and DR rate coefficients of the SH model goe to zero due to lack of  $\Delta n = 0$  contribution. The charge state distribution of Mo ions show that the Mo<sup>24+</sup> to Mo<sup>33+</sup> ions are not significantly populated in this range of temperatures and the reduced DR rate coefficients due to lack of  $\Delta n = 0$  DR channels may not be so problematic for steady-state cases. For time-dependent cases or in the case of transport from high temperature to low temperature regions, however, the uncertainties associated with the low DR rates will be non-negligible.

### 3.4.4 Radiative Power Losses

As illustrated in the Sect. 3.3.5, radiative power losses are useful outputs from a SH model. The agreement is reasonably good if the dominant contributions come from  $\Delta n > 0$  transitions. At low density and/or low temperature cases, most population is concentrated in the ground state and the most populated excited states may be metastable states. In this case, a SH model which inherently lacks of a forbidden transition or  $\Delta n = 0$  transition, will completely ignore the radiative contribution from these transitions. It is one of the reasons why uncertainties of a SH model are greatest for plasmas of neutral or near-neutral ions. Even worse, a SH model does not have the correct ground configuration for neutral or near-neutral ions with

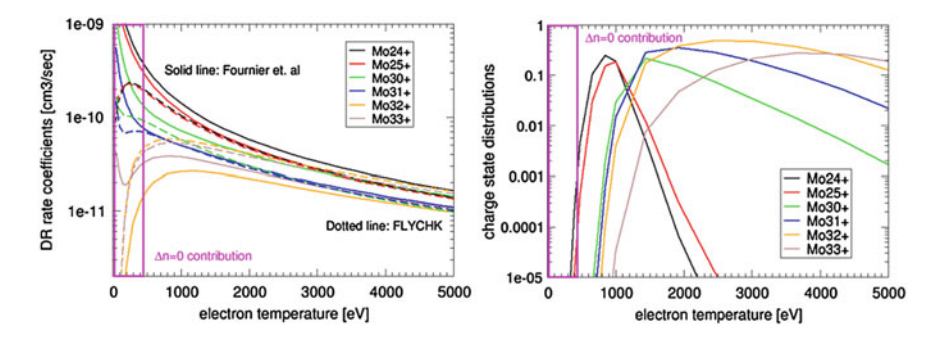


Fig. 3.15 DR rate coefficients (left) and Charge state distribution (right) of Mo ions are calculated as a function of electron temperature at coronal density

atomic number greater than 19. For example, the ground state of neutral K element is [Ar]4s in fine-structure model but the ground level of a SH model is  $(1)^2(2)^8(3)^9$  and 4s level is included in the excited configuration of  $(1)^2(2)^8(3)^8(4)$ . Therefore the radiative power losses for low temperatures of these elements involving neutral or first ionized states should not be used.

## 3.4.5 Continuum Lowering

At high densities, population distributions approach to the LTE limit and the continuum lowering model is important in determining the extent of high-lying states contained in the model. There are several approaches to implement this physical phenomenon, for example, imposing a cut-off limit where high-lying states above the continuum lowering limit are excluded in the model or modifying statistical weights of states as a function of plasma conditions as discussed in the Sect. 3.2.3. A cut-off approach by reducing ionization potentials adds to an uncertainty for a SH model. In the model of detailed atomic structures, for example, 3p and 3d states may be pressure-ionized while 3 s may survive the ionization potential depression (IPD). On the other hand, a SH model will remove 3s, 3p and 3d states at once since they are contained in one SH level. As the ionization balance at the LTE limit is determined by the statistical weight and energies, the inclusion of high statistical weights can lead to the shifted ionization balance. In addition, the spectral emission may be altered by satellite lines with spectator electrons at high-lying orbitals as shown in the example of the Sect. 3.4.1 [11, 48].

# 3.4.6 CR Models in High-Energy-Density Radiation-Hydrodynamic Simulations

The challenges of CR modeling (completeness, tractability, and accuracy) are compounded when the CR model is used within a larger computational model, such as the elaborate radiation hydrodynamic codes used to design high-energy-density experiments. When radiation transport and loss play a significant role in the energy balance of modeled plasma, it is critical to treat both the underlying atomic physics and the radiative transport with high accuracy. However, tractability also becomes more urgent, since the atomic model might be called by the hydrodynamic code for every spatial location at every time step of the simulation. The implementation of radiation transport algorithms in simulation codes is described in a separate chapter on radiation transport. These algorithms typically use coarse photon bins to couple emission from one part of the plasma to absorption in another, so spectroscopic accuracy is not as critical as accuracy in gross predictions such as <Z>. For such applications, SH models such as described in [2] offer a reasonable balance of completeness, tractability, and accuracy.

## 3.5 Summary

A collisional-radiative model employing screened-hydrogenic atomic levels which is general enough to be applied to a variety of plasma conditions has been described. The model is developed in such a way that the results converge to extreme cases at the coronal limit and the local thermodynamic equilibrium limit as well as collisional-radiative regime with and without non-thermal particles. Its limitations and validity ranges are extensively discussed with examples.

#### References

- 1. H.-K. Chung et al., High Energy Density Phys. 1, 3 (2005)
- 2. H.A. Scott, S.B. Hansen, High Energy Density Phys. 6, 39 (2010)
- 3. M.B. Schneider et al., Can. J. Phys. **86**, 259–266(8) (2008)
- 4. K.U. Akli et al., Phys. Plasmas 14, 023102 (2007)
- 5. M.E. Foord et al., J. Quant. Spectrosc. Radiat. Transfer 99, 712 (2006)
- 6. H.-K. Chung, R.W. Lee, High Energy Density Phys. 5, 1 (2009)
- 7. H.-K. Chung, K.B. Fournier, R.W. Lee, High Energy Density Phys. 2, 7 (2006)
- 8. B.I. Cho et al., Phys. Rev. Lett. 109, 245003 (2012)
- R.M. More, in Atomic physics in inertial confinement fusion, Applied Atomic Collision Physics, vol. 2 (Academic Press, New York, 1982)
- 10. H. Mayer, Methods of Opacity Calculations, LA-647, Los Alamos National Laboratory (1948)
- 11. A. Bar-Shalom et al., Phys. Rev. A 40, 3183 (1989)
- 12. C. Bauche-Arnoult, J. Bauche, M. Klapisch, Phys. Rev. A 20, 2424 (1979)
- 13. J. Bauche, C. Bauche-Arnoult, M. Klapisch, Adv. At. Mol. Phys. 23, 131 (1988)

- 14. O. Peyrusse, J. Phys. B: At. Mol. Opt. Phys. 32 (1999)
- 15. C. Bauche-Arnoult, J. Bauche, J. Quant. Spectrosc. Radiat. Transfer 71,189 (2001)
- 16. M.A. Mendoza et al., High Energy Density Phys. 7, 169 (2011)
- 17. Y.T. Lee, J. Quant. Spectrosc. Radiat. Transfer **38**, 131 (1987)
- 18. R. Marchand, S. Caille, Y.T. Lee, J. Quant. Spectrosc. Radiat. Transfer 43, 149 (1990)
- 19. R.W. Lee, J.K. Nash, Y. Ralchenko, J. Quant. Spectrosc. Radiat. Transfer 58, 737 (1997)
- 20. C. Bowen et al., J. Quant. Spectrosc. Radiat. Transfer 81, 71 (2003)
- 21. C. Bowen et al., J. Quant. Spectrosc. Radiat. Transfer 99, 102 (2005)
- 22. J.G. Rubiano et al., High Energy Density Phys. 3, 225 (2007)
- 23. C.J. Fontes et al., High Energy Density Phys. 5, 15 (2009)
- 24. H.-K. Chung et al., High Energy Density Phys. 9, 645 (2013)
- 25. S.B. Hansen, J. Bauche, C. Bauche-Arnoult, High Energy Density Phys. 7, 27 (2011)
- 26. S.B. Hansen et al., High Energy Density Phys. 3, 109 (2007)
- 27. J. Oxenius, Kinetic Theory of Particles and Photons (Springer, Berlin, 1986), pp. 21-65
- 28. H. Kramers, Philos Mag. 46, 836 (1923)
- 29. H. Van Regemorter, Ap. J. 136, 906 (1962)
- 30. R. Mewe, Astron. Astrophys. 20, 215 (1972)
- 31. A. Burgess, M.C. Chidichimo, Mon. Not. R. Astr. Soc. 203, 1269 (1983)
- 32. W. Lotz, Z. Phys. **216**, 241 (1968) Z. Phys. **220**, 266 (1969)
- 33. E.C. Shoub, Ap J. Suppl. Ser. 34, 259 (1977)
- 34. I.I. Sobelman, L.A. Vainshtein, E.A. Yukov, *Excitation of Atoms and Broadening of Spectral Lines*, 2nd edn. (Springer, Berlin, 1995), pp. 120–124
- 35. D.R. Inglis, E. Teller, Astrophys. J. **90**, 439 (1939)
- 36. J.C. Stewart, K.D. Pyatt, Astrophys. J. 144, 1203 (1966)
- 37. D. Mihalas, Stellar Atmospheres, 2nd edn., Ch. 4, 9,11 (W.H. Freeman, San Francisco, 1978)
- 38. O. Ciricosta et al., Phys. Rev. Lett. 109, 065002 (2012)
- 39. D. Hoarty et al., Phys. Rev. Lett. 110, 265003 (2013)
- 40. B.J.B. Crowley, High Energy Density Phys. 13, 84 (2014)
- 41. S.K. Son et al., Phys. Rev. X 4, 031004 (2014)
- 42. C.A. Iglesias, High Energy Density Phys. 12, 5 (2014)
- 43. A. Bar-Shalom, M. Klapisch, J. Oreg, J. Quant. Spectrosc. Radiat. Transfer 71, 169 (2001)
- 44. M.F. Gu, Astrophys. J. 590, 1131 (2003)
- 45. M.H. Chen et al., Phys. Rev. A 19, 2253 (1979)
- 46. D.A. Liberman et al., Phys. Rev. A **50**, 171 (1994)
- 47. S.M. Vinko et al., Nature 482, 59-62 (2012)
- 48. H.-K. Chung, M.H. Chen, R.W. Lee, High Energy Density Phys. 3, 57-64 (2007)
- 49. K.B. Fournier et al., Phys. Rev. A 54, 3870 (1996)

# Chapter 4 Collisional-Radiative Modeling for Radiation Hydrodynamics Codes

Howard A. Scott

**Abstract** Collisional-radiative models are used to provide material data to radiation hydrodynamics codes to model non-equilibrium conditions. Coupling the atomic kinetics to hydrodynamics and radiation transport presents multiple challenges, ranging from providing the required information over a wide range of conditions to maintaining energy conservation and numerical stability. We discuss some of the physical and numerical issues that arise and present modifications and extensions to the usual collisional-radiative formalism to address these issues.

### 4.1 Introduction

Collisional-radiative (CR) models provide a detailed description of the behavior of atoms (and molecules) in plasmas over a wide range of conditions. They have proven to be very useful tools for diagnosing plasma properties by analyzing emission spectra, but their utility extends far beyond this task. Inherent in the detailed description of level occupations and transition rates is the information underlying the basic material properties used in radiation hydrodynamics (RH) codes. Evaluating the material radiative properties (absorption and emission coefficients) and equation of state (EOS) with a CR model then extends the applicability of a RH code into regimes where the assumption of local thermodynamic equilibrium (LTE) is not valid, enabling modeling of a wider range of laboratory and astrophysical plasmas.

Applying CR models within a RH code presents multiple challenges. RH simulations of laboratory experiments often include many materials and span wide ranges in density and temperature. The CR model for each individual element included must then cover all charge states that may be accessed during the simulation. Computational efficiency becomes a major concern, so most RH simulations have used highly averaged models. Additionally, CR models must remain valid over the wide range of non-LTE conditions encountered during many simulations, including high-

density conditions where effects such as electron degeneracy and ionization potential depression (IPD) become important. Incorporating these effects into the CR model is straightforward in some aspects, but problematic in others.

Hydrodynamic and radiation transport calculations require not only basic material properties—energy density and pressure for hydrodynamics, absorption/emission coefficients for radiation transport—but also material responses, i.e. derivatives. When LTE applies, the required derivatives are usually those with respect to temperature and density. In the more general non-LTE case, other derivatives, e.g. with respect to photon intensities, may also prove useful. Fortunately, a straightforward extension of the CR solution provides most derivatives with little additional computational effort. The difficulties here lie in adapting algorithms in the RH code to use non-LTE material responses. In particular, radiation transport often depends quite strongly on material response and handling the full non-LTE response significantly complicates solution algorithms.

More subtle challenges arise from considering discretization effects. Maintaining energy conservation in a RH simulation with both EOS and radiative properties provided by CR models demands consistency in the discretized equations, reflecting the fact that the same microphysics is responsible for both types of material properties. Discretization in time and photon frequency affects accuracy and energy conservation in a manner only slightly more complicated than that of a corresponding LTE simulation. Discretization of energy levels in the CR model affects energy conservation in a less obvious manner and can produce inconsistencies in radiative properties or energy balance.

There are definite limitations on RH simulations using CR models. It is not feasible for an in-line CR evaluation to incorporate all the physics required for deriving detailed material properties, especially outside the weakly coupled, low density plasma regime. Nor is it realistic to expect that an in-line CR evaluation can provide the fidelity achieved by dedicated LTE opacity and EOS codes. However, using material and radiative properties from even highly approximate non-LTE models is preferable to using the best LTE information when LTE is a poor approximation. The philosophy espoused here is to use the best affordable CR models in the RH simulation, while taking care to avoid discretization effects as much as possible, to most accurately model the overall evolution of mass and energy. If desired, more detailed CR models can be utilized afterwards in a post-processing mode to check consistency or obtain detailed spectral predictions.

The following section presents the basic formalism and material properties considered in this chapter. Extensions of the basic formalism for calculating derivatives are presented in Sect. 4.3, along with comments about utilizing the derivatives in a RH code. Incorporating two high-density effects, ionization potential depression and electron degeneracy, into a CR model is addressed in Sect. 4.4. Section 4.5 analyzes effects arising from discrete photon frequencies and energy levels, while Sect. 4.6 then discusses issues arising from time discretization and operator splitting in the context of a radiation transport simulation.

# 4.2 Governing Equations

The basic collisional-radiative formalism has been presented in Chap. 3. We repeat it here both to establish the nomenclature used in this chapter and to provide expressions used in later sections and to define basic material properties of interest. We also specify the equations used for radiation transport, for both the "thermal" radiation transport that is prevalent in RH codes and for line radiation transport.

#### (a) Atomic Kinetics

The fundamental description utilized by a CR model consists of distributions of atoms (in any possible charge state), electrons and photons. The electrons can occupy discrete bound states, enumerated with a set of atomic levels, or a continuum of unbound (free) states. Each bound state i is characterized by its population  $y_i$ , statistical weight  $g_i$  and energy  $E_i$ . The distribution of atomic populations  $\mathbf{y}$  amongst the bound states is determined by the rate equation

$$\frac{d\mathbf{y}}{dt} = \mathbf{A}\mathbf{y} \tag{4.1}$$

where the rate matrix **A** includes all transitions between pairs of levels. The time derivative here is a total derivative and contains spatial transport terms. In this chapter we shall treat (4.1) in the Lagrangian context in which spatial transport terms are absent.

While we are primarily concerned with handling a general non-LTE distribution of populations, we first list properties of the LTE distribution for a given electron temperature  $T_e$  and density  $n_e$ . Within a given charge state, the bound states obey a Boltzmann distribution

$$\frac{y_i}{y_j} = \frac{g_i}{g_j} e^{-(E_i - E_j)/kT_e}$$
 (4.2)

while the populations of neighboring charge states are related by the Saha equation

$$\frac{N_{i+1}}{N_i}n_e = 2\left(\frac{2\pi m_e k T_e}{h^2}\right)^{3/2} \frac{Z_{i+1}(T_e)}{Z_i(T_e)} e^{-\Delta E/kT_e}$$
(4.3)

Here,  $N_i$ ,  $N_{i+1}$  are the total populations of charge states i, i+1, separated by ionization potential  $\Delta E$ , and

$$Z_{i} = \sum_{j \notin \{i\}} g_{j} e^{-(E_{j} - E_{j}^{0})/kT_{e}}$$
(4.4)

is the partition function for charge state i (with ground state energy  $E_j^0$ ) with the sum running over all bound states j within charge state i. We will at times use the subscript i to denote either charge state or level index, but the meaning will be clear from the context.

The transition rates themselves depend on the free electron and photon distributions and also determine the local free electron distribution, as dictated by number, charge and energy conservation. In most applications of CR models, the free electrons are assumed to equilibrate quickly and are described with a thermal distribution characterized by temperature  $T_e$ . Similarly, the ions are described with a thermal distribution characterized by temperature  $T_i$ . Non-local evolution of these thermal distributions occurs within the RH code using hydrodynamics and conduction. Non-thermal electron distributions can arise from a variety of physical processes and may also be present in a RH code. Using these non-thermal distributions within a CR model is straightforward and has been discussed in [1]. Evolving these distributions in time may be important for applications with particularly short timescales [2] or low densities [3], and can be done in conjunction with a CR model [3–5]. However, in this chapter we assume the electrons are thermalized and, at low densities, are described by the Maxwellian distribution

$$f_e(\varepsilon) = n_e 4\pi \left(\frac{1}{\pi k T_e}\right)^{3/2} \varepsilon^{1/2} e^{-\varepsilon/k T_e}$$
(4.5)

where  $\varepsilon$  refers to the electron energy and we have assumed nonrelativistic electrons with  $\varepsilon = \frac{1}{2}m\mathbf{v}^2$ . For a plasma which is overall charge neutral, the electron density will satisfy

$$n_e = \sum_i z_i y_i \tag{4.6}$$

where  $z_i$  is the net charge associated with level i.

The collisional rate  $C_{ij}$  for the  $i \rightarrow j$  transition of energy  $E_{ij} = E_j - E_i > 0$  is obtained by integrating over the electron distribution  $f_e$ 

$$C_{ij} = \int_{E_{ii}}^{\infty} \mathbf{v}(\varepsilon) \sigma_c^{ij}(\varepsilon) f_e(\varepsilon) d\varepsilon$$
 (4.7)

where  $\sigma_c^{ij}$  is the collisional cross section as a function of electron energy  $\varepsilon$ . The inverse  $j \to i$  rate can be obtained from the principle of detailed balance, which states that in equilibrium, any reaction is exactly counterbalanced by its inverse reaction (see [6] for a more detailed discussion). For an LTE population distribution and thermal electron distribution, we then have  $y_i C_{ij} = y_j C_{ji}$ .

Radiative transition rates can be obtained in a similar manner. The radiative rate  $R_{ij}$  for the  $i \rightarrow j$  transition is

$$R_{ij} = 4\pi \int_{0}^{\infty} \sigma_{\nu}^{ij} J_{\nu} \frac{d\nu}{h\nu}$$
 (4.8)

where  $\sigma_{\nu}^{ij}$  is the radiative cross section as a function of photon frequency  $\nu$  and  $J_{\nu}$  is the angle-averaged photon intensity as described below. In equilibrium, the inverse rates satisfy  $y_i R_{ij} = y_j R_{ji}$  but have both spontaneous and stimulated  $(\propto J_{\nu})$  components

$$R_{ji} = 4\pi \left(\frac{y_i}{y_j}\right)^{LTE} \int_0^\infty \sigma_{\nu}^{ij} \left(J_{\nu} + \frac{2h\nu^3}{c^2}\right) e^{-h\nu/kT_e} \frac{d\nu}{h\nu}$$
(4.9)

For bound-bound radiative transitions, the absorption cross section is described with the profile function  $\phi_{ij}$ 

$$\sigma_{v}^{ij} = \sigma^{ij}\phi_{ij}(v), \int \phi_{ij}(v) dv = 1$$
(4.10)

and is usually assumed to be non-zero only in a narrow frequency range centered around  $hv_{ij} = E_i - E_i$ . In this approximation, the transition rates are given by

$$R_{ij} = \frac{4\pi}{h\nu_{ij}} \sigma^{ij} \bar{J}_{ij} , R_{ji} = \frac{g_i}{g_j} \frac{4\pi}{h\nu_{ij}} \sigma^{ij} \left( \frac{2h\nu_{ij}^3}{c^2} + \bar{J}_{ij} \right)$$
(4.11)

where

$$\bar{J}_{ij} = \int_{0}^{\infty} J_{\nu} \phi_{ij} \left(\nu\right) d\nu \tag{4.12}$$

The primary output from a CR model is the atomic level population distribution. The population densities, along with the CR model parameters (energy levels and transition rates) then serve as the building blocks for the basic quantities of interest for the RH code—material energy density and pressure, plus absorption and emission coefficients.

#### (b) Material Properties

For a RH code, the primary material properties of interest are the energy density  $E_m$  and pressure  $P_m$ . Here we assume a low density plasma so that we may neglect particle interactions and use an ideal gas EOS for the thermal energy and pressure, augmented by the internal energy density due to the distribution of excited states. In this case,

$$E_{m} = \frac{3}{2}n_{e}kT_{e} + \frac{3}{2}n_{i}kT_{i} + E_{\text{int}}, E_{\text{int}} = \sum_{i} E_{i}y_{i}$$

$$P_{m} = n_{e}kT_{e} + n_{i}kT_{i}$$
(4.13)

Modifications to these expressions at high density will be considered in Sect. 4.4.

The absorption  $(\alpha_{\nu})$  and emission  $(\eta_{\nu})$  coefficients are constructed by summing over all radiative transitions

$$\alpha_{\nu} = \sum_{i < j} \sigma_{\nu}^{ij} \left( y_i - \frac{g_i}{g_j} y_j \right), \ \eta_{\nu} = \frac{2hv^3}{c^2} \sum_{i < j} \sigma_{\nu}^{ij} \frac{g_i}{g_j} y_j \tag{4.14}$$

where  $\sigma_{\nu}^{ij}$  is the cross section at frequency  $\nu$  for the  $i \to j$  radiative transition and we have neglected the contribution of scattering to the emission coefficient.

If the bound states have an LTE distribution, then the absorption and emission coefficients are related by Kirchoff's law

$$\frac{\eta_{\nu}}{\alpha_{\nu}} = \frac{2h\nu^3}{c^2} \frac{1}{e^{h\nu/kT_e} - 1} = B_{\nu}$$
 (4.15)

where  $B_{\nu}$  is the Planck function.

### (c) Radiation Transport

In contrast to ions and electrons, photons do not equilibrate quickly and can have very long mean free paths. Radiation transport methods are used to evolve the photon distribution in space and time, most commonly as an equation for the specific intensity  $I_{\nu}$ ,

$$\frac{1}{c}\frac{\partial I_{v}}{\partial t} + \vec{\Omega} \bullet \nabla I_{v} = -\alpha_{v}I_{v} + \eta_{v} = -\alpha_{v}\left(I_{v} - S_{v}\right) \tag{4.16}$$

where the second equality introduces the source function

$$S_{\nu} = \frac{\eta_{\nu}}{\alpha_{\nu}} \tag{4.17}$$

The specific intensity is related to the photon phase space distribution function  $f_{\gamma}$  by

$$I_{\nu} = \frac{2h\nu^{3}}{c^{2}} f_{\gamma}(\vec{r}, \nu, \vec{\Omega}, t)$$
 (4.18)

Because of the strong coupling between the radiation and matter, the radiation transport equation is solved together with an equation describing the relevant aspect of material evolution. In RH codes that must account for significant energy transport by radiation, this is usually the material energy equation

$$\frac{dE_m}{dt} = 4\pi \int \alpha_{\nu} \left( J_{\nu} - S_{\nu} \right) + Q \tag{4.19}$$

where  $J_{\nu}$  is the angle-averaged intensity

$$J_{\nu} = \frac{1}{4\pi} \int I_{\nu} d\Omega \tag{4.20}$$

and Q represents any additional energy sources.

In codes that are specialized to low densities, the material evolution is described directly by the CR system. In this case, the radiation in a narrow frequency range, e.g. a single strong line transition, directly couples to the level populations. The prototypical example of this type of system is the two-level atom with a single discrete radiative transition and a collisional transition. The source function for such a system, obtained under the approximation that the width of the spectral line is narrow (and assuming complete redistribution), becomes

$$S_{ij} = \frac{2h\nu_{ij}^3}{c^2} \frac{1}{(g_i y_i/g_j y_i) - 1} = (1 - \theta) \,\bar{J}_{ij} + \theta B_{ij}$$
 (4.21)

where  $B_{ij}$  is the Planck function evaluated at  $v_{ij}$  and  $\theta$  depends on  $C_{ij}$  and the spontaneous component of  $R_{ij}$ . Solution algorithms exploit the fact that  $S_{ij}$  is independent of frequency and is a linear function of  $\bar{J}$ . The complete source function, with contributions from overlapping line and continuum transitions, is more complicated but retains a strong dependence on  $\bar{J}$  at densities low enough that collisions do not dominate the transitions from the upper level.

## 4.3 Non-LTE Material Response

A stand-alone CR calculation calculates transition rates and, from those, population distributions for a given set of physical conditions—primarily the (electron or ion) density and temperature, plus the photon distribution. The calculation may involve a time evolution of the populations, but it does not involve a time evolution of the conditions. When used within a RH code, the mass density (plus elemental concentrations) fixes the total ion densities. Evolving the mass density and temperature is a task for the RH code, or at least for equations and algorithms outside the CR structure. The rate equation is predominantly linear in the populations and most solution methods only require evaluating the rates for the single set of conditions at the beginning of each timestep. The material properties passed to a RH code are then evaluated with updated populations from the end of the (atomic kinetics) timestep. By contrast, solution methods for evolving the non-linear equations of radiation transport and hydrodynamics over a timestep typically require evaluating material properties for multiple sets of conditions or, commonly, for the conditions at the beginning of the (hydrodynamics/radiation transport) timestep along with a set of derivatives to model the response of those properties to changing conditions throughout the timestep. For example, hydrodynamic simulations typically describe the material response with an EOS, including the associated thermodynamic derivatives. Thermal radiation transport algorithms depend on the relationship between E and T, including the specific heat, while efficient line radiation transport algorithms using some form of linearization depend on derivatives with respect to J.

The rate equation is only pseudolinear in the populations when trying to satisfy charge neutrality, as the electron density used to evaluate the rates itself depends on the populations. However, the non-linearity is usually quite mild and can be handled by iterating the CR calculation to converge the electron density. Solution methods for the rate equation that subdivide the timestep also may reevaluate rates with updated electron densities. In neither case do the physical conditions specified by the RH code—mass density, temperature and radiation spectrum—change between evaluations of the CR equations.

Forming derivatives of material properties dependent on the populations requires derivatives of the populations themselves. This is a crucial point, as the populations respond strongly to changes in the physical conditions. Failure to include accurate population derivatives can lead to material property derivatives that are drastically in error, severely affecting the stability and accuracy of the RH algorithms.

Fortunately, those population derivatives can be obtained without a great deal of additional effort. For example, the derivatives with respect to electron temperature can be obtained by integrating

$$\frac{d}{dt}\frac{\partial \mathbf{y}}{\partial T_e} = \frac{\partial \mathbf{A}}{\partial T_e}\mathbf{y} + \mathbf{A}\frac{\partial \mathbf{y}}{\partial T_e}$$
(4.22)

over a single timestep subject to the initial condition

$$\frac{\partial \mathbf{y}}{\partial T_e} = 0 \tag{4.23}$$

Derivatives of the transition rates can be calculated at the same time as the rates themselves at a small additional cost and (4.22) can be integrated in parallel with (4.1). For instance, discretizing (4.1) with the common fully implicit single step backwards Euler method produces

$$\frac{1}{\Delta t} \left( \mathbf{y}^{n+1} - \mathbf{y}^n \right) = \mathbf{A} \mathbf{y}^{n+1} \Rightarrow \mathbf{y}^{n+1} = (\mathbf{I} - \Delta t \mathbf{A})^{-1} \mathbf{y}^n$$
 (4.24)

while the equation for the temperature derivative becomes

$$\frac{1}{\Delta t} \left( \frac{\partial \mathbf{y}^{n+1}}{\partial T_e} - \frac{\partial \mathbf{y}^n}{\partial T_e} \right) = \frac{\partial \mathbf{A}}{\partial T_e} \mathbf{y}^{n+1} + \mathbf{A} \frac{\partial \mathbf{y}^{n+1}}{\partial T_e} \Rightarrow \frac{\partial \mathbf{y}^{n+1}}{\partial T_e} = (\mathbf{I} - \Delta t \mathbf{A})^{-1} \Delta t \frac{\partial \mathbf{A}}{\partial T_e} \mathbf{y}^{n+1}$$
(4.25)

Not all rates contribute to the right hand side of (4.25). For instance, radiative excitation, de-excitation and ionization rates are not explicitly dependent on temperature or electron density, while derivatives with respect  $\bar{J}$  to for a single transition result in only four non-zero entries in  $\partial \mathbf{A}/\partial \bar{J}$ .

It remains to relate the derivatives required by the RH code to those obtained from the CR system, which is solved at fixed  $\rho$  and  $J_{\nu}$ . A minor complication is that the

(self-consistent) temperature and electron density are not independent variables. The required derivatives can be obtained from

$$\left(\frac{\partial y_i}{\partial T}\right)_{\rho} = \left(\frac{\partial y_i}{\partial T}\right)_{n_e} + \left(\frac{\partial y_i}{\partial n_e}\right)_{T} \left(\frac{\partial n_e}{\partial T}\right)_{\rho} \tag{4.26}$$

$$\left(\frac{\partial y_i}{\partial \rho}\right)_T = \left(\frac{\partial y_i}{\partial \rho}\right)_{n_e} + \left(\frac{\partial y_i}{\partial n_e}\right)_{\rho} \left(\frac{\partial n_e}{\partial \rho}\right)_T \tag{4.27}$$

To calculate density derivatives, we use the fact that the CR system is linear in  $y_i$ , so  $(\partial y_i/\partial \rho)_{n_0} = y_i/\rho$ , and summing (4.27) over levels using (4.6) gives

$$\rho \left(\frac{\partial n_e}{\partial \rho}\right)_T = n_e \left[1 - \sum_i z_i \left(\frac{\partial y_i}{\partial n_e}\right)_{\rho}\right]^{-1} \tag{4.28}$$

A more problematic complication has to do with the fact that the physical state for the CR model is defined in terms of more variables than was true under the assumption of LTE. The derivatives measuring the response to changes in one variable with all other variables held constant from the CR calculation do not carry the same information as the corresponding derivatives from an LTE calculation. This is not problematic in calculating the derivatives with the CR model, but rather in using them in the RH code.

We illustrate this with the example of the specific heat at constant volume,  $c_V = \partial E_m/\partial T$ , a quantity used in thermal radiation transport and potentially in other contexts in a RH code. Consider the relationship between the material energy density  $E_m$ , the material properties and the radiation field:

$$E_m = \frac{3}{2} (n_e + n_i) kT + E_{\text{int}} (T, J_{\nu}, t)$$
 (4.29)

Here,  $n_e$  ( $n_i$ ) is the number density of the free electrons (ions), which are assumed to have a thermal distribution corresponding to the material temperature T (and we have assumed  $T_e = T_i = T$  for simplicity).  $E_{int}$  is the material internal energy, which depends not only on the temperature and density, but also on the radiation field, denoted by  $J_v$ , and on the time t. Since thermal radiation transport calculations are done at fixed mass density, all derivatives are taken at constant  $\rho$  and we then focus on the temperature and radiation field as the relevant variables.

For material in LTE, the internal energy at constant density depends only on temperature. The changes in material energy density and temperature are then related through the specific heat  $c_V$ :

$$\frac{dE_m}{dt} = c_V^{LTE} \frac{dT}{dt}, \ c_V^{LTE} = \left(\frac{\partial E_m}{\partial T}\right)_{I-R} \tag{4.30}$$

Implicit in this formulation is the assumption that either radiative interactions are completely unimportant or that the radiation also has a thermal distribution, i.e.  $J_{\nu} = B_{\nu}$ , where  $B_{\nu}$  is the Planck distribution. In the more general non-LTE formulation, the change of material energy density is comprised of three different types of terms:

$$\frac{dE_m}{dt} = \left(\frac{\partial E_m}{\partial T}\right)_{J_v} \frac{\partial T}{\partial t} + \sum_{v} \left(\frac{\partial E_m}{\partial J_v}\right)_T \frac{\partial J_v}{\partial t} + \left(\frac{\partial E_m}{\partial t}\right)_{J_v,T} \tag{4.31}$$

The first term on the right hand side of this expression describes the response of the material energy density to a change in temperature, with fixed radiation densities, while the second term describes the material response to a change in radiation at fixed temperature. The coefficient of the first term is the non-LTE specific heat, related to the LTE specific heat by

$$c_V^{LTE} = c_V^{NLTE} + \sum_{\nu} \left( \frac{\partial E_m}{\partial J_{\nu}} \right)_T \frac{\partial B_{\nu}}{\partial T} , c_V^{NLTE} = \left( \frac{\partial E_m}{\partial T} \right)_{J_{\nu}}$$
(4.32)

The last term on the right hand side arises from evolution of the material at fixed temperature and radiation, and acts as a source or sink of energy. We will consider this term further in Sect. 4.6, but will neglect it for the remainder of this discussion.

Non-LTE effects become significant at densities low enough so that collisional transition rates no longer dominate the important radiative rates. A numerical example illustrates the relative importance of the temperature and radiative responses to the specific heat. For this example, we calculate the specific heat of a Kr plasma at three different densities. Figure 4.1a–c show the specific heat as a function of temperature for ion number densities of  $10^{18}$ ,  $10^{20}$  and  $10^{22}$  cm<sup>-3</sup>, respectively. In each figure, the solid line gives the LTE specific heat,  $c_V^{LTE}$ , while the dotted line gives the non-LTE specific heat,  $c_V^{NLTE}$ , evaluated assuming a Planckian radiation field at the given temperature, and the dashed line gives  $c_V^{NLTE}$  evaluated assuming no radiation field.

At the highest of the three densities, LTE is a good approximation and the specific heat varies little with the radiation. As the density decreases, the difference between  $c_V^{LTE}$  and  $c_V^{NLTE}$  increases, and it becomes apparent that the material radiative response dominates the temperature response. Regardless of any other considerations, use of the LTE specific heat at low densities in the presence of non-Planckian radiation fields will not describe the material energetics correctly. Similarly, use of the non-LTE specific heat without accounting for the radiative response will not produce accurate results. Implications of this for radiation transport are discussed in [7].

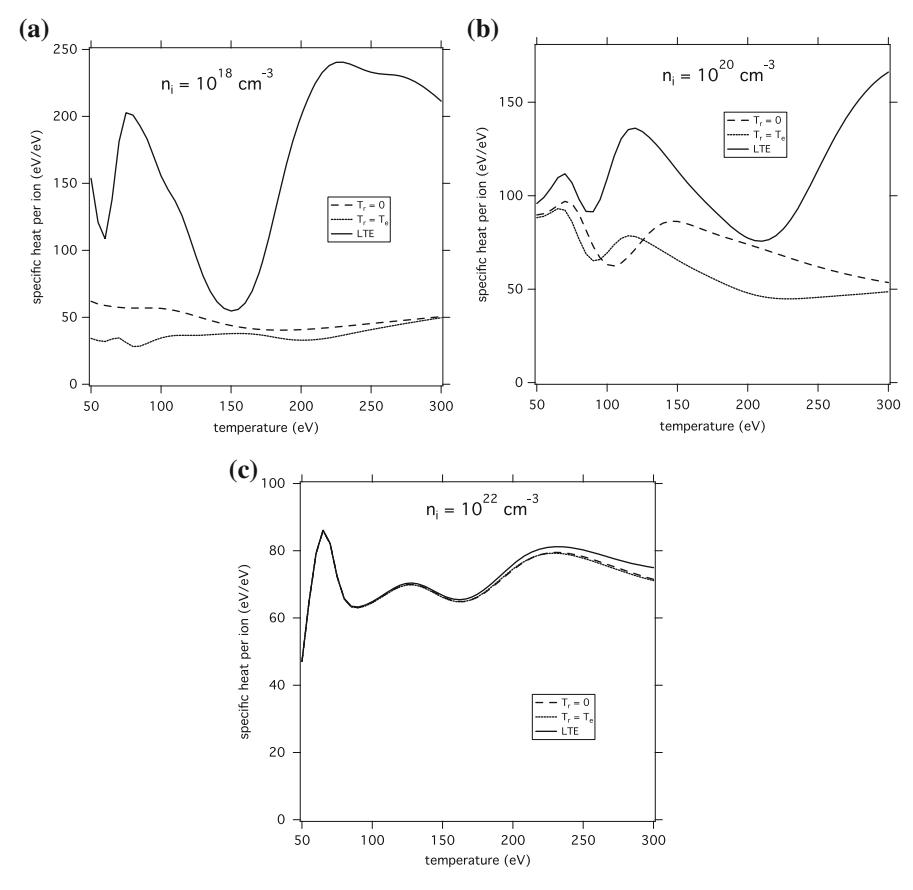


**Fig. 4.1** a Specific heat per ion as a function of temperature for a Kr plasma of number density  $10^{18}$  cm<sup>-3</sup>, in units eV/eV. The *solid line* gives the LTE specific heat, the *dotted line* gives the non-LTE specific heat for a Planckian radiation field with  $T_r = T_e$ , where  $T_e$  is the material temperature and  $T_r$  is the radiation temperature, and the *dashed line* gives the non-LTE specific heat for no radiation field ( $T_r = 0$ ). **b** Same as **a** for a number density of  $10^{20}$  cm<sup>-3</sup>. **c** Same as **a** for a number density of  $10^{22}$  cm<sup>-3</sup>

# 4.4 High Density Effects

### (a) Ionization Potential Depression

The starting point for almost all CR models is the development of an atomic model for each element, providing both the energy level structure for that element and information needed to calculate transition rates (e.g. oscillator strengths). This data is commonly provided for an "isolated atom", i.e. calculated in the absence of boundaries or neighboring ions. However, the plasma environment affects both the structure and the rates, and these changes must then be incorporated in the evaluation

of the CR model rather than in the atomic data. At low densities, the changes are minor and can be incorporated easily. At high densities, the changes are dramatic and impact many aspects of the CR model.

In the "isolated atom" limit of vanishing density, the partition function for a given element (or charge state) becomes infinite, since the atomic levels extend to infinity in principal quantum number with increasing degeneracy but finite energy. The electrostatic potential due to the presence of free electrons and neighboring ions at a finite density effectively lowers the ionization potential and truncates the partition functions. This phenomenon is referred to as "pressure ionization", "continuum lowering" or "ionization potential depression" (IPD). At low densities, this truncation may happen at higher principal quantum number n than those included in the CR atomic data and the effects are (hopefully) negligible. Under conditions obtained in recent experiments [8], the truncation occurs in the neighborhood of  $n \sim 2-3$ . Theoretical modeling of these experimental results is currently an active research area, as extant IPD models are not completely satisfactory for these conditions. For the purpose of this section, we adopt a specific IPD model and discuss its implementation in a CR model.

A widely-used model for IPD, due to Stewart and Pyatt [9], was described in Chap. 3 and we reproduce the relevant formulas here. An ion of net charge z after ionization (with z=1 for a neutral atom) experiences a reduction in ionization potential of magnitude

$$\Delta E_z = \frac{\left[ \left( 1 + a / \lambda_D \right)^{2/3} - 1 \right]}{2 (z^* + 1)}, \ z^* = \frac{\sum_i z_i^2 N_i}{\sum_i z_i N_i}$$
(4.33)

where  $z_i$  is the ion charge,  $\lambda_D$  is the Debye radius and a is the ion sphere radius

$$\lambda_D = \left\lceil \frac{4\pi e^2}{kT} (z^* + 1) n_e \right\rceil^{-1/2}, \ a = \left( \frac{3z}{4\pi n_e} \right)^{1/3}$$
 (4.34)

and, for simplicity, we have assumed  $T = T_e = T_i$ . At low density/high temperature, this expression limits to the Debye-Hückel model, while at high density/low temperature, it limits to the ion sphere model

$$\frac{a}{\lambda_D} \ll 1 : \Delta E_z = \frac{ze^2}{\lambda_D kT} \quad , \quad \frac{a}{\lambda_D} \gg 1 : \Delta E_z = \frac{3}{2} \frac{ze^2}{akT}$$
 (4.35)

A straightforward implementation of this in a CR model simply deletes levels in each charge state z that are bound by less than  $\Delta E_z$ . In practice, several difficulties arise from this simple implementation. The IPD changes the ionization balance by an amount depending on the plasma conditions, so the iterative process of obtaining a self-consistent value for  $n_e$  to maintain charge neutrality becomes more complicated.

Since the existence of a particular bound state depends discontinuously on  $n_e$ , the iterations may oscillate rather than converge. Similar statements apply to constructing derivatives with respect to temperature and electron density, as the energy levels  $E_i$  now also depend on the plasma conditions. The derivatives themselves will also be discontinuous, possibly leading to numerical difficulties in the RH code.

We also note that at high enough densities (or low enough temperatures), some charge states may end up with no bound states remaining, with the most neutral charge states disappearing first. Due to the approximate nature of the model, the remaining charge states may not be contiguous under all conditions. This can also lead to erroneous behavior in the CR model if not guarded against. The disappearance of the most neutral charge states at high density and low temperature crudely mimics the formation of nonlocalized conduction bands in metals, but the CR model lacks the necessary physics to transition to a solid state. See [10] for an attempt to link to some aspects of a solid state model.

Allowing the bound states to gradually disappear can ameliorate the problems associated with discontinuous behavior. Physical justifications for this are the broadening of the level with increased perturbations and fluctuations in the electrostatic potential due to thermal motions of the ions. In practice, the gradual disappearance is achieved by decreasing the degeneracy  $g_i$  of level i so that it smoothly vanishes over an appropriate range of densities. Zimmerman and More [11] introduced a simple version of this in the context of an average-atom model. A more comprehensive approach, the occupation probability formalism [12], derives the reduced degeneracies and partition function truncation from contributions of 2-particle interactions to the Helmholtz free energy, ensuring a thermodynamically consistent EOS in LTE. The application of this formalism to non-LTE simulations is discussed in [13].

The interactions that truncate the partition function also imply the existence of additional terms in the expressions for the plasma energy density and pressure. Coulomb interactions between charged particles, in particular, can make significant contributions to these quantities. The connection between reduced degeneracies/occupation probabilities and contributions to the free energy is discussed in [12], with the result that interactions linear in number density do not contribute to the energy density or pressure. This will be approximately true for most interactions in the low-density limit, and we neglect pressure terms from the reduced degeneracies.

The Coulomb interaction terms can be obtained from the free energy and, in general, provide a negative contribution to the pressure. At low density, using Debye-Hückel theory, the pressure contribution is

$$E_{coul} = -\frac{kT}{8\pi} \frac{1}{\lambda_D^3} = -\frac{1}{2} \frac{e^2}{\lambda_D} (z^* + 1) n_e, \ P_{coul} = \frac{1}{3} E_{coul}$$
 (4.36)

An analytical expression for the free energy term that extends this result to include electron degeneracy is presented in [14]. At high densities, the ion sphere limit for Coulomb interactions is

$$E_{coul} = -\frac{9}{10} \frac{e^2}{a} z^* n_e, \ P_{coul} = \frac{1}{3} E_{coul}$$
 (4.37)

Note that at sufficiently high densities, the total pressure can become negative due to the Coulomb term. However, at these densities non-LTE effects in the EOS are liable to be small and using values from a more consistent LTE EOS is likely to be a better option.

### (b) Electron Degeneracy

For thermal electrons described by temperature  $T_e$ , the Maxwellian distribution considered so far is only valid at densities low enough so the electrons are not degenerate. Higher densities, or lower temperatures, require use of the Fermi-Dirac distribution, in which the mean occupation of a state of energy  $\varepsilon$  is given by

$$F_e(\varepsilon) = \frac{1}{1 + e^{(\varepsilon - \mu)/kT_e}} \tag{4.38}$$

and the electron distribution function is

$$f_e(\varepsilon) = 4\pi \left(\frac{2m_e}{h^2}\right)^{3/2} \varepsilon^{1/2} F_e(\varepsilon) \tag{4.39}$$

Here,  $\mu$  is the chemical potential, related to the electron density  $n_e$  through

$$n_e = \int_0^\infty d\varepsilon f_e(\varepsilon) = \frac{4}{\sqrt{\pi}} \left(\frac{2\pi m_e k T_e}{h^2}\right)^{3/2} I_{1/2}(\mu/kT_e)$$
 (4.40)

where  $I_m$  is the Fermi-Dirac integral of order m and we have assumed non-relativistic electrons with  $\varepsilon = \frac{1}{2}m\mathbf{v}^2$ . In the low-density limit,  $-\mu/kT \gg 1$ , the chemical potential and electron density are related through

$$e^{\mu/kT_e} = \frac{n_e}{2} \left( \frac{h^2}{2\pi m_e kT_e} \right)^{3/2} = \frac{1}{2} n_e \lambda_e^3$$
 (4.41)

where  $\lambda_e$  is the electron thermal wavelength.

Transition rates, radiative properties and material properties must all be modified from the formulas used for low-density plasmas. A discussion of the thermodynamics of a degenerate electron gas is available from most textbooks on statistical mechanics, e.g. [15]. For convenience, we quote expressions for the electron energy density and pressure,

$$E_e = n_e k T_e \frac{I_{3/2}(\mu/kT_e)}{I_{1/2}(\mu/kT_e)}, \ P_e = \frac{2}{3} E_e$$
 (4.42)

A result of particular utility for CR models is the Saha equation for degenerate electrons [14]

 $\frac{N_{i+1}}{N_i}e^{\mu/kT_e} = \frac{Z_{i+1}(T_e)}{Z_i(T_e)}e^{-\Delta E/kT_e}$ (4.43)

Since this form of the Saha equation is valid for arbitrary degeneracy, we can use the detailed balance relationships derived for low-density plasmas simply substituting  $e^{\mu/kT}$  for each occurrence of  $1/2 n_e \lambda_e^3$ .

Including degeneracy, the transition rate for a collisional excitation of energy  $\Delta E$  becomes

$$C_{ij}^{cx} = \int_{\Delta E}^{\infty} \mathbf{v}(\varepsilon) \sigma_c^{ij}(\varepsilon) f_e(\varepsilon) [1 - F_e(\varepsilon - \Delta E)] d\varepsilon$$
 (4.44)

where the integral over the electron distribution now includes a blocking factor  $[1 - F_e]$  for the outgoing electron of energy  $\varepsilon - \Delta E$ . Expressing the cross section in terms of the collision strength  $\Omega \propto \varepsilon \sigma$  (or equivalently, the Gaunt factor), the transition rate is proportional to the integral

$$I^{cx} = \frac{4}{\sqrt{\pi}} \frac{1}{\lambda_e^3} \int_{\Delta E}^{\infty} \Omega(\varepsilon) \frac{1}{1 + e^{(\varepsilon - \mu)/kT_e}} \left[ 1 - \frac{1}{1 + e^{(\varepsilon - \Delta E - \mu)/kT_e}} \right] \frac{d\varepsilon}{kT_e}$$
(4.45)

where we have omitted the constants relating  $\Omega$  and  $\varepsilon\sigma$ . Since the collision strength varies slowly with energy, we first assume that the collision strength is a constant. The integral can then be done analytically, giving

$$I^{cx} = \frac{4}{\sqrt{\pi}} \frac{\Omega}{\lambda_e^3} \frac{e^{-\Delta E/kT_e}}{1 - e^{-\Delta E/kT_e}} \ln \left[ \frac{1 + e^{\mu/kT_e}}{1 + e^{(\mu - \Delta E)/kT_e}} \right]$$
(4.46)

while the same integral in the absence of degeneracy gives

$$I_{nd}^{cx} = \frac{4}{\sqrt{\pi}} \frac{\Omega}{\lambda_e^3} e^{(\mu - \Delta E)/kT_e}$$
 (4.47)

The ratio of these two integrals then provides a "degeneracy factor" which, when multiplied by a non-degenerate transition rate, produces the equivalent transition rate incorporating degeneracy effects

$$\beta^{cx} = \frac{e^{-\mu/kT_e}}{1 - e^{-\Delta E/kT_e}} \ln \left[ \frac{1 + e^{\mu/kT_e}}{1 + e^{(\mu - \Delta E)/kT_e}} \right]$$
(4.48)

The expression in brackets varies slowly with  $\mu/kT_e$ , becoming a constant,  $\Delta E/kT_e$ , in the high-density limit. The transition rate does not increase further with electron density, unlike the non-degenerate case, being restricted by the limiting value of the electron distribution function.

While the collision strength is not strictly constant, small deviations do not affect the degeneracy factor significantly. For collision strengths well approximated by a constant plus a logarithmic term (e.g. Gaunt factors of Mewe [16] or Van Regemorter [17]), the formula underestimates the numerical degeneracy factor by at most a factor of a few while the degeneracy factor itself decreases by ten orders of magnitude. Collision strengths of forbidden transitions tend to vary in leading order as  $\varepsilon^{-1}$  or  $\varepsilon^{-2}$  and for these transitions the formula overestimates the degeneracy factor by a similar factor. If higher accuracy is desired, numerical integrations corresponding to  $\ln(\varepsilon)$  and  $\varepsilon^{-n}$  terms could provide slowly varying corrections to the above degeneracy factor.

A collisional ionization of energy  $\Delta E$  produces two outgoing electrons of energy  $\varepsilon'$  and  $\varepsilon - \varepsilon' - \Delta E$  and the transition rate integral contains blocking factors for both electrons

$$C_{ij}^{ci} = \int_{\Delta E}^{\infty} d\varepsilon v(\varepsilon) f_e(\varepsilon) \int_{0}^{\Delta E} d\varepsilon' \sigma_c^{ij}(\varepsilon, \varepsilon') \left[1 - F_e(\varepsilon')\right] \left[1 - F_e(\varepsilon - \varepsilon' - \Delta E)\right]$$
(4.49)

Assuming that the differential cross section  $\sigma(\varepsilon, \varepsilon')$  is independent of  $\varepsilon'$  and that the collision strength is independent of  $\varepsilon$  leads to a degeneracy factor for collisional ionization rates of

$$\beta^{ci} = e^{-(\mu - \Delta E)/kT_e} \int_{\Delta E}^{\infty} \frac{d\varepsilon}{1 + e^{(\varepsilon - \mu)/kT_e}} \frac{1}{(\varepsilon - \Delta E)} \int_{0}^{\varepsilon - \Delta E} \frac{d\varepsilon'}{kT_e} \left[ 1 - \frac{1}{1 + e^{(\varepsilon - \varepsilon' - \mu)/kT_e}} \right]$$

$$\left[ 1 - \frac{1}{1 + e^{(\varepsilon - \varepsilon' - \Delta E - \mu)/kT_e}} \right]$$
(4.50)

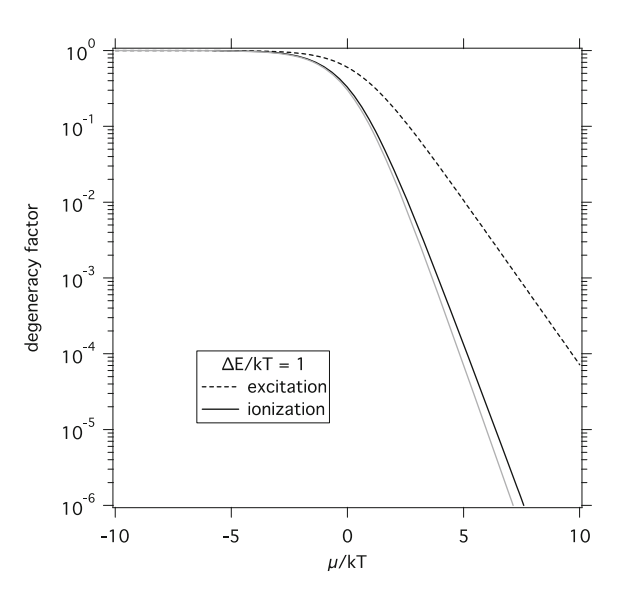
The double integral cannot be done analytically, but the expression

$$\beta^{ci} \approx \zeta \beta^{cx}$$
,  $\zeta = \ln\left(1 + e^{-\mu/kT_e}\right)$  (4.51)

provides a very good approximation over a wide range of parameters. Figure 4.2 presents these degeneracy factors for a transition with  $\Delta E/kT_e=1$ . Choosing a different value of  $\Delta E/kT_e$  shifts the curves slightly in  $\mu/kT_e$ , but does not change their character.

The degeneracy factor for ionization drops more sharply with increasing  $\mu/kT_e$  than the factor for excitation, due to the presence of blocking factors for both outgoing electrons. The main approximation here is the assumption that the differential

Fig. 4.2 Degeneracy factors for a transition with  $\Delta E/kT = 1$ . The dashed line gives the degeneracy factor for excitation  $\beta^{cx}$ . The solid black line gives the degeneracy factor for ionization  $\beta^{ci}$  from (4.51). The solid gray line gives  $\beta^{ci}$  from a numerical evaluation of (4.50)



cross section is independent of the outgoing electron energy. However, numerical integrations using a more realistic differential cross section [18] give results that are virtually indistinguishable from those obtained with a differential cross section independent of  $\varepsilon$ '.

Electron degeneracy also affects other transitions that involve free electrons. Photoionization produces a single outgoing free electron and requires an appropriate blocking factor, decreasing the absorption coefficient for photons close to threshold energy. Autoionization transitions should be treated in a similar manner, although the emitted electrons tend to be of relatively high energy and minimally affected by degeneracy.

More important are transitions between free electron states, i.e. bremsstrahlung and inverse bremsstrahlung, which do not affect the bound state distributions but can be critical in determining the energy balance of a dense radiating plasma. The effects of degeneracy on these absorption and emission processes have been discussed in the literature in varying levels of detail, e.g. [19, 20], but can be understood in terms of the previous discussion. Each such (absorption) transition involves a single incoming electron of energy  $\varepsilon$  and a single outgoing electron of energy  $\varepsilon - h\nu$ , with a cross-section inversely proportional to electron velocity (incorporating various quantum effects into a Gaunt factor). Accordingly, under the assumption of a constant Gaunt factor, the degenerate and non-degenerate treatments differ by the factor  $\beta^{cx}$ , with the substitution of  $h\nu$  for  $\Delta E$ . We note that plasma collective effects can also strongly affect radiative properties [21] and assume that these effects can be treated independently.

# 4.5 Detailed Balance, Energy Conservation and Discretization

The principle of detailed balance is used extensively in CR modeling to relate forward and inverse rates, ensuring that the CR model does indeed produce an equilibrium atomic population distribution when driven by thermal photon and electron distributions. As discussed in Sect. 4.2, Kirchoff's law, relating the radiative emission and absorption coefficients in LTE, is a corollary of this principle and ensures that there is no net energy transfer between radiation and matter when the radiation is also in equilibrium with the matter. However, the numerical realization of Kirchoff's law and, separately, total energy conservation depend on the discretization of the radiation field and the atomic levels.

The numerical issues can be demonstrated by considering a single radiative excitation/de-excitation, as the ratio of emission and absorption coefficients for each transition must also obey Kirchoff's law. Using the expressions for absorption and emission coefficients from Sect. 4.2b and assuming a Boltzmann distribution of excited states results in a source function

$$S_{\nu}^{ij} = \frac{2h\nu^3}{c^2} \frac{\frac{g_i}{g_j} y_j}{y_i - \frac{g_i}{g_j} y_j} = \frac{2h\nu^3}{c^2} \frac{1}{e^{E_{ij}/kT_e} - 1}$$
(4.52)

which is equal to the Planck function only for  $hv = E_{ij}$ . This discrepancy is not due to an assumption of a narrow line profile, but instead comes from treating the energy levels as monoenergetic. Since the cross section is not a delta function, a photon of energy hv can induce a transition of energy  $E_{ij} \neq hv$ . The consequences of this inconsistency become more significant as line profiles become wider, due to either increasing density or the use of statistical treatments such as unresolved transition arrays (UTA). A similar discrepancy will occur for radiative ionization/recombination transitions if the threshold photon energy does not match the transition energy.

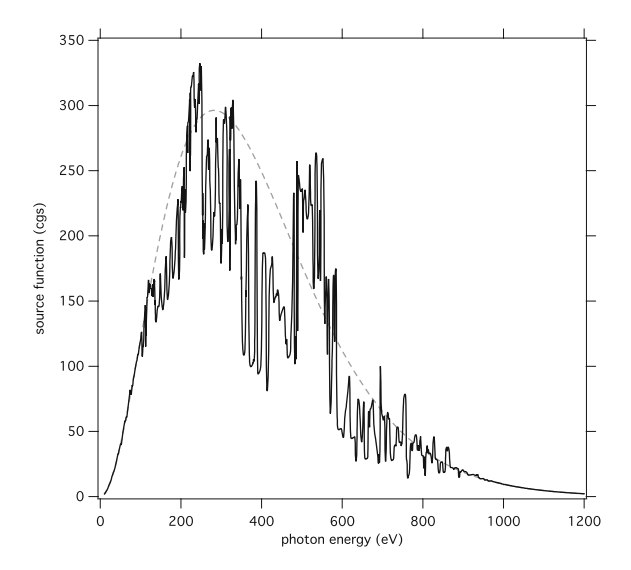
A physically motivated, but expensive, remedy would be to treat each energy level as having a finite width, dividing it into sublevels. This approach would allow (or require) including those (near-) elastic collisions that distribute populations within the energy level (as is done in some treatments of partial redistribution [6]). Fortunately, the correct LTE source function can be obtained by slightly modifying the emission coefficient from that given in (4.14) to account for the mismatch between the photon energy and the transition energy:

$$\eta_{\nu}^{ij} = \left(\frac{e^{E_{ij}/kT_e} - 1}{e^{h\nu/kT_e} - 1}\right) \frac{2h\nu^3}{c^2} \frac{g_i}{g_j} \sigma_{\nu}^{ij} y_j \tag{4.53}$$

The total source function calculated in this manner will match the Planck function when the populations have a thermal distribution.

This can be a critical issue when driving thermal radiation transport with a CR model under near-LTE conditions. Figure 4.3 shows the source functions obtained

Fig. 4.3 Source function for a Kr plasma with  $T_e = 100 \,\text{eV}$  and  $n_i = 10^{18} \,\text{cm}^{-3}$ . The *solid line* was obtained with uncorrected emission coefficients from (4.52), while the *dashed line* used (4.53)



with a screened-hydrogenic atomic model for Kr that uses superconfigurations and UTAs [22]. The CR model was evaluated in LTE for a material temperature of  $100\,\mathrm{eV}$  and an ion number density of  $10^{18}\,\mathrm{cm}^{-3}$ . The solid line was obtained with uncorrected emission coefficients, while the dashed line used (4.53) and is indistinguishable from the Planck function. The non-Planckian source function produces a gross imbalance in the material energy equation, leading to incorrect material temperatures. Figure 4.4 shows the steady-state material temperature obtained by integrating the material energy equation, as a function of radiation temperature for the same number density.

While this expression can be applied directly to emission at a specific frequency, energy equilibrium is a statement about frequency-integrated emission and absorption. To analyze this, we consider the discretized radiation field as used in both the CR model and in the radiation transport. We assume a multigroup description of the radiation field and denote a quantity X that has been averaged over group g as  $X_g$ , e.g. the intensity averaged over the group is given by

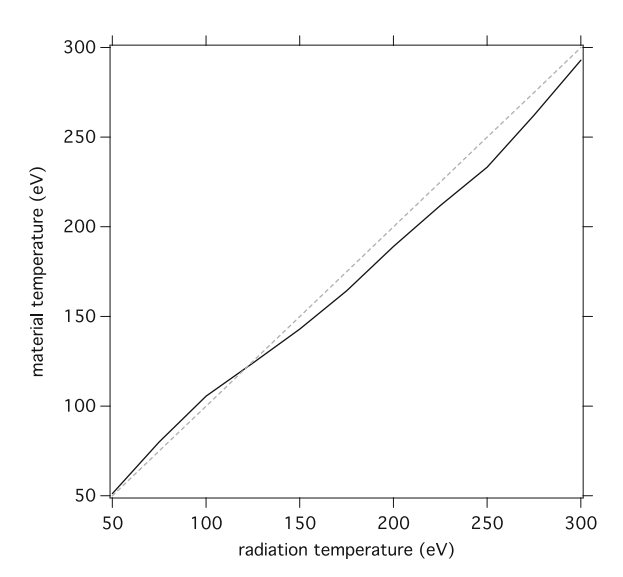
$$J_g = \frac{1}{\nu_g - \nu_{g-1}} \int_{\nu_{g-1}}^{\nu_g} J_{\nu} d\nu \tag{4.54}$$

The discretized material energy equation becomes

$$\frac{dE_m}{dt} = 4\pi \sum_{g} \alpha_g \left( J_g - S_g \right) (\nu_g - \nu_{g-1}) \tag{4.55}$$

100 H.A. Scott

Fig. 4.4 Steady-state material temperature obtained from material energy equation as a function of radiation temperature using uncorrected emission coefficients. The *dashed line* gives  $T_e = T_r$  as a reference



Evaluating this in equilibrium, each summand must be zero, giving the result for the discretized emission coefficient

$$\eta_g^{ij} = \frac{g_i}{g_j} \sigma_g^{ij} B_g y_j \tag{4.56}$$

where  $\sigma_g$  is a suitably averaged discretized cross section. To optimally capture transition peaks and thresholds, we apply (4.53) to the group containing that feature, while line wings and continua use (4.56).

These modifications to the emission coefficients ensure the correct equilibrium behavior, but they are not sufficient to guarantee energy conservation away from equilibrium. The underlying cause is the possible mismatch between the average photon energy  $h\bar{\nu}_g$  and the transition energy. For a single radiative excitation, each transition increases the material energy by  $E_{ij}$  while the radiation energy decreases by  $h\bar{\nu}_g$ . Multiplying both the absorption and emission coefficients by  $E_{ij}/h\nu_g$  restores energy conservation. In most cases, this correction is very small. However, it can become significant if, for efficiency or some other purpose, transition energies do not correspond to the level energies.

One additional degree of freedom in the connection between the CR model and radiation transport is that the definition of  $J_g$  does not uniquely specify the values of  $J_\nu$  within group g to be used for calculating transition rates. This freedom can be used to e.g. drive low-energy transitions with a better representation of a Planckian than would otherwise be possible with a small number of groups. If  $J_\nu$  differs from  $J_g$ , then the aforementioned correction must be modified to maintain energy conservation.

## **4.6** Conservation and Consistency in Non-LTE Thermal Radiation Transport

The material presented in the previous section applies to the CR model and is primarily aimed at achieving equilibrium information for use in thermal radiation transport. We now consider the more general non-equilibrium case, with the emphasis again on the material energy equation. In the following, the mass density is kept fixed and, for simplicity, we refer to a single material temperature T.

The goal for radiation transport is to obtain a self-consistent solution of the radiation transport equation and the material energy equation. Most transport algorithms used in RH codes assume that LTE holds and exploit that assumption to efficiently provide a consistent solution in terms of the material temperature. Consistency, as used here, means that the solution satisfies both equations when evaluated with updated temperatures and intensities. The solution will also conserve energy if the change in material energy density, as obtained by evaluating the EOS at the given temperature, matches the change in energy given by the material energy equation. The system of equations is both nonlocal and nonlinear in temperature, but many effective solution methods are available.

Our concern here is not the solution method, but the treatment of the material energy equation. For simplicity, we adopt a simple time discretization:

$$E_m(T^1) - E_m(T^0) = 4\pi \,\Delta t \int \alpha_{\nu} (J_{\nu}^1 - B_{\nu}(T^1)) d\nu \tag{4.57}$$

where the superscript "0" refers to the beginning of the timestep and the superscript "1" refers to the end of the timestep. The prevalent LTE approach to solving this set of equations uses a temperature expansion in the form

$$c_V^{LTE}(T-T^0) = 4\pi \,\Delta t \int \alpha_{\nu} (J_{\nu} - B_{\nu}(T^*) + \frac{\partial B_{\nu}}{\partial T}(T-T^*)) d\nu \tag{4.58}$$

where the superscript "\*" refers to an intermediate temperature (initially set to  $T^* = T^0$ ). The solution procedure solves for  $J_{\nu}$  and T, updates the source function, and repeats. Successive iterations should approach  $J_{\nu}^1$  and  $T^1$  as the algorithm converges. Using the specific heat to express the change in material temperature introduces an error into the energy balance, as the iterations actually converge to

$$c_V^{LTE}(T^1 - T^0) = 4\pi \,\Delta t \, \int \alpha_{\nu} (J_{\nu}^1 - B_{\nu}(T^1)) d\nu \tag{4.59}$$

instead of (4.57). In most cases, this error is small. In LTE, evaluating the EOS at the beginning of each iteration to update the material energy leads to

102 H.A. Scott

$$c_V^{LTE}(T - T^*) + E_m(T^*) - E_m(T^0) = 4\pi \,\Delta t \int \alpha_{\nu} (J_{\nu} - B_{\nu}(T^*) + \frac{\partial B_{\nu}}{\partial T} (T - T^*)) d\nu$$
(4.60)

which does converge to (4.57).

This formulation explicitly uses the fact that the both the material energy density and source function (which in LTE is the Planck function) are dependent only on the temperature. When LTE does not hold, then both the material energy density and source function (or emission coefficient) also depend on the intensity. An equivalent approach to that described above would use derivatives with respect to intensity as well as temperature, e.g.

$$S_v(T^*, J_v) \approx S_v(T^0, J_v^0) + \frac{\partial S_v}{\partial T}(T^* - T^0) + \sum_{v} \frac{\partial S_v}{\partial J_{v'}}(J_{v'} - J_{v'}^0)$$
 (4.61)

but requires significant changes to the radiation transport. Ignoring the radiation response terms and using an expansion in temperature (with a non-LTE source function), such as

$$c_V^{NLTE}(T^* - T^0) = 4\pi \,\Delta t \int \alpha_{\nu} [J_{\nu} - S_{\nu}(T^*) - \frac{\partial S_{\nu}}{\partial T}(T^* - T^0)] d\nu \tag{4.62}$$

may work but will not conserve energy, as the left hand side of this equation is no longer the change in material energy and the right hand side is no longer the change in radiation energy.

As discussed in Sect. 4.3, even if the conditions are in (or close to) LTE, the non-LTE specific heat can be much smaller than the LTE specific heat, leading to large temperature excursions or even divergence. A similar difficulty arises from expanding the source function (or emission coefficient). If the source function is close to a Planck function, using the temperature derivative without accounting for the material response to radiation may destabilize the solution algorithm. These issues are discussed in [7] and an ansatz designed for use under near-LTE conditions is proposed in [22].

One further difference from the LTE case arises from the fact that the material energy density itself is obtained from a time evolution of the CR system. We must now distinguish three values of the energy density:  $E_m^0$  at the beginning of the CR calculation,  $E_m^1$  at the end of the CR calculation (and the beginning of the radiation transport) and  $E_m^2$  at the end of the radiation transport. Both  $E_m^0$  and  $E_m^1$  are evaluated at the initial temperature  $T^0$ , with the difference between them due to evolution at fixed temperature, density and radiation intensity. The material energy equation becomes

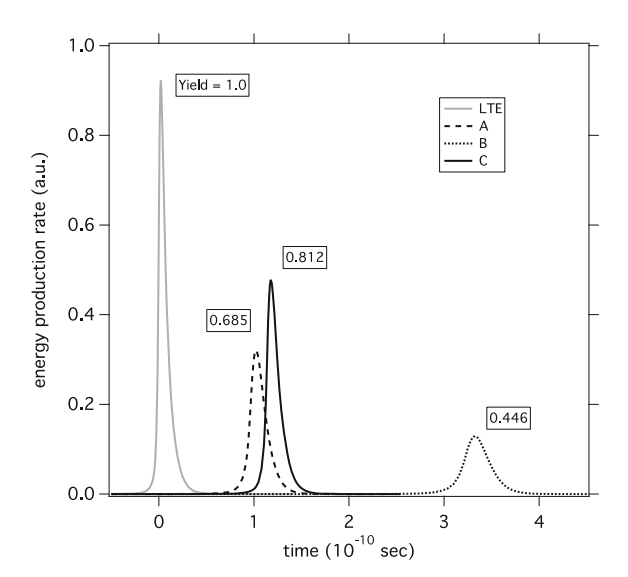
$$E_m^2 - E_m^1 = 4\pi \Delta t \int (\alpha_\nu J_\nu - \eta_\nu) d\nu + (E_m^0 - E_m^1)$$
 (4.63)

where the last term,  $E_m^0 - E_m^1$ , is an energy source (or sink) corresponding to the time derivative  $(\partial E_m/\partial t)_{I}$ .

As in the LTE case, the energy errors can be reduced by repeated evaluations of the CR model to update the material energy and the source function. As the solution converges, the neglected terms decrease in importance. This approach can be computationally expensive, but even a single iteration may improve the solution significantly.

These considerations have proven to be significant in RH simulations of indirectly driven inertial confinement fusion (ICF) capsules on the National Ignition Facility. Achieving energy production from a capsule requires a finely tuned implosion and energy conservation in the simulation is critical. Conditions in the DT-filled plastic capsule near the ablation surface are close to, but not in, LTE. Figure 4.5 presents the energy production rate as a function of time obtained from a simulation using four different treatments of the radiation transport. The production rates have been normalized relative to the total energy produced in the reference case and the time is relative to the peak production rate of the same case. The reference case assumed the material remained in LTE. The simulation for curve A adjusted the temperatures to conserve energy, while the simulation for curve B used the temperatures as obtained from the radiation transport. The simulation for curve C on each timestep evaluated the CR model with updated temperatures and intensities and re-evaluated the radiation transport one time to obtain a more consistent set of temperatures and material energy densities. Two or more iterations of this procedure did not change the results further. All curves are labeled with the total energy produced, relative to the LTE simulation. Differences between each pair of curves are experimentally significant.

**Fig. 4.5** Relative energy production rate as a function of time for a simulated ICF capsule implosion. The gray curve shows the result obtained assuming LTE. Curve A changed temperatures to conserve energy, while curve B used the temperatures as obtained from the radiation transport. Curve C evaluated the CR model with updated temperatures and intensities. All curves are labeled with the total energy produced, relative to the LTE simulation



104 H.A. Scott

## 4.7 Summary

Employing a collisional-radiative model in a radiation hydrodynamics code requires modifications to the usual formalism. Simulations require both material properties and response functions. Providing information for the high densities that may be encountered in a simulation requires including ionization potential depression and electron degeneracy. Maintaining energy conservation puts constraints on the discretized equations. These requirements can be met through straightforward modifications to the CR system, extending the range of a radiation hydrodynamics code to conditions that are far from LTE.

**Acknowledgments** The author gratefully acknowledges many enlightening conversations with George Zimmerman and John Castor. This work performed under the auspices of U.S. Department of Energy by Lawrence Livermore National Laboratory under Contract DE-AC52-07NA27344.

#### References

- 1. H.-K. Chung, M.H. Chen, W.L. Morgan, Y. Ralchenko, R.W. Lee, HEDP 1, 3–12 (2005)
- 2. J. Abdallah Jr, G. Csanak, Y. Fukuda et al., Phys. Rev. A 68, 063201 (2003)
- 3. G. Colonna, L.D. Pietanza, M. Capitelli, Spectrochim. Acta Part B 56, 587–598 (2001)
- 4. M.E. Sherill, J. Abdallah Jr., G. Csanak et al., JQSRT **99**, 584–594 (2006)
- 5. A.G. de la Varga, P. Velarde, F. de Gaufridy et al., HEDP 9, 542–547 (2013)
- 6. J. Oxenius, Kinetic Theory of Particles and Photons (Springer, Berlin, 1986)
- 7. H. Scott, HEDP 1, 31-41 (2005)
- 8. O. Ciricosta, S.M. Vinko, H.-K. Chung et al., Phys. Rev. Lett. 109, 065002 (2012)
- 9. J.C. Stewart, K.D. Pyatt, Astrophys. J. 144, 1203–1211 (1966)
- 10. B. Deschaud, O. Peyrusse, F.B. Rosmej, HEDP **15**, 22–29 (2015)
- 11. G.B. Zimmerman, R.M. More, JQSRT 23, 517–522 (1980)
- 12. D.G. Hummer, D. Mihalas, Astrophys. J. 331, 794–814 (1988)
- 13. I. Hubeny, D.G. Hummer, T. Lanz, Astron. Astrophys. 282, 151–167 (1994)
- 14. H.C. Graboske, D.J. Harwood, F.J. Rogers, Phys. Rev. 186, 210–225 (1969)
- 15. R.K. Pathria, *Statistical Mechanics* (Pergamon Press, Oxford, 1972)
- 16. R. Mewe, Astron. Astrophys. 20, 215-221 (1972)
- 17. H. Van Regemorter, Astrophys. J. 136, 906–915 (1992)
- 18. R.E.H. Clark, J. Abdallah Jr., J.B. Mann, Astrophys J 381, 597–600 (1991)
- 19. H. Totsuji, Phys. Rev. A 32, 3005–3010 (1985)
- 20. S. Eliezer, P.T. Leon, J.M. Martinez-Val, D.V. Fisher, Laser Part. Beams 21, 599–607 (2003)
- 21. G. Bekefi, Radiation Processes in Plasmas (Wiley, New York, 1966)
- 22. H.A. Scott, S.B. Hansen, HEDP 6, 39 (2010)

## Chapter 5 Average Atom Approximation in Non-LTE Level Kinetics

Vladimir G. Novikov

Abstract The non-LTE average atom model is used to obtain nonequilibrium plasma properties. The model assumes that an ion with average occupation numbers together with free electrons is contained in an electrically-neutral spherical cell. In this approximation the level kinetics equations can be written for mean occupation numbers with the rates calculated by using average atom wave functions. This model does not require an atomic database and satisfactorily describes non-stationary ionization (recombination) processes with a given radiation field accounting for density effects. A possible extension of the average atom model is connected with splitting the average ion into a set of ions representing a number of ion states. The possible inverse approach is based on reducing (averaging) the detailed atomic database into the extended average atom model database. It gives the radiative unresolved spectra atomic model, which may be used in-line in radiation hydrodynamics calculations due to a small computing time and acceptable accuracy. The calculation results of different approaches for some practical tasks are presented.

#### 5.1 Introduction

Investigation of hot plasmas produced in laser, beam or discharge devices requires to take into account its nonequilibrium character due to nonstationary ionization (recombination) and/or outgoing (incoming) radiation.

There are a number of approaches to this problem [1]. In addition to the local thermodynamic equilibrium (LTE) approximation one often resorts to the so-called coronal equilibrium (CE), in which the ions are considered in the ground state and all collisional excitations are removed simultaneously due to radiation decay because the plasma is completely transparent. A more general approximation is the collisional radiative steady state (CRSS) model, in which the radiation field is assumed

Vladimir G. Novikov-Deceased.

V.G. Novikov (⋈)

Keldysh Institute of Applied Mathematics, Russian Academy of Sciences, Moscow, Russia

© Springer International Publishing Switzerland 2016 Yu. Ralchenko (ed.), *Modern Methods in Collisional-Radiative Modeling of Plasmas*, Springer Series on Atomic, Optical, and Plasma Physics 90, DOI 10.1007/978-3-319-27514-7\_5 to be known, for example, it may be the Planckian field with the given radiation temperature. Let us mention here also the collisional radiative equilibrium (CRE) model, in which one assumes equilibrium state for some configuration of radiating plasma. The different models and approaches were analyzed in detail at a number of Non-LTE Code Comparison Workshops [2].

All these models require an atomic database with energy levels, oscillator strengths, and other data that may be not available or sufficiently complete. We will consider here the collisional radiative average atom model (CR-AA) that does not need an atomic database and includes, in principle, all possible states and transitions [3].

The average atom model assumes that an ion with average occupation numbers along with free electrons is contained in an electrically-neutral spherical cell. In this approximation the level kinetics equations can be written for mean occupation numbers with the rates calculated using average atom wave functions. This model describes non-stationary ionization (recombination) processes with a given radiation field.

In spite of its simplicity, the CR-AA model requires large-scale computation due to nonlinear system of equations and a large number of iterations to reach a convergent solution. As a matter of fact, it turns out that it is more preferable to build the so-called extended CR-AA model on the basis of CR-AA, where the splitting of the average ion into set of ions representing a number of ion states is fulfilled. The average atom database allows one to get a complete and non-detailed (averaged) description of ion states. The calculations in the extended CR-AA model are simpler than in CR-AA. The shortcoming here is that unlike the CR-AA model the density effects are ignored in this approach.

Extension of this approach results in a method where one reduces the detailed atomic database obtained experimentally or with advanced atomic codes [4–7] into an extended *average* database. It can then produce radiative unresolved spectra atomic model [8] that may be used in-line in radiation hydrodynamics (RHD) calculations due to a small computing time and acceptable accuracy [9].

The calculation results using the above mentioned approaches for tin plasmas show simplicity and reliability of the presented methods.

## 5.2 Level Kinetics Equations

Plasma properties are determined by its ionization stage and electron populations of the ground and excited ion states or, in other words, by the number of ions with ionization degree k found in some state s; we will denote this number by  $n_{ks} = n_{ks}(\mathbf{r}, t)$ . Thus the relative concentration of ions is  $x_{ks} = n_{ks}/n_a$ , where  $n_a = \rho N_A/A$  is the heavy particle density (ions and atoms),  $\rho$  is the matter density, with  $N_A$  being the Avogadro number and A the atomic weight.

In the absence of macroscopic transport processes, the concentrations  $x_{ks}$  must obey the balance conditions [1, 10, 11]:

$$\frac{dx_{ks}}{dt} = \sum_{k's'} (x_{k's'} w_{k's'\to ks} - x_{ks} w_{ks\to k's'}), \qquad (5.1)$$

where  $w_{ks \to k's'}$  is the total probability of transition per second per ion from the state ks to the state k's' due to collisional or radiative processes.

The probabilities of collisional processes are determined by the density of free electrons and their energy distribution. The probabilities of radiation processes essentially depend on the photon distribution function, more precisely, on how much of the radiation remains (is reabsorbed) in the plasma. If a considerable part of radiation is reabsorbed, but the condition of local thermodynamic equilibrium is not fulfilled, then the radiation transfer equation and level kinetics equations must be solved simultaneously and self-consistently.

In the case of a single spectral line (two-level system), starting from these equations one can obtain the well-known Bieberman–Holstein integro-differential equation for the distribution of electron population of an excited state [10, 12, 13], assuming that the excited state is much less populated than the ground state. In the general case solving these equations does not seem to be possible due to a huge number of ion states in the plasma and the necessity of a detailed description of the numerous elementary processes with the complex geometry of plasma formations accounted for.

There exist a number of approximations to (5.1). We start with the simplest one for level kinetics based on the average occupation numbers of one-electron levels  $N_v$ :

$$N_{\nu} = \sum_{ks} x_{ks} N_{\nu}^{ks} \,, \tag{5.2}$$

where  $N_{\nu}^{ks}$  is the number of electrons on the level  $\nu$  in the state ks. Hereafter a one-electron level  $\nu$  is understood as the set of quantum numbers  $n\ell$  (the principal quantum number n and the orbital quantum number  $\ell$ ) that specify the state of the electron in a spherically-symmetrical self-consistent potential.

In the average atom approximation for a nonequilibrium plasma the average occupation numbers  $N_{\nu}$  are determined from the condition of balance of electrons with respect to the energy levels  $\varepsilon_{\nu}$  with statistical weights  $g_{\nu}$  [3, 14–16]:

$$\frac{dN_{\nu}}{dt} = \left(1 - \frac{N_{\nu}}{g_{\nu}}\right) S_{\nu} - N_{\nu} L_{\nu}.\tag{5.3}$$

Here  $S_{\nu}$  is the total rate (more precisely, the flux), measured in 1/s, of the processes leading to an increase of the number of electrons in the state  $\nu$ , and  $L_{\nu}$  is the total rate of the processes leading to a decrease of the number of electrons in that state:

$$S_{\nu} = \sum_{\mu < \nu} N_{\mu} (\alpha_{\mu\nu}^{abs} + \alpha_{\mu\nu}^{ex}) + \sum_{\mu > \nu} N_{\mu} (\alpha_{\mu\nu}^{em} + \alpha_{\mu\nu}^{dex}) + \alpha_{\nu}^{ir} + \alpha_{\nu}^{phr} + \alpha_{\nu}^{dc}, \quad (5.4)$$

$$L_{\nu} = \sum_{\mu < \nu} (1 - \frac{N_{\mu}}{g_{\mu}}) (\alpha_{\nu\mu}^{em} + \alpha_{\nu\mu}^{dex}) + \sum_{\mu > \nu} (1 - \frac{N_{\mu}}{g_{\mu}}) (\alpha_{\nu\mu}^{abs} + \alpha_{\nu\mu}^{ex}) +$$
 (5.5)

$$\alpha_{\nu}^{ii} + \alpha_{\nu}^{phi} + \alpha_{\nu}^{ai}$$
. (5.6)

We use the following notation for the rates of the processes considered (the number of the corresponding transitions occurring during one unit of time per one ion, normalized to one electron on level  $\nu$ ):  $\alpha_{\mu\nu}^{ex}$  and  $\alpha_{\nu\mu}^{dex}$  for excitation and quenching (de-excitation) of the level  $\nu$ ,  $\alpha_{nu}^{ii}$  and  $\alpha_{\nu}^{ir}$  for impact ionization and three-body recombination;  $\alpha_{\mu\nu}^{abs}$ ,  $\alpha_{\nu\mu}^{em}$  for absorption and emission in lines;  $\alpha_{\nu}^{phi}$  and  $\alpha_{\nu}^{phr}$  for photoionization and photorecombination; and  $\alpha_{\nu}^{ai}$  and  $\alpha_{\nu}^{dc}$  for autoionization and dielectronic capture.

#### 5.3 The Rates of Collisional and Radiative Processes

To calculate the rates of elementary processes one usually uses the formulas obtained in the works [11, 13, 17, 18]. In our approach we will base on the work [3], where the oscillator strengths, energy levels and other requisite quantities are calculated on the basis of the Hartree–Fock–Slater self-consistent field model [3, 19]. The rates of the direct and inverse processes are connected by the conditions of the principle of detailed balance; at equilibrium from these conditions should follow the Fermi–Dirac distribution of level occupancies for each of the considered processes. This yields a simply connection between direct and inverse processes.

## 5.3.1 Excitation by Electron Impact

In the first order of the perturbation theory the most universal approach to calculate the cross sections of collisional processes is the distorted wave approximation and its modifications [11, 20]. The wave function of electron in an ion field is calculated by using the Hartree–Fock–Slater model with the mean occupation numbers  $N_{\nu}$  (shell occupancies). Here and below we will assume the ion state to be a configuration average state with average (non-integer) or fixed (integer) occupation numbers.

The cross section of ion excitation from state  $\gamma_0$  to state  $\gamma$  with electron excitation from level  $n\ell$  to level  $n'\ell'$ , normalized to one electron, could be presented as [11, 21] (we will use atomic units unless specified):

$$\sigma_{\gamma_0\gamma}^{ex}(\varepsilon) = \sum_{\kappa} \left[ \sigma_{\kappa}'(n\ell, n'\ell') + \sigma_{\kappa}''(n\ell, n'\ell') \right], \tag{5.7}$$

where  $\sigma'_{\kappa}(n\ell, n'\ell')$  includes direct and indirect parts of electron-ion interaction,  $\sigma''_{\kappa}(n\ell, n'\ell')$  is the exchange interaction term:

$$\sigma_{\kappa}'(n\ell, n'\ell') = \frac{4\pi^3}{(2\ell+1)k^2} \sum_{\lambda, \lambda'} D_{n\ell, n'\ell'; \varepsilon\lambda, \varepsilon'\lambda'}^{\kappa} \left( D_{n\ell, n'\ell'; \varepsilon\lambda, \varepsilon'\lambda'}^{\kappa} - \sum_{\kappa'} E_{\varepsilon\lambda, n'\ell'; n\ell, \varepsilon'\lambda'}^{\kappa'\kappa} \right), \tag{5.8}$$

$$\sigma_{\kappa}''(n\ell, n'\ell') = \frac{4\pi^3}{(2\ell+1)k^2} \sum_{\lambda, \lambda'} \left( \sum_{\kappa'} E_{\varepsilon\lambda, n'\ell'; n\ell, \varepsilon'\lambda'}^{\kappa'\kappa} \right)^2.$$
 (5.9)

Here  $k=(2\varepsilon)^{1/2}$  is the momentum of incident electron;  $\varepsilon$ ,  $\varepsilon'$  and  $\lambda$ ,  $\lambda'$  are the energies and orbital momentum of electron before and after collision,  $D^{\kappa}_{n\ell,n'\ell';\varepsilon\lambda,\varepsilon'\lambda'}$  and  $E^{\kappa'\kappa}_{\varepsilon\lambda,n'\ell';n\ell,\varepsilon'\lambda'}$  are the direct and exchange electron interaction terms, which may be expressed through Slater integrals  $R^{(\kappa)}_{\alpha,\beta;\alpha',\beta'}$  and 3jm-, 6j-Wigner symbols:

$$D_{n\ell,n'\ell';\epsilon\lambda,\epsilon'\lambda'}^{\kappa} = \sqrt{\frac{(2\ell+1)(2\ell'+1)(2\lambda+1)(2\lambda'+1)}{2\kappa+1}} \times \tag{5.10}$$

$$\times \begin{pmatrix} \kappa & \ell & \ell' \\ 0 & 0 & 0 \end{pmatrix} \begin{pmatrix} \kappa & \lambda & \lambda' \\ 0 & 0 & 0 \end{pmatrix} R_{n\ell, n'\ell'; \epsilon\lambda, \epsilon'\lambda'}^{(\kappa)}, \tag{5.11}$$

$$E_{\varepsilon\lambda,n'\ell';n\ell,\varepsilon'\lambda'}^{\kappa'\kappa} = (-1)^{\kappa+\kappa'} \sqrt{(2\kappa+1)(2\ell+1)(2\ell'+1)(2\lambda+1)(2\lambda'+1)} \times (5.12)$$

$$\times \begin{pmatrix} \kappa' & \ell & \lambda' \\ 0 & 0 & 0 \end{pmatrix} \begin{pmatrix} \kappa' & \lambda & \ell' \\ 0 & 0 & 0 \end{pmatrix} \begin{Bmatrix} \kappa' & \ell & \lambda' \\ \kappa & \lambda & \ell' \end{Bmatrix} R_{\varepsilon\lambda, n'\ell'; n\ell, \varepsilon'\lambda'}^{(\kappa')}, \quad (5.13)$$

$$R_{\alpha,\beta;\alpha',\beta'}^{(\kappa)} = \int \int \frac{r_{<}^{\kappa}}{r_{<}^{\kappa+1}} R_{\alpha'}(r') R_{\beta'}(r') R_{\alpha}(r) R_{\beta}(r) dr dr', \qquad (5.14)$$

$$r_{<} = min\{r, r'\}, \quad r_{>} = max\{r, r'\}.$$
 (5.15)

Summing over  $\kappa$  and  $\kappa'$  in the direct and exchange integrals is determined by the difference from zero of corresponding Wigner symbols. The maximal orbital numbers  $\lambda$  and  $\lambda'$  are limited by existing of the region of classical motion of electron with given energy  $\varepsilon$  inside the atomic cell, i.e. until

$$2\varepsilon + 2V(r_0) - \frac{\lambda_{max}(\lambda_{max} + 1/2)}{r_0^2} > 0,$$

where  $r_0$  is the radius of the atomic cell, V(r) is the interatomic potential. It should be noted that at high energies sometimes 40–50 terms on  $\lambda$ ,  $\lambda'$  have to be accounted to get acceptable results, but in this case simpler formulas can be used.

When considering the dipole transitions at comparatively high energy for incident electron one can greatly simplify (5.7) leaving in the sum over  $\kappa$  only the first term with  $\kappa = 1$ . As a result we get the Bethe formula

$$\sigma_{\gamma_0\gamma}^{ex}(\varepsilon) = \frac{4\pi}{k^2 \Delta \varepsilon} f_{\gamma_0\gamma} \ln \frac{q_0}{k - k'}, \tag{5.16}$$

where  $\Delta \varepsilon = \varepsilon_{n'\ell'} - \varepsilon_{n\ell}$  is the energy of transition  $n\ell \to n'\ell'$ ,  $f_{\gamma_0\gamma}$  is the oscillator strength,  $q_0 = \min\{k + k', \sqrt{2|\varepsilon_{n\ell}|}\}$ .

Bethe approximation in many cases gives significant error, but it is used for fitting more accurate calculations or experimental data, such as the widely known Van Regemorter formula [17]

$$\sigma_{\gamma_0\gamma}^{ex}(\varepsilon) = \frac{2\pi^2}{\sqrt{3}} \frac{f_{\gamma_0\gamma}}{\varepsilon \Delta \varepsilon} \chi(\varepsilon/\Delta \varepsilon), \tag{5.17}$$

where  $\varepsilon$  is the energy of incident electron, and  $\chi(\varepsilon/\Delta\varepsilon)$  is the fitting function.

The rate of collisional processes, i.e. the number of excitation events per unit time (1/s) per ion is proportional to the electron density  $n_e$  (cm<sup>-3</sup>) and the average of the cross section  $\sigma_{\gamma_0\gamma}$ , multiplied by the speed of the electron  $v=\sqrt{2\varepsilon}$ , over electron distribution function:

$$\alpha_{\gamma_0\gamma}^{ex} = n_e a_0^3 \nu_0 < \sigma_{\gamma_0\gamma}^{ex} v > = 6.1 \cdot 10^{-6} n_e \int_{\Delta \varepsilon}^{\infty} \sqrt{2\varepsilon} \, \sigma_{\gamma_0\gamma}(\varepsilon) F(\varepsilon) d\varepsilon, \tag{5.18}$$

where  $a_0 = 0.529 \cdot 10^{-8}$  cm and  $v_0 = 4.13 \cdot 10^{16}$  1/s are the Bohr radius and the atomic frequency,  $F(\varepsilon)$  is the electron distribution function at temperature T (we assume it Maxwellian with  $\theta = kT$  in atomic units)

$$F(\varepsilon) = \frac{2}{\sqrt{\pi}} \sqrt{\varepsilon} \; \theta^{-3/2} \; e^{-\varepsilon/\theta}.$$

A simple expression for the excitation rate using the following analytic approximation to Van Regemorter fitting was proposed in [11] (Fig. 5.1):

$$\alpha_{\gamma_0\gamma}^{ex} = 3.07 \cdot 10^{-8} \, n_e \, \frac{f_{\gamma_0\gamma} \, e^{-\Delta\varepsilon/\theta}}{\theta^{1/2} \, \Delta\varepsilon} \, \ln\left(2 + \frac{1}{1.78 \, \Delta\varepsilon/\theta}\right). \tag{5.19}$$

For the inverse process of de-excitation the detailed balance gives:

$$\alpha_{\gamma\gamma_0}^{dex} = \frac{g_{n'\ell'}}{g_{n\ell}} e^{\Delta\varepsilon/\theta} \alpha_{\gamma_0\gamma}^{ex}.$$
 (5.20)

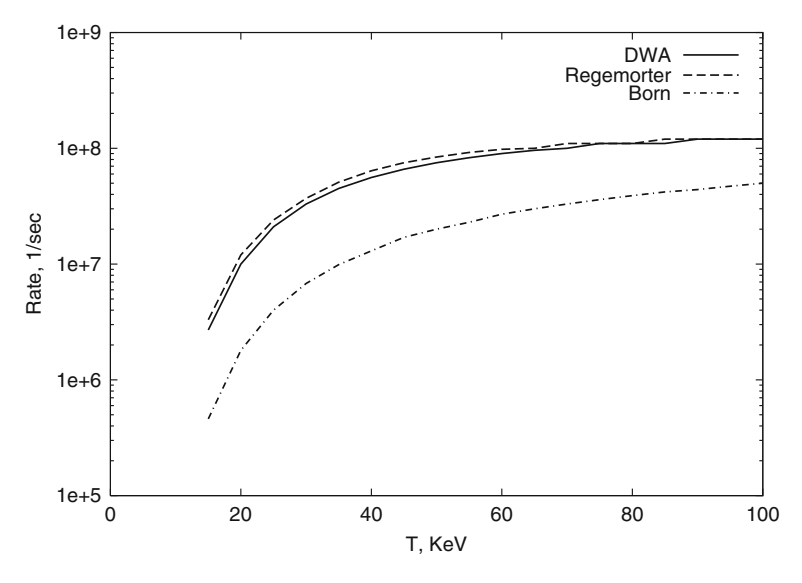


**Fig. 5.1** Excitation rate of 4d–5p transition in Xe XI ion at density  $\rho=10^{-5}$  g/cm³, calculated by using distorted wave method (DWA), Van Regemorter formula (Regemorter) and Born approximation (Born)

## 5.3.2 Electron-Impact Ionization and Three-Body Recombination

The expressions for electron excitation may be easily rewritten for ionization processes. The collisional ionization cross section for electron with quantum numbers  $n\ell$  (it comes to free state  $\varepsilon^*\lambda^*$ ) one can obtain from (5.7), supposing that exciting electron in the state  $\gamma$  is placed in the continuum:

$$\sigma_{\gamma_0\gamma}^{ii}(\varepsilon) = \sum_{\lambda^*} \int_{0}^{(\varepsilon - \varepsilon^i)/2} \frac{d\sigma_{\gamma_0\gamma}^{ii}}{d\varepsilon^*} (1 - n_{\varepsilon^*}) d\varepsilon^*, \tag{5.21}$$

where  $\varepsilon^i$  is the ionization energy from the level  $n\ell$  ( $\varepsilon^i = -\varepsilon_{n\ell}$ ),  $\varepsilon_{n\ell}$  is the electron energy with quantum numbers  $n\ell$ ,  $\varepsilon$  is the incident electron energy and

$$n_{\varepsilon^*} = \frac{1}{1 + \exp\left(\frac{\varepsilon^* - \zeta}{\theta}\right)} \tag{5.22}$$

is the free electron distribution function with the chemical potential  $\zeta$ .

The differential ionization cross section  $d\sigma_{\gamma_0\gamma}$  have to be summed over  $\lambda^*$  and integrated over the energy  $\varepsilon^*$  of the ionized electron, as a result we get

$$d\sigma_{\gamma_0\gamma}^{ii} = \sum_{\kappa} \left[ d\sigma_{\kappa}'(n\ell, \varepsilon^* \lambda^*) + d\sigma_{\kappa}''(n\ell, \varepsilon^* \lambda^*) \right], \tag{5.23}$$

where

$$d\sigma'_{\kappa}(n\ell, \varepsilon^*\lambda^*) = \frac{4\pi^3}{(2\ell+1)k^2} \sum_{\lambda,\lambda'} D^{\kappa}_{n\ell, \varepsilon^*\lambda^*; \varepsilon\lambda, \varepsilon'\lambda'} \times \tag{5.24}$$

$$\times \left( D_{n\ell,\varepsilon^*\lambda^*;\varepsilon\lambda,\varepsilon'\lambda'}^{\kappa} - \sum_{\kappa'} E_{\varepsilon\lambda,\varepsilon^*\lambda^*;n\ell,\varepsilon'\lambda'}^{\kappa'\kappa} \right) d\varepsilon^*, \tag{5.25}$$

$$d\sigma_{\kappa}''(n\ell,\varepsilon^*\lambda^*) = \frac{4\pi^3}{(2\ell+1)k^2} \sum_{\lambda,\lambda'} \left( \sum_{\kappa'} E_{\varepsilon\lambda,\varepsilon^*\lambda^*;n\ell,\varepsilon'\lambda'}^{\kappa'\kappa} \right)^2 d\varepsilon^*.$$
 (5.26)

For the ionization rate similar to (5.18) we have:

$$\alpha_{\gamma_0\gamma}^{ii} = 6.1 \cdot 10^{-6} n_e \int_{\varepsilon^i}^{\infty} \left( \sum_{\lambda^*} \int_{0}^{(\varepsilon - \varepsilon^i)/2} \frac{d\sigma_{\gamma_0\gamma}^{ii}}{d\varepsilon^*} (1 - n_{\varepsilon^*}) d\varepsilon^* \right) \sqrt{2\varepsilon} F(\varepsilon) d\varepsilon. \quad (5.27)$$

The rate of the inverse process of three-body recombination is:

$$\alpha_{\gamma\gamma_0}^{ir} = 1.17 \cdot 10^{-24} g_{n\ell} \frac{n_e}{\theta^{3/2}} e^{\varepsilon^i/\theta} \alpha_{\gamma_0\gamma}^{ii}.$$
 (5.28)

The simplest approximation for the ionization cross section is the classical Thomson formula

$$\sigma_{\gamma_0 \gamma}(\varepsilon) = \pi \, \frac{\varepsilon - \varepsilon^i}{\varepsilon^i \, \varepsilon^2}. \tag{5.29}$$

At high electron energies the Born approximation gives for the cross section

$$\sigma_{\gamma_0\gamma}(arepsilon) \sim rac{\ln(arepsilon/arepsilon^i)}{arepsilon \; arepsilon^i},$$

from which we arrive at the well known Lotz formula for ionization rate [18] (Fig. 5.2):

$$\alpha_{\gamma_0\gamma}^{ii} = 2.0 \cdot 10^{-7} \, n_e \, \frac{1}{\varepsilon^i} \int_{\varepsilon^i/\theta}^{\infty} \frac{e^{-t}}{t} dt = 2.0 \cdot 10^{-7} \, n_e \, \frac{E_1(\varepsilon^i/\theta)}{\varepsilon^i}, \tag{5.30}$$

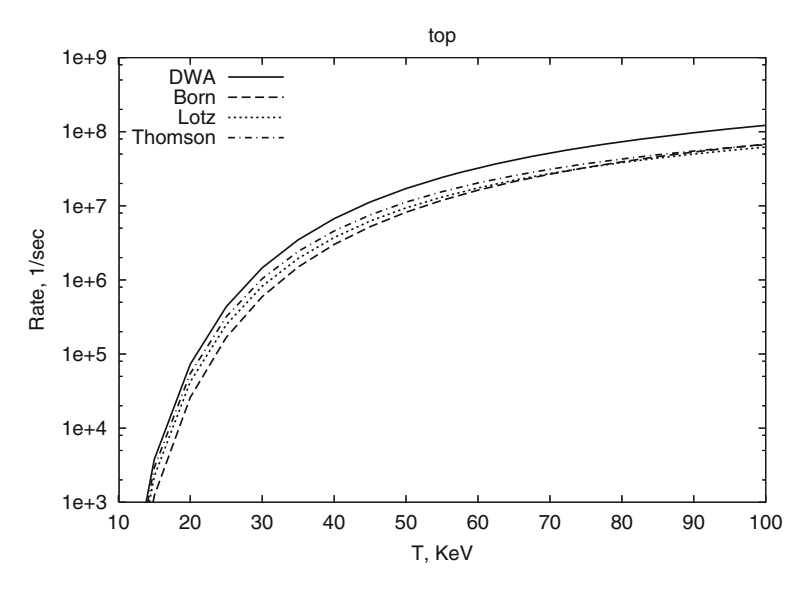


Fig. 5.2 Ionization rate of the level 4d of Sn X versus electron temperature at mass density  $10^{-5}$  g/cm<sup>3</sup>, calculated with distorted wave approximation (DWA), Born, Thomson, and Lotz formula

where

$$E_1(x) = \int_{-\infty}^{\infty} \frac{e^{-t}}{t} dt. \tag{5.31}$$

## 5.3.3 Autoionization and Dielectronic Capture

The autoionization probability can be described by combining de-excitation and ionization processes. Consider a transition  $\gamma_0 \to \gamma$  with ionization of electron from level  $n^*\ell^*$  into continuum with energy  $\varepsilon$  and orbital momentum  $\lambda$  with de-excitation of electron  $n\ell$  to  $n'\ell'$  ( $\varepsilon_{n'\ell'} < \varepsilon_{n\ell}$ ), then from (5.7), (5.21) we get

$$w_{\gamma_0 \gamma}^{ai} = \sum_{\kappa} \left[ w'_{\kappa} (n\ell, n^* \ell^*; n' \ell') + w''_{\kappa} (n\ell, n^* \ell^*; n' \ell') \right],$$

$$(5.32)$$

$$w'_{\kappa} (n\ell, n^* \ell^*; n' \ell') = \frac{2\pi}{(2\ell^* + 1)} \sum_{\lambda} D_{n\ell, n^* \ell^*; n' \ell', \epsilon \lambda}^{\kappa} \left( D_{n\ell, n^* \ell^*; n' \ell', \epsilon \lambda}^{\kappa} - \sum_{l} E_{n\ell, n^* \ell^*; n' \ell', \epsilon \lambda}^{\kappa' \kappa} \right),$$

$$w_{\kappa}''(n\ell, n^*\ell^*; n'\ell') = \frac{2\pi}{(2\ell^* + 1)} \sum_{\lambda} \left( \sum_{\kappa'} E_{n\ell, n^*\ell^*; n'\ell', \varepsilon\lambda}^{\kappa'\kappa} \right)^2.$$
 (5.33)

A simpler approach is based on the dipole approximation [22]:

$$w_{n\ell,n^*\ell^*;n'\ell'}^{ai} = \frac{2\pi}{g_{n^*\ell^*}} \frac{f_{n'\ell',n\ell}}{\omega} \frac{g_{n'\ell'}}{g_{n\ell}} \left( \sum_{\tilde{\ell}} \frac{\ell^* + \tilde{\ell} + 1}{2} \int_{0}^{r_0} \frac{R_{n^*\ell^*}(r) R_{\varepsilon\tilde{\ell}(r)}}{r^2} dr \right)^2, (5.34)$$

where  $\omega = \varepsilon_{n\ell} - \varepsilon_{n'\ell'}$ ,  $\varepsilon = \omega + \varepsilon_{n^*\ell^*} > 0$ .

The quantity inside the parentheses can be calculated in the hydrogen-like approximation using connection between the matrix elements of the acceleration and of the position vector.

To get the autoionization rate (1/s) from level  $n^*\ell^*$  it is required to sum (5.32) over all possible states  $\gamma_0$ ,  $\gamma$ :

$$\alpha_{n^*\ell^*}^{ai} = 4.1 \cdot 10^{16} \sum_{n\ell \ n'\ell'} N_{n\ell} \left( 1 - \frac{N_{n'\ell'}}{g_{n'\ell'}} \right) (1 - n_{\varepsilon}) \ w_{\gamma_0 \gamma}^{ai}. \tag{5.35}$$

The rate of dielectronic capture into the level  $n^*\ell^*$  can be calculated from autoionization rate using detailed balance:

$$\alpha_{n^*\ell^*}^{dc} = 1.17 \cdot 10^{-24} g_{n^*\ell^*} \frac{n_e}{\theta^{3/2}} e^{\varepsilon/\theta} \sum_{n'\ell', n\ell} N_{n'\ell'} \left( 1 - \frac{N_{n\ell}}{g_{n\ell}} \right) w_{\gamma_0 \gamma}^{ai}.$$
 (5.36)

## 5.3.4 Rates of Radiative Processes

It is convenient to express the rates of radiation processes in terms of the corresponding cross sections, which are reduced to one-electron occupancies [13, 19]. For radiation excitation  $\mu \to \nu$ , i.e. absorption in a spectral line with the profile  $\Phi_{\mu\nu}(\omega)$ , we have (Assuming a total redistribution over frequencies)

$$\alpha_{\mu\nu}^{abs} = \nu_0 \int \frac{\sigma_{bb}^{\mu\nu} \Phi_{\mu\nu}(\omega) J_{\omega}}{\omega} d\omega, \tag{5.37}$$

where

$$\sigma_{\rm bb}^{\mu\nu} = 2\pi^2 \alpha f_{\mu\nu},\tag{5.38}$$

 $\alpha$  is the fine structure constant,  $f_{\mu\nu}$  is the one-electron oscillator strength,  $\nu_0 = 4.13 \cdot 10^{16}$  1/s is the atomic frequency, and  $J_{\omega}$  is the integrated over angles radiation intensity  $I_{\omega}$ , i.e.  $J_{\omega} = \int I_{\omega} d\Omega$ . If  $J_{\omega}$  is expressed in TW/(cm<sup>2</sup>·eV), it has to be multiplied by  $C_W = 4.23 \cdot 10^{-3}$  to convert it into atomic units.

For the radiative de-excitation  $\nu \to \mu$  accounting for induced emission and using detailed balance relationship we have [13]:

$$\alpha_{\nu\mu}^{em} = \nu_0 \frac{g_{\nu}}{g_{\mu}} \exp\left(\frac{\varepsilon_{\nu} - \varepsilon_{\mu}}{\theta}\right) \int \frac{\sigma_{bb}^{\mu\nu} \Phi_{\mu\nu}(\omega)}{\omega} \left(\frac{\omega^3}{\pi^2 c^2} + J_{\omega}\right) e^{-\omega/\theta} d\omega, \quad (5.39)$$

where c = 137.036 is the speed of light in atomic units.

If the line width is small in comparison with the characteristic length of radiation field variation, then  $\Phi_{\mu\nu}(\omega) = \delta(\omega - \omega_0)$ ,  $\omega_0 = \varepsilon_{\nu} - \varepsilon_{\mu}$ , and, approximately,

$$\alpha_{\mu\nu}^{abs} = 3.2 \cdot 10^{10} \omega_0^2 f_{\mu\nu} W(\omega_0), \tag{5.40}$$

$$\alpha_{\nu\mu}^{em} = 3.2 \cdot 10^{10} \omega_0^2 \frac{g_{\nu}}{g_{\mu}} f_{\mu\nu} [1 + W(\omega_0)], \tag{5.41}$$

where  $W(\omega)$  is the spectral density of photons:

$$W(\omega) = \frac{\pi^4}{60\sigma} \frac{J_{\omega}}{\omega^3} = 1.58 \cdot 10^7 \frac{J_{\omega}}{\omega^3},$$
 (5.42)

where  $\sigma = 1.028 \cdot 10^{-7}$  TW/(cm<sup>2</sup> eV<sup>4</sup>) is the Stefan-Boltzmann constant.

Similar formulas for photo-ionization and photo-recombination may be written as

$$\alpha_{\mu}^{phi} = \nu_0 \int \frac{\sigma_{\rm bf}^{\mu}(\omega) J_{\omega}}{\omega} d\omega, \tag{5.43}$$

$$\alpha_{\mu}^{phr} = \nu_0 g_{\mu} \exp\left(\frac{\zeta - \varepsilon_{\mu}}{\theta}\right) \int \frac{\sigma_{\rm bf}^{\mu}(\omega)}{\omega} \left(\frac{\omega^3}{\pi^2 c^2} + J_{\omega}\right) e^{-\omega/\theta} d\omega, \tag{5.44}$$

where  $\zeta$  is the chemical potential. We assume that the free electron system is in equilibrium with the given temperature  $\theta = kT$  (in atomic units).

In the Kramers approximation the photo ionization cross section from level  $\mu$  with the effective charge  $Z_{\mu} = Z_{n\ell}$  has a form

$$\sigma_{\rm bf}^{\mu}(\omega) = \frac{64\pi \,\alpha}{3\sqrt{6}} \, \frac{Z_{\mu} \, |\varepsilon_{\mu}|^{3/2}}{g_{\mu}} \, \frac{1}{\omega^3},\tag{5.45}$$

that for the photo ionization rate from level  $n\ell$  gives

$$\alpha_{\mu}^{phi} = u_{\mu} \int_{|\varepsilon_{\mu}|}^{\infty} \frac{W(\omega)}{\omega} d\omega, \tag{5.46}$$

where

$$u_{\mu} = 4.45 \cdot 10^{10} Z_{\mu} \frac{|\varepsilon_{\mu}|^{3/2}}{2(2\ell+1)}.$$

Photo recombination rate in this approximation is written as

$$\alpha^{phr}(\mu) = 0.704 \, g_{\mu} \frac{n_e}{N_A} \frac{u_{\mu}}{\theta^{3/2}} \, e^{|\varepsilon_{\mu}|/\theta} \int_{|\varepsilon_{\mu}|}^{\infty} \frac{e^{-\omega/\theta}}{\omega} \left[1 + W(\omega)\right] d\omega. \tag{5.47}$$

Here it is assumed that at small densities [19]

$$e^{\zeta/ heta}pprox rac{1}{2}\left(rac{2\pi}{ heta}
ight)^{3/2}a_0^3n_e.$$

## 5.4 Configuration Accounting in the Extended CR-AA Model

The extension of the average atom model is connected with splitting the average ion into a set of ion configurations  $Q_{ks} = \{N_{n\ell}^{ks}\}$  with the occupancies  $N_{n\ell}^{ks}$  and the average energy  $E_{ks}$  calculated using Hartree–Fock–Slater model with the given occupation numbers [19].

The simplest way to do this is to prepare a data base for free ions with excitations limited by some energy (it may include many-electron excitations). The number of shells is also limited by  $n = n_{max}$ . In our calculations for k-ion excitations we make use of the limiting energy  $\Delta E_{max} = 2.5 \cdot I_k$  where  $I_k$  is the corresponding ionization potential. The calculations were made with different  $n_{max}$  assuming convergence.

In this model the concentrations  $x_{ks}$  of the  $Q_{ks}$  state of the ion satisfy the system of kinetic level equations:

$$\frac{dx_{ks}}{dt} = -x_{ks} \left( \sum_{s'} R_{ks \to k-1, s'} + \sum_{s'} I_{ks \to k+1, s'} + \sum_{s'} T_{ks \to ks'} \right) + \tag{5.48}$$

$$+\sum_{s'} x_{k+1,s'} R_{k+1,s'\to j,s} + \sum_{s'} x_{k-1,s'} I_{k-1,s'\to j,s} + \sum_{s'} x_{ks'} T_{ks'\to ks}.$$
 (5.49)

The expressions for rates are the same as for the CR-AA model, but the meaning of some values is slightly different. The rate of recombination from the ion state  $Q_{ks}$  to the state  $Q_{k-1,s'}$  is given by:

$$R_{ks \to k-1,s'} = \alpha^{ir}(ks \to k-1,s') + \alpha^{phr}(ks \to k-1,s') + \alpha^{dc}(ks \to k-1,s'),$$
(5.50)

where  $\alpha^{ir}(ks \to k-1, s')$ ,  $\alpha^{phr}(ks \to k-1, s')$  and  $\alpha^{dc}(ks \to k-1, s')$  are the rates of three-body recombination, photorecombination and dielectronic capture, respectively, due to transition of the electron with quantum numbers  $n\ell$  (the change of occupancies takes place such that  $N_{n\ell}^{k-1,s'} = N_{n\ell}^{ks} + 1$ ). Similarly, the rate of ionization from state  $Q_{ks}$  to state  $Q_{k+1,s'}$  is given by

$$I_{ks \to k+1,s'} = \alpha^{ii}(ks \to k+1,s') + \alpha^{phi}(ks \to k+1,s') + \alpha^{ai}(ks \to k+1,s'),$$
(5.51)

where  $\alpha^{ii}(ks \to k+1, s')$ ,  $\alpha^{phi}(ks \to k+1, s')$  and  $\alpha^{ai}(ks \to k+1, s')$  are the rates of impact ionization, photoionization and autoionization, respectively, by the transition of electron with quantum numbers  $n\ell$   $(N_{n\ell}^{k+1,s'} = N_{n\ell}^{ks} - 1)$ .

The rates of transitions from state  $Q_{ks}$  to state  $Q_{ks'}$  without change of ionization stage are defined as follows:

$$T_{ks \to ks'} = \begin{cases} \alpha^{ex}(ks \to ks') + \alpha^{abs}(ks \to ks'), & \text{if} \quad E_{ks} < E_{ks'}, \\ \alpha^{dex}(ks \to ks') + \alpha^{em}(ks \to ks'), & \text{if} \quad E_{ks} > E_{ks'}, \end{cases}$$
(5.52)

where  $E_{ks}$  is the energy of ion state ks,  $\alpha^{ex}(ks \to ks')$  and  $\alpha^{dex}(ks \to ks')$  are the rates of excitation and de-excitation by electron impact, and  $\alpha^{abs}(ks \to ks')$ ,  $\alpha^{em}(ks \to ks')$  are the rates of radiative excitation (absorption) and radiative emission, respectively, with the transition of electron with quantum numbers  $n\ell \to n'\ell'$  (for the occupancies we have  $N_{n\ell}^{k,s} = N_{n\ell}^{ks} - 1$ ,  $N_{n'\ell'}^{k,s} = N_{n'\ell'}^{ks} + 1$ ).

## 5.5 Reducing Detailed Level Kinetics to Extended CR-AA Model

In the case of high-Z elements the number of ion states with detailed level description that should be taken into account can be very large. That is why it is necessary to use some approximations to reduce the system of kinetic equations (see, for example, such approaches in [24, 25]). We consider here another approximation called "radiative unresolved spectra atomic model" presented in [8, 9].

Let for the given substance and some region of temperature and density the photon energy grid be chosen such that it describes the characteristics of emission (absorption) spectra for this substance. We assume that separate strong lines are placed inside some intervals of the grid, and the width of such lines should be much smaller than the step of the grid  $[E_i, E_{i+1}], i = 1, 2, ..., n_E$ . For the simplified description of ionization stage of plasma we join the energy levels of an ion with multiplicity k into groups s with close energy (superstates). The superstate s can include a subset of levels of some configuration, all levels of the configuration, or levels of several configurations.

Let  $x_{ks}$  be the concentration of such superstate and  $g_{ks}$  the corresponding statistical weight  $(k = 1, 2, ..., Z, s = 0, 1, 2, ..., s_{max})$ . The average energy  $E_{ks}$  of the superstate is defined as

$$E_{ks} = \frac{1}{g_{ks}} \sum_{\gamma J \in ks} g_{ks\gamma J} E_{ks\gamma J},$$

where the quantum numbers  $\gamma$  and the angular momentum J define the state of an ion with the energy  $E_{ks\nu J}$ . Obviously,

$$g_{ks} = \sum_{\gamma J \in ks} g_{ks\gamma J}.$$

In a view of the given energy intervals the preliminary data processing of the detailed information on spectral lines  $ks\gamma J \rightarrow k's'\gamma'J'$  is carried out for every ion. For the description of lines between two superstates s and s' of an ion multiplicity k the total oscillator strengths  $gf_i(ks,ks')$  (gf-factor) is distributed over intervals  $i=1,2,\ldots$  of the chosen energy grid such that

$$\overline{gf}_{i}(ks, ks') = \sum_{\gamma J \in ks, \gamma' J' \in ks'} gf(ks\gamma J, ks'\gamma' J'), \tag{5.53}$$

where summation is performed only over transitions with the energy in interval i:

$$\omega(ks\gamma J, ks'\gamma'J') = E_{k's'\gamma'J'} - E_{ks\gamma J} \in (E_i, E_{i+1}).$$

The average energy for this super-transition is then:

$$\overline{\omega}_{i}(ks, ks') = \frac{\sum_{\gamma J \in ks, \gamma' J' \in ks'} \omega(ks\gamma J, ks'\gamma' J') gf(ks\gamma J, ks'\gamma' J')}{gf_{i}(ks, ks')}$$
(5.54)

including transitions with

$$\omega(ks\gamma J, ks'\gamma'J') \in (E_i, E_{i+1}). \tag{5.55}$$

The photoionization thresholds are defined by similar expressions:

$$\overline{\varepsilon}_{i}(k+1,s';k,s) = \frac{\sum\limits_{\gamma J \in ks, \gamma' J' \in k+1,s'} \varepsilon(ks\gamma J,k+1,s'\gamma' J')g_{k+1,s'\gamma' J'}}{\sum\limits_{\gamma J \in ks, \gamma' J' \in k+1,s'} g_{k+1,s'\gamma' J'}}, \quad (5.56)$$

where

$$\varepsilon(ks\gamma J, k+1, s'\gamma'J') = E(k+1, s'\gamma'J') - E(ks\gamma J) \in (E_i, E_{i+1}),$$
 (5.57)

The system of level kinetics equations for the superstate concentrations  $x_{ks}$  is the same as for extended CR-AA (see (5.49)), but now the content of it is different.

For a given photon energy interval  $[E_i, E_{i+1}]$  the rate of radiative excitation (absorption in lines) is defined by:

$$\alpha_{ks,ks'}^{abs} = 3.2 \cdot 10^{10} \sum_{i=1}^{n_E} \frac{\overline{gf}_i(ks,ks')}{g_{ks}} \overline{\omega}_i^2(ks,ks') W\left(\frac{\overline{\omega}_i(ks,ks')}{\theta}\right), \quad (5.58)$$

where  $\overline{\omega}_i(ks, ks')$  is the center of the line group, and  $\overline{gf}_i(ks, ks')$  is the oscillator strength (gf-factor) averaged over the interval  $[E_i, E_{i+1}]$ . The emission rate is then given by:

$$\alpha_{ks',ks}^{em} = 3.2 \cdot 10^{10} \sum_{i=1}^{n_E} \frac{\overline{gf}_i(ks,ks')}{g_{ks'}} \overline{\omega}_i^2(ks,ks') \left[ 1 + W \left( \frac{\overline{\omega}_i(ks,ks')}{\theta} \right) \right]. \quad (5.59)$$

To solve the linear system (5.49), the Gauss-Jordan method is applied with account of the block character of the matrix (see, for example [23]).

Having ion concentrations  $x_{ks}$  one can calculate opacity and emissivity using detailed spectral information [19]:

$$\varkappa'(\omega) = n_a a_0^2 \left\{ \sum_{ks\gamma J} x_{ks} \sum_{ks'\gamma'J'} \frac{g_{ks\gamma J}}{g_{ks}} 2\pi^2 \alpha f(ks\gamma J; ks'\gamma'J') \Phi_{ks\gamma J, ks'\gamma'J'}(\omega) + \right.$$

$$\left. + \sum_{ks} x_{ks} \sigma_{\rm bf}^{ks}(\omega) + \sigma_{\rm ff}(\omega) \right\},$$
 (5.61)

$$j'(\omega) = n_a a_0^2 \left\{ \sum_{ks'\gamma'J'} x_{ks'} \sum_{ks\gamma J} \frac{g_{ks'\gamma'J'}}{g_{ks'}} 2\pi^2 \alpha f(ks\gamma J; ks'\gamma'J') \Phi_{ks\gamma J, ks'\gamma'J'}(\omega) + (5.62) \right. \\ \left. + \sum_{ks} x_{ks} \sigma_{\text{fb}}^{ks}(\omega) + e^{-\omega/\theta} \sigma_{\text{ff}}(\omega) \right\} \left( \frac{\omega^3}{4\pi^3 c^2} + I_\omega \right), (5.63)$$

$$\Phi_{ks\gamma J,ks'\gamma'J'}(\omega) = \frac{1}{\sqrt{\pi}D}K\left(\frac{\omega - \omega_{ks\gamma J,ks'\gamma'J'}}{D}, \frac{\Gamma}{D}\right),\tag{5.64}$$

where  $\omega_{ks\gamma J,ks'\gamma'J'} = |E_{ks\gamma J} - E_{ks'\gamma'J'}|$ ,  $\Gamma = \Gamma_{ks\gamma J,ks'\gamma'J'}$  is the Lorentz line width (including electron and natural broadening), and D is the Doppler parameter.

When solving the radiation transfer equation, the part of emissivity  $j'(\omega)$  contributed by the induced radiation and proportional to  $I_{\omega}$  has to be moved over to absorption coefficient  $\varkappa'(\omega)$ .

## 5.6 The Calculation Algorithm

In a quasi-stationary approximation  $(dN_{\nu}/dt=0)$  we can transform the nonlinear system (5.3) to an expression that is convenient for application of iterative methods. As the rates  $S_{\nu}$  and  $L_{\nu}$  depend not only on all occupancies but also on the level energies  $\varepsilon_{\nu}$  and the oscillator strengths  $f_{\mu\nu}$ , which, in turn, are determined by the state of the average ion, it is convenient to form two iteration cycles. The first one is on the self-consistent potential  $V^{(p)}(r)$ ,  $p=0,1,2\ldots$  with the given occupation numbers  $N_{\nu}$  that satisfy system (5.3) for fixed p. With this potential (and corresponding energy levels  $\varepsilon_{\nu}^{(p)}$  and oscillator strengths  $f_{\mu\nu}^{(p)}$ ), the solution of (5.3) is obtained with the additional iteration procedure according to:

$$N_{\nu}^{(s)} = \frac{N_{\nu}^{(s-1)} + S_{\nu}^{(s-1)} \tau}{1 + \left(L_{\nu}^{(s-1)} + S_{\nu}^{(s-1)}/g_{\nu}\right)/\tau}, \qquad s = 1, 2, 3 \dots$$
 (5.65)

with the iterative step

$$\tau = \frac{0.1}{\max_{\nu} \frac{dN_{\nu}}{dt}}.$$
 (5.66)

To improve convergence, a relaxation procedure is used where  $N_{\nu}^{(s)}$  is replaced by  $\sqrt{N_{\nu}^{(s)} N_{\nu}^{(s-1)}}$  for the next iteration.

After iterations (5.65) had converged, the resulting occupation numbers were used to determine the new potential  $V^{(p+1)}(r)$ , energy levels  $\varepsilon_{\nu}^{(p+1)}$  and oscillator strengths  $f_{\mu\nu}^{(p+1)}$  by solving the Hartree–Fock–Slater system of equations with the given occupation numbers  $N_{\nu}$ . Then the two processes are repeated until the condition

$$\max_{\nu} \left| N_{\nu} \left( \varepsilon_{\nu}^{(p+1)}, f_{\mu\nu}^{(p+1)} \right) - N_{\nu} \left( \varepsilon_{\nu}^{(p)}, f_{\mu\nu}^{(p)} \right) \right| < 10^{-6}$$
 (5.67)

is satisfied.

Using this procedure we obtain average occupation numbers, electron energy levels and electron wave functions that are consistent with the given radiation field  $J_{\omega}$ . These are then used to calculate the absorption coefficients and emissivities of the plasma. The resulting coefficients make it possible to get a more accurate value of the radiation field by solving the radiation transfer equation. The described iteration cycles are then repeated until there is complete consistency between the radiation field  $J_{\omega}(\mathbf{r})$  and the level populations  $N_{\nu}(\mathbf{r})$ .

#### 5.7 Results of Calculation for Tin Plasma

The CR-AA model was applied to calculation of radiative properties of tin plasmas in a wide range of temperatures and densities. The effects of different approaches on the level kinetics calculations are analyzed in Figs. 5.3, 5.4 and 5.5.

In Fig. 5.3 we present the difference between the CR-AA model and the extended CR-AA model for temperature  $T=15.85\,\mathrm{eV}$  (for other temperatures the behavior is similar). As one can see from this figure, there exists a big difference in coronal limits between the CR-AA and the extended CR-AA models that is due to the different ionization potentials in these models. At high densities the discrepancy results from the fact that the atomic database for the extended CR-AA model was calculated for free ions while for the CR-AA calculations the ion state is assumed at non-zero density. Our CR-AA model therefore reproduces pressure ionization with a smooth transition to LTE average atom model at high densities.

The effect of dielectronic recombination at the same temperature of  $T=15.85\,\mathrm{eV}$  is presented in Fig. 5.4. One can see from the picture that the difference between two approaches (with and without dielectronic recombination) decreases from 30% at electron densities smaller than  $10^{16}\,\mathrm{cm}^{-3}$  to zero at densities higher than  $10^{20}\,\mathrm{cm}^{-3}$  when three-body recombination becomes the dominant recombination mechanism.

The effect of optical thickness on the mean ion charge is shown in Fig. 5.5. These calculations were carried out for flat tin layers with thickness L=0 and  $L=100 \,\mu m$ . As one can see from the picture, the mean ion charge inside the  $100 \,\mu m$  layer at

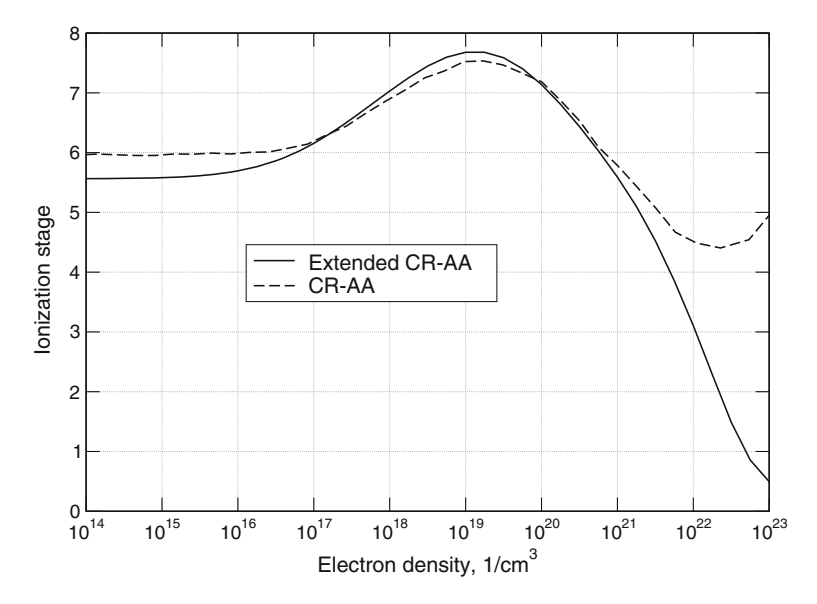


**Fig. 5.3** Comparison of Sn mean ion charge  $\overline{Z}$  in CR-AA and extended CR-AA models at temperature  $T=15.85\,\mathrm{eV}$ 

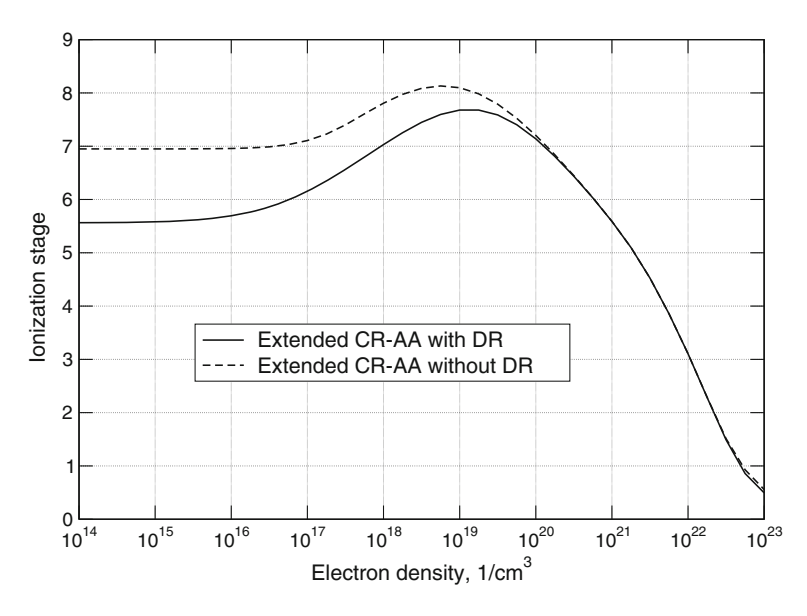


**Fig. 5.4** Effect of dielectronic recombination on the mean ion charge in CR-AA model at electron temperature  $T=15.85\,\mathrm{eV}$ 

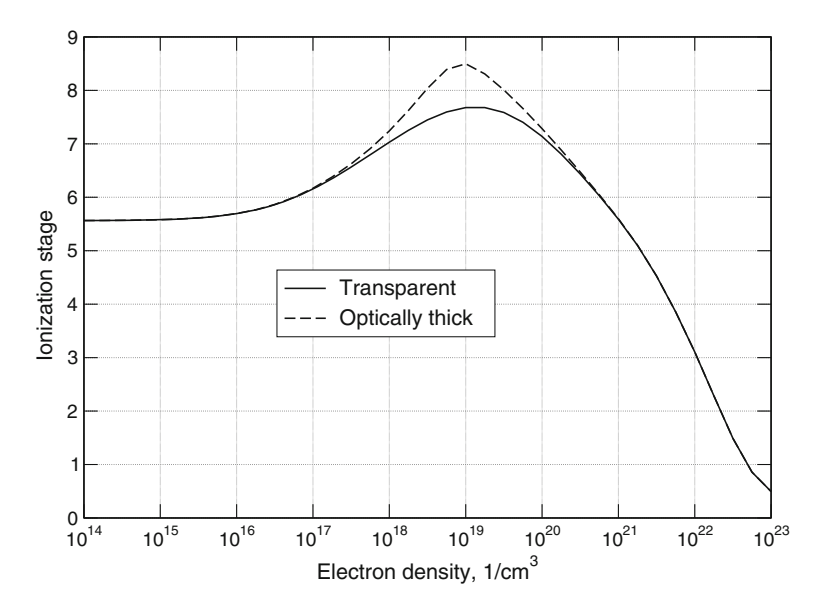


Fig. 5.5 Comparison of the mean ion charge in CR-AA model at temperature  $T=15.85\,\mathrm{eV}$  for optically thin (solid line) and optically thick (dashed line) tin flat layer with thickness  $L=100\,\mu\mathrm{m}$ 

electron density  $10^{19}\,\mathrm{cm^{-3}}$  is  $15\,\%$  larger than for the optically thin layer. As well known, the opacity effects result in the increased populations of excited states which enhances ionization. At higher densities, both optically thin and optically thick plasmas reach the Saha-LTE regime.

The isotherms of the mean ion charge for tin plasmas calculated with the extended CR-AA model in a wide range of temperatures and densities are presented in Figs. 5.6 and 5.7. It should be emphasized that calculations with the CR-AA model are more laborious than with the extended CR-AA model as the latter makes use of the atomic database generated in advance.

In order to provide convenient usage of non-LTE data in hydrodynamics codes (including, in particular, opacities and emissivities), it is beneficial to perform preliminary calculations of the tables for two limiting cases, namely, for transparent and optically thick plasmas [26]. In Figs. 5.6 and 5.7 the dependence of  $\overline{Z}$  for Sn plasma at different temperatures is shown over a wide range of electron densities. Figure 5.6 corresponds to optically thin case, while Fig. 5.7 presents the mean ion charge in the center of a Sn flat layer with the thickness of to  $100\,\mu m$ .

For the electron densities  $n_e \sim 10^{18}-10^{20}\,\mathrm{cm^{-3}}$  (the value depends on temperature)  $\overline{Z}$  changes from coronal equilibrium to LTE. The difference between the optically thin and optically thick cases is maximal when plasma approaches LTE and reaches 30%. The populations of the emitting levels here may be several times larger than for the optically thin plasma. Of course, the increase in emissivity will be offset by opacity. Therefore, the problem must be solved using the radiation transport equation self-consistently with the level kinetics.

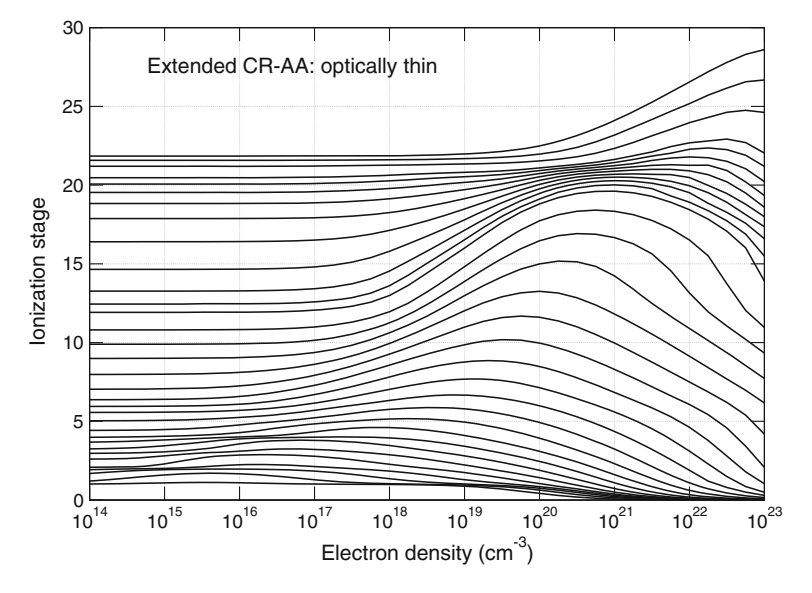


Fig. 5.6 Isotherms of mean ion charge for Sn plasma in extended CR-AA model (optically thin case). The grid step for curves at different temperatures from  $T=1\,\mathrm{eV}$  (bottom line) up to  $T=498\,\mathrm{eV}$  (top line) equals to  $\Delta \lg T=0.1$ )

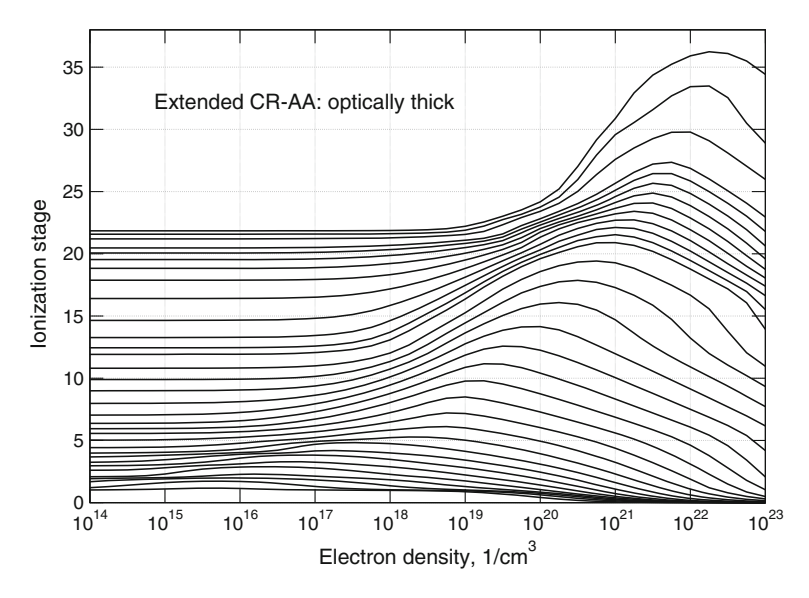


Fig. 5.7 Isotherms of mean ion charge for Sn plasma in extended CR-AA model (optically thick flat layer with thickness  $L=100\,\mu\text{m}$ . The grid step for curves is the same as in Fig. 5.6

The tables for two limiting cases can be used to obtain appropriate coefficients at arbitrary radiation field using a generalized escape factor as the ratio of outgoing radiation to the radiation "produced" inside the layer:

$$\xi = \frac{\int F_{rad} dS}{4\pi \int \int j_{\omega} d\omega dV},$$

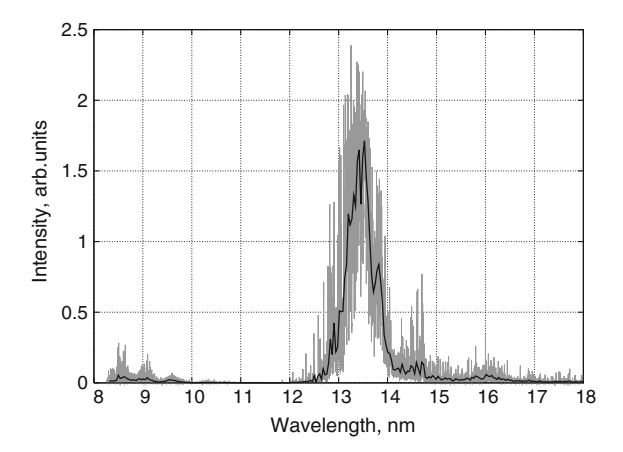
where  $F_{rad}$  is the radiative flux, S is the square of the layer surface, and the emissivity in the denominator is integrated over the volume and photon energy. When solving the radiation transport equation one may use opacity and emissivity coefficients interpolated between transparent and optically thick cases [27–29]:

$$j_{\omega} = \xi j_{\omega}^{0} + (1 - \xi) j_{\omega}^{1}, \tag{5.68}$$

$$k_{\omega} = \xi k_{\omega}^{0} + (1 - \xi)k_{\omega}^{1}. \tag{5.69}$$

Here index "0" corresponds to the transparent case and index "1" to the optically thick case. As this parameter depends on the solution of the radiation transport equation, several iterations (e.g., on the order of 3) are required for  $\xi$  starting from the transparent case to get the parameter which is consistent with the actual radiation field.

Fig. 5.8 Emission spectrum of the tin cylindrical layer with radius  $R = 100 \,\mu\text{m}$  at temperature  $T = 32 \,\text{eV}$  and electron density  $n_e = 10^{19}$  1/cm<sup>3</sup>. Detailed calculation with 20000 photon groups (*gray*) and calculation reduced to extended CR-AA model on 100 groups (*solid line*)



The interpolation method gives reasonable results in a wide range of electron densities. The method is extremely efficient but requires substantial effort to prepare tables for transparent and optically thick cases. The interpolation formulas (5.68) and (5.69) can also be used for other quantities such as  $\overline{Z}$ , level occupancies and so on.

In Fig. 5.8 the emission spectrum of the tin cylindrical layer with radius  $R = 100 \,\mu\text{m}$  at temperature  $T = 32 \,\text{eV}$  and electron density  $n_e = 10^{19} \,\text{cm}^{-3}$  is presented.

**Acknowledgments** This work was supported by the Russian Science Foundation under Grant No. 14-11-00699.

### References

- 1. D. Salzmann, Atomic Physics in Hot Plasmas (Oxford University Press, New York, 1998)
- H.-K. Chung, C. Bowen, C.J. Fontes et al., Comparison and analysis of collisional-radiative models at the NLTE-7 workshop High Energy Density Physics, vol. 9, Issue 4, pp. 645–652
- 3. B.F. Rozsnyai, Collisional-radiative average-atom model for hot plasmas. Phys. Rev. B **55**(6), 7507–7521 (1997)
- Yu. Ralchenko, A.E. Kramida, J. Reader, NIST ASD Team, NIST Atomic Spectra Database ver.4.1.0). http://physics.nist.gov/asd (2011). National Institute of Standards and Technology, Gaithersburg, MD. Accessed 22 June 2012
- R.D. Cowan et al., CATS: Los Alamos National Laboratory, Los Alamos, New Mexico. http://aphysics2.lanl.gov/tempweb
- 6. Gu M.F., The code FAC: Stanford University. http://kipac-tree.stanford.edu/fac
- I.Yu. Tolstikhina, S.S. Churilov, N. Ryabtsev, K.N. Koshelev, in *Atomic Tin Data, in the Book EUV Sources for Lithography*, ed. by V. Bakshi (SPIE Press, Bellingham, 2005)
- 8. V.G. Novikov, K.N. Koshelev, A.D. Solomyannaya, *Radiative Unresolved Spectra Atomic Model* (Physics of Extreme States of Matter, Chernogolovka, 2010)
- D.A. Kim, V.G. Novikov, G.V. Dolgoleva et al., EUV-source modeling with account of detailed level kinetics included in-line into gasdynamic calculations, Preprint of the Keldysh Institute of Applied Mathematics, No. 51. p. 23 (2012)
- L.M. Biberman, V.S. Vorob'ev, I.T. Yakubov, Kinetics of nonequilibrium low-temperature plasma (M.: Nauka, 1982)

- 11. L.A. Vainshtein, I.I. Sobel'man, E.A. Yukov, *Excitation of Atoms and Broadening of Spectral Lines* (Springer, New York, 1995)
- 12. V.A. Abramov, V.I. Kogan, V.S. Lisitsa, Radiation transfer in lines. Problemy teorii plazmy (Problems of plasma theory), eds. by M.A. Leontovich, B.B. Kadomtsev—Energoatomizdat, vol. 12 (1982). (in Russian)
- 13. D. Mihalas, Stellar Atmospheres, 2nd edn. (W.H.FREEMAN & Co., San Francisco, 1978)
- D.E. Post, R.V. Jensen, C.B. Tarter et al., Steady state radiative cooling rates for low density high temperature plasmas. Atomic Data Nucl. Data Tables, vol. 20, pp. 397–439 (1977)
- 15. S.A. Belkov, G.V. Dolgoleva, Average ion model for calculating the kinetics of ionization, occupancies of the excited levels and spectral coefficients of radiative transfer in the code SNDP, Problems of atomic science and technic, Methods and codes for numerical solution of problems of mathemaical physics (VANT, Seriya Metody i programmy), vol. 1, pp. 59–61 (1992)
- 16. P.D. Gasparyan, in *Slater Models of Average Ion for Short Description of Dense Plasmas in Problems of Equilibrium and Non-equilibrium Radiation Gasdynamics*, ed. by V.E. Fortov, Encyclopedia of Low-Tmperature Plasma, Seria B, vol. 3, book 1 (M.: Nauka, 2005)
- H. Van Regemorter, Rate of collisional excitation in stellar atmospheres. Astrophys. J. 136, 906 (1962)
- 18. W. Lotz, Electron-impact ionization cross-sections for atoms up to Z=108. Ztschr. Phys. 232, 101-107 (1970)
- A.F. Nikiforov, V.G. Novikov, V.B. Uvarov, Quantum-Statistical Models of Hot Dense Matter: Methods for Computation Opacity and Equation of State (Birkhauser Verlag, Basel, Boston, Berlin, 2005)
- S.M. Younger, Electron-impact ionization cross sections for highly ionized hydrogen- and lithium-like atoms. Phys. Rev. A. 22, 111 (1980)
- 21. V.S. Zakharov, V.G. Novikov, Modelling of ionization composition in argon plasma with fast electrons. Matem. Mod. **20**, 3–13 (2008)
- Zhdanov V.P. Dielectronic recombination. Problemy teorii plazmy (Problems of plasma theory), eds. by M.A. Leontovich, B.B. Kadomtsev, Energoatomizdat, vol. 12, pp. 79–93 (1982). (in Russian)
- G. Sharma, A. Agarwala, B. Bhattacharya, A fast parallel Gauss-Jordan algorithm for matrix inversion using CUDA. Comput. Struct. 128, 31–37 (2013)
- S.B. Hansen, J. Bauche, C. Bauche-Arnoult, M.F. Gu, Hybrid atomic models for spectroscopic plasma diagnostics. HEDP 3, 109–114 (2007)
- 25. J. Abdallah Jr, M.E. Sherrill, The reduced detailed configuration accounting (RDCA) model for NLTE plasma calculations. High Energy Density Phys. 4, 124 (2008)
- 26. V.G. Novikov, A.D. Soomyannya, Spectral characteristics of plasma consistent with radiation. High temperature (Teplofizika vysokih temperatur), vol. 36, N. 6. pp. 858–864 (1998)
- V.G. Novikov, S.V. Zakharov, Modeling of non-equilibrium radiating tungsten liners. JQSRT 81(1–4), 339–354 (2003)
- V.G. Novikov, V.V. Ivanov, K.N. Koshelev et al., Calculation of tin emission spectra in discharge plasma: the influence of reabsorption in spectral lines. High Energy Density Phys. 3(1–2), 198– 203 (2007)
- K.N. Koshelev, V.V. Ivanov, V.G. Novikov et al., RZLINE code modeling of distributed tin targets for laser-produced plasma sources of extreme ultraviolet radiation. J. Micro/Nanolithog. MEMS MOEMS(JM3) 11(2) (2012)

# Chapter 6 Collisional-Radiative Modeling and Interaction of Monochromatic X-Rays with Matter

## O. Peyrusse

**Abstract** Interaction of intense, short and monochromatic X-ray pulses with matter is a new field open by the advent of X-ray free electron laser facilities. If the photon energy exceeds at least one inner-shell photoionization threshold, radiation interacts with the basic atomic constituents and the matter, driven into a highly non-equilibrium state, must be described with an adequate model. Here, we discuss some problems arising when seeking to apply a collisional-radiative model in this context. Emphasis is placed upon practical solutions or computational strategies to treat these conditions of irradiation.

#### 6.1 Introduction

The advent of X-ray free electron lasers (XFELs) has opened a new field of research in Physics [1]. The interest of these sources is that they are short (less than 100 fs), monochromatic and tunable (up to 20 keV of photon energy, depending on facilities) with a high repetition rate (of about 100 pulses per second). The interaction of such radiation with matter involves mainly inner-shell electrons primarily through the process of photoionization and to a lesser extend through resonant photoexcitation. Subsequent phenomena such as Auger electron production, fluorescence, collisional ionization and excitation, 3-body recombination, etc. drive the matter in a highly non-equilibrium, rapidly evolving state whose description must rely on a proper collisional-radiative (CR) description, i.e. with a well-defined set of rate equations. In some cases, while the interaction itself is highly dependent on the atomic kinetics, the subsequent evolution of an irradiated sample, i.e. the post-pulse evolution, is also strongly dependent on the kinetics through many relaxation processes including hydrodynamics expansion and cooling. As a consequence, XFEL interaction with

128 O. Peyrusse

matter is a clear test bed for CR modeling simply because it requires a rate-equation description of the microscopic processes occuring during and after the interaction.

First, we need to recall the salient features of the interaction of X-rays with matter. Unlike low energy photons which interacts with valence electrons through single or multi-photon processes, high energy photons interact with electrons from inner shells. Photoionization of these electrons results in the formation of core-holes. At low intensity, such core-holes are quickly filled by Auger or radiative decay. For high intensities, further core-holes are likely to be produced by "one-photon sequential photoionization" so that so-called hollow atoms may be produced. In some situations, because the number of X-ray photons is huge, a saturation of the X-ray absorption has been observed [2], even in the hard x-rays range [3]. In all cases, the analysis of the interaction may be complex due to the competition of the different processes (including collisional processes) which requires careful CR calculations.

So far the most commonly observed mechanism of X-ray absorption by atoms is the so-called "sequential multiple photon absorption" which correspond to single photon absorption steps, sequentially ionizing or photoexciting electrons. There are also some clear evidences of two-photon absorption [4, 5]. However, although these X-ray multiphoton processes deserve to be studied from a fundamental point of view, they do not seem to play an important role in XFEL physics and we shall not consider them further in the text.

There are basically three situations of XFEL-interaction, namely with gas, small objects (like large molecules or clusters) and solids. Each one has its own specificity which deserves a dedicated discussion.

## 6.2 Atomic Model Construction for the Modeling of X-Ray Interaction with Matter

Modeling and understanding the interaction between intense x-ray pulses and single atoms is a prequisite for the study of matter under strong x-ray irradiation. As usual in CR modeling, a critical aspect is *completness* of the considered energy level atomic structure. Here, the difficulty is that one has to consider the possibility of creating many inner-shell holes (with more or less photoexcited states in some cases) and that the subsequent processes lead to considering numerous levels to incorporate all important channels for population relaxation fluxes. If further secondary collisional processes are considered, there is a need to consider excitation from the valence shell in the ions of interest (as in usual CR models of *thermal plasmas*).

The fact that more or less deep inner-shell holes are inevitably produced (depending on the X-ray photon energy) increases considerably the number of accessible states compared with purely thermal plasma situations. For computing the interaction of X-ray radiation with matter, it is neither useful nor even necessary to consider a *detailed level accounting approach* (or DLA approach). Electronic configurations suffice to capture the physics of the problem (this is the so-called *detailed* 

configuration accounting (DCA) approach. Nevertheless, even for moderate-Z material, the number of electronic configurations to include remains a daunting computational challenge.

The way to generate a relevant list of configurations for the x-ray interaction problem can be seen by using the simple six-electron carbon atom as an example. One considers first:

- 1. A single ground initial configuration.
- 2. An x-ray photon energy greater than the carbon K-edge.
- 3. No secondary collisional processes.

Starting from the configuration  $1s^22s^22p^2$  in neutral carbon, the sequential removal of one-electron (by one-electron photoionization) in the different subshells gives:

```
• in C<sup>+</sup>:

1s<sup>2</sup>2s<sup>2</sup>2p

1s<sup>2</sup>2s2p<sup>2</sup>

1s2s<sup>2</sup>2p<sup>2</sup>
```

```
• in C<sup>2+</sup>:

1s<sup>2</sup>2s<sup>2</sup>

1s<sup>2</sup>2s2p

1s2s<sup>2</sup>2p

1s<sup>2</sup>2p<sup>2</sup>

1s2s2p<sup>2</sup>

2s<sup>2</sup>2p<sup>2</sup>
```

• etc.

At the end, one gets 27 configurations (from C-I to C-VII). What is noticeable is the appearance of an hollow configuration in  $C^{2+}$ . Another important point is that, such a list provides automatically the important channels for Auger and radiative relaxation. If one considers for instance the last configuration of  $C^+$ , namely  $1s2s^22p^2$ . This configuration may relax through Auger decay (giving  $1s^22s^2$ ,  $1s^22s2p$  or  $1s^22p^2$ ) or through radiative decay (giving  $1s^22s^22p$ ). These *relaxed* configuration are present in the above set of configurations.

This simple set remains however too restrictive if one considers the influence of the *secondary* processes induced by the photoelectrons and the Auger electrons, i.e. all the collisional processes. So, the previous set must be augmented by considering single excitations from the valence shell (and possibly from the first inner-shell) in the lower energy configuration of each charge state.

Another possibility, which increases a lot the final list of configurations to consider, consists in starting directly with a set of ground and excited configurations in the initial atom (instead of the unique configuration of neutral carbon in the previous

130 O. Peyrusse

example). Applying the sequential ionization procedure gives a large list of configurations which have to be take into account in long pulse irradiation (greater than about 10 fs) where collisional processes take place during the photoionizing x-ray pulse itself.

Given a list of configurations relevant for a particular problem, we then obtain all the required coupling rates. Although simple hydrogenic formulations are often used (see for instance [6]), these rates must be based on a proper configuration-averaged quantum mechanical formulation of the necessary atomic data (decay rates, photoionization cross section, collisional cross sections) [7]. Moreover, the calculation of proper photoexcitation rates requires a proper averaging of all the lines connecting two configurations (giving a so-called *unresolved transition array* or UTA profile). Position and width of these profiles can be computed from the UTA theory [8]. In some cases, when the Spin-Orbit interaction has important effects on spectra, it is necessary to resort to the Spin-Orbit-Split Array (SOSA) theory [9].

## **6.3** Interaction with Gas

By varying the photon energy and the pulse duration, different scenarios on ionization of a low Z gas such as Neon have been observed [10] and simulated [11]. When X-ray photons have insufficient energy to ionize a K-shell electron, ionisation up to Ne<sup>8+</sup> proceeds via a sequence of 2p electron ionization. When X-ray photons have sufficient energy to ionize a 1 s electron, ionization up to Ne<sup>10+</sup> proceeds via a combination of K-shell photoionization along with Auger ionization (2p ionization and refilling of the 1 s shell). For the shortest pulses (less than a few tens of fs), i.e. shorter than the Auger refilling rate, ionization of the highest charge states is suppressed due to the rapid formation of hollow atoms. In similar conditions and for high intensities (>10<sup>17</sup> W/cm<sup>2</sup>), a population inversion can be reached between the core-hole states  $1s2s^22p^6$  (pumped from the ground state of Neon) and the states  $1s^22s^22p^5$  so that lasing may occur [12]. Here this lasing transition competes with Auger decay toward the states  $1s^22s^22p^4$ .

These studies have been extended to higher Z rare gas such as Krypton [13] and Xenon [14, 15] but for very low densities. In the latter case and for 1.5 keV photons, an ultra-efficient ionization (charge states up to Xe<sup>36+</sup>) have been measured [14].

These very low density situations are particularly interesting since one can assume that all the "free" electrons produced from the interation, i.e. photoelectrons and Auger electrons escape the sample. Consequently, the only important processes are photoionization, photoexcitation (and possibly stimulated emission) along with Auger and radiative relaxation. None of these rates depend on the electron density and temperature. The external parameter entering the rates is just the XFEL intensity. As discussed below, such a time-dependent situation lends itself to Monte-Carlo simulations although the traditional approach is a direct determination of the population vector **N** from the rate equation system, i.e.

$$\frac{d\mathbf{N}}{dt} = \mathbf{T} \cdot \mathbf{N} \tag{6.1}$$

for which a simple fully implicit differencing gives

$$\mathbf{A}(t + \Delta t) \cdot \mathbf{N}(t + \Delta t) = \mathbf{N}(t) \tag{6.2}$$

with  $A = 1 - T(t + \Delta t)\Delta t$ . T is the rate equation matrix which depends on the imposed XFEL intensity at  $t + \Delta t$ . Most often the temporal shape of the pulse is assumed to be gaussian.

When dealing with high Z, this direct approach for solving the rate-equation system has two bottlenecks. The first one is the completeness of the configuration list allowing a proper description of all the possible photoionization and photoexcitation pathways. As stated in [14] and, for photoionizing or photoexciting the M-shell of xenon ions, this may involves tens of millions of configurations. A consequence is the prohibitive number (billions) of rates coupling these configurations which have to be evaluated. The second bottleneck is the numerical solution (at each time step) of the CR system itself (i.e. the inversion of matrix A).

To circumvent the problem raised in [14], a *superconfiguration* approach (based on [16]) has been proposed [17].

In this approach the possible photoexcitation channels are approximately accounted for by a large supershell which can contain a fixed number  $n_{ex}$  of photoexcited electrons from the M-shell (see Table 6.1 for neutral Xe). This number  $n_{ex}$  which corresponds to the sequential photoexcitation processes depends on the XFEL intensity so that a convergence must be found by increasing its value. One notices that the list given in Table 6.1 is just a starting list. By removing one electron such that  $n \geq 3$  (n is the principal quantum number; deeper electrons cannot be photoionized by 1.5 or 2 keV photons), another list of SCs can be generated for Xe<sup>+</sup>, and so on. At the end a large list of SCs determining the size of the CR system is obtained. For  $n_{ex} = 5$ , one gets about 95,000 superlevels which remains a manageable number. As shown in Fig. 6.1, this approach explains the occurence of the Xe<sup>36+</sup> ions observed in experiments of ion yield measurements of XFEL irradiated Xenon [14].

**Table 6.1** Superconfiguration set in neutral Xe with  $n_{ex} = 3$  (see text)

```
Superconfiguration  \frac{(1s)^2 (2s2p)^8 (3s3p)^8 (3d)^{10} (4s4p4d)^{18} (5s5p)^8}{(1s)^2 (2s2p)^8 (3s3p)^8 (3d)^9 (4s4p4d)^{18} (5s5p)^8 (4f5d5f6s6p6d6f7s7p7d7f8s8p8d8f)} \\ (1s)^2 (2s2p)^8 (3s3p)^7 (3d)^{10} (4s4p4d)^{18} (5s5p)^8 (4f5d5f6s6p6d6f7s7p7d7f8s8p8d8f)} \\ (1s)^2 (2s2p)^8 (3s3p)^7 (3d)^{10} (4s4p4d)^{18} (5s5p)^8 (4f5d5f6s6p6d6f7s7p7d7f8s8p8d8f)^2 \\ (1s)^2 (2s2p)^8 (3s3p)^7 (3d)^9 (4s4p4d)^{18} (5s5p)^8 (4f5d5f6s6p6d6f7s7p7d7f8s8p8d8f)^2 \\ (1s)^2 (2s2p)^8 (3s3p)^6 (3d)^{10} (4s4p4d)^{18} (5s5p)^8 (4f5d5f6s6p6d6f7s7p7d7f8s8p8d8f)^2 \\ (1s)^2 (2s2p)^8 (3s3p)^6 (3d)^{10} (4s4p4d)^{18} (5s5p)^8 (4f5d5f6s6p6d6f7s7p7d7f8s8p8d8f)^3 \\ (1s)^2 (2s2p)^8 (3s3p)^7 (3d)^8 (4s4p4d)^{18} (5s5p)^8 (4f5d5f6s6p6d6f7s7p7d7f8s8p8d8f)^3 \\ (1s)^2 (2s2p)^8 (3s3p)^6 (3d)^9 (4s4p4d)^{18} (5s5p)^8 (4f5d5f6s6p6d6f7s7p7d7f8s8p8d8f)^3 \\ (1s)^2 (2s2p)^8 (3s3p)^5 (3d)^9 (4s4p4d)^{18} (5s5p)^8 (4f5d5f6s6p6d6f7s7p7d7f8s8p8d8f)^3 \\ (1s)^2 (2s2p)^8 (3s3p)^5 (3d)^{10} (4s4p4d)^{18} (5s5p)^8 (4f5d5f6s6p6d6f7s7p7d7
```

132 O. Peyrusse

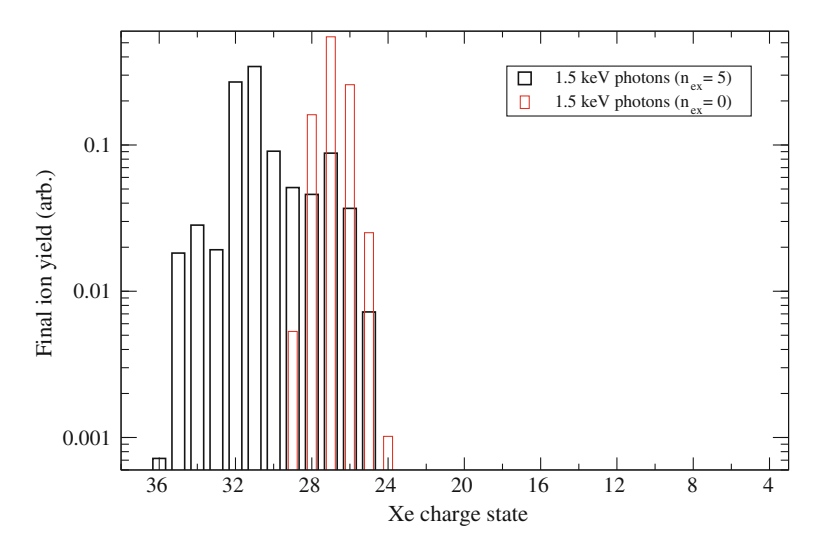


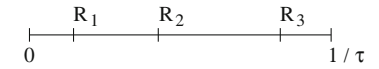
**Fig. 6.1** Xenon charge state yields calculated for an 80 fs X-ray pulse, an intensity of  $1.11 \times 10^{17} \text{W/cm}^2$  and a photon energy of 1.5 keV. The *black bars* correspond to a calculation with  $n_{ex} = 5$  (see text) while the *red bars* correspond to a calculation with  $n_{ex} = 0$ 

As mentionned above and because the rates of the important processes do not depend on unknown parameters, this problem lends itself to the use of the so-called Kinetic Monte Carlo (KMC) method. The method has been developed to simulate systems obeying a master equation (see for instance [18, 19]) when the rates of the processes are known. Up to now, its application to atomic population kinetics has been limited. One can mention a work realized within the average atom model [20]. Recent implementations of this method in the context of XFEL interaction with complex atoms has been reported [21, 22]. In this approach, the required rates must be computed in advance, or possibly at each time step [22] because for a given case, the number of atomic states turns out to be limited compared to the huge number of accessible states. Indeed, an advantage of this method is that it automatically selects the important atomic states describing the population set evolution.

The essence of the KMC algorithm is a simulation of the random jumps from an initial state to a set of final possible states. After each jump, one considers the subsequent possibilities: end of the simulation (according to some criteria) or follow up with a new jump. In principle, the rates depend on time through external parameters such as temperature, density or radiative intensity. Let us consider first the case where the rates do not depend on time. Suppose that at a given time t, the system is in the atomic state i, from which the system can evolves toward many other states j as the result of processes characterized by the rates  $P_{ij}$ . From i, the number of possible transitions remains limited and its sum reads

$$\frac{1}{\tau} = \sum_{i} P_{ij} \tag{6.3}$$

**Fig. 6.2** Selection of the final state according to the different rates



where  $\tau$  is the *lifetime* of state *i*. Indeed, the *waiting time* for the system in state *i*, to jump to another state has clearly the (Poisson) distribution

$$f(t) = \frac{1}{\tau} e^{-t/\tau}.$$
 (6.4)

One easily sees that  $\int_0^\infty t \ f(t)dt = \tau$ . The way to generate a random time step  $\Delta t$  obeying a Poisson distribution such as (6.4) from a random number r uniformly distributed in the intervall [0, 1] is wellknown, one has

$$\Delta t = -\tau \ln r. \tag{6.5}$$

So the algorithm consists in choosing first a random time  $\Delta t$  according to (6.5) after which a transition occurs. Second step consists in choosing randomly which transition occurs. For this, a rate number k is assigned to each non-zero transition rate from i so that  $P_{ij} = R_1$ ,  $P_{ij'} = R_2$ ,  $P_{ij''} = R_3$ , etc. Then, (6.3) rewrites  $\sum_k R_k = 1/\tau$ . One chooses a second random number s also uniformly distributed in the interval [0, 1]. According to Fig. 6.2, If  $s/\tau$  lies between 0 and  $R_1$  then the system jumps to the final state associated to the rate  $R_1$ , if  $s/\tau$  lies between  $R_1$  and  $R_1 + R_2$ , then the system jumps to the final state associated to the rate associated to the rate  $R_2$ , etc.

More generally, considering the sums  $S_{\ell} = \sum_{k=1}^{\ell} R_k$ , if  $s/\tau$  is between  $S_{\ell-1}$  and  $S_{\ell}$  then the system jumps to the state corresponding to the rate  $R_{\ell}$ . Population of this state is increased by one (while the previous one is decreased by one) and the time is updated, i.e. t becomes  $t + \Delta t$ . The simulation can continue until the time exceeds some fixed value. The set of states reached during a whole simulation is called a *Monte Carlo Trajectory*.

It is necessary to run many MC trajectories until the results are converged. The final population histogram is divided by the number of MC trajectories considered. It gives the final population distribution. Other histograms concerning the ion yield, the fluorescence spectrum or the emitted electrons, can also be recorded during the MC trajectory.

Let us consider now the case where the rates depend on time. The procedure is the same except that, instead of Formula (6.5), the time increment  $\Delta t$  is defined so that

$$\sum_{k} \int_{t}^{t+\Delta t} R_k(t)dt = -\ln r \tag{6.6}$$

while the sums  $S_{\ell}$  are to be evaluated at  $t + \Delta t$  since at this time, the system is still in the same state.

134 O. Peyrusse

For the problem of a dilute gas irradiated by an XFEL, one can divide the rates in two categories: those which depend on the radiative intensity (photoionization, photoexcitation and stimulated emission) and those which do not (Auger and radiative relaxation). Rates that belong to the latter category do not depend on time and formally, the left term of (6.6) takes the form

$$\sum_{k} \int_{t}^{t+\Delta t} R_{k}(t)dt = A \, \Delta t + B \int_{t}^{t+\Delta t} I(t)dt \tag{6.7}$$

where I(t) is XFEL intensity. Taking a gaussian temporal shape for the XFEL pulse, on has to find  $\Delta t$  so that

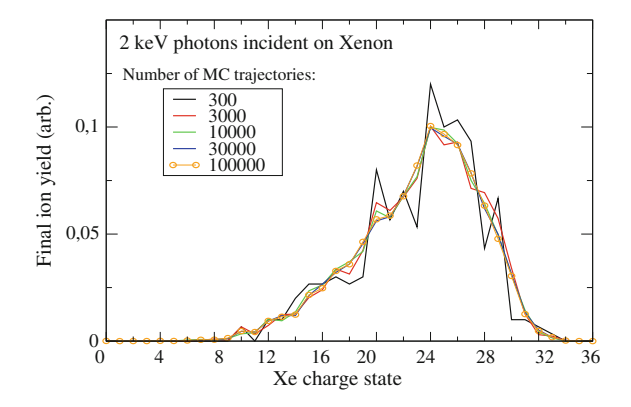
$$A \Delta t + B I_{XFEL} \int_{t}^{t+\Delta t} \exp[-(t - t_o)^2/a^2] dt = -\ln r$$
 (6.8)

where  $I_{XFEL}$  is the peak XFEL intensity. Practically, one can make use of the standard function  $P(x) = \frac{1}{\sqrt{2\pi}} \int_{-\infty}^{x} e^{-t^2/2} dt$  for which powerful analytical approximations exist [23]. Each MC trajectory end up when the current time exceeds the pulse duration.

Compared with a direct solution of the time-dependent CR system (6.2), the KMC approach has a spectacular efficiency as shown in Fig. 6.3 which displays a calculation of the ion yield of Xe, after a pulse of 2 keV photons (80 fs FWHM,  $10^{17}$  W/cm<sup>2</sup>), as a function of the number of MC trajectories. The convergence is practically reached after a few thousands of MC realizations.

Similarly, this method can be extended to plasmas where collisional processes are important as long as the history of the electron density and temperature, i.e.  $N_e(t)$  and  $T_e(t)$  are known. Also, steady-state situations where  $N_e$  and  $T_e$  are kept constant can be adressed with the KMC method. The ending duration of a simulation is then the time needed to reach a steady-state equilibrium.

Fig. 6.3 Monte-Carlo simulation of the Xenon charge state yield for an 80 fs X-ray pulse, an intensity of  $10^{17}$ W/cm<sup>2</sup> and a photon energy of 2 keV. Results converge with the number of realizations. The (super) level list used in these calculations is that of Fig. 6.1 (with  $n_{ex} = 5$ )



## 6.4 Interaction with Small Objects

When a small object (a more or less large molecule, a cluster) is irradiated by Xrays, some electrons are first removed from the single atoms and then, more and more electrons leaves the object. As a consequence, a strong Coulomb potential develops so that electrons leaving the object are slowing down and are finally bringing back by this Coulomb potential. After many photoionization events (and also Auger ejection events), the Coulomb energy may be higher than the kinetic energy of the leaving electrons. In that case electrons are trapped in the Coulomb potential. Thermalizing, they contribute to the heating of the object and to further collisional ionization events. The object becomes a so-called *nanoplasma*. The subsequent expansion of the object is either a Coulomb explosion either a simple thermal expansion or both, i.e. a Coulomb explosion of the outer shells of the object and a thermal expansion of the core. Which expansion dominates depends on the composition (type of atoms), on the size of the object and on the photon energy. For this reason, it is difficult to give a general law describing the macroscopic behavior of a small object under x-ray irradiation but in any case, simulations must be supported by a collisionalradiative model. From the CR modeling point of view, this context does not differ from that of the interaction with a not too dilute gas, i.e. where collisional processes are not negligible. Also, one may have to implement a multi-element CR model which respects the stoechiometry of the object.

To emphasize the interest of these studies, one cannot forget that one of the most exciting prospects of research with XFELs is direct imaging of non-periodic nanoscale objects such as bio-molecules, living cells and viruses [24]. This technique is called *coherent x-ray diffraction imaging* and has already been demonstrated [25], even on large viruses [26]. Interested readers can refer to [1, 27–30] and references therein. In any case, samples irradiated by intense pulses of x-rays turn into a highly excited, very transient systems after and during exposure. The x-ray pulse must be short enough (for recording information before the destruction of the object) and intense enough (to get enough diffracted signal). It can be shown that the diffraction pattern from a sample is given by the square modulus of a scattering amplitude which depends on the spatial position of the atoms and on the atomic scattering factors of these different atoms. Its measured value is an average over the temporal shape of the x-ray pulse. The problem of the evolution of the atomic positions has been studied through molecular dynamics simulations [31] and hydrodynamical models [32, 33]. The calculation of the time-averaged atomic form factors amounts to average (locally) over the various species weighted by their populations which evolves according to a rate-equation system [34].

#### **6.5** Interaction with Solids

It is of crucial importance to investigate the interaction of intense femtosecond x-ray pulses with solids in order to understand damage threshold mechanisms (for x-ray optics) [35], to understand some aspects of non-thermal phase transitions induced by x-rays [36] or to control the creation of isochorically heated samples for warm/hot dense matter studies [37] (radiative properties of dense plasmas, equation-of-state, etc.).

For rather low fluence irradiation, many experimental results rely on a *post-mortem* analysis of the irradiated samples (size and depth of the craters; analysis of changes in the morphology of the material, etc.). For larger fluences where irradiation leads to the creation of a plasma, one can try to measure somehow the dynamics of the sample and to get different informations from emission/absorption spectroscopy. Interpretation of these experiments relies on numerical models based on different approaches to describe the full dynamics of a sample.

Models describing the dynamics of the ions can be of *continuum* type, e.g. hydrodynamics models [32, 38], or of *corpuscular* type, e.g. classical molecular dynamics models [39] when extended to bulk solids by using proper periodic conditions in the simulations. In all cases, it remains convenient to model the free electrons as a continuous gas, i.e. described locally by an electron density  $N_e(t)$  and an electron temperature  $T_e(t)$ . Here again, we will focus on the collisional-radiative aspect of the problem. Compared with the case of the interaction with dilute gas, one needs to follow the evolution of the free electron distribution during and after the pulse. Because of our main focus, we will assume an instantaneous thermalization of the free electrons. This hypothesis allows us to define, at each instant, an electron temperature, i.e. to characterize the free electrons by a maxwellian distribution or a Fermi-Dirac distribution in a cold or warm material.

The treatment of the interaction by means of a CR model (which basically relies on a *chemical picture*) in a cold or warm material at solid density leads to some difficulties [40] such as:

- The need for a correct (or at least coherent) continuum lowering model.
- A possible degenaracy of the free electrons. Then, besides the use of a Fermi-Dirac distribution, rates must include proper Pauli-Blocking factors.
- The need to take into account processes involving electrons from the valence band. This imposes a generalization of some processes.

The need to define an electron temperature leads to consider a further equation describing the internal energy of the electron fluid. Numerically, This points turns to be a very *stiff* aspect of the problem since atomic kinetics depends sensitively on temperature.

Last, the deposition of the X-ray energy into the solid must be considered with care.

All these points are discussed in the following.

# 6.5.1 Population Kinetics and Atomic Structure at Solid Density

The CR treatment of the interaction of x-rays with a solid-state material always leads to consider density effects to be handled with a formulation of continuum lowering (CL) [41, 42]. The CL problem (called also *Ionization Potential Depression*) is old, complex and still open. This problem will not be discussed here. Moreover, one needs to discriminate between amorphous solids and metals which present a valence band of degenerated delocalized electrons. In the former case, one can consider the neutral atoms as the initial atomic structure seen by the X-rays (even though continuum lowering can affect this structure). The latter case is different in the sense that the initial state of matter must be seen as a degenerated dense plasma. There is indeed a population of free electrons described by a Fermi-Dirac distribution.

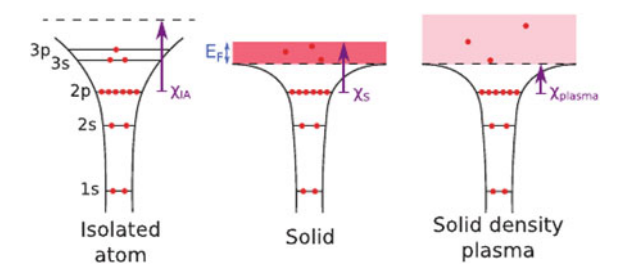
Figure 6.4 depicts the three situations of interest taking Al as an example: The isolated atom which is reminded on the left, the solid (middle) and the heated solid (right). The upper band represents schematically a *valence band* (VB) of degenerated electrons and  $\chi_s$  in the middle figure is the photoionization L-edge in the solid (distinct from the work function which is the energy necessary to extract an electron from the whole solid). In other words,  $\chi_s$  is the minimum energy required to transfer an electron from the L-shell just above the Fermi energie  $E_F$ . On the right figure, the band depicts non degenerated free electrons. Its upper frontier is not limited.  $\chi_{plasma}$  is here the ionization potential of Al<sup>3+</sup> lowered of a quantity called *continuum lowering*.

For Al, it is wellknown that the three outer electrons, namely  $3s^23p$  are delocalized at solid density. For treating the interaction of X-rays with the inner-shells with a collisional-radiative model, it is thus reasonable to start a calculation from a population of Al<sup>3+</sup> ions embbeded into a degenerated free electron gas. The question is then, how to handle some important electron processes taking place into the solid just after the inner-shell photoionization by X-rays?

To precise this question, let us consider for instance the Auger effect following a 1s photoionization in the solid:

$$1{\rm s}2{\rm s}^22{\rm p}^6({\rm VB})^3\to 1{\rm s}^22{\rm s}^22{\rm p}^6({\rm VB})+\bar{e}_{Auger}$$

**Fig. 6.4** Schematics of the bound- and free-electron structure of Al in the isolated neutral atom, the *solid* and the hot *solid* density plasma, respectively



where VB stands for valence band electrons. Clearly, since VB electrons are just free electrons in a standard CR model, this effect cannot be taken into account. However, let us consider the 3-body recombination:

$$1s2s^22p^6(VB)^2(VB) \rightarrow 1s^22s^22p^6(VB) + \bar{e}$$
.

Comparing these two reactions, one sees that both left and right sides are equivalent. This suggests that Auger effect in the solid can be considered as a *generalized* 3-body recombination (TBR) which is the simple Auger effect in the cold solid while it turns to be a standard TBR if temperature is high (where the VB no longer exist).

Similarly, the fluorescence following a 1s photoionization in the solid:

$$1s2s^22p^6(VB)^3 \rightarrow 1s^22s^22p^6(VB)^2 + h\nu$$

can be considered as a *generalized* radiative recombination process.

In order to establish a proper link between different processes, one needs to firmly define what are the necessary rates in a degenerated plasma. First of all, the free electron gas is described by a Fermi-Dirac distribution  $F(\varepsilon) = \frac{g(\varepsilon)}{1+e^{(\varepsilon-\mu)/T_{\varepsilon}}}$  where  $g(\varepsilon)$  is the density of states. For independent particles (a very good approximation for simple metal such as Al)  $g(\varepsilon)$  has the form  $g(\varepsilon) = \frac{\sqrt{2}}{\pi^2 N_{\varepsilon}} \left(\frac{m_{\varepsilon}}{\hbar^2}\right)^{3/2} \sqrt{\varepsilon}$  while the chemical potential  $\mu$  is obtained from the normalization condition  $\int_0^\infty F(\varepsilon) d\varepsilon = 1$ .

Then, the 3-body recombination rate between two configurations c' and c reads,

$$T_{c'c} = N_e^2 \int_0^\infty \int_0^\infty \frac{d\Sigma_{c'c}^{3b}}{d\varepsilon'} \sqrt{\frac{4\varepsilon'\varepsilon''}{m_e^2}} F(\varepsilon') F(\varepsilon'') P(\varepsilon) d\varepsilon' d\varepsilon''$$
 (6.9)

where  $\frac{d\Sigma_{c'c}^{3b}}{d\varepsilon'}$  is the 3-body differential cross section,  $\varepsilon'$  and  $\varepsilon''$  are the energies of the two incoming electrons and  $\varepsilon$  is the energy of the outgoing electron in the recombination process ( $\varepsilon = \chi_{cc'} + \varepsilon' + \varepsilon''$  where  $\varepsilon = \chi_{cc'}$  is the ionization potential between c and c'). In (6.9),  $P(\varepsilon) = 1 - F(\varepsilon)$  is a *Pauli-blocking* factor. It takes into account the space available in the Fermi-Dirac distribution. For high temperatures, this factor is equal to 1 and the Fermi-Dirac distribution turns into a maxwellian distribution. The 3-body differential cross section is deduced from the collisional ionization differential cross section  $\frac{d\sigma_{cc'}^{ion}}{d\varepsilon'}$  by means of the microreversibility relation

$$\frac{d\Sigma_{c'c}^{3b}}{d\varepsilon'} = \frac{g_c}{g_{c'}} \frac{\varepsilon}{\varepsilon'\varepsilon''} \frac{h^3}{16\pi m_e^2} \frac{d\sigma_{cc'}^{ion}}{d\varepsilon'}$$
(6.10)

while the total ionization cross section reads  $\sigma_{cc'}(\varepsilon) = \int_0^{\varepsilon - \chi_{cc'}} \left( \frac{d\sigma_{cc'}^{ion}}{d\varepsilon'} \right) d\varepsilon'$ . A current assumption for  $\frac{d\sigma_{cc'}^{ion}}{d\varepsilon'}$  is that it is only a function of the incoming electron energy  $\varepsilon$ , i.e.  $\frac{d\sigma_{cc'}^{ion}}{d\varepsilon'} = \frac{\sigma_{cc'}^{ion}}{(\varepsilon - \chi_{cc'})}$ .

As discussed above, a link can be established between the Auger effect in the cold solid and the 3-body recombination by using a probability formalism [43]. The *generalized* 3-body recombination rate is written as

$$T_{c'c}^G = (1 - f(T_e)) \Gamma_{c'c} + f(T_e) T_{c'c}$$
(6.11)

where  $\Gamma_{c'c}$  is the Auger rate in the cold solid. The probability  $f(T_e)$  is defined from the free space determined from Fermi-Dirac statistics, i.e.

$$f(T_e) = \int_{\mu(T_e)}^{\infty} F(\varepsilon, T_e) d\varepsilon.$$
 (6.12)

In such a way, f(0) = 0 so that the rate is equal to  $\Gamma_{c'c}$  in the cold solid while at high temperature, f approaches 1 and the rates tends to the classical 3-body rate  $T_{c'c}$ . Similarly, one can define a *generalized* radiative recombination rate as

$$T_{c'c}^G = (1 - f(T_e)) A_{c'c} + f(T_e) R_{c'c}$$
(6.13)

where  $A_{c'c}$  is the fluorescence rate in the cold solid while  $R_{c'c}$  is the radiative recombination rate which reads

$$R_{c'c} = \int_0^\infty \sigma_{c'c}^{rr}(\varepsilon) \sqrt{\frac{2\varepsilon}{m_e}} F(\varepsilon) d\varepsilon \tag{6.14}$$

in which the radiative recombination cross section  $\sigma_{c'c}^{rr}$  is linked to the photoionization cross section  $\sigma_{cc'}^{ph}$  by the microreversibilty relation

$$\sigma_{cc'}^{ph}(h\nu) = \frac{g_{c'}}{g_c} \frac{2m_e c^2 \varepsilon}{(h\nu)^2} \sigma_{c'c}^{rr}(\varepsilon)$$
 (6.15)

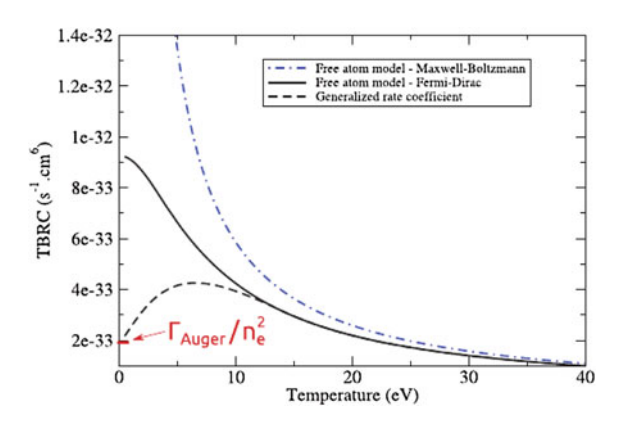
with  $h\nu = \varepsilon + \chi_{cc'}$ .

Figure 6.5 displays a generalized 3-body rate coefficient (dashes), corresponding to the reaction  $1s^22s^22p^5 + \bar{e}' + \bar{e''} \rightarrow 1s^22s^22p^6(VB) + \bar{e}$ . This shows how the formulation discussed above provides the transition between the cold solid to the heated solid. The influence on the occupancy of free-states is illustrated in Fig. 6.6 which displays a zero-dimensional calculation of the temperature reached at rather low intensity  $I = 10^{13} \text{ W/cm}^2$  in aluminum. One can see the importance of including the above discussed solid-state effects by comparing with a standard CR calculation using a maxwellian distribution for the free electrons. These calculations make use of a coherent coupling of the population kinetics with the evolution of  $T_e$ , a point which is adressed just below.

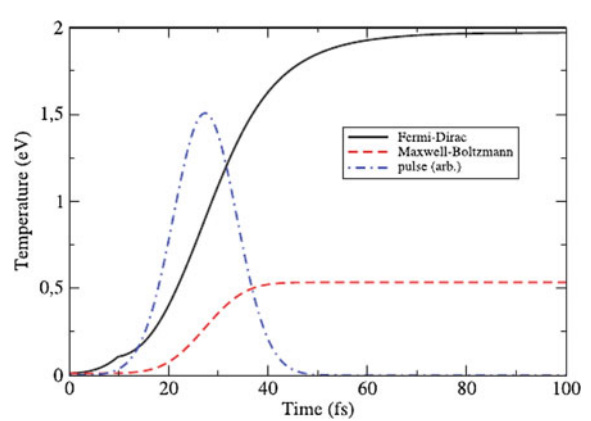
# 6.5.2 Temperature and Population Evolution

The rate equation system (6.1) can alternatively be written in term of the fractions  $f_i = N_i/N_{ion}$  where  $N_{ion}$  is the atom density.

Fig. 6.5 Generalized 3-body recombination rate in Al (dashes) compared with a standard 3-body recombination rate calculated with Fermi-Dirac and Maxwell-Boltzmann distribution, respectively (from [40])



**Fig. 6.6** Evolution of  $T_e$  in Al when using a Fermi-Dirac distribution and a Maxwell-Boltzmann distribution, respectively. The irradiation conditions are  $10^{13}$  W/cm<sup>2</sup> in a pulse of 15 fs (FWHM) and a photon energy of 92 eV (from [40])



$$\frac{d\mathbf{f}}{dt} = \mathbf{T} \cdot \mathbf{f}, \qquad \sum_{i} f_{i} = 1. \tag{6.16}$$

(Note: system (6.16) lends itself to CR modeling in a Lagrangian cell of volume V(t) where the number of atoms  $N_{ion}V(t)$  remains constant.)

Just as system (6.16) can be stiff, the equation governing the evolution of  $T_e$  can simultaneously be stiff due to the large dependencies of rates on temperature. It is convenient to write this equation under the form

$$\frac{d\varepsilon_e}{dt} = W(t) \tag{6.17}$$

where the term W on the right contains the source of heating, i.e. the power deposited by the X-rays and eventually a term due to the radiation losses. In an hydrodynamics code, W must also include other source/loss terms such as thermal conduction, work of the thermal electronic pressure and energy exchange with the ions [38].  $\varepsilon_e$  is

the internal thermal energy of the electrons per mass unit so that  $\rho \varepsilon_e$  is an energy per volume unit if  $\rho$  is the mass density. The form given to  $\varepsilon_e$  corresponds to the equation-of-state of the electron gas which includes the contribution of free and bound electrons. Its simplest form is

$$\rho \varepsilon_e = \rho E_e + N_{ion} \sum_i (e_i - e_{i_o}) f_i$$
 (6.18)

where  $\rho E_e$  is the kinetic energy density of the free electrons (e.g.  $\frac{3}{2}N_ekT_e$  for a non-degerated electron gas). Second term is the ionization/excitation energy in which  $e_i - e_{i_o}$  is the energy of level i (which can be a configuration in a DCA description, see Sect. 6.2) with respect to some reference level  $i_o$  (the same during a whole calculation).

We will describe here two approaches to overcome the *stiffness* of the problem of solving (6.16) and (6.17). The first one, that we will call *Entire linearization procedure* considers the total electron internal energy. It is not fully implicit in the sense that the deposited energy remains explicit (in the term W of (6.17)). The second approach, called *Electron temperature linearization procedure*, focuses on the energy density of free electrons rather than on the total electronic energy density. It does not explicitly conserves energy but it has proven to be stable and accurate in another context [44].

#### **6.5.2.1** Entire Linearization Procedure

Whatever the state of the free electron gas, i.e. degenerated or not, (6.18) can be shortened as

$$\varepsilon_{e} = g(T_{e}) + \mathbf{E}.\mathbf{f} \tag{6.19}$$

If the solution is known at instant t (superscript "-"), we wish to know the solution at instant  $t + \Delta t$  (superscript "+"). The updated value  $\varepsilon_e^+$  simply reads, from (6.17)  $\varepsilon_e^+ = \varepsilon_e^- + W \Delta t$ .

Then, with (6.18), an implicit discretization of (6.16), (6.17) gives the system

$$\begin{cases}
\left[\mathbf{1} - \Delta t \mathbf{T}(T_e^+)\right] \cdot \mathbf{f}^+ = \mathbf{f}^- \\
g(T_e^+) + \mathbf{E} \cdot \mathbf{f}^+ = \varepsilon_e^- + W \Delta t
\end{cases}$$
(6.20)

whose unknown quantities are the set  $\mathbf{x}^+ \equiv (\mathbf{f}^+, T_e^+)$ .

Suppose one has n levels (or configurations) in the problem. Previous system can be reformulated by defining a function F acting on the set  $\mathbf{x}^+$ . F is defined as

$$F_i = \sum_{j=1}^{n} U_{ij} f_j^+ - f_i^- \qquad i = 1, n$$
 (6.21)

with  $U_{ij} = \delta_{ij} - \Delta t T_{ij}(T_e^+)$ , and

$$F_{n+1} = \sum_{j=1}^{n} E_j f_j^+ + g(T_e^+) - \varepsilon_e^- - W \Delta t.$$
 (6.22)

System (6.20) reduces to n + 1 functional relations to be zeroed, i.e.

$$F_i\left(\mathbf{f}_1^+, \mathbf{f}_2^+, \dots, \mathbf{f}_n^+, T_e^+\right) = 0, \quad i = 1, n+1.$$
 (6.23)

These equations can be solved iteratively by linearization. More precisely, after iteration q, the new solution is written as  $(\mathbf{f}^{(q)} + \delta \mathbf{f}, T_e^{(q)} + \delta T_e)$  with  $\mathbf{f}^{(0)} = \mathbf{f}^-$  and  $T_e^{(0)} = T_e^-$  when starting the procedure. The linearization gives,

$$F_i\left(\mathbf{f}^{(q)} + \delta\mathbf{f}, T_e^{(q)} + \delta T_e\right) \simeq F_i\left(\mathbf{f}^{(q)}, T_e^{(q)}\right) + \sum_{j=1}^n \frac{\partial F_i}{\partial \mathbf{f}_j} \delta \mathbf{f}_j + \frac{\partial F_i}{\partial T_e} \delta T_e.$$

Zeroing the new  $F_i$  gives the linear system

$$\mathbf{J}^{(q)}.\delta\mathbf{x} = -\mathbf{F}\left(\mathbf{x}^{(q)}\right) \tag{6.24}$$

with 
$$\mathbf{x}^{(q)} \equiv \left(\mathbf{f}^{(q)}, T_e^{(q)}\right)$$
 and,  $J_{ij} = \frac{\partial F_i}{\partial f_j}$   $(j = 1, n), J_{in+1} = \frac{\partial F_i}{\partial T_e}$ .

This scheme involves a derivation of the rates with respect to  $T_e$ . In the maxwellian case, one can easily obtain analytical formulations of the derivatives. With a Fermi-Dirac distribution, it is necessary to rely on accurate numerical derivatives (see for instance the finite difference scheme *fdjac* described by Press et al. [45]).

It can be efficient to include the constraint  $\sum_i f_i = 1$  by replacing one of the equations (6.21) by the equation  $F_i = \sum_i f_i^+ - 1$ . Also, at each step, one can check that the sum  $\sum_{i} \delta f_{j}$  is essentially zero.

#### 6.5.2.2 **Electron Temperature Linearization Procedure**

This scheme focuses on the kinetic energy density of the free electrons (instead of the total internal energy, see (6.18)). Then one considers the evolution

$$\frac{dE_e}{dt} = Q ag{6.25}$$

where Q is the heating rate (per mass unit) of the free electrons only (to be defined below). Keeping  $N_e/\rho$  constant over one time step (this quantity can be updated after), the temperature evolution follows (from 6.18 and 6.19)

$$\frac{dT_e}{dt} = \left(\frac{\partial g}{\partial T_e}\right)^{-1} Q \tag{6.26}$$

(for a perfect electron gas, one has  $\frac{\partial g}{\partial T_e} = \frac{3}{2} \frac{N_e}{\rho}$ ). The heating (or cooling) rate of the free electrons is calculated as

$$Q = \frac{1}{M_{ion}} \sum_{i,j} f_i P_{ij} \Delta E_{ij}, \qquad (6.27)$$

where  $P_{ij}$  is the rate of process i - j in which the energy  $\Delta E_{ij}$  (positive or negative) given to the free electrons. Processes contributing to Q are electron collisional ionization and excitation, photoionization, Auger relaxation (and all inverse processes). In (6.27),  $M_{ion}$  is the ion mass while  $f_i$  is the fractional population of level i. We neglect free-free processes here.

In (6.27), the rates have a strong dependence on temperature. To solve (6.26), one expands Q about the current temperature as

$$Q(T_e^+) = Q(T_e^-) + \frac{\partial Q}{\partial T_e} (T_e^+ - T_e^-).$$
 (6.28)

Then, injecting (6.28) into (6.26) gives an equation for  $T_e^+$ ,

$$\frac{T_e^+ - T_e^-}{\Delta t} = \left(\frac{\partial g}{\partial T_e}\right)^{-1} \left[ Q(T_e^-) + \frac{\partial Q}{\partial T_e} (T_e^+ - T_e^-) \right]. \tag{6.29}$$

A crucial point here is the evolution of the derivative of the heating rate which depends on both the derivatives of the rates and on the derivatives of the population fractions. From (6.27) one gets

$$M_{ion} \frac{\partial Q}{\partial T_e} = \sum_{i,j} \frac{\partial P_{ij}}{\partial T_e} \Delta E_{ij} f_i + \sum_{i,j} P_{ij} \Delta E_{ij} \frac{\partial f_i}{\partial T_e}.$$
 (6.30)

Here again, one needs the derivatives of the rates with respect to  $T_e$  but also, the derivatives of the population set f. These quantities can be obtained by derivating system (6.16), i.e.  $\frac{\partial}{\partial T_e} \frac{d\mathbf{f}}{dt} = \frac{\partial}{\partial T_e} \mathbf{T} \cdot \mathbf{f}$  then the set  $\frac{\partial \mathbf{f}}{\partial T_e}$  evolves according to

$$\frac{d}{dt} \left( \frac{\partial \mathbf{f}}{\partial T_e} \right) = \mathbf{T} \cdot \left( \frac{\partial \mathbf{f}}{\partial T_e} \right) + \frac{\partial \mathbf{T}}{\partial T_e} \mathbf{f}. \tag{6.31}$$

With the initial condition  $\frac{\partial \mathbf{f}}{\partial T_e} = 0$ , this differential system for the  $\frac{\partial f_i}{\partial T_e}$  can be integrated in parallel with the system for the  $f_i$ , i.e.  $\frac{d\mathbf{f}}{dt} = \mathbf{T} \cdot \mathbf{f}$  for which the standard differencing reads

$$\frac{\mathbf{f}^{+} - \mathbf{f}^{-}}{\Lambda t} = \mathbf{T}(T_e^{-}).\mathbf{f}^{+}.$$
 (6.32)

At the end, i.e. after the obtention of  $T_e^+$ , a single iteration allows to update the electron density from a calculation of the average ionization.

This approach has the interest of being more implicit with respect to the heating (or the cooling). It is somewhat less demanding than the entire linearization procedure.

## 6.5.3 Energy Deposition

In many cases, the X-ray radiative intensity  $I_{\nu_o}$  in a material can described by its *corpuscular* character (i.e. in term of photons). Then, for instance in 1D planar geometry,  $I_{\nu_o}$  obeys the formal transfer equation

$$\cos\theta \frac{dI_{\nu_o}}{dz} = -k_{\nu_o}I_{\nu_o} \tag{6.33}$$

where  $\theta$  is the incidence angle with respect to the discretization axis z,  $hv_o$  is the energy of an incident XFEL photon while  $k_{v_o}$  is the local opacity at this photon energy. Equation (6.33) leads to the Beer-Lambert attenuation law

$$I_{\nu_o}(z,t) = I_{XFEL}(t) e^{-k_{\nu_o} z/\cos\theta}$$
(6.34)

 $I_{XFEL}(t)$  being the incident x-ray intensity.

If one neglects free-free absorption, the power deposited (per volume unit) by the X-rays reads locally,

$$P_{abs}(z,t) = h\nu_o \sum_{i,i'} N_i W_{ii'}(I_{\nu_o}(z,t)) + h\nu_o \sum_{i,i'} N_i Q_{ii'}(I_{\nu_o}(z,t))$$
(6.35)

where the sums run over all pairs of levels connected by processes involving XFEL photons. Consequently,  $W_{i\,i'}$  is either a photoionization rate or a stimulated recombination rate (depending on  $N_e$ ). Similarly,  $Q_{i\,i'}$  is either a photoexcitation rate or a stimulated emission rate. A formulation of these rates as a function of the respective cross sections or Einstein coefficients can be found in many textbooks (see for instance [46]) or, at different levels of approximation in the atomic structure, in articles (see for instance [6, 47] or [38]).

Neglecting free-free absorption means that incident photons have an energy greater than the first ionization threshold. The problem of the free-free absorption of UV or XUV radiation in cold or warm dense matter is beyond the scope of this text (for a recent discussion, see [48] or [49] and references therein).

In some situations, multilayer materials at low fluence (this is the case of X-ray optics for which a careful evaluation of damage thresholds is important), the intensity does not follow the Beer-Lambert law because of interference effects due to the wave-like nature of radiation. In that case, the deposited power must be obtained

from a calculation of the complex amplitude  $\tilde{\mathbf{E}}$  of the electric field ( $\mathbf{E} = \tilde{\mathbf{E}} e^{i\omega_o t}$ ) in the material, i.e. by solving the Helmoltz equation

$$\Delta \tilde{\mathbf{E}} + k_o^2 \tilde{n}^2 \tilde{\mathbf{E}} = 0 \tag{6.36}$$

where  $k_o = \hbar \omega_o / \hbar c$ .  $\tilde{n}$  is the complex refractive index which reads [50], at  $\omega_o$ ,

$$\tilde{n} = n_r - i \, n_i \tag{6.37}$$

with  $n_r = 1 - \frac{2\pi r_o c^2}{\omega_o^2} N_{ion} \, \phi_1(\omega_o)$  and  $n_i = \frac{2\pi r_o c^2}{\omega_o^2} N_{ion} \, \phi_2(\omega_o)$ .  $N_{ion}$  is the local atom density,  $r_o$  is the classical electron radius and, with  $b^{-1} = \pi h c r_o$ ,

$$\phi_1(\omega_o) = Z + b\hbar \int_0^\infty \frac{\omega^2 \mu(\omega) d\omega}{\omega_o^2 - \omega^2},\tag{6.38}$$

$$\phi_2(\omega_o) = \frac{\pi}{2} b \, \hbar \omega_o \, \mu(\omega_o). \tag{6.39}$$

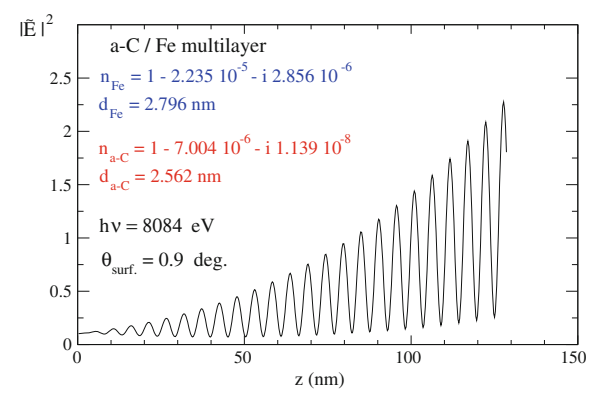
Z is the nuclear charge and  $\mu(\omega)$  is the local opacity per atom in the material. This quantity is likely to vary as it depends on the population kinetics. Note that through  $\mu(\omega)$ ,  $\phi_1$  is linked to  $\phi_2$  by the so-called Kramers-Kronig relation. Because of the (principal value) integral involving the spectral opacity in (6.38), the numerical cost of this approach may be important.

For fixed values of the complex refraction index of a (cold) multilayer, Fig. 6.7 illustrates the repartition of the radiative intensity at 8 keV and for a grazing incidence, inside the material.

Finally, the mean power (per volume unit) deposited locally reads (from the Joule-Lenz's law)

$$P_{abs} = n_r n_i \varepsilon_o \omega_o |\tilde{\mathbf{E}}|^2$$
.

Fig. 6.7 Squared electric field amplitude  $|\tilde{\mathbf{E}}|^2$  (normalized to the incident field  $|\tilde{\mathbf{E}}_o|^2$ ) in a cold multilayer made of 24 stacked bilayers of the type (amorphous-C/Fe). d corresponds to the *thickness* of a Fe layer and of an a-C layer, respectively. Radiation (at 8.084 keV) is from the *right* 



# 6.5.4 Modeling of Al, V and Ag Samples Irradiated in the X-UV or X-Ray Range

In this paragraph, we present a few significant examples of 1D hydrodynamics simulations of solid samples irradiated by an XFEL. In the last case (Ag), this fluid description has proven to be fully relevant by a direct comparison with measurements. These calculations include a CR modeling of the interaction with an x-ray laser according to the recipes discussed above. Other aspects of the corresponding hydro-code are discussed elsewhere [38].

Figure 6.8 displays the evolution of various macroscopic quantities in the interaction of a short (20 fs) and intense ( $10^{16}$  W/cm²) pulse of 92 eV photons with a bulk target of Al. These quantities are summed over all the cells and weighted by the corresponding surfacic masses  $m = \rho \Delta x$ . The thick solid curve is the total energy deposited by the x-ray laser, the thin solid line is the electron internal energy, dashed line is the ion internal energy, dotted line is the matter kinetic energy and long dashed line is the total radiated power. With the time evolution, one can follow how the XFEL radiation energy is deposited first on the electrons, which after some delay, transfer their energy to the ions. Then, as seen on the kinetic energy curve, the matter starts to move. Quickly along with the heating, some fraction of the energy is radiated by the resulting plasma. this radiation decreases one picosecond after the pulse has switched off.

Taking the previous conditions as an example of typical irradiation, it is instructive to see the importance of the 3-body recombination process on the heating. For this purpose, we artificially modified 3-body recombination by multiplying the corresponding rates by a reduction factor in the rate-equation system (for each cell of the hydro-simulation). Results are displayed in Fig. 6.9 on a snaphot of the electron temperature profile, for an instant close to the heating maximum. Upper curve is the normal calculation, i.e. without modifying the 3-body recombination rates. One clearly sees how the heating is affected by 3-body recombination. Here, the reason

Fig. 6.8 Total power deposited (erg/cm<sup>2</sup>/s) deposited by an XFEL  $(10^{16}\text{W/cm}^2\text{ intensity}, 20\text{ fs}$  FWHM, 92 eV photon energy), total ion internal energy (erg/cm<sup>2</sup>), total matter kinetic energy (erg/cm<sup>2</sup>) and total radiated power  $P_{rad}$  (erg/cm<sup>2</sup>/s). To display all quantities in the same figure, a multiplier has been applied to  $P_{xfel}$  and  $P_{rad}$  (from [38])

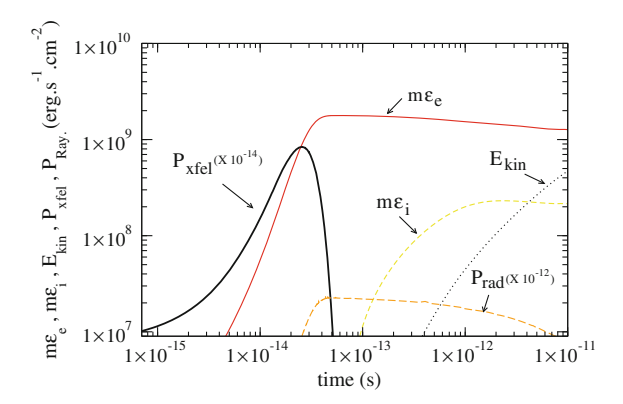
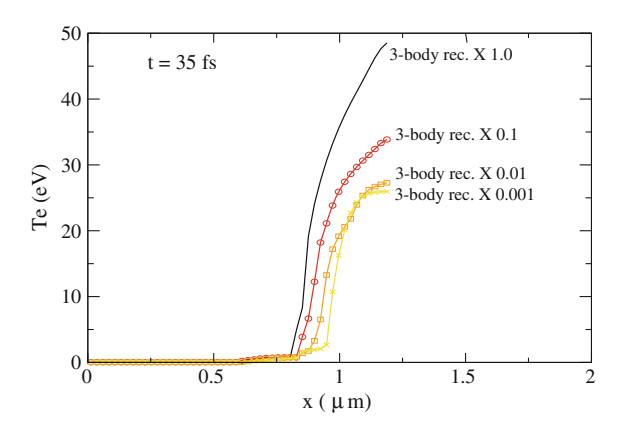


Fig. 6.9 Influence of the 3-body recombination process on the heating. Calculated spatial profiles of  $T_e$  in a bulk target of Al for an instant close to the heating maximum (radiation comes from the right). Irradiation conditions of Fig. 6.8. The profiles correspond to four different calculations where all the 3-body recombination rates have been multiplied by the reduction factors reported in the figure (from [38])



is that, during the X-ray pulse itself, this process provides continuously a population flux of recombined  $1s^22s^22p^6$  states from which further photon absorption can occur.

We discuss now the hydrodynamic behavior of a selected case, namely, a simulation performed for a  $2 \times 10^{17} \,\mathrm{W/cm^2}$ , 15 fs pulse of 92 eV photons, incident on bulk vanadium. In Fig. 6.10, the characteristic profiles of  $\rho$ ,  $T_e$ ,  $T_i$  and  $\langle Z \rangle$  are given for two particular instants. At the instant of maximum heating (left),  $T_e$  goes up to 160 eV while the ions are still cold. As shown in Fig. 6.10 (right), the out-flowing plasma results in an inward motion of deeper layers and, after a few picoseconds, the compression increases so that a strong shock develops in the solid. Such shock waves which result from an impulsive load (here the expanding material) are discussed in the book of Zel'dovich and Raizer [51]. Here, the shock is strong enough to induce a significant decoupling between  $T_i$  and  $T_e$  in the shock front. Again, it is important to keep in mind the chemical picture of the underlying CR model which must be able to follow the matter from the solid state to the plasma state. Like aluminium, cold vanadium is a metal which can be considered as a degenerated plasma whose ionization corresponds to the number of electrons in the valence band (although the shape of the density-of-state is somewhat less simple than for aluminum). We assumed for vanadium two valence electrons so that the initial ionization is 2.

Finally, one presents experimental measurements showing that the previously discussed description of dense matter irradiated by an XFEL, i.e. by means of an adequate CR model coupled with hydrodyanmics, is satisfactory. In these experiments, Thin silver foils of about  $0.5-1\,\mu m$  were heated by hard x-rays pulses of 60 fs duration, 8.9 keV of photon energy and intensities of about  $5\times10^{15}$  W/cm². In these conditions, X-ray photoionization of the Ag L-shell is the main interaction channel while the creation of a heated population of free electrons results from competing processes including Auger and radiative decay (fluorescence), collisional ionization/recombination. Measurements were of two types: one which deals with the hydrodynamics behavior by measuring the expansion of the foil, the other which is a recording of the fluorescence spectrum emitted by the plasma and resulting mostly from inner-shell photoionization. The former is based on the phase and amplitude

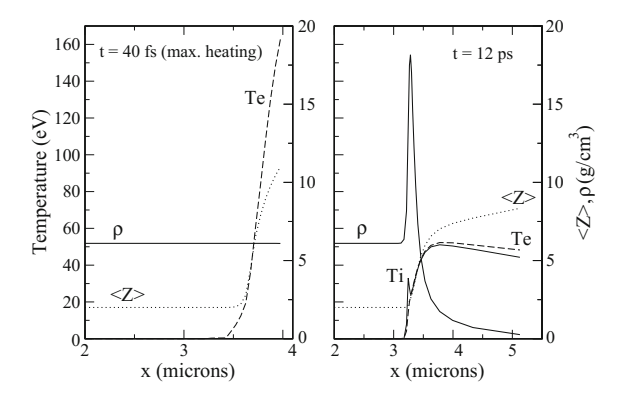
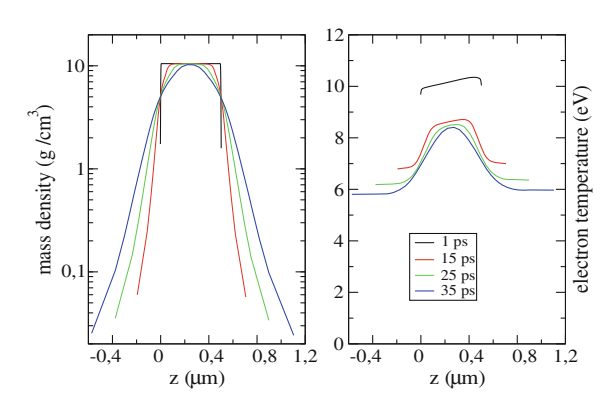


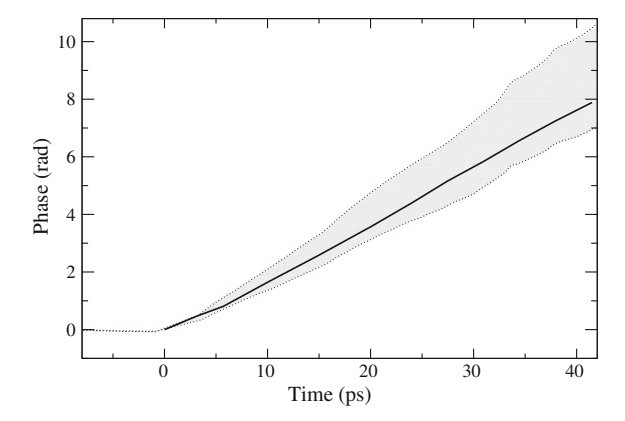
Fig. 6.10 Spatial dependence of the electron temperature  $(T_e)$ , the ion temperature  $(T_i)$ , the density  $(\rho)$  and the average ionization (< Z >) for two instants: t = 40 fs  $(left\ figure)$ —t = 12 ps  $(right\ figure)$ . The temperatures refer to the right axis while the densities and < Z > refer to the left axis. The simulation corresponds to a pulse duration of 15 fs (FWHM), with 92 eV photons and an intensity of  $2 \times 10^{17} \mathrm{W/cm^2}$ , incident from the right on a vanadium target

Fig. 6.11 Mass density (*left*) and electron temperature (*right*) spatial profiles at 1, 15, 25 and 35 ps after XFEL pulse irradiation  $(5.7 \times 10^{15} \text{W/cm}^2, 60 \text{ fs}, 8.9 \text{ keV photons})$  of a 0.5  $\mu$ m thick silver foil (from [37])



analysis of infrared beams (IR-probes) reflected from the sample surface (Fourier Domain Interferometry or FDI), as a function of time (see [37] for more details). The latter is X-ray emission spectroscopy in the range 2.8–3.5 keV [52].

In the present conditions (incident photons of 8.9 keV and weakly ionized Ag), the interaction and the subsequent evolution were described with a CR model including about 3800 configurations (just in the first ionization stages of Ag). Macroscopic behavior of the heated matter is calculated by solving hydrodynamics in one-dimensional geometry together with XFEL energy deposition, transport by thermal conduction and electron-ion energy exchange (again, see [38] for more details). Figure 6.11 shows the calculated density and electron temperature spatial profiles resulting from a simulation (XFEL is incoming from the right). One sees that the sample center stays near solid density during the first tens of picoseconds. The longitudinal heating (~10eV) is predicted to vary only by 10% between the



**Fig. 6.12** Comparison of the calculated phase temporal evolutions of the IR-probe with measurements, of the back surface of an Ag foil irradiated by an XFEL. The experimental error on the phase is illustrated by the *light gray* area. Calculation is the *thick black line* (from [37])

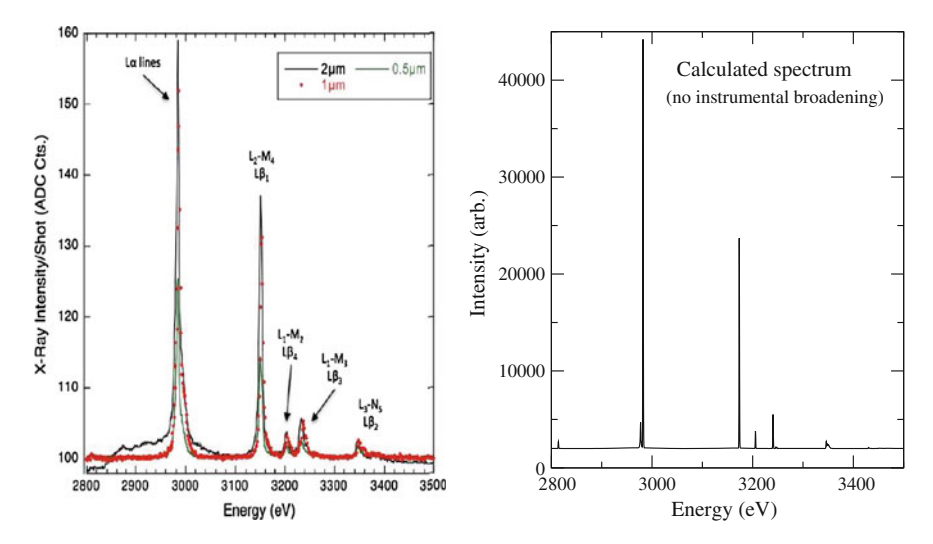


**Fig. 6.13** *Left* Silver L-shell spectra recorded for three foil thicknesses (from [52])—Emerging fluorescence Ag spectrum calculated using the Spin-Orbit Split arrays formalism in the conditions of Fig. 6.11

front and the rear surface. This shows that during about a few picoseconds, XFEL pulses can induce rather uniform longitudinal heating of a solid density sample. Figure 6.12 shows a comparison between the temporal evolution of the phase as measured by the FDI diagnostic and calculated from hydro-simulations. The good agreement obtained here gives a good confidence in the previous description of XFEL interaction and of its subsequent evolution. The second source of confidence in the modeling is provided by analyzing the fluorescence spectrum. Figure 6.13 displays

experimental spectra recorded in the experiments for different foil thicknesses (left). The lines are properly identified. The right figure shows a calculated spectrum of the radiation emerging from the foil at an instant close to the maximum heating in the simulations of Fig. 6.11. Working with configurations, we found that the Spin-Orbit Split Arrays (SOSA) formalism reproduces well the experimental spectrum. Also, since the fluorescence (which is very short) is well reproduced, one can infers a correct calculation of the XFEL absorption in the material.

### 6.6 Conclusion

We have described how CR models inserts in the description of the interaction of monochromatic x-rays with matter. Depending on the size, the density and the structure of the sample, the implementation of a CR model (always based on a chemical picture of matter) is necessarily specific. Mostly based on a Detailed Configuration Accounting or even on a Superconfiguration Accounting approach, this modeling remains challenging and relies on advanced methods of atomic physics in plasmas.

**Acknowledgments** I am grateful to Basil Deschaud who drew my attention to errors and made suggestions for improvements.

#### References

- 1. J.P. Marangos et al., Contemp. Phys. **52**, 551 (2011)
- 2. B. Nagler et al., Nat. Phys. **5**, 693 (2009)
- 3. H. Yoneda et al., Nat. Commun. 5, 5080 (2014)
- 4. G. Doumy et al., Phys. Rev. Lett. 106, 083002 (2011)
- 5. K. Tamasaku et al., Nat. Photonics **8**, 313 (2014)
- 6. H.-K. Chung et al., High Energy Density Phys. 1, 3 (2005)
- 7. O. Peyrusse, J. Phys. B At. Mol. Phys. **32**, 683 (1999)
- 8. J. Bauche et al., Adv. At. Mol. Phys. 23, 131 (1987)
- 9. C. Bauche-Arnoult et al., Phys. Rev. A 31, 2248 (1985)
- 10. L. Young et al., Nature 466, 56 (2010)
- 11. O. Ciricosta et al., High Energy Density Phys. 7, 111 (2011)
- 12. N. Rohringer et al., Nature **481**, 488 (2012)
- 13. B. Rudek, D. Rolles, S.-K. Son et al., Phys. Rev. A **87**, 023413 (2013)
- 14. B. Rudek, S.-K. Son, D. Rolles et al., Nat. Photonics **6**, 858 (2012)
- 15. H. Fukuzawa et al., Phys. Rev. Lett. **110**, 173005 (2013)
- 16. O. Peyrusse, J. Phys. B At. Mol. Phys. 33, 4303 (2000)
- 17. O. Peyrusse, B. Deschaud, D. Rolles, J. Phys. B At. Mol. Phys. 47, 011001 (2014)
- 18. A.B. Bortz, M.H. Kalos, J.L. Lebowitz, J. Comput. Phys. 17, 10 (1975)
- 19. D.T. Gillepsie, J. Comput. Phys. 22, 403 (1975)
- 20. J. Albritton, in Laser Program Annual Report 84 (LLNL) UCRL-50021-84 (1985)
- 21. S.-K. Son, R. Santra, Phys. Rev. A 85, 063415 (2012)
- 22. P.J. Ho et al., Phys. Rev. Lett. 113, 253001 (2014)
- 23. M. Abramowitz, I.A. Stegun, Handbook of Mathematical Functions (Dover, New York, 1965)

- 24. K.J. Gaffney, H.N. Chapman, Science **316**, 1444 (2007)
- 25. H.N. Chapman et al., Nat. Phys. 2, 839 (2006)
- 26. M.M. Seibert et al., Nature 470, 78 (2011)
- 27. M. Bergh et al., Quaterly Rev. Biophys. 41, 181 (2008)
- 28. H.M. Quiney, K.A. Nugent, Nat. Phys. 7, 142 (2011)
- S. Boutet et al., Science 337, 362 (2012)
   H.N. Chapman et al., Philos, Trans. R. Soc. B 369, 20130313 (2013)
- 31. R. Neutze et al., Nature **406**, 752 (2000)
- 32. S.P. Hau-Riege et al., Phys. Rev. E 69, 051906 (2004)
- 33. S.P. Hau-Riege et al., Phys. Rev. E 71, 061919 (2005)
- 34. U. Lorentz et al., Phys. Rev. E 86, 051911 (2012)
- 35. M. Stömer et al., in *Proceedings of SPIE*, vol. 8078, id. 80780G (2011)
- 36. N. Medvedev, H.O. Jeschke, B. Ziaja, New J. Phys. 15, 015016 (2013)
- 37. A. Lévy et al., Phys. of Plasmas (2015)
- 38. O. Peyrusse, Phys. Rev. E 86, 036403 (2012)
- 39. M. Bergh et al., Phys. Rev. E **70**, 051904 (2004)
- 40. B. Deschaud, O. Peyrusse, F.B. Rosmej, Europhys. Lett. 108, 53001 (2014)
- 41. S.M. Vinko et al., Nature 482, 59 (2012)
- 42. O. Ciricosta et al., Phys. Rev. Lett. **109**, 065002 (2012)
- 43. F.B. Rosmej, Europhys. Lett. 76, 1081 (2006)
- 44. H.A. Scott, R.W. Mayle, Appl. Phys. B 58, 35 (1994)
- 45. W.H. Press et al., Numerical Recipes (Cambridge University Press, Cambridge, 1992)
- H.R. Griem, Principles of Plasma Spectroscopy (Cambridge University Press, Cambridge, 1997)
- 47. R. Florido et al., Phys. Rev. E 80, 056402 (2009)
- 48. S.M. Vinko et al., High Energy Density Phys. 5, 124 (2009)
- 49. C.A. Iglesias, High Energy Density Phys. 6, 311 (2010)
- 50. B.L. Henke, E.M. Gullikson, J.C. Davis, At. Data Nucl. Data Tables 54, 181 (1993)
- 51. Y.B. Zel'dovich, Y.P. Raizer, *Physics of Shock Waves and High-Temperature Hydrodynamic Phenomena* (Academic Press, New York, 1967)
- 52. J. Dunn et al., in *Proceedings of SPIE*, vol. 8140, id. 81400O (2011)

# Chapter 7 Spectral Modeling in Astrophysics—The Physics of Non-equilibrium Clouds

G.J. Ferland and R.J.R. Williams

**Abstract** Collisional-radiative spectral modeling plays a central role in astrophysics, probing phenomena ranging from the chemical evolution of the Universe to the energy production near supermassive black holes in distant quasars. The observed emission lines form in non-equilibrium clouds that have very low densities by laboratory standards, and are powered by energy sources which themselves are not in equilibrium. The spectrum is the result of a large number of microphysical processes, thermal statistics often do not apply, and analytical theory cannot be used. Numerical simulations are used to understand the physical state and the resulting spectrum. The greatest distinction between astrophysical modeling and conventional plasma simulations lies in the range of phenomena that must be considered. A single astronomical object will often have gas with kinetic temperatures of  $T \sim 10^6$ ,  $10^4$ , and  $T < 10^3$  K, with the physical state ranging from molecular to fully ionized, and emitting over all wavelengths between the radio and x-ray. Besides atomic, plasma, and chemical physics, condensed matter physics is important because of the presence of small solid "grains" which affect the gas through catalytic reactions and the infrared emission they produce. The ionization, level populations, chemistry, and grain properties must be determined self-consistently, along with the radiation transport, to predict the observed spectrum. Although the challenge is great, so are the rewards. Numerical spectral simulations allow us to read the message contained in the spectrum emitted by objects far from the Earth that existed long ago.

G.J. Ferland (⋈)

University of Kentucky, Lexington, KY 40506, USA e-mail: Gary.J.Ferland@uky.edu

G.J. Ferland

School of Mathematics and Physics, Queen's University Belfast, Belfast BT7 1NN, Northern Ireland, UK

R.J.R. Williams

AWE Plc, Aldermaston, Reading RG7 4PR, UK e-mail: robin.williams@awe.co.uk

#### 7.1 Introduction

There is a long history of observations of "nebulae", astronomical objects that are resolved on the sky, dating back to Ptolemy in around AD 150. Messier's catalogue in the 18th century listed over 100 nebulae and star clusters. Only when spectroscopy became possible in the very early 20th century was it found that some nebulae, today known as "galaxies", were themselves far more distant and populous star clusters than those previously identified, while the others had emission-line spectra. The Orion Nebula, Fig. 7.1, was the first of these emission-line nebulae to be discovered, in 1610 [1]. As so often in astronomy, this discovery was the result of an emergent technology, the development of the telescope.

Once spectra were available, it was soon realized that the emission-line objects consisted of diffuse gas with very low density, high vacuum by terrestrial standards, and were powered either by photoionization from a central star (the majority), or by passing shock waves. It was further realized that the conditions in these emission-line nebulae were far different from laboratory conditions, due to the low density and the fact that they are powered by a set of disequilibrium processes. Menzel collected the early papers into two books [2, 3] which are good introductions to the subject.

Most of the quantitative information we have about the cosmos comes from spectroscopy. Emission-line spectra are often used to measure the abundances of the elements, or to derive the kinetic temperature, gas density, or mass, of emitting regions. Such investigations are a foundation for understanding how nuclear processes in stars created the elements which make up the Earth, or how exotic objects such as super-



**Fig. 7.1** The *left panel* shows the optical image of the Orion Nebula. The Trapezium stars in the center power it. The *right panel* an IR image of the same region. The "BN-KL Object", the bright objects in the *upper right*, are not visible in the optical due to dust extinction. The *left panel* image from NASA, ESA, M. Robberto (STScI/ESA) and the Hubble Space Telescope Treasury Project Team. The *right* image is from the European Southern Observatory/M. McCaughrean

novae and quasars generate energy. Graduate texts which survey this field include [4–7]. The line-of-sight motion of emitting material may also be determined from the Doppler shift of the line emission. Slit spectroscopy and, more recently, integral field spectroscopy may be used to map the kinematics across spatially-resolved sources.

Astrophysics is by its nature an observational, not experimental, science. Because of this, the astronomical community has long used numerical simulations as a touchstone in understanding spectra. Osterbrock reviews the early history of theoretical understanding of nebulae, including the first numerical models, in [8].

This Chapter reviews our current understanding of the low-density emission-line regions we encounter in astrophysics, with an emphasis on numerical simulations of photoionized clouds. Remington et al. [9] presents a similar review with an emphasis on higher densities and their counterparts in the lab while [10] goes into quantitative spectroscopy of nebulae. This Chapter stresses the differences between the astronomical and laboratory problems. Two striking differences are that astrophysical plasmas are hydrogen rich, apart from a few special cases (Wolf-Rayet stars and nebulae, some supernova ejecta) and they have very low density, dilute radiation field, and long path lengths.

Much of this Chapter was influenced by our development of the plasma simulation code CLOUDY, last reviewed by [11], a publicly available spectral simulation code that is often applied to these problems.

# 7.2 Working with Real Nebulae: The Observational Questions We Are Trying to Answer

The underlying physics in most emission-line nebulae is similar, and is outlined in this section. It helps to have an example, and we use the Orion Nebula, a very familiar line-emitting region which can be seen with the naked eye. O'Dell [12, 13] give an overview of Orion and its physics. The left panel of Fig. 7.1 shows the Orion Nebula as viewed with visible light. The glowing gas is a photoionized layer on the surface of a relatively dense, cold cloud of molecular material. The gas is photoionized by the newly-born hot stars visible in the center of the left panel. An important component of the optical line emission is the Balmer spectrum, which is the origin of the astronomical name for the Orion Nebula, and other similar sources: "H II regions."

The hot stars which produce the ionized layer are very short lived in cosmic terms, generally with lifetimes less than a million years. H II regions are important because they trace both star formation, due to their short lives, and the creation of elements heavier than He by generations of stars as they form, evolve, and die, by analysis of the nebular emission lines.

H II regions are but one example of emission-line nebulae. Many stars are also bright in the ultraviolet spectrum towards the end of their lifetimes, resulting in other types of nebula. End products of stellar evolution such as the planetary nebulae

around the white dwarf embers left behind by stars with masses similar to our Sun, and the supernovae generated by far more massive stars, allow us to directly observe the elements produced by nuclear processes inside stars. Dying stars ejects enriched material into the surrounding interstellar medium, which can be used in later generations of star formation. The atoms that make up the Earth, and its residents, have been through the cycle of stellar birth, life, and death several times.

Quasars, members of the class of Active Galactic Nuclei (AGN) [6], occur as part of a brief phase during galaxy formation, and are the brightest objects in the Universe. Their strong emission lines are believed to be produced by debris near accreting supermassive ( $M \sim 10^8 - 10^9 \, \rm M_{sun}$ ) black holes. Although astronomers cannot do an experiment, we do have one big advantage over laboratory physics: we have a time machine. Very luminous objects can be observed at great distances from the Earth. Due to the finite speed of light, we see distant objects as they were when the light was produced. The brightest quasars can be observed at very large distances corresponding to look-back times within a Gyr of the creation of the Universe, 13.8 Gyr ago. The spectrum allows us to trace both the formation of galaxies and the expansion of the Universe, over look-back times approaching 13 Gyr.

Photoionization of relatively low density gas, the emphasis of this chapter, produces the emission lines in all of these astronomical objects. The energy source is a star, neutron star, white dwarf, or black hole. They generate energy by nuclear, gravitational, or other processes, which is radiated as a broad-band continuum. This emission has a shape, or spectral energy distribution (SED), that may be something like a blackbody, but more generally is non-thermal, that is, could not be described by a Planck function.

Typical SEDs of two types of quasars are shown in Fig. 7.2. The brighter portions in the UV/optical are mainly produced by hotter regions of an accretion disk surrounding the supermassive black hole that forms in the center of massive galaxies. Different parts of the SED originate in different regions in the quasar, so the observed SED is a result of a variety of phenomena that occur in different locations and by different processes.

A significant fraction of the energy in the SED shown in Fig. 7.2 is at hydrogenionizing energies,  $h\nu \geq 13.6\,\mathrm{eV} \approx 1\,\mathrm{Ryd}$ , corresponding to wavelengths  $\lambda \leq 911.6\,\mathrm{\mathring{A}}$ . This energy/wavelength is pivotal in astrophysics because hydrogen is by far the most common element, comprising some 90% of nuclei by number. Helium makes up most of the remaining 10%, with elements heavier than helium amounting to something like 1000 ppm. Because of the large abundance of hydrogen, its ionization potential is a useful reference energy. It also presents a problem—if significant column densities of atomic hydrogen are present,  $M(H) \geq 10^{18}\,\mathrm{cm}^{-2}$ , the  $\mathrm{H}^0$  photoelectric opacity will make it impossible to observe shorter wavelengths.

The "primary mechanism", so-called in the original literature, is the process by which the SED is converted into an emission-line spectrum. This is illustrated in the right side of Fig. 7.2. Ionizing photons strike nearby gas and will ionize it, following absorption of the photon by an atom. The resulting photoelectron has residual kinetic energy  $h\nu$  – IP, where the incident photon energy and ionization potential of the atom are used, and this kinetic energy is shared with surrounding electrons. Electrons

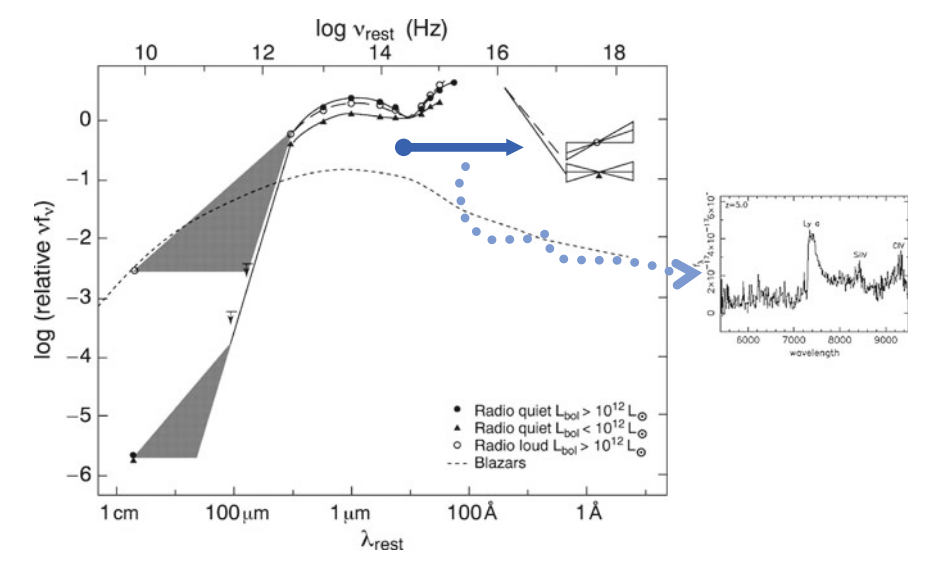


**Fig. 7.2** The "primary mechanism" energizing photoionized nebulae, illustrated for the case of gas near the *black hole* in an AGN. The *black lines* indicate the observed SED for two classes of active galaxies, radio loud (those with strong synchrotron radio emission) and radio quiet. Hydrogenionizing energies are to the *right* of the *left* edge of the *horizontal blue line*. The SED over this line can photoionize and heat (by the photoelectric effect) surrounding clouds, and is reprocessed into the emission line spectrum shown at the *right*. Adapted from [6]

undergo inelastic collisions with atoms of the heavier elements, resulting in internal excitation and line emission. Eventually the electron recombines with an ion and produces emission lines as it cascades from level to level, finally reaching the ground state.

The insert to the right of Fig. 7.2 is part of the vacuum UV spectrum of a distant quasar which has been Doppler shifted into the optical by the expansion of the Universe. Ionizing photons produced by the accretion disk are absorbed by nearby clouds and converted into this spectrum following photoionization and photoelectric heating. The photons in the spectrum last interacted with matter in a newly forming galaxy and were produced when the universe was under two billion years old.

The emphasis of this Chapter is on photoionized environments such as an H II region or quasar. But there are other cases in which mechanical energy, perhaps produced by winds or passing shocks, deposit energy and ionize the gas. Some examples include jets from young stars, magnetohydrodynamic (MHD) waves and magnetic reconnection, the late phases of supernovae when the ejecta encounters surrounding stationary gas, and the background flux of extremely high-energy particles known as cosmic rays. Although the fundamental energy source is different, the recombination and emission physics described below is very similar.

Figure 7.3 shows the UV/optical spectrum of central regions of the Orion Nebula (Fig. 7.1). Our goal is to use this spectrum to measure the chemical composition of the

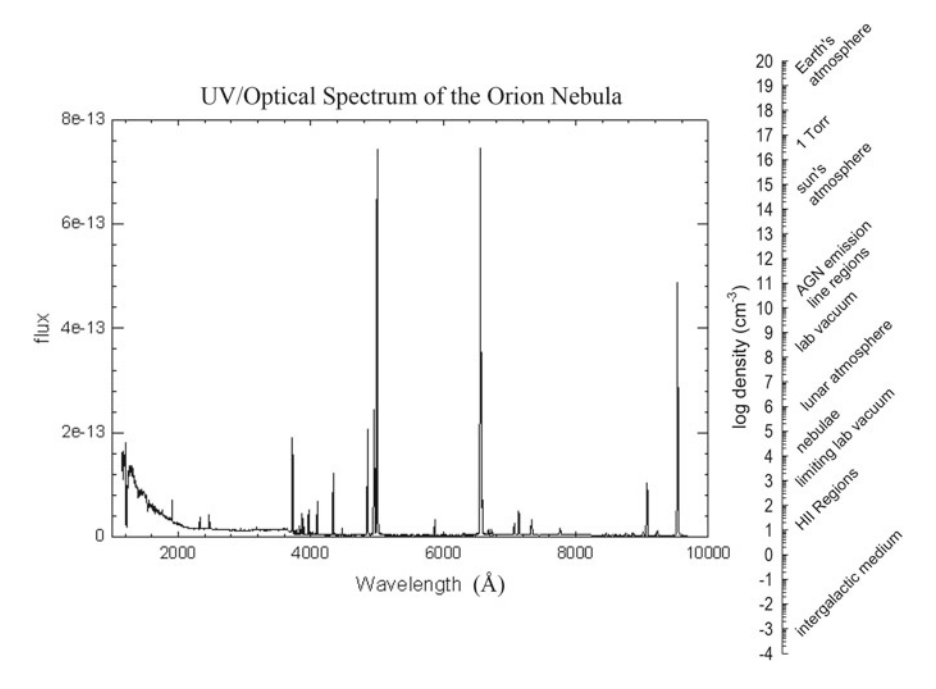


Fig. 7.3 The *left panel* shows the optical/UV spectrum of the Orion Nebula. The *right panel* shows the range of densities encountered in astronomical and lab environments. Adapted from [6]

gas, its density, temperature, pressure, and kinematic state. The essential difficulty is that the gas is so far from thermodynamic equilibrium that it makes little sense to compare its physical state with LTE quantities.

The extreme NLTE state of the gas is the result of its low density, and exposure to a wide range of energy sources. The right side of Fig. 7.3 shows a density scale with various terrestrial and astronomical environments shown. The Earth's atmosphere is the highest density plotted, and a typical laboratory vacuum is roughly in the middle. The emitting gas in quasars is a bit denser than a typical lab vacuum, while H II regions correspond to a very hard terrestrial vacuum. The result is that collisions between particles in the gas occur very slowly, a few collisions per month in some cases. In essence, the gas is not well coupled to itself.

The gas is pushed into extreme NLTE because of the many different energy sources which energize it. These include the central stars in the case of the Orion Nebula. They have a "color" temperature, given by roughly fitting the stellar SED with a Planck Function, of  $\sim 4 \times 10^4$  K, but the radiation field is geometrically diluted, as the near-thermal stellar sources occupy only a small fraction of the volume, so that it has an energy density temperature of  $\sim 50$  K. At the same time the gas is exposed to the Cosmic Microwave Background (in strict thermodynamic equilibrium, STE) with  $T \sim 2.7$  K, cosmic rays, with kinetic energies of MeV–TeV but an energy-density temperature of  $\sim 1$  eV, and other background light sources produced both within

our galaxy and by distant quasars. Because of the wide variety of dissimilar energy sources, and the low density, the physical state of the gas in Fig. 7.1 is the result of complex microphysical processes which cannot be handled by analytical theory. The message carried by the spectrum shown in Fig. 7.1 is best read by reference to complete numerical simulations of physical processes with the gas.

Other complexities are introduced by the fact that we can only observe and not experiment. Figure 7.1 compares optical (left) and infrared (right) images of the Orion Nebula. This shows the selection effects inherent in astronomical observations. The four bright stars in the center, the Trapezium, power the surrounding emission in the left image by photoionization, as described above. The infrared image on the right shows the nebula and the Trapezium, but also the "BN-KL" object, the bright emission above and to the right of the Trapezium. BN-KL is not seen with visible light due to extinction by "dust grains" mixed with the gas. These grains are small solid particles formed from heavy elements, and have sizes typically a micron or smaller, through the processes by which they form are not yet well understood. Dust particles affect conditions in the gas by acting as catalysis sites for various reactions. They heat the gas by electron photoejection following absorption of UV starlight.

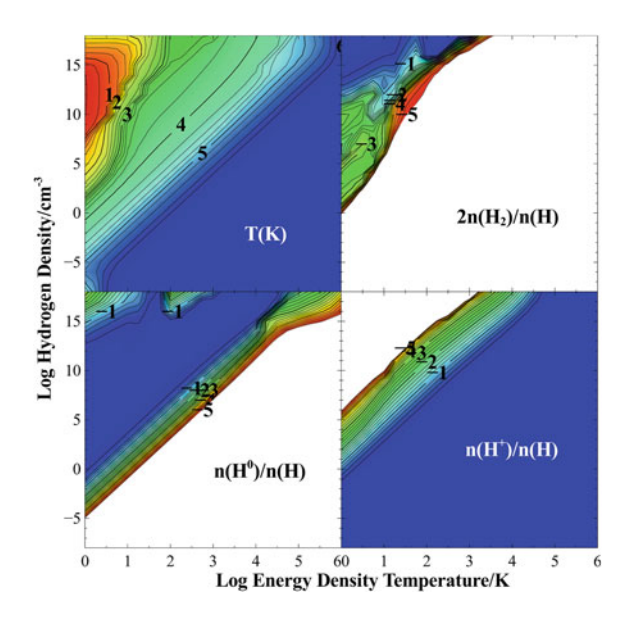
The BN-KL object generates its great luminosity by depositing mechanical energy from stellar winds rather than by nuclear processes. The stars within BN-KL are still in very early stages of formation. Fast stellar winds occur as gravity brings the star together and the kinetic energy of the wind is converted into heat when it strikes surrounding gas. The bright 'fan' in the upper right is emission from shocked  $H_2$ .

So to understand Fig. 7.1, we must consider not only plasma physics, but also condensed matter physics and chemistry. Besides mixing a variety of disciplines, astronomical environments present a very wide range of temperature and density. Consider Fig. 7.1 once again. The glowing gas in the left panel has a kinetic temperature of  $\sim 10^4$  K, i.e.  $\sim 1$  eV. The gas in the "fan" shown in the right panel has a kinetic temperature of  $\sim 10^3$  K. Images in the x-ray band reveal hot,  $\sim 10^6$  K, gas produced by shocks created by winds from the Trapezium stars. We need to develop tools to predict spectra of all of these regions.

We close this section by illustrating the results of photoionization model calculations which span the required range of physical conditions. The gas properties, that is, whether it is molecular, atomic, or ionized, and the internal level populations of its constituents, are basically set by the gas density and SED and intensity of the light striking it. The right side of Fig. 7.3 shows the densities of common emission line regions together with terrestrial and laboratory sources. The density range we must consider is approximately  $10^{-10} \, \mathrm{cm}^{-3} \le n(\mathrm{H}) \le 10^{20} \, \mathrm{cm}^{-3}$ . The low density is below that of the intergalactic medium (IGM) while the upper density is typical of the atmospheres of some stars or accretion disks.

We must be prepared to consider kinetic temperatures over a broad range. The high-T end is set by the requirement that some electrons are bound to nuclei to emit lines, which sets the limit  $T \le 10^8$  K, although in CLOUDY we treat temperatures as high as  $10^{10}$  K, the temperature above which processes such as pair production act to prevent the electron temperature from increasing [14], so that the electron and ion temperatures may decouple. The low end of the range is 2.7 K, the temperature of the

Fig. 7.4 The physical properties of gas with solar composition is shown across a wide range of gas density and radiation field intensity. The upper left panel shows the log of the kinetic temperature as a function of gas density (the vertical axis) and the energy density of the radiation field (the horizontal axis). The other three panels show logs of the hydrogen molecular fraction,  $2n(H_2)/n(H)$ , and atomic and ion fraction. Adapted from [11]



cosmic microwave background at the current epoch. As this is close to a blackbody field, gas cannot reach a lower temperature in equilibrium.

To investigate the effects of the light intensity we take as an SED a blackbody with a color temperature of  $T_{color} = 10^6$  K and vary its energy-density temperature  $T_u = (u/a)^{1/4}$  K. Here u is the total energy density in all wavelengths [erg cm<sup>-3</sup>] and a is the Stefan radiation-density constant.

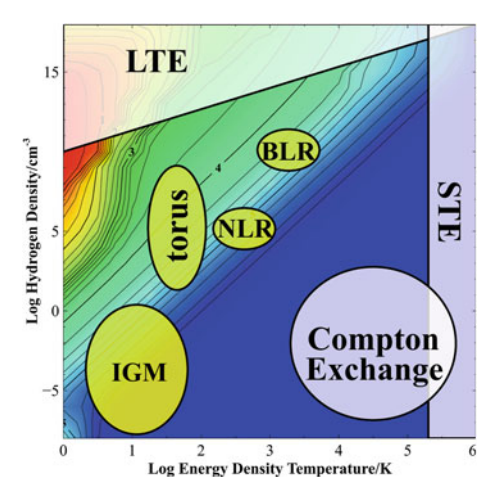
Figure 7.4 shows predicted properties of gas over the range of density and temperature encountered in different astronomical environments. The gas has solar composition and  $T_u$ , the independent axis, varies between 1 and  $10^6$  K. The latter corresponds to a radiation field in STE since the energy density and color temperatures are equal. Most clouds encountered in astrophysics have a gas and energy density that lies somewhere in Fig. 7.4.

The upper left panel of Fig. 7.4 shows the predicted gas kinetic temperature. This ranges from low values typical of cold molecular gas in the upper left-hand low- $T_u$ —high-n(H) corner of the figure, to high values in the high- $T_u$ —low-n(H) lower right end. The gas temperature closely approaches the color temperature  $T_{color}$  when  $T_u \equiv T_{color}$ , as it must from thermodynamics. The right edge of the figure corresponds to a radiation field in STE since  $T_u \equiv T_{color}$ . There is no physical lower bound to the gas kinetic temperature.

The remaining panels of Fig. 7.4 show the physical state of hydrogen. The gas is highly ionized in the high- $T_u$ —low-n(H) quadrant. The gas becomes first atomic then molecular as the radiation field grows fainter and the gas denser.

Figure 7.5 is an annotated version of Fig. 7.4 summarizing some physical limits. Gas in the high-density region of the figure will be in local thermodynamic equilibrium, LTE, where the level populations are in Boltzmann equilibrium, but not with the

Fig. 7.5 This panel identifies some physical and thermodynamic limits in white and shows where some regions in AGN are located in yellow, for the calculations shown in Fig. 7.4. A wide range of densities, and various energy-density temperatures of the 10<sup>6</sup> K blackbody, are shown. Adapted from [11]



radiation field. The gas is in STE when the ionization, level populations, and radiation field are given by the same temperature. This occurs at the right edge of Fig. 7.5, where  $T_u \equiv T_{color}$ . The temperature in the lower-right quadrant is determined by Compton electron-photon energy exchange.

Figure 7.5 also shows where some of the emission-line regions of AGN are located, as a 10<sup>6</sup> K black body is comparable to the main ionizing spectrum for these objects. The broad-lined region (BLR) is likely to be the skin of an accretion disk near the supermassive black hole. Line emission from material at temperatures  $\sim 10^4$  K, and is characterized by resonance line emission, is observed with line widths of 500- $30,000 \,\mathrm{km} \,\mathrm{s}^{-1}$ . It is believed that this relatively cool material may be surrounded by more diffuse material close to Compton equilibrium, at a temperature of  $\sim 10^7$  K. The narrow-lined region (NLR) may be molecular clouds further out in the host galaxy, irradiated by the radiation field of the AGN. Line widths, as suggested by the name, are smaller than for the BLR but still significantly greater than the thermal width, up to  $1000 \,\mathrm{km} \,\mathrm{s}^{-1}$ ; emission in forbidden lines such as [OIII] 4959, 5007. The molecular torus, is dusty warm molecular gas that exists outside the accretion disk, but inside the NLR: the radiation field in this material is reduced by intervening obscuration. The inter-galactic medium (IGM) is lower gas density which exists in the space between galaxies. This is illuminated by the weak Cosmic background radiation field: the ionizing component of this, at least in the early universe, was dominated by the population of AGN.

Figures 7.4 and 7.5 show that many diverse phenomena are simply manifestations of different regimes of atomic and molecular physics. This is the approach we take in our modeling. If the microphysics is done at an elementary level, without compromise, the macrophysics will follow.

We developed CLOUDY to model environments like those discussed above. Perhaps the greatest distinction between CLOUDY and traditional CR modeling codes is the cross-disciplinary and pan-spectral nature of astronomy. We solve for the ion-

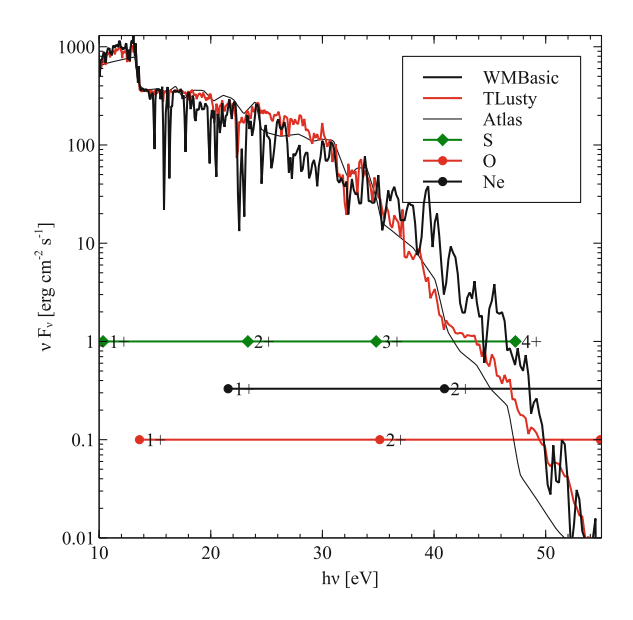
ization and level populations, as is typical for any CR code. For an astrophysical plasma, this problem must be solved for a mixture of different species, where the electron density depends on the ionization of each of them. We also determine the chemical state and molecular emission, and temperature, charge, and drift velocities of the dust particles. We do this for gas that is so cold that it is fully molecular or so hot that there are no bound electrons We discuss all of these in our last review of CLOUDY, [11]. In the remaining parts of this chapter, we focus on the ionization and level populations.

## 7.3 Approaches to Astronomical Spectral Modelling

This section outlines how a model of an astronomical object is created. To continue with our example of Orion, the basic problem is to take the spectrum shown in Fig. 7.3 and use it to understand what is happening in Fig. 7.1. The spectrum depends on a range of detailed microphysics. This means that it is a complex problem to model the spectrum, but also why the spectrum contains such a wealth of information about the kinematic and thermal state of the emitting gas and its composition. We proceed by setting a number of boundary conditions and then do a self-consistent simulation of the cloud.

The radiation field of the Trapezium stars is the basic driver. Spectroscopists have determined parameters of these stars, such as the effective temperature, luminosity, and surface gravity, which can be used to predict the detailed atmospheric structure and hence the radiation field which they emit. Figure 7.6, taken from [15], compares

Fig. 7.6 Stellar SED and ions of interest in the Orion Nebula. The Atlas SED represented the state of the art 30 years ago. The WMBasic and TLusty SEDs are today's start of the art. The horizontal lines indicate ionization potentials for the O, Ne, and S ions that are strong in the spectrum of Orion. Taken from [15]



the predicted Trapezium SEDs for calculations by three different groups. The "Atlas" calculation, created in the late 1970s, is shown for its historical interest only. The "WMBasic" and "TLusty" calculations represent today's state of the art. The modern calculations have significantly more detail in the predicted spectra than Atlas, but the major difference is at photon energies  $h\nu \geq 35\,\mathrm{eV}$ , where the modern calculations are  $\sim 1$  dex brighter. [Ne III] is the highest ionization species seen in the spectrum of an H II region and is produced by this part of the SED. For reference, Fig. 7.6 also shows the ionization potentials of other ions that emit strongly in Fig. 7.3. The stars emit little radiation with  $h\nu > 54\,\mathrm{eV}$ .

The SED shown in Fig. 7.6 cannot be directly observed due to photoelectric opacity of the local interstellar medium. Atomic hydrogen prevents photons with  $h\nu > 13.6\,\mathrm{eV}$  from reaching the Earth. Most of the hydrogen in the stars' atmosphere is ionized due to its high temperature,  $\sim 4 \times 10^4\,\mathrm{K}$ , but there is enough to produce the absorption "Lyman jump" at 13.6 eV. The detailed structure that is present in the modern SEDs are absorption lines produced by atoms and ions in the star's atmosphere.

The WMBasic and TLusty SEDs do not agree with one another, especially at higher energies, an uncertainty which must be taken into account in the modeling. In practice this becomes an iterative procedure, with the two SEDs used to predict the spectrum, other parameters adjusted, and finally a "best-fitting" SED chosen (we settled on WMBasic in [15]).

Having set the radiation field, the next step is to specify the basic properties of the gas and dust that it strikes. First is its chemical composition, the relative abundances of hydrogen, helium, and heavier elements. This affects the relative intensities of the lines shown in Fig. 7.3, but they are also sensitive to the photoionization model we shall construct. Again it is necessary to iterate to find a satisfactory model. The cosmic context also constrains the composition since the abundances of the elements in this part of the galaxy have been determined for other nebulae and stars, including the Sun.

Grains must also be included. Many of their properties are also set by the context, since there have been many studies of extinction properties of grains in other locations. The existence of the grains also affects the amount of an element that remains in the gas phase. Some elements, especially Al, Ca, Ti, and Fe, are virtually missing from the gas phase, and produce no lines, because they are locked up in the grains.

Next the gas density must be specified. This can be determined from emission line ratios. The first, and still widely used, density indicator is the [O II]  $\lambda 3727$  doublet whose relative intensities are density dependent, as shown by [16]. The other commonly used indicator is a similar doublet of [S II] in the red.

The separation of the cloud from the Trapezium stars is the next parameter. The intensity of the radiation field,  $4\pi J$  [erg cm<sup>-2</sup> s<sup>-1</sup>], varies as  $r^{-2}$  where r is the star-cloud separation. The surface brightness S(line) [erg cm<sup>-2</sup> s<sup>-1</sup> sr<sup>-1</sup>] of the reprocessed emission from the gas is also proportional to  $4\pi J$ , so the separation can be directly determined from observations of line surface brightnesses [17]. This approach has been used to recreate the 3D geometry of the inner Orion nebula [18].

Having set these parameters by direct observation, from the astrophysical context, or from spectrum synthesis, the last step is to use a code such as CLOUDY to self-consistently determine the physical state of the nebulae by comparison of models with the observed spectrum. The gas kinetic temperature is determined by balancing heating and cooling processes, processes which add or subtract kinetic energy from the electrons. Steady state is usually assumed, along with the assumption that the free electrons have a Maxwell-Boltzmann velocity distribution in ionized regions of the nebula, as suggested by consideration of the relevant timescales [4, 19].

Figure 7.7 shows the predicted thermal, ionization, and chemical state of gas along a ray going into the center of the left panel of Fig. 7.1. The independent axis is the separation from the Trapezium stars, which are off to the left in Fig. 7.7.

The gas kinetic temperature is nearly isothermal at shallow regions,  $r < 1.9 \times 10^{17}$  cm, with  $T \approx 10^4$  K as shown in the top panel. This is the H<sup>+</sup> region of the nebula, where the Lyman continuum from the stars is relatively unextinguished and the heavier elements are photoionized up to the first to third ionization stages. The dominant heating process is photoionization of hydrogen, the "primary mechanism" described in [2]. Most emission produced in the H<sup>+</sup> region occurs at optical wavelengths.

The H<sup>+</sup>-H<sup>0</sup> ionization front occurs at a depth of  $r \approx 1.9 \times 10^{17}$  cm and is the point where the stellar Lyman continuum is been extinguished. The strength of the ionization cross section for H means that the transition from material dominated by H<sup>+</sup> to material dominated by H<sup>0</sup> occurs in a very narrow zone. Only beyond this front can species with ionization potentials less than 13.6 eV exist with significant populations, so atoms and first ions are found here. The gas is warm, with temperatures  $100 \, \text{K} \le T \le 10^3 \, \text{K}$ , and is mainly heated by the Balmer continuum emitted by the stars and absorbed by grains or the heavier elements. The H<sup>0</sup> region is often referred to as a "PDR", standing for either photodissociation region [20] or photon-dominated region [21]. Most emission from the H<sup>0</sup> region occurs in the infrared.

Depths significantly deeper than  $r \approx 1.9 \times 10^{17}$  cm are cold ( $T < 100 \, \mathrm{K}$ ) and molecular, with H<sub>2</sub> and CO the most common molecules. Conditions are determined by high-energy penetrating x-ray and low-energy light produced by the stars, and by cosmic rays. The molecular cloud emits most strongly in the radio, mainly by molecular rotational transitions.

The calculation shown in Fig. 7.7 was time steady. This is a good approximation in the  $H^+$  layer, where the high temperature and large electron fraction ensures that collisions are fast. The assumption becomes more questionable as we go into colder atomic and molecular regions. Collisions at the deepest point are slow because of both the low temperature and the large mass of the collision partners. For instance, cooling can be dominated by CO emission following  $H_2$ –CO collisions. Calculations of the cold chemistry show that time dependence is important here [22, 23].

Figure 7.8 shows the predicted spectrum. This is what we would observe with a telescope and detector that could detect the full UV—optical—infrared—radio spectrum of a point in the center of the left panel of Fig. 7.1. This observation cannot be done today.

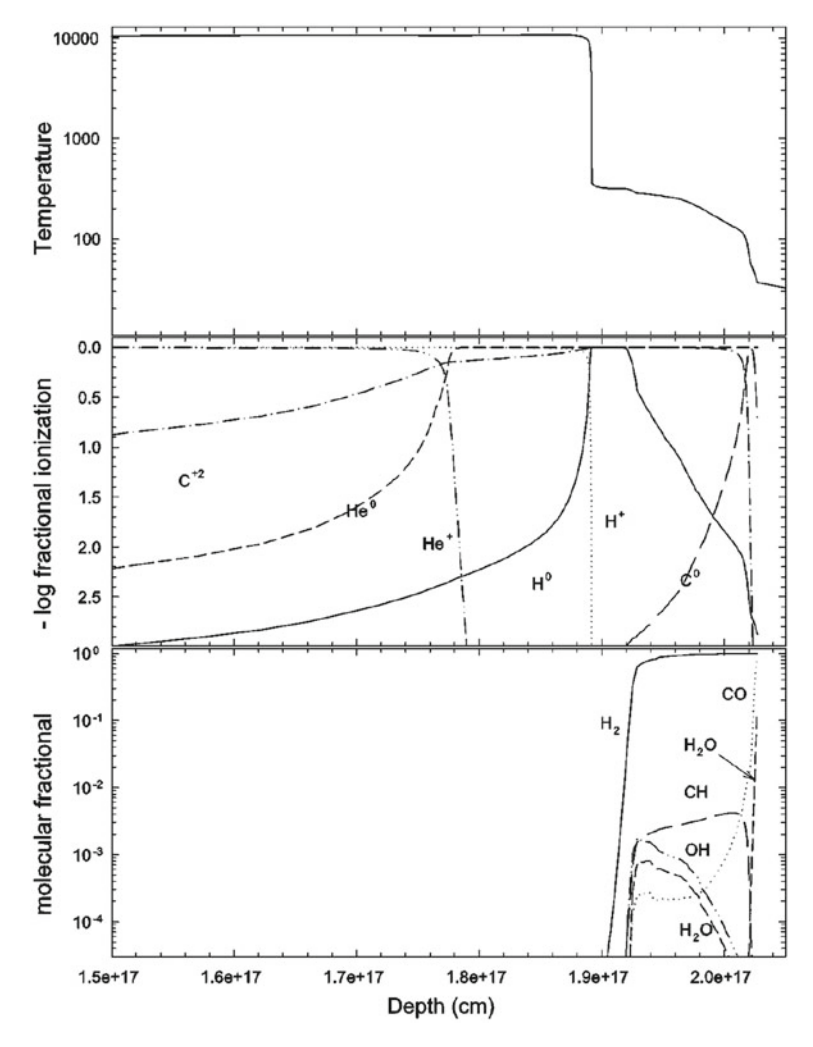
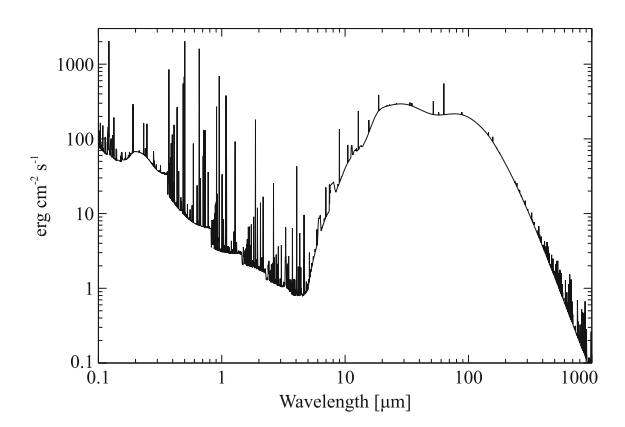


**Fig. 7.7** The temperature and chemical state of gas in Orion along a ray passing from the star (off the figure to the *left*) into successive ionized, neutral, and molecular regions. Adapted from [10]

The continuum shortward of 5  $\mu m$  is a combination of starlight (the Rayleigh-Jeans tail of the SED of the hot stars), and atomic emission, mainly free-bound, two-photon, and free-free emission produced by  $H^+$  in the ionized layer. The large continuous emission bump centered on  $\sim 20-100\,\mu m$  is thermal emission from warm dust grains, mainly in the  $H^+$  and  $H^0$  layers. The sharper features around 5–10  $\mu m$  are due to emission from large molecules, collectively know as Polycyclic Aromatic Hydrocarbons (PAHs), which form near the  $H^+-H^0$  transition. Emission from the small particles and large molecules are an important diagnostic of the gas properties.

**Fig. 7.8** The predicted spectrum of central regions of Orion



Emission lines from a wide variety of ions, atoms, and molecules occur across Fig. 7.8. Lines of atoms and ions found in the  $H^+$  region dominate much of the spectrum shorter than  $10\,\mu\text{m}$ . The strong line at the shortest wavelength shown is H I L $\alpha$ , mainly produced by recombination in the  $H^+$  region. The strongest lines in the optical band are recombination lines of H and He, and forbidden lines of C, N, O, Ne, and S. This part of the spectrum should be compared with Fig. 7.3. Although it is hard to judge from the plots themselves, the calculation shown in Fig. 7.8 is a good fit to Fig. 7.3.

Most lines in the infrared are formed in the H<sup>+</sup> or H<sup>0</sup> regions by fine structure transitions within the ground term of the common elements. Emission lines in the far infrared and mm regime are produced by rotational transitions with molecules at the deepest parts of the cloud.

The result of this exercise is the complete prediction of the ultraviolet through radio spectrum. This is the best way to gain insight into the physics and nature of the cloud. The assumptions that have gone into this calculation are described next.

# 7.4 Spectral Calculations

## 7.4.1 The Ionization Balance in the ISM Limit

Textbooks on the interstellar medium (ISM), e.g. [4–7], write the ionization balance of an ion as the equivalent two-level system:

$$\frac{n(i+1)}{n(i)} = \frac{\Gamma(i)}{\alpha(i+1)n_e} \tag{7.1}$$

where n(i+1) and n(i) are the densities of two adjacent ionization stages,  $\alpha(i+1)$  is the total recombination rate coefficient of the ion (cm<sup>3</sup> s<sup>-1</sup>) and  $\Gamma(i) = \int \phi_{\nu} \sigma_{\nu} d\nu$ 

is the photoionization rate (s<sup>-1</sup>). Here  $\phi_{\nu}$  is the flux of ionizing photons [photons s<sup>-1</sup> cm<sup>-2</sup> Hz<sup>-1</sup>],  $\sigma_{\nu}$  is the photoionization cross section [cm<sup>-2</sup>] and the integral is over ionizing energies. In photoionization equilibrium  $\Gamma(i)$  is related to the flux of ionizing photons while in collisional ionization equilibrium  $\Gamma(i) = q(i)n_e$  where q(i) is the collisional ionization rate coefficient.

This assumes that recombinations to all excited states will eventually decay to the ground state and that all ionizations occur out of the ground state, a good approximation for low densities and dilute radiation fields. When this "equivalent two-level" model is valid, only the ground state and ionization out of it, and the continuum together with summed recombination coefficients representing captures to all excited states, need be considered.

These approximations greatly simplify the computational problem. Collections of ground and inner shell photoionization cross sections are given by [24], collisional ionization rate coefficients by [25], and summed recombination rate coefficients are computed as in [26, 27] and listed on Badnell's web site. The ionization balance can be easily computed with such data.

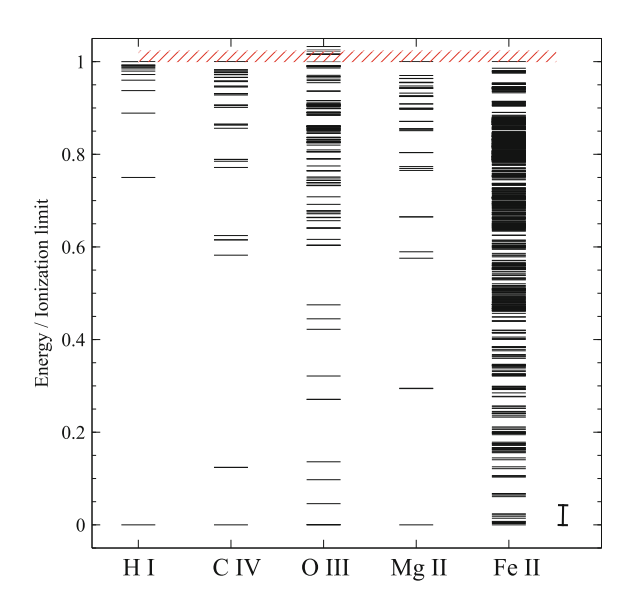
This approach extends over to the chemistry. Most codes use databases similar to UDfA, the UMIST Database for Astrochemistry [28], often referred to as simply UMIST. Complex molecules are treated as a single state with no internal structure. Rate coefficients do not depend on density and the internal level populations. The chemical data needed to implement a more complete model simply do not exist today.

Are these approximations valid? We consider atoms and ions, the subject of this book. Figure 7.9 shows energy-level diagrams for five ions responsible for strong UV and optical emission lines seen in nebulae. The level energies are given relative to the species' ionization potential to make comparisons simpler. The gas kinetic temperature in a photoionized cloud with cosmic composition is typically  $\sim$ 5% of the ionization potentials of the species that are present. The vertical bar at the right indicates this 5 % energy so that we can easily see which states are accessible. As can be seen, this energy corresponds to some of the lowest accessible levels in the ions: the population of these levels by collisional excitation functions is like a leak in the side of the reservoir of thermal energy in the plasma, preventing it from heating further, as the energy fed into the levels is lost by radiative processes. Emission in lines forbidden by the standard quantum transition rules is particularly important in this regard. The long timescales applicable for astrophysical systems mean that processes which occur at rates which are negligible for laboratory plasmas can become important. Once a forbidden line photon is emitted, the low line opacity means that it is likely to escape the system, rather than be re-absorbed. In collisionally-ionized plasmas the peak abundance of an ion with ionization potential IP occurs at a temperature of about IP/2, so the populations of excited levels of such ions are far larger than for a photoionized plasma.

Besides the equivalent two-level system approximation, most astronomical plasma emission codes further assume that emission from low-lying levels of the elements

<sup>&</sup>lt;sup>1</sup>See http://amdpp.phys.strath.ac.uk/tamoc/RR/, http://amdpp.phys.strath.ac.uk/tamoc/DR/.

Fig. 7.9 Experimental energy levels for some elements. The energy levels are taken from NIST [29] and are given relative to the ionization potential. Of these ions, only data for O III includes autoionizing levels. The bar at right, corresponding to E/IP = 0.05, is the typical kinetic energy in a photoionized gas and is shown to indicate which levels are energetically accessible



heavier than H shown in Fig. 7.9 is not affected by the ionization/recombination process, so that they can be treated as separate problems (H-like and He-like species are not treated this way, as described below). The C IV  $\lambda1549$ , Mg II  $\lambda2978$ , and [O III]  $\lambda\lambda$  5007, 4959 multiplets are produced by the lowest excited levels of their ions. These levels are much closer to ground than to the continuum, so they should be most directly coupled to the ground state. The fact that, at low densities, nearly all of the population of a species is in the ground state further justifies this assumption.

This "independent ionization/emission" approximation is also suggested from consideration of the relevant timescales. The recombination time of a typical ion is  $\sim 1$  h at a density of  $n \sim 10^{10} \, \mathrm{cm}^{-3}$ . The line-emission timescales are much faster, with collisional excitation timescales of  $\sim 0.1$  s and photon emission occurring within  $\tau \sim 10^{-7}$  s for a typical permitted transition. Collisional / emission processes within the low-lying levels occur on timescales that are  $\tau \geq 4$  dex faster than ionization—recombination. As a result, most codes first solve for the ionization distribution of an element, then for the line emission from each ion. They are treated as separate problems.

This is not even remotely true for H-like and He-like ions. Figure 7.9 shows H I on the left. The first excited level occurs at an energy  $E \approx (1-1/n^2) \approx 0.75$  of the ionization limit, where n=2 is the principal quantum number of the lowest excited level. As a result the lowest level is much closer to the continuum above it than to the ground state below it. There should be little collisional coupling between excited states and ground at low densities and photoionization temperatures. Most emission is produced following recombination from the ion above it, rather than collisional excitation from the ground state.

In CLOUDY we treat these two iso-electronic systems without simple approximations. We use a unified model that extends from H to Zn [30–32], for both the H-like and He-like isoelectronic sequences. The full collision-radiative-ionization problem is solved to determine both the level populations and the ionization, so the two are entirely self-consistent. As shown in Figs. 7.4 and 7.5, our model of the ionization and chemistry of hydrogen does go the correct high and low-density limits, and goes to STE when exposed to a true blackbody. This is only possible when the ionization and level populations are self consistently determined by solving the full collisional-radiative problem.

Systems with an especially complex structure, such as Fe II, are a major exception to the discussion so far. Fe II has levels extending, nearly uniformly, between the ground state and the continuum, as shown in the right of Fig. 7.9. The atomic physics of Fe II is especially complex due to the large number of electrons. Unfortunately Fe II emission is strong in a number of astrophysically important classes of objects, including quasars and shocked regions. This is a worst case, with our treatment discussed by [33].

Although the H and He-like sequences have complete models, CLOUDY now uses the equivalent two-level atom for remaining ions. The essential difficulty is the critical role played by the highly excited states shown in Fig. 7.9. These levels are long lived due to smaller spontaneous decay rates. At the same time, the cross section for collisions increases for higher levels. At high density and temperature the highly-excited levels of all ions will have significant population. Collisional ionization from excited states becomes important, and the use of summed recombination coefficients is highly approximate, so both assumptions in the equivalent two-level system (7.1) break down. As a result the approximation that the ionization and level populations are decoupled can break down even for the heavier elements shown in the center of Fig. 7.9.

To some extent collisional effects upon the recombination process can be approximated in the summed-recombination approach. Large sets of collisional-radiative models exist. The Atomic Data and Analysis Structure (ADAS) collection [34] is perhaps the most extensive. Collisional suppression of dielectronic recombination has a long history [35] and is important because dielectronic recombination is often the dominant recombination process for many-electron ions. Comprehensive modeling results can be distilled into simple but highly approximate correction factors that account for collisional effects in excited levels and suppression of the recombination process [36]. The improves the range of validity of the summed-recombination approach.

Our coding of the full collision-radiative-ionization problem for the H- and Helike isoelectronic sequences means that we can use these models to show where the equivalent two-level system approximation breakdown occurs. In Fig. 7.10 we consider the ionization of hydrogen in a collisionally-ionized gas at a single temperature, over a broad range of density. The figure, taken from [37], shows how collisional-radiative effects, mainly involving highly excited levels, cause the hydrogen ionization to go from the equivalent two-level system in the low-density limit to statistical equilibrium at high densities.

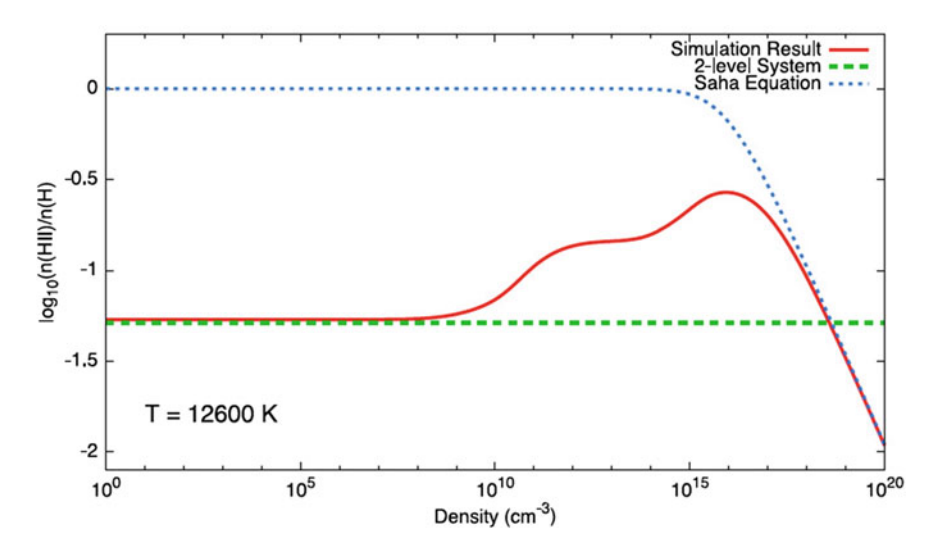


**Fig. 7.10** Showing the ionization of hydrogen changing from the low-density limit, on the *left*, to thermodynamic statistical equilibrium at high densities. The *solid red line* is the numerical result, the *green dashed line* is the two-level system result, and the *blue dotted line* is the result given by the Saha-Boltzmann equation. Taken from [37]

In the high-density limit, as might be found in some stellar atmospheres, accretion disks near black holes, or certain lab plasmas, the ionization balance is given by the Saha-Boltzmann equation:

$$\frac{n(i+1)}{n(i)} = \frac{g_e}{n_e} \frac{(2\pi mkT)^{3/2}}{h^3} \frac{u(i+1)}{u(i)} \exp(-\chi_i/kT)$$
 (7.2)

where n(i+1) and n(i) are the densities of the ion and atom,  $g_e$  and  $n_e$  are the electron statistical weight and density, the u's are partition functions, and  $\chi_i$  is the ionization potential of the atom [38, 39]. In this limit, shown as the blue dotted line in Fig. 7.10, the ionization depends exponentially on the temperature and inversely linearly on the electron density. At the microphysical level this can be understood as a balance between collisional ionization,  $n(i) + e \rightarrow n(i+1) + 2e$ , and three-body recombination,  $n(i+1) + 2e \rightarrow n(i) + e$ , the inverse process.

The solution in the low-density limit, the collisional equivalent two-level system given by (7.1), is

$$\frac{n(i+1)}{n(i)} = \frac{n_e q(i)}{n_e \alpha(i+1)} = \frac{q(i)}{\alpha(i+1)}$$
(7.3)

and is given as the green-dashed line. It does not depend on density but has an exponential dependence on temperature, as does (7.2), because of the temperature exponential that enters in the collisional ionization rate coefficient  $q_{ion}$ .

The red line in Fig. 7.10 shows the CLOUDY collisional-radiative solution. It goes between the equivalent two-level approximation, (7.3), valid at  $n \le 10^9 \, \mathrm{cm}^{-3}$ , and the Boltzmann-Saha limit at high densities, (7.2), valid at  $n \ge 10^{18} \, \mathrm{cm}^{-3}$ . Although many sources, such as the Orion Nebula, are safely in the low-density limit, the emission-line clouds in quasars or the inner regions of accretion disks have intermediate densities, where neither approximation holds.

The situation is actually worse than that suggested by Fig. 7.10 at intermediate densities. This figure is for an optically thin cell of gas, but the Lyman lines will be optically thick in a cloud with realistic column densities. This causes an overpopulation of excited states due to line trapping, in turn shifting the ionization "bump" to lower densities.

For more highly-charged ions, the scaling introduced by charge dependences means their populations also will behave much like Fig. 7.10, but at considerably higher densities.

The physics of highly-excited levels of many-electron systems can be affected by several physical processes that have diagnostic potential. Figure 7.11 shows a cartoon representation of the structure of the generalized model we are developing for these systems. The figure also indicates some important processes that occur in a typical complex ion. The box at left represents the range of energies shown in Fig. 7.9, and the boxes to the right show the energies that are affected by the recombination processes described below.

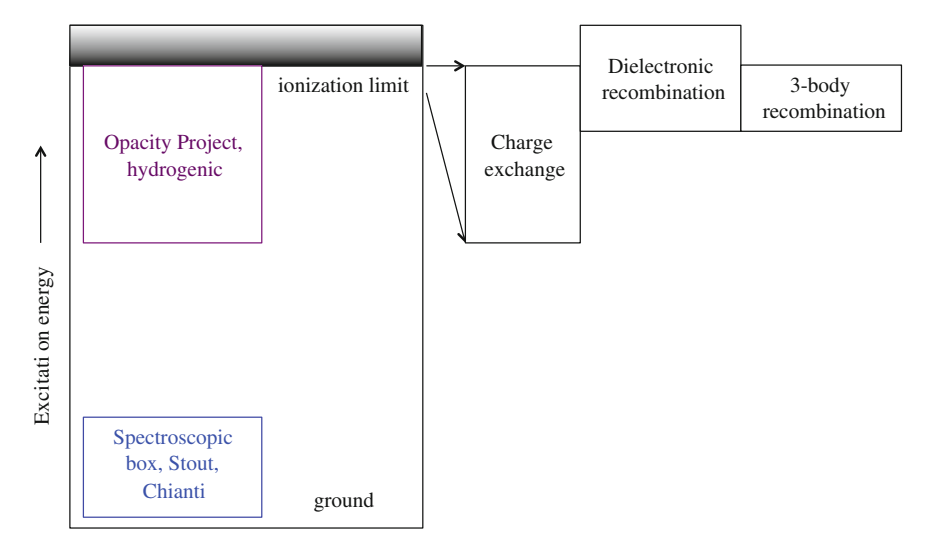


**Fig. 7.11** Typical levels and physical processes in a heavy-element ion. The vertical axis represents energy, as in Fig. 7.9, but is schematic for simplicity. The spectroscopic box contains the lower levels that make the strongest lines, and which we treat with high-quality tabulated data, as much as possible. Higher Rydberg levels line within the *upper smaller box*. The *three boxes* to the *right* indicate important recombination processes with an indication of where the recombined electron is captured by the atom

The ground state and ionization limits are at the bottom and top of the left-most box. Several regions exist within this. The "spectroscopic box" consists of the low-lying levels that produce familiar optical/UV lines such as C IV  $\lambda1549$ , Mg II  $\lambda2798$ , or [O III]  $\lambda5007$ . We use the highest possible quality atomic data from databases such as Chianti [40, 41], LAMDA [42] for molecules, or our Stout database [43]. When we wish to update atomic data or introduce new species, we add them to our Stout database. As much as possible collisional rates come from configuration interaction calculations, often from the R-matrix suite of codes, since accurate rates are critical for the spectroscopy and the energy balance in the plasma. Our goal is to obtain the highest quality spectroscopic predictions for lines that form with the spectroscopic box, along with the correct prediction of the ionization.

Highly-excited levels do not produce strong lines but are important because of their effects on the ionization and the role they play in determining the population of lower levels. Several sources of data exist. The updated Opacity Project [44] has energy levels, transition probabilities, and photoionization cross sections for 14 elements, extending up to n=10. For higher levels the hydrogenic approximation may be used. A large fraction of the radiative recombinations are to these excited levels. In CLOUDY, we use the data available from Badnell, which is the largest collection of radiative recombination data.

Dielectronic recombination (DR), a process where a free electron is captured by exciting a bound electron, forming an autoionizing state that can decay into bound levels, is the dominant recombination process for most ions. Again for DR we use data from Badnell,<sup>3</sup> which is also the largest collection available for this process.

The DR process is limited to energies within kT of the ionization limit, so, as shown in the right part of Fig. 7.11, it will mainly populate levels that are close to the ionization limit. The summed DR rates listed in ISM textbooks and the Badnell web site assume that all these populations eventually decay to the ground state.

It has long been known that DR is suppressed by collisional ionization at moderate to high densities [35, 45, 46]. Studies of approximate corrections to dielectronic suppression [36] show that the ionization of low stages of iron can change by nearly 1 dex at densities of  $\approx 10^{10} \, \text{cm}^{-3}$ . As stressed in that paper, these results are highly approximate, with an uncertainty in the suppression of order the correction itself. A full solution of the populations of the excited states must be done to get the right answer.

The balance between the fast conjugate processes of collisional ionization and three-body recombination that ensures that the populations in the very high levels are close to Boltzmann equilibrium with the population of the continuum above them at sufficiently high densities.

As described below, and discussed in [15], many ions do not have experimental measures of the energies of autoionizing levels. This introduces a fundamental uncertainty in the rate of this very fast process.

<sup>&</sup>lt;sup>2</sup>http://amdpp.phys.strath.ac.uk/tamoc/RR/.

<sup>&</sup>lt;sup>3</sup>http://amdpp.phys.strath.ac.uk/tamoc/DR.

Charge exchange (CX) recombination is a quasi-chemical process, where an electron transfers between one atom or ion and another. For example, in the process  $H^0 + A^{n+} \rightarrow H^+ + A^{*,(n-1)+}$ , an ion  $A^{n+}$  captures an electron from a hydrogen atom, placing it into a highly excited state of the next lower ionization stage. The CX process is strongest where there is a coincidence in the excitation energy between the initial and final states, so that for exchange with atomic hydrogen the level which is populated is typically  $\sim 13.6 \, \text{eV}$  below the ionization limit. CX is always important in determining the ionization state of the gas, and can also produce diagnostic emission lines in a variety of astronomical sources [47]. The strongest sources of CX emission are environments well away from equilibrium, where atomic hydrogen coexists with heavier elements in highly ionization stages. This occurs, for instance, in the upper levels of planetary or comet atmospheres, where the highly ionized solar wind strikes neutral gas [48]. Again, the problem is to track that electron as it decays, emits photons, and eventually reaches ground, or is collisionally ionized.

These processes form a highly coupled set of problems that should be solved simultaneously. In nature, thousands of levels are involved, a number too large to be handled with current computers. A very large amount of atomic data is also needed. The approach that has been taken in astrophysics, until now, has been to treat these as sets of independent processes in the low-density limit, perhaps with highly approximate corrections for density effects. Correctly treating processes in excited states will strongly affect the spectrum we observe. Large fusion plasma codes and databases such as ADAS solve these nested problems with various condensation techniques, ending with a relatively small system that can be solved quickly with accurate results [34]. It is then practical to solve such systems, on the fly, in the type of large-scale calculation of a cloud that CLOUDY does.

## 7.5 The Physics of the Astronomical Problem

The Boltzmann equation, which describes the statistics of particles in a plasma system, may be written as

$$\frac{\partial f_i}{\partial t} + v_i \cdot \nabla f_i + \frac{F}{m_i} \cdot \frac{\partial f_i}{\partial v_i} = \left(\frac{\partial f_i}{\partial t}\right)_{\text{coll}} + \left(\frac{\partial f_i}{\partial t}\right)_{\text{source}} + \left(\frac{\partial f_i}{\partial t}\right)_{\text{sink}}, \quad (7.4)$$

where  $f_i = f_i(r, v, t)$  is the phase space density for species i in position, velocity and time, which changes as a result of advection, the bulk forces F, particle collisions which change the particle momentum, and source and sink terms which couple the Boltzmann equations for different particle species. Due to the expense of treating the full six-dimensional phase space of the system for each of the species, models are often calculated in terms of moments of this equation, e.g. assuming Maxwellian particle distributions. In fact, for astrophysical plasmas, it is often assumed that the sources and sinks dominate, and that the system can be described by the simpler population balance equation

$$\frac{D_i n_i}{Dt} = \left(\frac{\partial n_i}{\partial t}\right)_{\text{source}} + \left(\frac{\partial n_i}{\partial t}\right)_{\text{sink}},\tag{7.5}$$

where  $n_i = n_i(r, t)$  is the number density of the particles, and  $D_i/Dt$  is an advective derivative, which may be species dependent but is often assumed to be zero.

It is interesting to consider the set of species over which the index *i* operates. A typical laboratory plasma will be carefully prepared to be dominated by just a few species: electrons, and selected ions which constitute either the system under study (perhaps just D and T for a fusion plasma), or low abundance impurities either added for diagnostic purposes or as the result of contamination, and intended to be maintained at levels which do not strongly impact the overall plasma state.

As discussed earlier, astrophysical plasmas are also often dominated by e, H and  $H^+$ , but the cosmic abundances of heavier elements are often high enough that they have a non-negligible effect on the state of the plasma, either because they contribute significantly to the heating and cooling, or because of processes such as the rapid charge exchange  $O+H^+\Leftrightarrow O^++H.$  Not only this, but the regime of astrophysical plasma modelling extends to temperatures at least as low as the cosmic background temperature where molecules and molecular ions are the dominant species. Molecules have their own complex physics of excitation and reaction; some of the molecules may aggregate into solid particles and mantles of icy material surrounding them.

While modelling the spectra of astrophysical plasmas requires that a wide diversity of species be treated, some simplifications can be made compared to the case of laboratory plasmas. In astrophysical nebulae, the incident continuum and material density are often low enough that the timescales for radiative or collisional excitation are far longer than those for radiative decay, such that the populations of ions in multiply excited states are small. Figure 7.9 illustrates that for many astrophysically-important ions, there are also relatively few low-lying levels which would have significant populations from thermal excitation.

In some classical processes, such as Auger ionization and dielectronic recombination, multiply-excited states are a key element. However, the lifetimes of these states are sufficiently small that for astrophysical plasmas they can be treated as transition states of an overall process that couples singly-excited ions, and hence do not need to be modeled explicitly.

# 7.6 Future Opportunities and Challenges

# 7.6.1 New Spectroscopic Opportunities

A spectrometer is the workhorse instrument in any astronomical observatory, and will remain so until starships like the Enterprise become a reality. Images are what capture the public imagination, but the hard quantitative science is obtained from spectra.



**Fig. 7.12** This shows four very new or future large-budget missions which will concentrate on spectroscopy. Going clockwise from the *upper left*, they are Athena, courtesy ESA (from http://www.cosmos.esa.int/web/athena), The Thirty Meter Telescope, courtesy TMT International Observatory (http://www.tmt.org/gallery/photo-illustrations), JWST, courtesy NASA (from http://jwst.nasa.gov/images\_jwst.html), and ALMA, courtesy ALMA Observatory (from http://www.almaobservatory.org/en/visuals/images). They operate in X-ray, optical, IR, and radio wavelengths

As stressed in this chapter, the spectrum is formed in a highly non-equilibrium gas which includes solids and molecules.

A new epoch of astrophysical spectroscopy is upon us. New and very expensive instruments are being designed and built that will obtain spectra with exquisite detail, of objects now too faint to be studied, out to times far back in the history of the Universe. Figure 7.12 shows four major observatories, one recently-completed and three that are now being built, that together cover the electromagnetic spectrum. Clockwise from the upper left, these are Athena, an ESO mission that will operate in the X-ray regime; the Thirty Meter Telescope, which will operate in the optical and near IR; NASA's James Webb Space Telescope (JWST), which will operate in the near and mid-IR; and ALMA, a now operational radio telescope operating at shorter radio wavelengths.

Together this array of instruments will be able to study an object across the electromagnetic spectrum. Each observatory offers far greater detector area than its processors and so can detect much fainter and more distant objects, or get much better signal to noise spectra of the brighter objects we now study. Being able to detect fainter objects means that we will be able to study examples farther back in time.

This is important since we wish to trace the evolution of the universe, how galaxies and stars form, and how the elements heavier than He are created.

The expansion of the universe also results in the observed spectrum being Doppler shifted to longer wavelengths. Astronomers use this red shift as a direct observational measure of the look-back time to the source. However, it also means that to observe the most distant sources, observatories must be developed to work in longer wavelength bands. In particular, at high redshifts emission at longer wavelengths than the Lyman limit becomes redshifted into the infrared.

Our understanding of nearby, bright, and previously studied, objects will also improve greatly. Much higher signal to noise means we will be able to obtain better spectra and detect fainter lines on familiar objects. This allows new emission-line diagnostics to be formed, as well as permits the first-ever exploration of faint lines. Detecting fainter lines inevitably leads to new discoveries, along with the need for more complete line-finding lists.

The missions shown in Fig. 7.12, the type of data they will obtain, and the challenges for non-equilibrium simulations and spectroscopy, are briefly described next.

Atacama Large Millimeter/submillimeter Array (ALMA) (http://www.almao bservatory.org/) is a newly-operational radio telescope situated high in the Atacama desert. It works at higher frequencies and shorter wavelengths than previous instruments. Long-look spectra of nearby objects have shown a forest of emission lines, mostly rotational transitions of molecules, but many not yet identified. Of greater interest to the plasma community is that ALMA can detect radio recombination lines corresponding to  $\Delta n = 1$  transitions occurring around  $n \sim 40$  for hydrogen. Such emission can trace ionized gas in regions that are highly obscured by dust [49]. Curiously, the most frequently cited study of the emission of these levels, [50], has not been revised. There have been recent revisions in collisional rate coefficients for Rydberg levels [51–53] which should affect these predictions.

Athena (http://www.cosmos.esa.int/web/athena) is a recently approved ESA mission to do X-ray spectroscopy. It will detect hot, ~10<sup>6</sup>–10<sup>7</sup> K gas through emission mainly from moderately to highly ionized second and third row elements, together with Fe and Ni. Non-equilibrium effects come in when the gas cooling time is faster than the recombination time [54, 55]. Line emission is mainly from valence transitions of highly-ionized species along with inner-shell and satellite transitions of more neutral species.

**The Thirty Meter Telescope** (http://www.tmt.org/) will detect near-ultraviolet to mid-infrared light, and so can obtain spectra like Fig. 7.3, and the insert in Fig. 7.2, but with much better resolution and signal to noise. The spectra such a monster might obtain of the Orion Nebula are unimaginable. But its main goal is to obtain much better observations of very high redshift, high look-back time, objects.

James Webb Space Telescope (JWST) (http://jwst.nasa.gov/) is NASA's major astronomy mission. It will obtain spectra over the near to mid infrared. In the local universe this will detect emission from low-ionization species, molecules, and PAHs. It will be unique in doing optical/UV spectroscopy of the high redshift universe.

## 7.6.2 And the Grand Challenges to Exploiting Them

The instrumentation described above represent an investment of many billions of dollars. The spectra they will obtain are the best way to understand the universe around us. The grand challenges to using these spectra to their full potential, from the modeling perspective, are the following:

• Grand challenge: Complete the spectroscopy begun by Edlén and cohort long ago
There are large gaps in our knowledge of such basic spectroscopic data as energy
levels for many ions. Consider Fig. 7.9. Of these common species, only O III has
autoionizing energy levels tabulated in NIST [29]. Other species may have only a
few levels. Such fundamental spectroscopic data are needed for all non-equilibrium
modeling.

To cite one example, the [S II]—[S III] spectrum provides one of the most fundamental ionization, temperature, and density diagnostics accessible to ground based astronomers. Yet the dielectronic recombination rate, the rate for the fastest process converting S<sup>2+</sup> into S<sup>+</sup>, could not be predicted because of the lack of basic spectroscopic data involving autoionizing levels. We were, to some extent, able to work around this by combining observations of the Orion H II region, CLOUDY models, and quantum calculations [15]. The derived rate is still uncertain. The rate would be accurately know if the energies of the autoionizing levels were known. Basic spectroscopic data are needed to explore spectra in the new regimes which will be opened up by new instrumentation. The ability to see more deeply will reveal many lines with no identification. The spectroscopic needs for the molecules that are observed in the radio are even greater.

Basic spectroscopic data are of lasting value. Much of the data listed in the NIST compilations of today are decades old but are still performing excellent service. Any effort put into the basic data today will help future generations of researchers.

- Grand challenge: radiative and collisional data for complex systems

  Most collisional and radiative rates come from large-scale computations. The data
  needs are so vast that experiments, which are costly and time consuming, can only
  be done for a few systems. Careful experiments are used to confirm whether the
  computational results are valid.
  - Complex systems such as Fe II, shown on the right of Fig. 7.9, present computational challenges due to the large number of levels involved. Configuration-interaction calculations require a large number of states, and good spectroscopic data for these states. The result is that there are few calculations of complex systems, and the agreement between different calculations of the same system is not good. This is also true for molecules, as well as processes such as charge exchange which occur through quasi-molecular interactions. These present major challenges in computational physics and physical chemistry.
- Grand challenge: full simulations of the astronomical systems

  The present review has concentrated on the emission properties of essentially static plasmas. There has been little mention of material dynamics, but this is clearly a crucial issue when non-equilibrium modeling is performed. All astronomical

objects are moving, and the gas visible in Fig. 7.1 is a photo-evaporative flow moving away from the surface of a background molecular cloud. If the flow is much slower than atomic processes then it will only establish the "target" that is struck by ionizing photons. If the flow is fast then it will change the microphysics by introducing advective terms in all of the rate equations. This changes the ionic, chemical, and thermal balance. The presence of a flow will, of course, also result in great changes in the radiative transfer.

It is not now possible to simultaneously solve the microphysics, at the level of a true non-equilibrium collisional-radiative model, and compute the flow and do the radiative transfer. We have done first steps with one-dimensional D-critical flows [56, 57] and the effects on the very strongest lines were not dramatic. Weak lines such as near-infrared H<sub>2</sub> emission could be strengthened by large factors due to molecules flowing into ionized regions and emitting before they are photodissociated.

This challenge is a multi-disciplinary effort involving hydrodynamics, really magnetohydrodynamics if a full simulation is to be done, radiative transfer, and non-equilibrium collisional radiative modeling.

This review can only hint at the range of challenges and possibilities presented by quantitative spectroscopy, the science of deriving physical parameters from astronomical spectra. Astrophysical sources represent ready-built laboratories to explore the physics of matter in extreme conditions, if we can build the advanced telescopes and spectrometers to detect and measure the light which they emit. Spectral modeling is how we read the message contained in that light.

Acknowledgments The authors thank Queen's University, Belfast and the University of Durham for their hospitality. Marios Chatzikos & Francisco Guzman Fulgencio made very helpful suggestions when reviewing the manuscript. GJF acknowledges support by NSF (1108928, 1109061, and 1412155), NASA (10-ATP10-0053, 10-ADAP10-0073, NNX12AH73G, and ATP13-0153), and STScI (HST-AR-13245, GO-12560, HST-GO-12309, GO-13310.002-A, and HST-AR-13914), and to the Leverhulme Trust for support via the award of a Visiting Professorship at Queen's University Belfast (VP1-2012-025). Contains material © British Crown Owned Copyright 2016/AWE.

#### References

- 1. T.G. Harrison, QJRAS 25, 65 (1984)
- 2. D.H. Menzel, Selected Papers on Physical Processes in Ionized Plasmas (1962)
- 3. D.H. Menzel, E.A. Milne, Selected Papers on the Transfer of Radiation (1966)
- 4. L. Spitzer, *Physical Processes in the Interstellar Medium* (Wiley-Interscience, New York, 1978), p. 333
- A.G.G.M. Tielens, The Physics and Chemistry of the Interstellar Medium (Cambridge University Press, Cambridge, 2005)
- 6. D.E. Osterbrock, G.J. Ferland, *Astrophysics of Gaseous Nebulae and Active Galactic Nuclei*, 2nd edn. (University Science Books, Sausalito, 2006)
- 7. B.T. Draine, *Physics of the Interstellar and Intergalactic Medium* (Princeton University Press, 2011)

- 8. D.E. Osterbrock, *Pioneer Nebular Theorists from Zanstra to Seaton: and Beyond*, in *Ionized Gaseous Nebulae*, Revista Mexicana de Astronomia y Astrofisica Conference Series, vol. 12, ed. by W.J. Henney, J. Franco, M. Martos (2002), pp. 1–7
- B.A. Remington, R.P. Drake, D.D. Ryutov, Rev. Mod. Phys. 78, 755 (2006). doi:10.1103/ RevModPhys.78.755
- 10. G.J. Ferland, ARA&A 41, 517 (2003). doi:10.1146/annurev.astro.41.011802.094836
- G.J. Ferland, R.L. Porter, P.A.M. van Hoof, R.J.R. Williams, N.P. Abel, M.L. Lykins, G. Shaw,
   W.J. Henney, P.C. Stancil, Revista Mexicana de Astronomia y Astrofisica 49, 137 (2013)
- 12. C.R. O'dell, ARA&A 39, 99 (2001). doi:10.1146/annurev.astro.39.1.99
- 13. G.J. Ferland, PASP **113**, 41 (2001). doi:10.1086/317983
- 14. S.L. Shapiro, A.P. Lightman, D.M. Eardley, ApJ 204, 187 (1976). doi:10.1086/154162
- N.R. Badnell, G.J. Ferland, T.W. Gorczyca, D. Nikolić, G.A. Wagle, ApJ 804, 100 (2015). doi:10.1088/0004-637X/804/2/100
- 16. M.J. Seaton, D.E. Osterbrock, ApJ 125, 66 (1957). doi:10.1086/146282
- J.A. Baldwin, G.J. Ferland, P.G. Martin, M.R. Corbin, S.A. Cota, B.M. Peterson, A. Slettebak, ApJ 374, 580 (1991). doi:10.1086/170146
- 18. Z. Wen, C.R. O'dell, ApJ 438, 784 (1995). doi:10.1086/175123
- 19. L. Spitzer, *Physics of Fully Ionized Gases*, 2nd edn. (Interscience, New York, 1962)
- 20. A.G.G.M. Tielens, D. Hollenbach, ApJ 291, 722 (1985). doi:10.1086/163111
- 21. A. Sternberg, A. Dalgarno, ApJS 99, 565 (1995). doi:10.1086/192198
- 22. F. Bertoldi, B.T. Draine, ApJ 458, 222 (1996). doi:10.1086/176805
- E. Herbst, E.F. van Dishoeck, ARA&A 47, 427 (2009). doi:10.1146/annurev-astro-082708-101654
- D.A. Verner, G.J. Ferland, K.T. Korista, D.G. Yakovlev, ApJ 465, 487 (1996). doi:10.1086/ 177435
- 25. G.S. Voronov, At. Data Nucl. Data Tables 65, 1 (1997). doi:10.1006/adnd.1997.0732
- N.R. Badnell, M.G. O'Mullane, H.P. Summers, Z. Altun, M.A. Bautista, J. Colgan, T.W. Gorczyca, D.M. Mitnik, M.S. Pindzola, O. Zatsarinny, A&A 406, 1151 (2003). doi:10.1051/0004-6361:20030816
- 27. N.R. Badnell, ApJS 167, 334 (2006). doi:10.1086/508465
- D. McElroy, C. Walsh, A.J. Markwick, M.A. Cordiner, K. Smith, T.J. Millar, A&A 550, A36 (2013). doi:10.1051/0004-6361/201220465
- A. Kramida, Yu. Ralchenko, J. Reader, NIST ASD Team, NIST atomic spectra database (ver. 5.2). National Institute of Standards and Technology, Gaithersburg, MD (2014). http://physics. nist.gov/asd. Accessed 28 Nov 2014
- R.P. Bauman, R.L. Porter, G.J. Ferland, K.B. MacAdam, ApJ 628, 541 (2005). doi:10.1086/ 430665
- R.L. Porter, G.J. Ferland, P.J. Storey, M.J. Detisch, MNRAS 425, L28 (2012). doi:10.1111/j. 1745-3933.2012.01300.x
- V. Luridiana, S. Simón-Díaz, M. Cerviño, R.M.G. Delgado, R.L. Porter, G.J. Ferland, ApJ 691, 1712 (2009). doi:10.1088/0004-637X/691/2/1712
- E.M. Verner, D.A. Verner, K.T. Korista, J.W. Ferguson, F. Hamann, G.J. Ferland, ApJS 120, 101 (1999). doi:10.1086/313171
- H.P. Summers, W.J. Dickson, M.G. O'Mullane, N.R. Badnell, A.D. Whiteford, D.H. Brooks, J. Lang, S.D. Loch, D.C. Griffin, Plasma Phys. Control. Fusion 48, 263 (2006). doi:10.1088/ 0741-3335/48/2/007
- 35. K. Davidson, ApJ 195, 285 (1975). doi:10.1086/153328
- D. Nikolić, T.W. Gorczyca, K.T. Korista, G.J. Ferland, N.R. Badnell, ApJ 768, 82 (2013). doi:10.1088/0004-637X/768/1/82
- Y. Wang, G.J. Ferland, M.L. Lykins, R.L. Porter, P.A.M. van Hoof, R.J.R. Williams, MNRAS 440, 3100 (2014). doi:10.1093/mnras/stu514
- 38. S. Chandrasekhar, Radiative Transfer (1960)
- D. Mihalas, Stellar Atmospheres, 2nd edn. (W. H. Freeman and Co., San Francisco, 1978), p. 650

- 40. K.P. Dere, E. Landi, H.E. Mason, B.C. Monsignori Fossi, P.R. Young, A&AS 125, 149 (1997)
- 41. E. Landi, G. Del Zanna, P.R. Young, K.P. Dere, H.E. Mason, ApJ **744**, 99 (2012). doi:10.1088/0004-637X/744/2/99
- 42. F.L. Schöier, F.F.S. van der Tak, E.F. van Dishoeck, J.H. Black, A&A 432, 369 (2005)
- 43. M.L. Lykins, G.J. Ferland, R. Kisielius, M. Chatzikos, R.L. Porter, P.A.M. van Hoof, R.J.R. Williams, F.P. Keenan, P.C. Stancil, ArXiv e-prints (2015)
- N.R. Badnell, M.A. Bautista, K. Butler, F. Delahaye, C. Mendoza, P. Palmeri, C.J. Zeippen, M.J. Seaton, MNRAS 360, 458 (2005). doi:10.1111/j.1365-2966.2005.08991.x
- 45. R.A. Sunyaev, L.A. Vainshtein, Astrophys. Lett. 1, 69 (1968)
- 46. A. Burgess, H.P. Summers, ApJ 157, 1007 (1969). doi:10.1086/150131
- P.C. Frisch, D.J. McComas, Space Sci. Rev. 176, 101 (2013). doi:10.1007/s11214-010-9725-0
- 48. P. Tremblin, E. Chiang, MNRAS 428, 2565 (2013). doi:10.1093/mnras/sts212
- 49. N. Scoville, L. Murchikova, ApJ **779**, 75 (2013). doi:10.1088/0004-637X/779/1/75
- M. Brocklehurst, M. Salem, Comput. Phys. Commun. 13, 39 (1977). doi:10.1016/0010-4655(77)90025-X
- D. Vrinceanu, R. Onofrio, H.R. Sadeghpour, ApJ 780, 2 (2014). doi:10.1088/0004-637X/780/ 1/2
- D. Vrinceanu, R. Onofrio, H.R. Sadeghpour, ApJ 747, 56 (2012). doi:10.1088/0004-637X/ 747/1/56
- 53. D. Vrinceanu, Phys. Rev. A **72**(2), 022722 (2005). doi:10.1103/PhysRevA.72.022722
- 54. O. Gnat, A. Sternberg, ApJS 168, 213 (2007). doi:10.1086/509786
- M. Chatzikos, R.J.R. Williams, G.J. Ferland, R.E.A. Canning, A.C. Fabian, J.S. Sanders, P.A.M. van Hoof, R.M. Johnstone, M. Lykins, R.L. Porter, MNRAS 446, 1234 (2015). doi:10.1093/mnras/stu2173
- W.J. Henney, S.J. Arthur, R.J.R. Williams, G.J. Ferland, ApJ 621, 328 (2005). doi:10.1086/ 427491
- W.J. Henney, R.J.R. Williams, G.J. Ferland, G. Shaw, C.R. O'Dell, ApJ 671, L137 (2007). doi:10.1086/525023

# Chapter 8 Validation and Verification of Collisional-Radiative Models

Yu. Ralchenko

Abstract Quality control is as relevant to scientific computer codes as to any other software. For complex collisional-radiative (CR) models that are used to calculate plasma population kinetics parameters and spectra, each CR code is expected to be thoroughly tested and verified not only against experimental data but also against fundamental principles governing plasma population kinetics. In this Chapter we describe the advanced methods for validation and verification of CR models that were developed at the series of Non-Local Thermodynamic Equilibrium (Non-LTE) Code Comparison Workshops. In addition, the Monte Carlo approach to analysis of uncertainty propagation in CR is exemplified.

## 8.1 Introduction

Collisional-radiative (CR) modeling [1] generally refers to calculation of state populations and spectra in plasmas that are away from local thermodynamic equilibrium (LTE) or coronal equilibrium (CE). Speaking of optically thin plasmas, the LTE populations and spectra can in principle be calculated analytically using only level energies, radiative transition probabilities and autoionization rates. However, both CE and CR simulations make use of large sets of collisional data which immediately suggests application of numerical methods and development of complex computer codes. A properly built CR model is to reach the LTE and CE limits at very high and very low densities, respectively, and therefore we will treat CE as a subset of CR modeling.

The literature on CR simulations is immense. In addition to textbooks on plasma spectroscopy [2–5] and extensive reviews [6], thousands of papers describe how CR modeling is used to calculate state populations and spectra in dilute astrophysical plasmas, magnetic and inertial confinement fusion devices, sources of bright light for extreme ultraviolet lithography, laser-produced plasmas, and many other

National Institute of Standards and Technology, Gaithersburg, MD 20899-8422, USA e-mail: yuri.ralchenko@nist.gov

Yu. Ralchenko (⋈)

hot and cold plasmas. There exist CR models for neutral and near-neutral ions, highly-charged ions, multi-component plasmas, plasmas under strong external electromagnetic fields, plasmas under influence of an external radiation field, even for low-temperature molecular plasmas, although we will not discuss molecules in the present Chapter. The list of CR model applications would be prohibitively long to present here.

The CR approach does not provide a universal recipe for a rigorous calculation of emission or absorption spectra as well as population kinetics parameters in an arbitrary plasma. Generally, one would first determine which atomic (or ionic) states are relevant for the problem in question and which physical processes connecting those states are the most important ones. Then the atomic data are to be either independently calculated or obtained from other sources, such as atomic databases. In many cases a CR model may have to include the plasma size and opacity effects, depression of the ionization potential in plasmas, deviation of the particle energy distribution function from the equilibrium Maxwellian distribution, photon propagation in the media, spectral line broadening, and instrumental effects on the final spectrum. This incomplete list of the frequently included effects makes it very clear that the modern CR models are in fact sophisticated software packages, and some may run for days or even weeks to reach the final result. Such a complexity of the CR codes calls for development of reliable methods and tools to analyze such important issues as uncertainty propagation and code validation and verification. This is the topic of the present Chapter.

## 8.2 Tests and Uncertainty Analysis of CR Models

The intrinsic complexity of extensive collisional-radiative models describing many thousands or even millions of atomic states makes it immensely challenging to carry out a detailed and meticulous analysis of their applicability and validity. This is not unique for CR modeling but rather is typical for complex computational models and codes used in modern science and engineering. In 2005, Post and Volta [7] called for a paradigm shift with regard to validation and verification (V&V) of complex scientific codes across various fields of research. Later the National Research Council produced an extensive report titled "Assessing the Reliability of Complex Models: Mathematical and Statistical Foundations of Verification, Validation, and Uncertainty Quantification (VVUQ)" [8] that became an important contribution to our approach to development and analysis of complex models. In particular, this report addresses the mathematical foundations of VVUQ methodologies, identifies the best practices and key principles, and discusses education of the VVUQ community and application of VVUQ to predictive science and engineering. The VVUQ is defined in the NRC report as follows [8]:

- Verification. How accurately does the computation solve the underlying equations of the model for the quantities of interest?
- Validation. How accurately does the model represent reality for the quantities of interest?
- Uncertainty quantification (UQ). How do the various sources of error and uncertainty feed into uncertainty in the model-based prediction of the quantities of interest?

Rephrasing B. Boehm's succinct informal definitions [9], verification and validation address the questions "Are we building the model right?" and "Are we building the right model?" We postpone the discussion of V&V for CR codes to the next subchapters meantime turning to the UQ.

The data uncertainty propagation analysis for CR codes is a rather intuitive procedure that has been discussed in several publications (see, e.g., [10]). Back in 2002, Summers et al. [11] mentioned that "... a systematic approach to error is overdue in this area," however it seems that today several groups are actively exploring this field. Very recently Bautista et al. [12] developed an analytical approach that reduces to linear sets of algebraic equations for the coupled uncertainties among all levels included in a model. They also discuss intrinsic uncertainties in atomic data proposing to estimate them from the dispersion in the results from various independent calculations. The general analytical methods for analyzing uncertainty propagations may however suffer from such deficiencies as, for instance, the implicit assumption of normal distribution for uncertainties and the Taylor expansion implying the uncertainties be small relative to the corresponding quantities. These problems are eliminated in implementations of the inherently simple Monte Carlo (MC) methods [13, 14] for UO. The authors of [14] introduce two types of uncertainty estimates. The "baseline uncertainty" is quantified as the variance between different theoretical approaches and thus represents the spread of the available atomic data. Importantly, for reliable baseline uncertainty estimates it is imperative to have a very clear understanding of strengths and weaknesses of different methods. The second type, the "method sensitivity," describes correlated uncertainties for models of varying size but employing the same theoretical approach. This type is much more time and resource intensive as compared to baseline uncertainty estimates and requires MC simulations that may become very demanding computationally. Fortunately, MC codes can be well optimized and/or parallelized and thus the computation times can be very reasonable.

The MC approach to uncertainty propagation analysis in CR models can be exemplified with a relatively simple steady-state calculation of the most general kinetic characteristics. Many results discussed in the present and following subchapters were obtained with the collisional-radiative code NOMAD [15]. This CR package provides extensive computational capabilities for plasma population kinetics and spectra modeling. NOMAD solves the first-order (non-)linear differential rate equation that mainly uses externally calculated atomic data for such parameters as energies, transition probabilities, and collisional cross sections. The use of cross sections allows non-Maxwellian simulations for an arbitrary electron energy distribution function although in most cases some simplifications (two-Maxwellian, rectangular, or Gaussian distributions) may suffice. NOMAD can solve time-dependent rate equations with account of laser photopumping, interaction with heavy particles (charge

exchange, excitation, ionization), or external radiation field. The opacity effects can be included in the escape factor formalism when calculating the state populations; then a detailed spectrum is determined using a one-dimensional (1-D) solution of the radiative transfer equation. So far NOMAD was successfully applied to numerous problems addressing spectroscopy of plasmas from solar corona to plasma opening switches to z-pinches to dense laser-produced plasmas.

The plasma parameters to be analyzed here with the MC method are the mean ion charge  $\overline{Z}$  and the second central moment  $\sigma_2$  defined as:

$$\overline{Z} = \sum_{Z,i} Z \cdot N_{Z,i}, \tag{8.1}$$

$$\sigma_2 = \sum_{Z,i} (Z - \overline{Z})^2 \cdot N_{Z,i} \tag{8.2}$$

where Z is the ion charge and  $N_{Z,i}$  is the population of the state i in ion Z, with the normalization condition

$$\sum_{Z,i} N_{Z,i} = 1. (8.3)$$

Consider a very limited collisional-radiative model for Ne that includes only ground states of ions from neutral Ne<sup>0+</sup> to He-like Ne<sup>8+</sup> and two physical processes, namely, ionization and recombination, with the rates calculated with the Flexible Atomic Code (FAC) [16]. NOMAD was used to solve the steady-state rate equations and determine ionization distributions for the fixed electron density  $n_e = 10^8$  cm<sup>-3</sup> in the range of electron temperatures  $T_e = 0.1 - 100 \,\mathrm{eV}$ . The low density was chosen to reduce contribution of stepwise excitation to the ionization balance although this restriction, as was found in more detailed simulations, is not of high importance. The MC calculations involve multiplication of all ionization and recombination rates by factors that are randomly selected from a particular distribution. The distribution used here was the normal distribution for the logarithm of the rate rather than the rate itself. This is known as the Galton, or log-normal, distribution [17]. Such approach can naturally include very large variations of the input parameters. Since most of random number generators select a number between 0 and 1, one has to make use of an additional technique to produce normal distribution. For the present studies we implement the fast and efficient Marsaglia method [18]. Then, in order to preserve the detailed balance principle for direct and inverse rates in a Maxwellian plasma, both parameters are to be multiplied by the same factor. This is not of particular importance for low-density simulations where ionization balance is primarily established due to collisional ionization and radiative and/or dielectronic recombination; these obviously are not the direct and inverse processes. However it is physically justified to implement this procedure for a general case.

The solid (red) curve in Fig. 8.1 shows the calculated  $\sigma_2$  versus  $\overline{Z}$  dependence with the mean ion charge monotonically increasing with the increase of temperature.

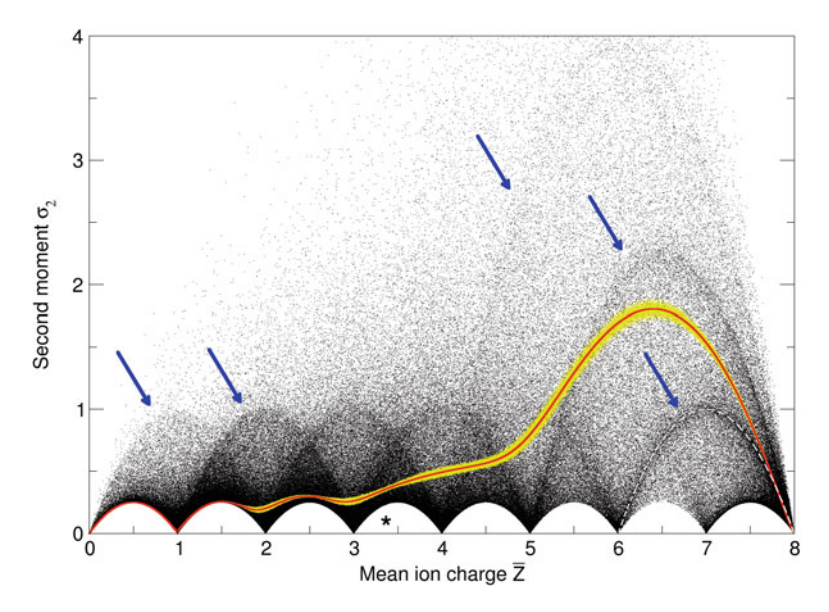


Fig. 8.1 Monte Carlo (MC) simulations of the second central moment  $\sigma_2$  as a function of the mean ion charge  $\overline{Z}$  for Ne at electron density  $10^8$  cm<sup>-3</sup> in the temperature range of  $0.1\,\text{eV}$  to  $100\,\text{eV}$ . Solid (red) line original CR calculation; yellow (light) band: MC calculation with the log-normal standard deviation of 0.05; black points MC calculation with the log-normal standard deviation of  $10.4\,\text{eV}$  show several attraction limits when only two ions are primarily populated

The results of the two MC steady-state runs, each with about 700,000 calculations, are presented as small dots. Run A, with the standard deviation of the log-normal distribution of 0.05, is shown by the bright (yellow) band near the solid curve of the initial CR calculation. As this distribution is very narrow, all variations in the  $(\overline{Z}, \sigma_2)$  plane are confined, as expected, to a rather narrow area around the original result. However, increasing the standard deviation to 10 results in a very different picture with a number of clearly visible patterns, some of which are indicated by arrows. Consider the manifold of unfilled areas at the bottom of the plot marked by an asterisk. The presence of such regions with no points is a consequence of the fact that the minimal width of an ion distribution is reached when only the two *neighboring* ions are populated. Generally, when only two ions  $Z_1$  and  $Z_2$  are populated, the second moment is represented by a parabola in the  $(\overline{Z}, \sigma_2)$  plane:

$$\sigma_2(Z_1, Z_2) = (\overline{Z} - Z_1)(Z_2 - \overline{Z}). \tag{8.4}$$

The smallest possible values of  $\sigma_2$  are thus just the union of arcs with  $|Z_1 - Z_2| = 1$ . The other curves marked by the arrows in the figure indeed correspond to the two-ion distributions of populations. Another example is given by the dashed curve that shows the "attraction" limit of points between 6 and 8 and which is a parabola  $(\overline{Z}-6)(8-\overline{Z})$ .

Similar structures appear also for the MC runs with a more extensive model for carbon that includes intra-ion processes such as excitation, deexcitation and spontaneous radiative decay for more than 120 states for all ionization stages. However, with increase of density the spread of data points becomes smaller due to the similar modification of direct and inverse processes. This behavior is expected since in the Saha-LTE limit ionization distribution are independent of atomic data.

## 8.3 Overview of NLTE Code Comparison Workshops

The concept of comprehensive cross-code comparisons for NLTE plasmas was inspired by the Opacity Code Workshops [19] that provided insight into the problem areas of LTE opacity codes. The core idea of NLTE code benchmarking is in devising a series of test cases that would emphasize different features of plasma population kinetics. This approach seems logical for computer code validation and it is accepted for other code comparisons, for instance, in cosmological radiative transfer [20] or spectral line broadening and shapes [21, 22]. It is extremely difficult to conduct a benchmark experiment on plasma population kinetics that would produce an unambiguous set of independently determined plasma parameters, such as density and temperature, as well as kinetic characteristics, e.g., ionization distributions. This unfortunate situation calls for development of computational methods aimed at meaningful comparison of different models and computer codes used in plasma population kinetic simulations.

The first NLTE workshop was held at the National Institute of Standards and Technology (NIST) in 1996 [23]. Then a *virtual* workshop [24] was held where several submissions were processed and the results distributed among the participants for online discussions. Since then the meetings are being regularly held every other year [25–30] with the last one, NLTE-9, organized in 2015. Importantly, these workshops not only allow the developers of CR models to test their codes under various plasma conditions but also provide an opportunity for the participants to have extensive discussions on outstanding problems, physical effects, numerical issues, and new experiments. Furthermore, this series of code comparisons has been instrumental in motivating dedicated experiments. This has led to a genuine two-sided interaction that has furthered progress in this area, with an ensemble of codes sufficiently mature to orient experimental efforts, and sufficiently characterized experiments that can be considered as benchmarks for the theory.

It would be unrealistic to expect a (almost) perfect agreement between different codes even in terms of the global kinetic characteristics. The primary distinction may come at the most basic feature of a CR model, namely, the description of the atomic structure. Some codes are written for atomic levels, the others use more generalized representations in configurations, superconfigurations, or even average atom approximation. Some codes represent a hybrid approach with atomic states of different nature (e.g., fine structure levels and relativistic configurations within one model) [31, 32]. Adding to this the variety of approximations used to calculate the

relevant atomic data makes the whole comparison approach almost hopeless. Yet, as will be seen below, the methods and techniques developed at the NLTE workshops provide a very promising environment that can help CR developers in validation and verification of their codes.

The test cases offered to the workshop participants covered a wide range of species and plasma conditions. Such elements as C, Ne, Al, Ar, Fe, Kr, Xe are often used in plasma diagnostics. The Au cases were inspired by the high importance of this element for inertial confinement fusion, while W is currently a leading candidate for the plasma-facing material in the divertor region of the ITER international tokamak. In most test cases, the plasma conditions are defined by the specific values of  $T_e$  and  $n_e$  and the plasma is assumed to be optically thin. The temperatures and densities extended from 3 to 30,000 eV and from  $10^{10}$  cm<sup>-3</sup> to  $10^{24}$  cm<sup>-3</sup>, respectively. Some cases also included opacity effects, external radiation field (reduced Planckian), non-Maxwellian electron energy distribution functions (e.g., hot electrons represented by a high-temperature Maxwellian). In other cases, the models were restricted by the highest principal quantum number n to study convergence of the results with n. The significant variation in the plasma parameters allowed us to explore various issues, from model completeness to ionization potential lowering to dielectronic recombination (DR) contributions etc.

The difficulty of developing reliable NLTE models for complex atomic systems was decisively demonstrated already at the very first workshop. It was found that different models show a surprising discrepancy of about 20 units for the mean ion charge of gold at electron density  $n_e = 10^{21} \, \mathrm{cm}^{-3}$  and electron temperatures  $T_e$  near 2000 eV. For these parameters the Au plasma condition is only slightly different from the coronal equilibrium and thus one would expect the codes to agree much better. The ensuing discussions and continuing analysis over several workshops revealed that several important factors contributed to this discrepancy, in particular, model completeness, different representations of atomic structure, and different account of dielectronic recombination in codes.

The remarkable importance of DR in hot plasmas is well appreciated in the community since the pioneering work of Burgess [33] who successfully resolved an outstanding problem of ionization balance in solar corona. Yet before the NLTE workshops no clear example was available in the literature that would unambiguously identify differences that arise from different treatment of DR in collisional-radiative codes. One of the suggested tasks for NLTE-6 was to calculate population parameters for M-shell Ar ions between 50 and 600 eV at electron densities of  $10^{12}$  and  $10^{23}$  cm<sup>-3</sup>. It was specifically requested to perform two similar calculations, one with and another without dielectronic recombination. The calculated parameters ( $\overline{Z}$  and  $\sigma_2$  are shown in Fig. 8.2) revealed that practically all codes agree for no-DR case while the spread in  $\overline{Z}$  may reach almost 5 units for the open-shell ions. This observation immediately resulted in new research on dielectronic recombination including development of novel methods to better specify contributions of different channels to the total DR rate.

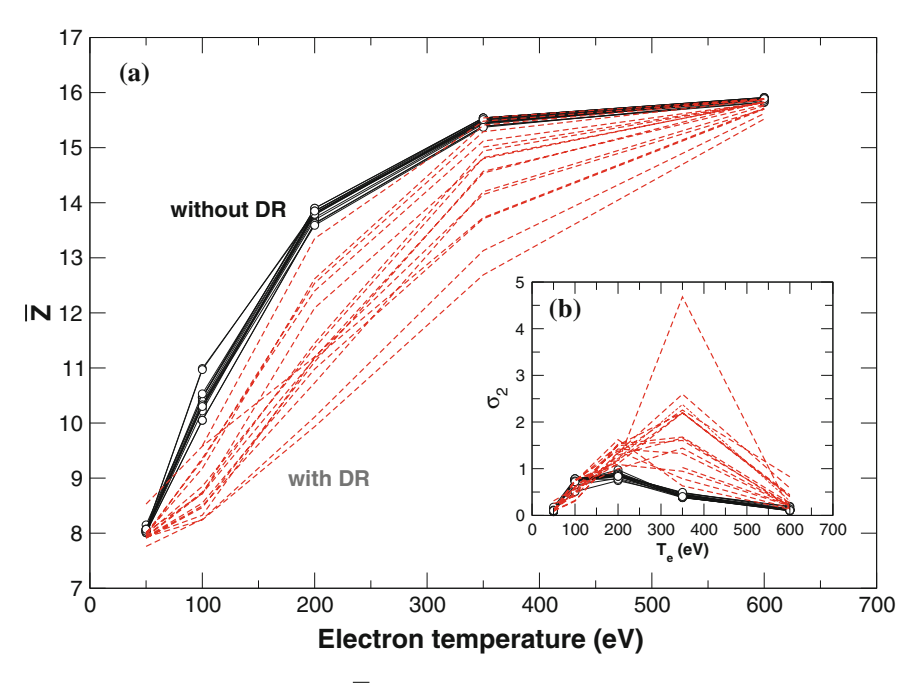


Fig. 8.2 NLTE-6: mean ion charge  $\overline{Z}$  (a) and second central moment  $\sigma_2$  (b) for steady-state Ar plasma at electron density  $n_e = 10^{12}$  cm<sup>-3</sup>. *Solid lines* with *open circles* represent calculations without dielectronic recombination (DR) while *dashed lines* show the results with account of DR

## **8.4 Code Comparison Parameters**

Due to a very large size of submitted datasets, a meaningful comparison of complex collisional-radiative models can only be achieved with the help of specialized software tools providing comprehensive selection options as well as visual representation of the compared quantities. From the first NLTE workshop, it was decided to develop a versatile user-friendly web interface that would allow unlimited access to the submitted data. Such interactive interface was indeed developed and then updated and enhanced several times with addition of new population kinetics parameters and new options for data manipulation. The examples of the early versions of the workshop databases can be found at <a href="http://nlte.nist.gov/SAHA">http://nlte.nist.gov/NLTE4</a> for NLTE-4. Note that the data therein as well as in the present chapter are unattributed to preserve the distinct style of the workshops.

# 8.4.1 List of Parameters for Steady-State Cases

The physical parameters that can be selected with the database interface are combined into several groups that are listed below. Each of the parameters can be presented in

a tabular (ASCII) or graphical form, and the online generated plots offer a number of options for data visualization and comparison.

- Global parameters (vs. temperature and/or density)
  - Total number of ionization stages
  - Total number of energy levels
  - Total statistical weight over all states
  - Mean ion charge  $\overline{Z}$
  - Second central moment  $\sigma_2$  (variance)
  - Difference  $(\Delta \overline{Z}, \Delta \sigma_2)$  (with regard to a reference code)
  - Third central moment (skewness)
  - Internal energy
  - Partition function
  - Maximal principal quantum number over all ion stages
  - Total, bound-bound, bound-free, and free-free radiative power losses
- Ion charge-stage parameters (for one combination of temperature and density; vs. ion charge)
  - Ion charge-state populations
  - Ionization potential (from the corresponding ground state)
  - Total number of levels
  - Total statistical weight
  - Maximal principal quantum number for an ion stage
  - Effective ionization rates (absolute or fractional) total, collisional, photoionization, or autoionization
  - Effective recombination rates (absolute or fractional) total, three-body, radiative, or dielectronic
  - $-\alpha/S$  ratio (i.e., recombination to ionization ratio)
  - Net rate
  - Excitation-autoionization rate
  - Dielectronic recombination rate for  $\Delta n = 0$  and  $\Delta n > 0$  channels
- Level population parameters (vs. energy or level number)
  - Statistical weight
  - Level population  $N_i$
  - Ratios  $N_i/N_{Saha}$  and  $N_i/N_{LTE}$  (explained below)
  - Shell populations
  - Occupation numbers
  - Population influx (absolute and fractional) total, excitation or deexcitation, radiative, ionization or three-body recombination, photorecombination, dielectronic recombination or dielectronic capture
  - Population outflux (absolute and fractional)

total, excitation or deexcitation, radiative, ionization or three-body recombination, photoionization, autoionization

- Spectra (vs. energy or wavelength)
  - Total, bound-bound, bound-free and free-free emission
  - Total, bound-bound, bound-free and free-free transmission
  - Spectrum for a selected ion stage

Some of these parameters and their importance for code comparisons are discussed in the next subchapters. Of course, the compared quantities are not all equally important or exhaustive. It is the variety and comprehensive nature of the available physical characteristics that make their usage and intercomparisons highly valuable. Note also that the present discussion of the workshop results does not aim at a comprehensive analysis of the underlying physics but rather at demonstration of the developed tools and methods for code comparisons.

In addition to steady-state cases characterized by fixed values of electron temperature and density, several NLTE workshops included time-dependent cases with  $T_e(t)$  and  $n_e(t)$  prescribed on a linear of logarithmic grid of time steps. For these situations, the amount of data for atomic states (levels) as a function of time would be prohibitively large, therefore the interface only allows selection of global parameters as a function of time or ion parameters as a function of ion charges at a specific time.

## 8.4.2 Global Parameters

The meaning of the global parameters is the most straighforward and generally hardly requires any detailed discussion. The mean ion charge, radiative power losses and other quantities are well defined, calculated by each and every CR code, and widely used in the literature. The total statistical weight over all ion stages indicates the completeness of the model; note that Chap. 1 in this book addresses completeness in much detail.

As mentioned above, it is rather demanding to carry out accurate measurements of global parameters even from sufficiently uniform plasmas. Nonetheless, such experiments can indeed be feasible, in particular in low-density fusion devices such as tokamaks and stellarators. The measured radiative power losses for krypton [34] that were used to benchmark the NLTE-5 calculations are presented in Fig. 8.3a as a shaded band in the electron temperature range of  $10-5000\,\text{eV}$ . The simulation results at a typical density of  $10^{14}\,\text{cm}^{-3}$  are shown as lines with symbols in (a), and figure (b) shows the calculated values of  $\overline{Z}$ . As frequently observed, the CR codes agree quite well with the experiment and between themselves near the closed-shell ions (Ne-like and He-like) while there is a substantial discrepancy for the open-shell ions (the "sausage" effect).

Simple 1-D plots of global kinetic quantities versus plasma parameters provide the first hint of agreement between codes. A somewhat more detailed picture can

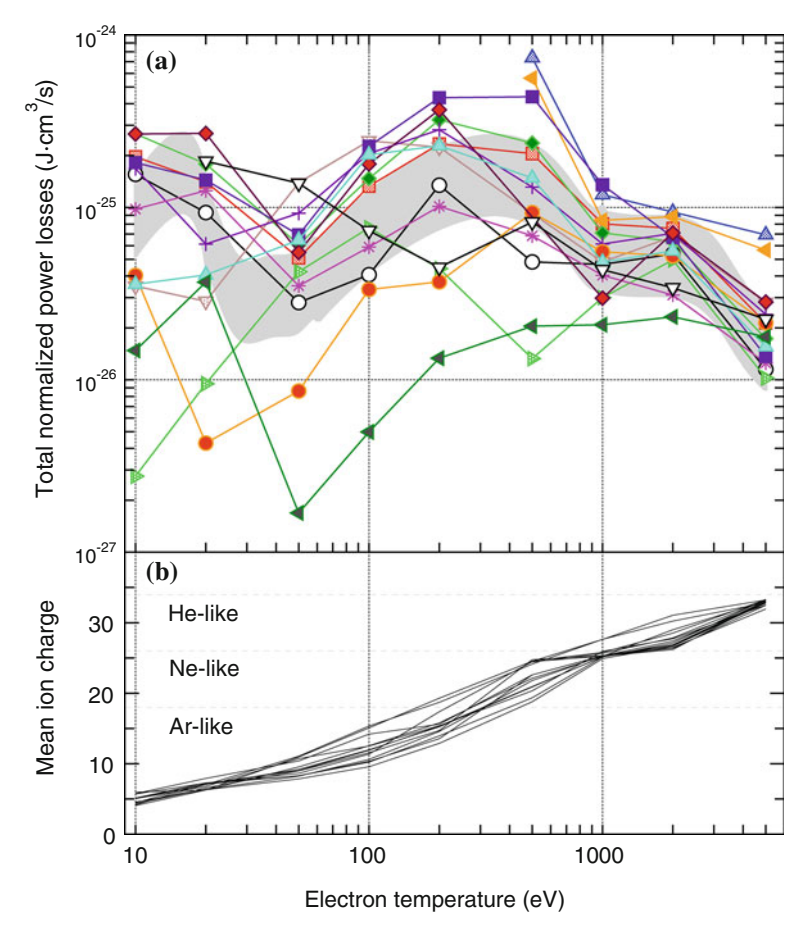


**Fig. 8.3** Radiative power losses (**a**) and mean ion charge (**b**) for Kr at the electron density of  $10^{14}$  cm<sup>-3</sup> (NLTE-7 comparisons). The shaded band in (**a**) shows the experimental results [34]

be inferred from a simultaneous analysis of several quantities. This however can become less practical for a large number of codes. One of the possible options used at the NLTE workshops is the visualization analysis of  $\overline{Z}$  and  $\sigma_2$  deviations from a reference code. Let the reference code values of mean ion charge and second moment for a fixed density be  $\overline{Z}_r(T_e)$  and  $\sigma_{2r}(T_e)$ . Then for each code i and each value of  $T_e$  the NLTE database software can generate the differences  $\Delta Z_{ri} = Z_r(T_e) - Z_i(T_e)$  and  $\Delta \sigma_{2ri} = \sigma_{2r}(T_e) - \sigma_{2i}(T_e)$  and plot  $\Delta \sigma_{2ri}$  versus  $\Delta Z_{ri}$  for all codes and all values of temperature or density. An example of such "Kandinsky" plot (the name coined by C. Bowen) for the  $10^{14}$  cm<sup>-3</sup> tungsten plasma between  $1200\,\mathrm{eV}$  and  $2400\,\mathrm{eV}$  is given in Fig. 8.4. The reference code point (0,0) is marked by a large red circle. One can clearly notice similar behavior for several groups of codes, for instance, those represented by solid circles (to the right from the (0,0) point) or by solid squares.

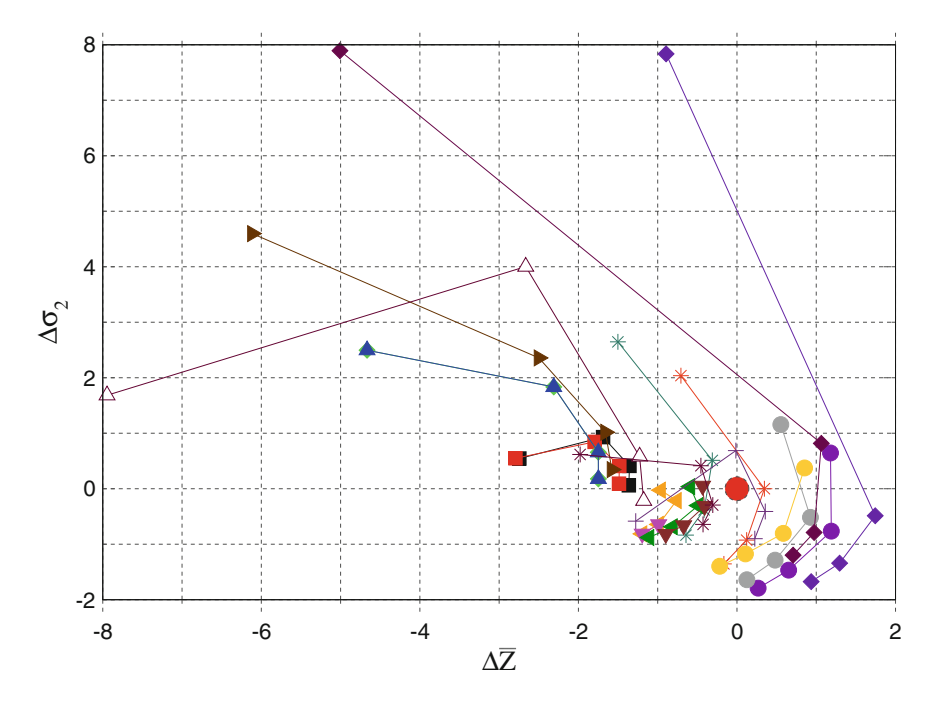


**Fig. 8.4** Example of a  $(\Delta \overline{Z}, \Delta \sigma_2)$  plot for the tungsten plasma at  $T_e = 1200 - 2400 \,\text{eV}$  and  $n_e = 10^{14} \,\text{cm}^{-3}$ . The large solid (red) corcle at (0,0) represents the reference point. The lines with symbols show calculations with different codes (NLTE-8)

While such rather general (dis-)agreement in the  $(\overline{Z}, \sigma_2)$  dependence of code results does not provide much insight into the underlying physics, it can nonetheless serve as a first step in elaborate comparisons.

## 8.4.3 Ion Parameters

More detailed information on plasma kinetics can be obtained from ion parameters that can be selected for only one combination of temperature and density (or other input parameters). The output is presented as a function of the ion charge.

#### 8.4.3.1 Ion Statistical Weight

The variety of CR models and their completeness can be illustrated by comparison of the ion total statistical weights  $G_Z$  included in particular codes. Figure 8.5 shows the  $G_Z$  values from twelve participating codes for the magnetic-fusion W case at 9000 eV (NLTE-7). The range of the ions with the largest abundances is shown

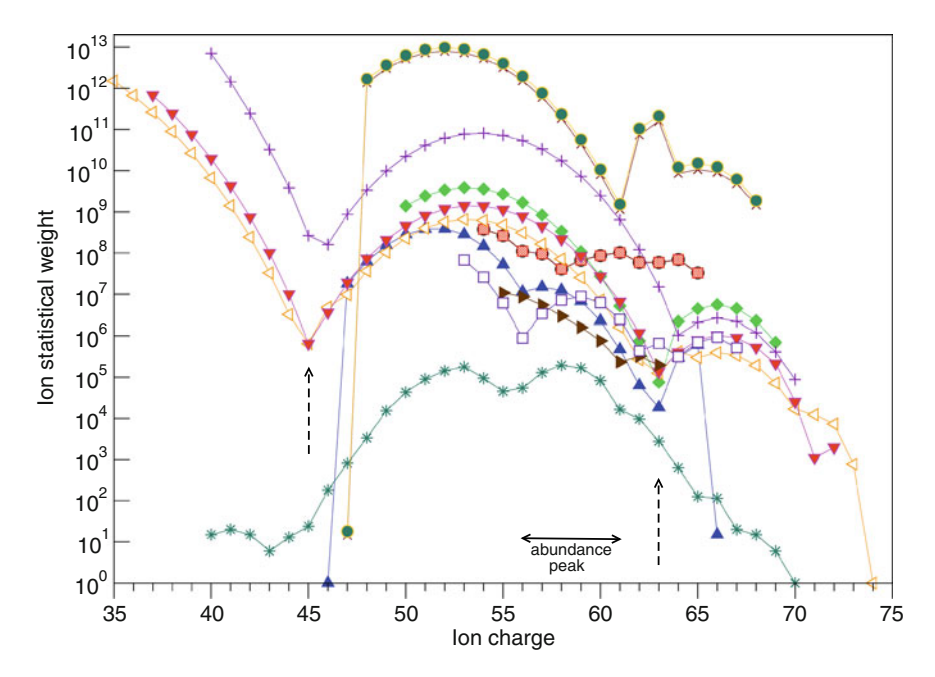
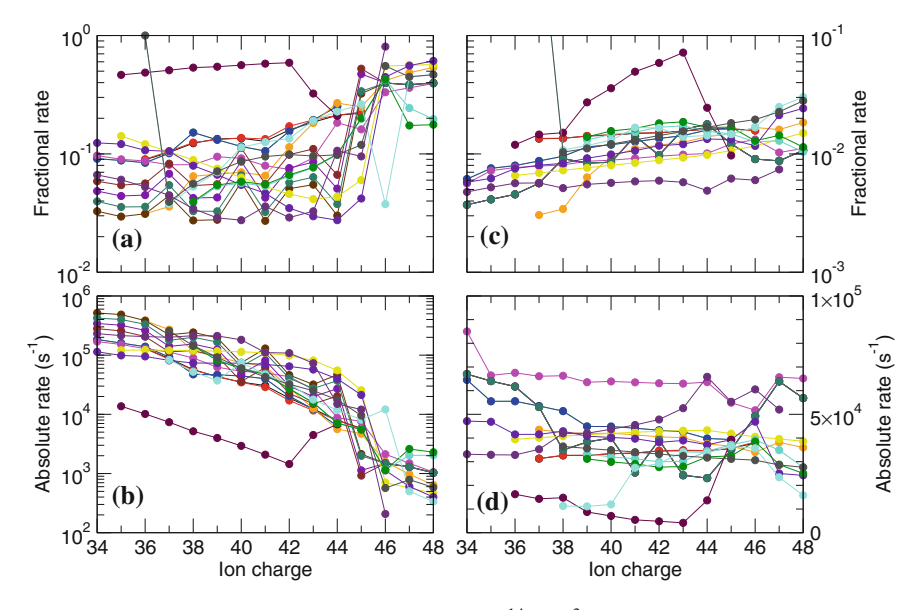


Fig. 8.5 Total statistical weight for tungsten ions used in the NLTE-7 codes (case of  $n_e = 10^{14}$  cm<sup>-3</sup> and  $T_e = 9000 \, \text{eV}$ )

by the horizontal line with arrows. One can see that the difference in statistical weights can reach eight orders of magnitude (at, e.g.,  $Z \sim 50$ ) for some models. The codes with the largest  $G_Z$  are typically of hydrogenic or hybrid nature while the detailed codes based on the atomic level representation have the smallest total weights. Another clearly identifiable feature in the plot is the sharp minima for  $G_Z$  near the ions with one electron over the closed shells (Cu-like W<sup>45+</sup> and Na-like W<sup>63+</sup>). For these ions marked by the vertical lines with arrows, the single excitations of the outermost electron produce a very limited number of states. Many codes do include inner shell excitations as well yet the number of possible combinations of angular momenta and, accordingly, the total number of states and the total statistical weight pale in comparison with the ions with open shells. In this particular case those are the M-shell ions, for which even single-electron excitations produce a large number of possible permutations of electron angular moments thereby resulting in an extremely rich structure.

#### **8.4.3.2** Effective Rates

One of the most important options provided at the NLTE workshops is the ability to perform thorough comparisons of various ionization and recombination channels. The effective rate for a particular inter-ion process (e.g., collisional ionization or



**Fig. 8.6** Effective rates for W ions at 1800 eV and 10<sup>14</sup> cm<sup>-3</sup> (NLTE-8). **a** Collisional ionization (fractional rate), **b** autoionization (absolute rate), **c** radiative recombination (RR) (fractional rate), **d** dielectronic recombination (absolute rate)

radiative recombination) is defined as the sum of all rates weighted with the state populations of the initial ion and summed over all final states. Thus defined, the effective rates certainly bear significant dependence on the populations, which may differ between codes. If, for instance, one CR code does not include forbidden radiative transitions that may effectively remove metastable character of some atomic states, then those states would significantly contribute to the total ionization flux and thus markedly modify the effective ionization rate.

The effective rates for several processes connecting neighboring ions of W as a function of ion charge are presented in Fig. 8.6. These calculations were performed at 1800 eV and  $10^{14}$  cm<sup>-3</sup> for the NLTE-8 workshop. Figure 8.6a, and c show the *fractional* rates for collisional ionization (CI) and radiative recombination (RR), while Fig. 8.6b and d present the *absolute* rates for autoionization (AI) and dielectronic recombination. For ions with Z < 45 (Cu-like W) the effective CI rates contribute less than 20% and therefore the main ionization channel is excitation followed by autoionization (EA). The sharp increase in the fractional CI rates at Z = 45 and above is rather due to the decrease of the EA rates which is evident in Fig. 8.6b. The Cu-like W<sup>45+</sup> has only one electron in the N shell and thus no  $\Delta n = 0$  excitations are possible. Although the effective autoionization rates calculated by different codes contribute about 90–95% to the total ionization rate, there is a considerable difference on the order of a factor of 4 in the absolute rates, as can be seen in Fig. 8.6b. Again, as the  $\Delta n = 0$  autoionization is very important at Z < 45, the results are dependent on the model completeness, which in this particular case is related to

(i) the highest principal quantum number of the included atomic states and (ii) detailed description of the shell structure that may not be achieved in hydrogenic-type codes. However, the difference in the dielectronic recombination rate (absolute) is somewhat smaller, mostly within a factor of 2 only.

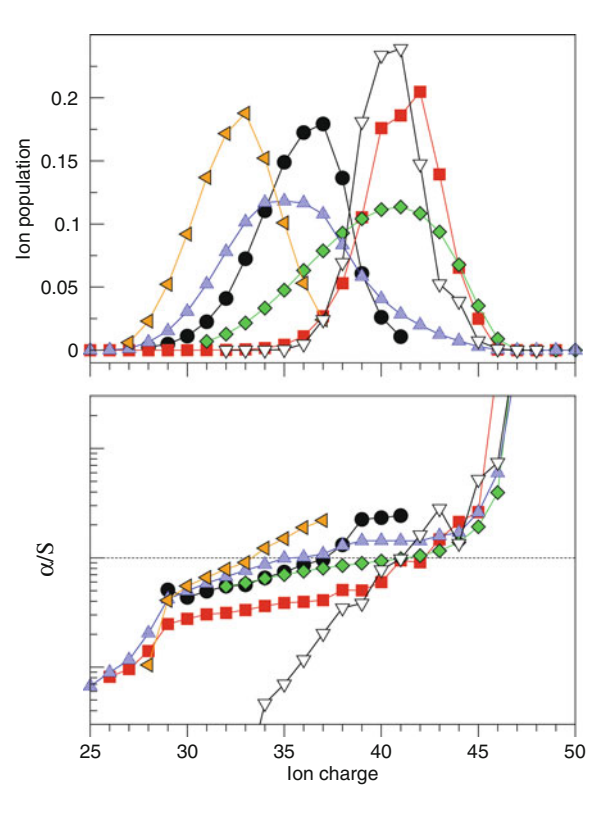
#### 8.4.3.3 $\alpha$ /S Ratio

Under a steady state condition, the ratio of populations for adjacent ions is simply the ratio of the corresponding effective ionization S and recombination  $\alpha$  rates (provided multi-electron processes are negligible):

$$\frac{N_Z}{N_{Z+1}} = \frac{\alpha_{Z+1,Z}}{S_{Z,Z+1}}. (8.5)$$

This ratio turns out to be a useful tool to explore the shape of the ion charge distribution. Figure 8.7 shows several calculated ion populations for the W case (NLTE-8) at 1200 eV and  $10^{14}$  cm<sup>-3</sup> (top) and the  $\alpha/S$  ratio for the same codes (bottom). Generally the ionization rates decrease with ion charge faster than the recombination rates

Fig. 8.7 Top W ion populations for several codes (NLTE-8) at 1200 eV and  $10^{14}$  cm<sup>-3</sup>; bottom  $\alpha/S$  ratios at the same conditions



and therefore  $\alpha/S$ , on average, increases with Z. Certainly, effects of excitation-autoionization or dielectronic recombination may modify such monotonic behavior but the general trend is rather universal. Hence,  $\alpha/S=1$  approximately corresponds to the ionization distribution peak (dominant ion stage), the slope of the ratio is related to the width of the ionization distribution, and rapid changes in the distribution can be traced back to the evolution of  $\alpha/S$ . All these features are easily identified in Fig. 8.7.

#### 8.4.3.4 Net Rate

The net rate  $\tilde{R}$  is defined as the difference in total ionization and total recombination fluxes between two ions divided by their averaged population:

$$\tilde{R} = \frac{N_Z \cdot S_{Z,Z+1} - N_{Z+1} \cdot \alpha_{Z+1,Z}}{(N_Z + N_{Z+1})/2}.$$
(8.6)

For steady-state cases  $\tilde{R}$  should be zero for all ions (within the uncertainties due to rounding errors) while for time-dependent problems that are frequently studied at NLTE workshops this parameter does not vanish. Even for the former cases, a simple plot of  $\tilde{R}$  values can sometimes point to inconsistencies in data reporting or some intrinsic issues with a particular calculation.

#### **8.4.3.5** Time-Dependent Parameters

Many terrestrial and astrophysical non-LTE plasmas evolve on timescales that prevent them from rapidly reaching a steady state. It was thus natural to include time-dependent (TD) cases in code comparisons. Unlike steady-state cases that are normally solved through the rate matrix diagonalization, a collisional-radiative analysis of transient plasmas necessarily requires solution of a first-order differential rate equation that may greatly extend the calculation time.

One of the most interesting TD cases from NLTE-7 addressed relaxation of atomic populations in a plasma after it is illuminated by an x-ray free-electron laser (XFEL). It was assumed that at time t=0 the entire population of a 50-eV Ar plasma at three different densities is in the excited state  $1s2s^22p^63p$ , which is produced from the ground state of the Ne-like ion Ar<sup>8+</sup> by a 100%-efficient selective photoexcitation with XFEL. Then the Ar ions are allowed to relax to a new equilibrium condition over a relatively long time and the information on state populations is collected on a logarithmic grid. The initial state is clearly an autoionizing one which decays on a typical AI scale of  $\sim 10^{-14}$  s; this rate is the fastest among all relevant physical processes under the problem conditions and thus one may expect the ion to undergo a very fast AI at the shortest times.

Indeed, as seen from Fig. 8.8 with the results at  $n_e = 10^{10}$  cm<sup>-3</sup>, the mean ion charge of the plasma increases from  $\overline{Z} = 8$  at t = 0 to  $\overline{Z} = 9$  within less than  $10^{-14}$  s

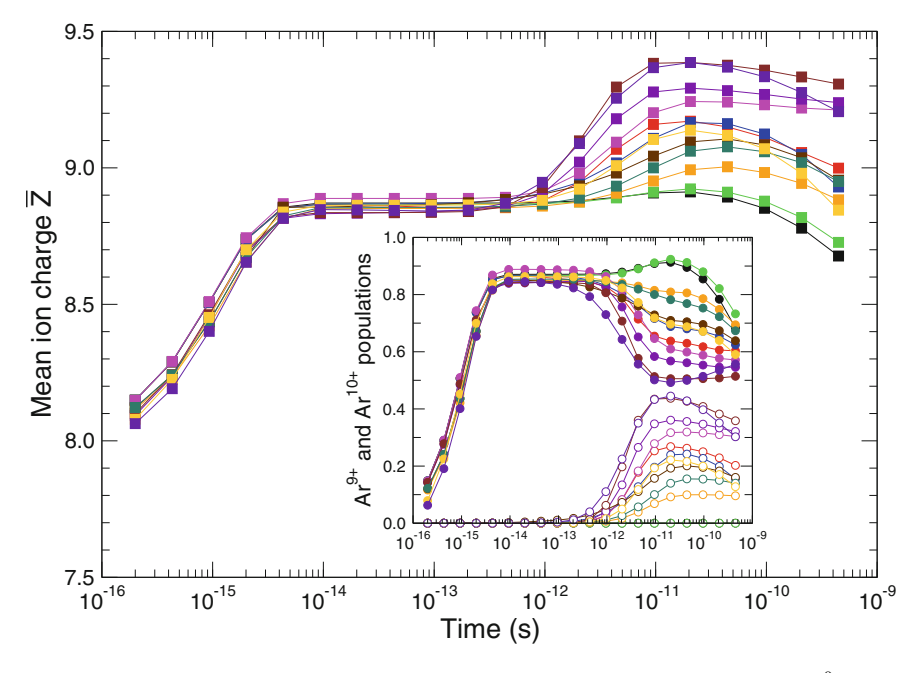


**Fig. 8.8** Time evolution of the mean ion charge of Ar (NLTE-7). Inset: population of  $Ar^{9+}$  (solid circles) and  $Ar^{10+}$  (open circles) versus time

for all codes. The system evolution, however, starts to vary significantly after  $10^{-12}$  s pointing out to different representation of collisional redistribution of population. Some codes exhibit shift towards higher ionization stages which is especially clear in the figure inset presenting the total populations of  $Ar^{9+}$  and  $Ar^{10+}$ . Analysis of ion structure and rates showed that the number of the included ionization stages and the account of autoionization into *autoionizing states in the next ion* are among the most important factors affecting ionization evolution [29].

# 8.4.4 Data for Atomic States

The number of atomic states included in different CR codes can vary by orders of magnitude. For example, the hydrogenic-type codes used to calculated the W cases at NLTE-8 included about 600–1000 states, while the most detailed codes contained up to 10<sup>6</sup> states (although still relativistic configurations rather than atomic levels!). Such a diversity in the number of states and differences in their physical nature exacerbate the comparisons and ask for development of new techniques. Some of these methods implemented at the NLTE workshops emphasize deviations of calculated populations from the equilibrium (e.g., Saha or LTE) values. The others

developed for rate analyses may accentuate relative rather than absolute values that are easier to compare. In this section we discuss some of the most detailed parameters used to compare population characteristics of atomic states.

#### 8.4.4.1 Populations and Population Fluxes

The populations of atomic states depend on their interactions with other levels and thus incoming and outgoing population fluxes. The elementary population flux is defined here as the product of the initial state population and the rate of the particular process that connects initial and final states. One can introduce a number of derivative quantities, such as a total population flux between two states (e.g., radiative plus collisional for transitions within an ion), a total flux into a state or out of it, or an effective flux between ionization stages. A clear understanding of population fluxes for atomic states helps one identify importance of various processes for a particular state as well as for spectra production. Below we use notations  $\Gamma$  and  $\Theta$  for the incoming and outgoing population fluxes defined as:

$$\Gamma_i = \sum_{j \neq i} N_j R_{ji},\tag{8.7}$$

$$\Theta_i = N_i \sum_{j \neq i} R_{ij} \tag{8.8}$$

where summation extends over all other atomic states in the model and  $R_{ji}$  is the sum of all rates from state j to state i.

As an example, consider the steady-state populations of atomic levels of Ge-like  $W^{42+}$  at 2400 eV and  $10^{14}~\rm cm^{-3}$  calculated with the NOMAD code for NLTE-8. This particular simulation includes about 1400 relativistic configurations, many of which are autoionizing. It should be emphasized that all figures below can be automatically generated for any participating code or combination thereof.

Figure 8.9 presents relative state populations (the total population in all ions is 1) in the top left panel, populations per statistical weight  $N_i/g_i$  (top right), population influx  $\Gamma_i$  (bottom left) and statistical weights  $g_i$  (bottom right). The x-axis x=E/IP is the level energy in units of the first ionization potential so that x=1 corresponds to the energy of the next ground state and thus the states with x>1 are autoionizing. As expected for low-density plasmas of highly-charged ions, the ground level  $4s^24p_-^2$  at x=0 is the most populated one. The two next excited states, the metastable members of the ground configuration  $4s^24p_-4p_+$  and  $4s^24p_+^2$ , also have large populations due to small probabilities of forbidden radiative transitions between the  $4s^24p^2$  states. Another pair of metastable levels is identified at  $x\approx0.86$ ; these states that belong to the inner-shell excited configuration  $3d^94s^24p^24d$  have very small radiative decay rates due to selection rules.

The state populations per unit of statistical weight are shown in Fig. 8.9b. If some states would be in the (partial) LTE equilibrium, their  $N_i/g_i$  distribution would follow

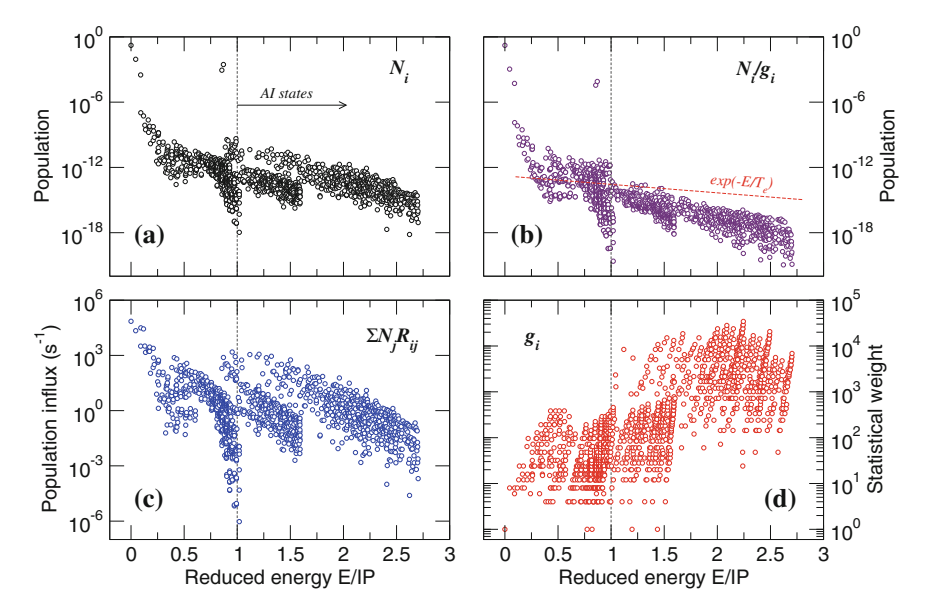


**Fig. 8.9** Population parameters for Ge-like W<sup>42+</sup> at 2400 eV and  $10^{14}$  cm<sup>-3</sup> (NOMAD calculations). **a** Relative populations, **b** relative populations per statistical weight, **c** population influxes, **d** statistical weights. The *dashed line* shows the slope of the Boltzmann exponent  $\exp(-E_i/T_e)$ 

the Boltzmann exponent  $\exp(-E/T_e)$  which is shown by the dashed line. Although some states (e.g., autoionizing states just above the ionization limit x=1) are rather close to LTE, generally this is not the case for such low-density high-temperature plasma.

In addition to the total population influxes (Fig. 8.9c) or outfluxes for each state, the database interface allows one to analyze specific population channels. As shown in Sect. 8.4.1, it is possible to generate absolute or relative population fluxes for all important processes affecting populations of all included states. Figure 8.10 represents the relative influxes (left) and outfluxes (right) for the same  $(2400 \, \text{eV}, 10^{14} \, \text{cm}^{-3})$  NOMAD results of Fig. 8.9. The first row of plots shows contribution of collisional (electron-impact) excitation and deexcitation. For most of the AI states, this channel is very weak for both influx and outflux. Nonetheless, for some states between x = 1.2 and x = 2.0 it contributes more than 50% to the total influx since the dielectronic capture rate is small due to low AI rates. In turn, these states can effectively decay via radiative transitions, and thus the relative excitation/deexcitation outfluxes for all AI states are below  $10^{-6}$ . Furthermore, they are as small for the non-AI states except for a few metastables.

The second and third rows present fractional fluxes for spontaneous radiative decays and autoionization (dielectronic capture), respectively. Again, under low-density conditions, radiative decay is the primary depopulation mechanism for non-AI states with x < 1. Even for many AI states, the radiative decay rates that scale

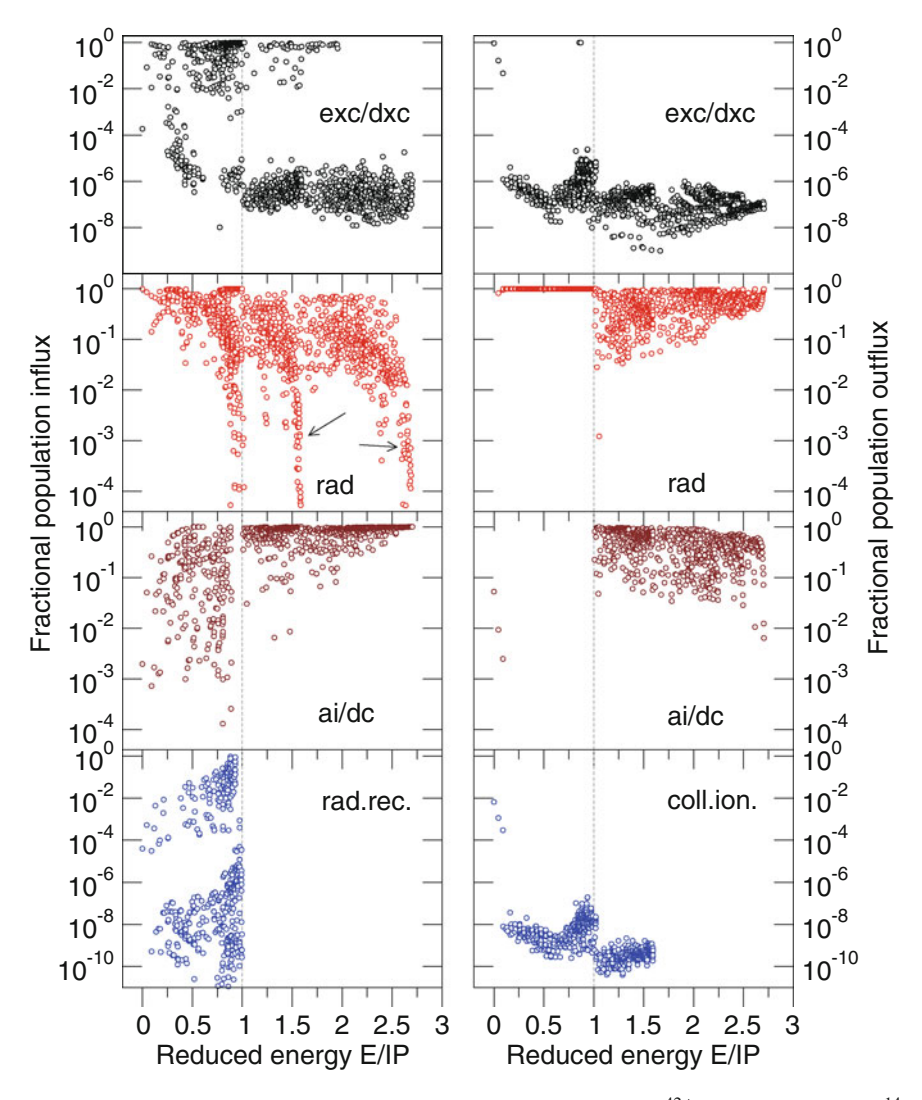


**Fig. 8.10** Relative population influxes and outfluxes for Ge-like W<sup>42+</sup> at 2400 eV and 10<sup>14</sup> (NOMAD calculations). *Left panel* (*top to bottom*) influx for collisional excitation and deexcitation, radiative decay, autoionization and dielectronic capture, radiative recombination. *Right panel* (*top to bottom*) outflux for collisional excitation and deexcitation, radiative decay, autoionization and dielectronic capture, collisional ionization

with the ion charge approximately as  $Z^4$  become very strong for Z=42 reaching or even exceeding the typical autoionization rates of  $10^{13}$  to  $10^{14}$  s<sup>-1</sup>. The primary radiative decay proceeds via transition of the inner electrons, e.g.,  $3d^{10}4s^24pnl-3d^94s^24p^2nl$ , and radiative processes due to transitions of the spectator nl electron are much weaker. This can be easily seen from the radiative influxes for nl series

marked by arrows in the figure. The only radiative population channel here is due to transitions from the higher states, for which the outermost electron has a higher value of n. Since radiative rates rapidly fall with n and the energy differences for transitions between high-n states are small, the relative contributions of spontaneous decays to the influxes into AI states also drop significantly, typically below 1%. On the other hand, autoionization and dielectronic capture remain the primary (de-)population processes for the majority of AI states. Somewhat unexpectedly, some low excited states in  $W^{42+}$  also receive most of population via autoionization from  $W^{41+}$  and the ground state of the Ge-like ion is depopulated via dielectronic capture at the level of about 5%. Finally, collisional ionization and, to a lesser degree, radiative recombination are generally negligible for population balance although RR seems to be quite important for the highest-n states below the ionization energy.

## 8.4.4.2 Ratio of Level Populations to Saha Populations

Determination of atomic state populations in NLTE plasmas normally requires a full-scale numerical treatment. The only realistic case where populations can be calculated analytically is the Saha-LTE (Boltzmann) distribution. This regime corresponds to a situation when collisional processes are much stronger than the radiative ones, and thus it is typical for high densities and/or low temperatures. It is well known that for high n the radiative rates decrease approximately as  $1/n^3$ , while collisional rates increase as  $n^4$ . Therefore, the high-n singly-excited states rapidly approach the Saha-LTE conditions with respect to the next ion, or more specifically, to the proper ionization limit for a particular series of atomic states.

The Saha-LTE distribution for high-n states is a general feature that should not depend on code properties, and therefore one can make use of the ratios of level populations  $N_i$  to the analytically calculated Saha-LTE populations  $N_{i,Saha}$  (also known as the b-factors [6]) as a test for the correct  $n \to \infty$  limit of populations. This technique has been extensively used at NLTE workshops. Since introduction of different ionization limits would considerably complicate both calculation and interpretation of the results, it was found acceptable to use Saha-LTE populations calculated according to the next ground state:

$$N_{i,Saha} = \frac{g_i}{g_0^+} \left(\frac{h^2}{2\pi m_e T}\right)^{3/2} n_e e^{(IP - E_i)/T} N_0^+$$
 (8.9)

where  $g_i$  and  $g_0^+$  are the statistical weights of the state i in the ion Z and the next ground state, IP is the first ionization potential of the ion Z,  $E_i$  is the energy of the state i calculated from its ground state, and  $N_0^+$  is the population of the next ion ground state.

There exist several criteria describing transition from the NLTE to Saha-LTE populations within an ion Z. One of them, the Griem boundary [2], that requires collisional processes to be at least an order of magnitude stronger than the radiative ones defines the lowest principal quantum number of the Saha states as:

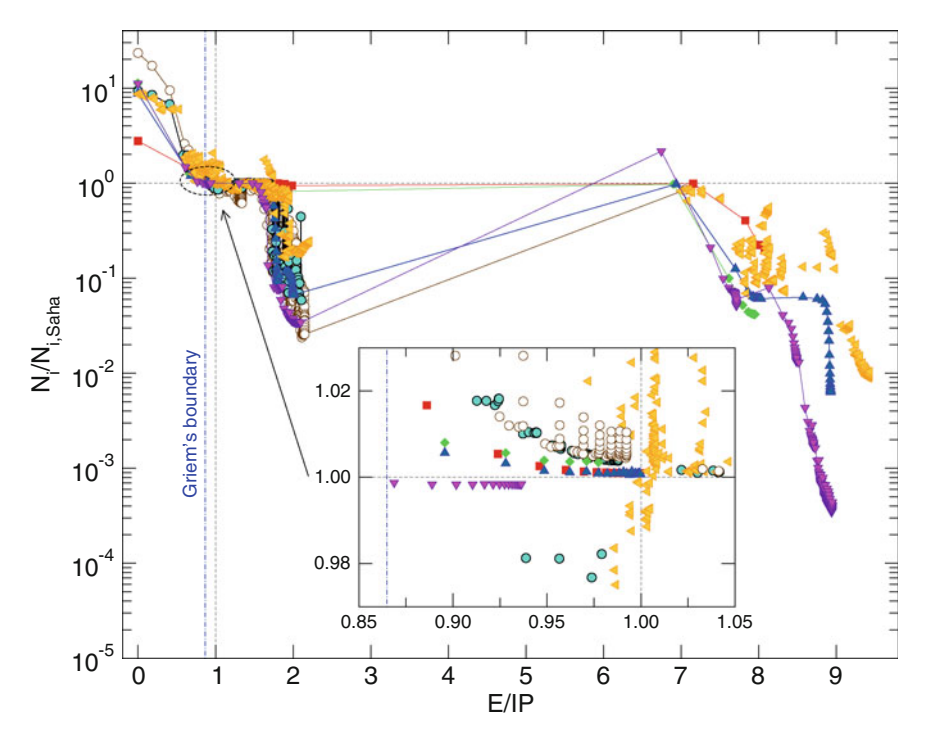


Fig. 8.11 Ratio of state populations to Saha populations (8.9) for  $Ne^{4+}$  at 10 eV and  $10^{18}$  cm<sup>-3</sup> (NLTE-7)

$$n_G \approx 165 \cdot (Z+1)^{12/17} (T_e/n_e^2)^{1/17}.$$
 (8.10)

where  $T_e$  is in eV and  $n_e$  is in cm<sup>-3</sup>. For tungsten ions in multi-keV magnetic fusion plasmas that have been frequently studied at NLTE workshops, this boundary is on the order of 100 and thus practically all CR models do not reach the Saha-LTE condition for high states. Nonetheless, for many other cases, the temperature and density are such that the transition is clearly identifiable.

Figure 8.11 presents the  $N_i/N_{i,Saha}$  ratios at 10 eV and  $10^{18}$  cm<sup>-3</sup> (NLTE-7) for Ne<sup>4+</sup>, which is the most abundant ion under these conditions. The ionization potentials used in different CR models may vary (the NIST Atomic Spectra Database value is  $126.247 \pm 0.012$  eV [35]) and therefore it is more convenient to plot the ratios as a function of the reduced ionization energy  $x = E_i/IP$ . With this scaling the first ionization limit (i.e., the ground state of Ne<sup>5+</sup>) has x = 1 for all models.

For detailed codes, the ground configuration  $2s^22p$  (or its lowest level  ${}^2P_{1/2}$ ) is the convergence limit for the  $2s^22pnl$  series while other series converge to excited states. For instance, the AI states in the range 1 < x < 2 are associated with  $2s2p^2nl$  and  $2^23ln'l'$  series. Those states are primarily populated via dielectronic capture from the next ground state and depopulated via autoionization, and thus they are in

the Saha equilibrium with the ratio close to one. For high n, the autoionization rate due to ejection of the outer electron falls as  $1/n^3$ , yet the radiative transitions of the inner electrons (2–2 or 2–3) are practically independent of n. As a result, the state populations become much smaller than the corresponding Saha values. Note also that the AI states with the hole in the K-shell have energies at x > 6.5, and no model includes empty-K-shell ions.

The inset in Fig. 8.11 zooming in the range of  $0.85 \le x \le 1.05$  provides a better picture of how the populations reach the Saha-LTE equilibrium. Some codes, e.g., up triangles (blue), squares (red) and diamonds (green), unambiguously show convergence towards the (1,1) point in the plot. Other codes, however, converge to a different point (for instance, the down triangle results seem to approach (0.938,0.997)) which may indicate some issues with, for instance, reporting the results or inconsistencies in calculation of the ionization potential lowering. Note also that the Griem boundary gives here a very good estimate of transition to the Saha-LTE regime.

#### **8.4.4.3** Ratio of Populations to LTE Populations

The Saha-LTE ratios discussed above emphasize connections to the next ion ground state. A different type of comparison is obtained when the ratio is taken to the Boltzmann population calculated from the same ion's ground state,  $N_i/N_{i,LTE}$ , where

$$N_{i,LTE} = \frac{g_i}{g_0} N_0 e^{-E_i/T_e}.$$
 (8.11)

with  $N_0$  being the ground state population and  $g_0$  its statistical weight.

For all codes the ratio is of course 1 for the ground state. It also remains constant within the groups of atomic states that are in a partial LTE (pLTE) corresponding to the electron temperature  $T_e$  and thus such groups can be visually identified. If the effective temperature of pLTE is different from  $T_e$ , the corresponding groups would still be distributed along straight lines in such a plot.

The  $N_i/N_{i,LTE}$  values for Ne<sup>3+</sup> at 10 eV and  $10^{18}$  cm<sup>-3</sup> (NLTE-7) are shown in Fig. 8.12. As for the Saha ratios in the previous section, the high-n non-AI states and some of the AI states are in partial LTE corresponding to the original  $T_e$  (the ratios are horizontal), although not necessarily with its own ground state.

#### 8.4.4.4 Shell Populations and Occupation Numbers

The shell populations  $\mathcal{Z}(n)$  are calculated as the relative populations of atomic states with the outermost electron in the shell n. Thus  $\mathcal{Z}(n)$  are defined according to:

$$\Xi_n = \sum_{i} N_i \cdot \delta(n, n_{max}) \tag{8.12}$$

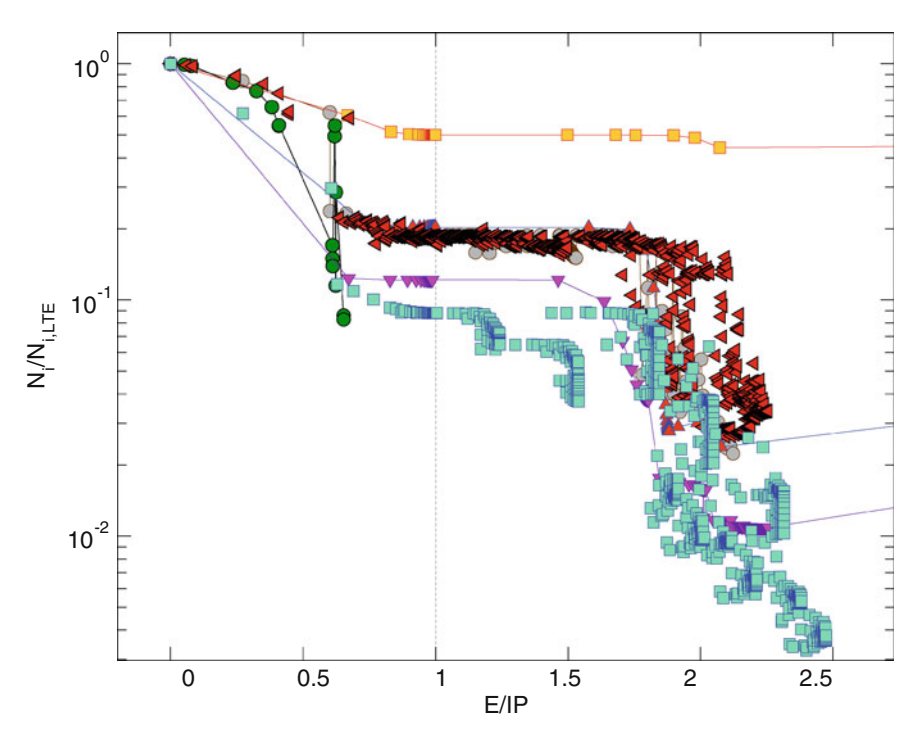


**Fig. 8.12** Ratio of state populations to LTE (Boltzmann) populations (8.11) for  $Ne^{3+}$  at 10 eV and  $10^{18}$  cm<sup>-3</sup> (NLTE-7)

where  $n_{max}$  is the principal quantum number of the outermost electron and  $\delta(n, n_{max})$  is the Kronecker symbol. The database interface also allows one to calculate the shell populations per statistical weight.

The term "occupation number" is well defined in quantum mechanics, in particular in the second quantization theory. In the context of state populations, the occupation number  $\Psi_z(n)$  represents the average number of electrons in a shell n for a particular ion stage Z:

$$\Psi_z(n) = \sum_{i=1} N_i \cdot w_i(n) \tag{8.13}$$

where  $w_i(n)$  is the number of electrons in the shell n for the state i. Unlike other parameters that provide a rather detailed picture of level populations, the shell populations and occupation numbers represent a more general, averaged visualization which nonetheless may capture important trends. However, an obvious drawback of this approach is that both shell populations and occupation numbers do not distinguish between non-AI and AI states.

## 8.4.4.5 Spectra Comparisons

It would be fair to say that spectra comparisons provide the most broad and exhaustive approach to analysis of CR codes. Such features as, e.g., code structure and quality of atomic data, account of forbidden transitions, or ionization potential lowering, may be revealed in the number of spectral lines or their positions and intensities. Throughout the history of the NLTE workshops, synthetic spectra have always been one of the central discussion points.

Our approach to spectra comparisons includes several components. Typically the participants are asked to generate spectra within a specific wavelength (or energy) range with a prescribed resolution taking into account just natural and Doppler broadening. As the emphasis of the NLTE workshops is on population kinetics, it was found acceptable to neglect spectral line broadening and shapes in spectra generation. Furthermore, these topics are the subject of the recently initiated series of workshops on Spectral Line Shapes in Plasmas [21, 22].

In addition to bound-bound, bound-free, free-free, and total spectra within a spectral band, the spectra from different ionization stages are often requested as well. Figure 8.13 shows several calculated spectra from Se-like W<sup>40+</sup> at 1800 eV (NLTE-8). The hydrogenic codes that are shown in panels (c), (d) and (e) exhibit spectral features that are rather different from the calculations performed with the detailed-level-accounting or hybrid codes. It is also encouraging to see that the calculations in (a) and (f) produced with different relativistic-configuration-averaged codes are almost indistinguishable except for a slight intensity mismatch.

No matter how close the results from different codes may be, it is the agreement with the detailed benchmark experimental data that provides the ultimate criteria for code validity. Such comparisons with high-quality data, primarily spectra, are an important component of NLTE workshops. So far the CR codes were benchmarked against laser-produced (Xe, Kr) and magnetic fusion (Ar) plasmas. In some cases, the workshop participants were given an experimental spectrum with the goal to determine the primary plasma parameters, such as electron density and temperature, from the measurements. A very detailed discussion of such analysis for L-shell ions of Kr is given in [29]. It was found in particular that the results generally confirmed the typically quoted uncertainties for such diagnostics of 20% in electron temperature and factors of about two in density.

# **8.5** Concluding Remarks

The goal of extensive comparisons between collisional-radiative codes is not to find out which code is better or the best. The NLTE workshops rather aim at understanding why different CR models disagree, what their limitations and regimes of applicability are, and what can be learned from such comparisons. Over the last twenty years since the first NLTE workshop, we were able to comprehensively test our codes, pinpoint a number of important issues for CR modeling, and discuss possible solutions.

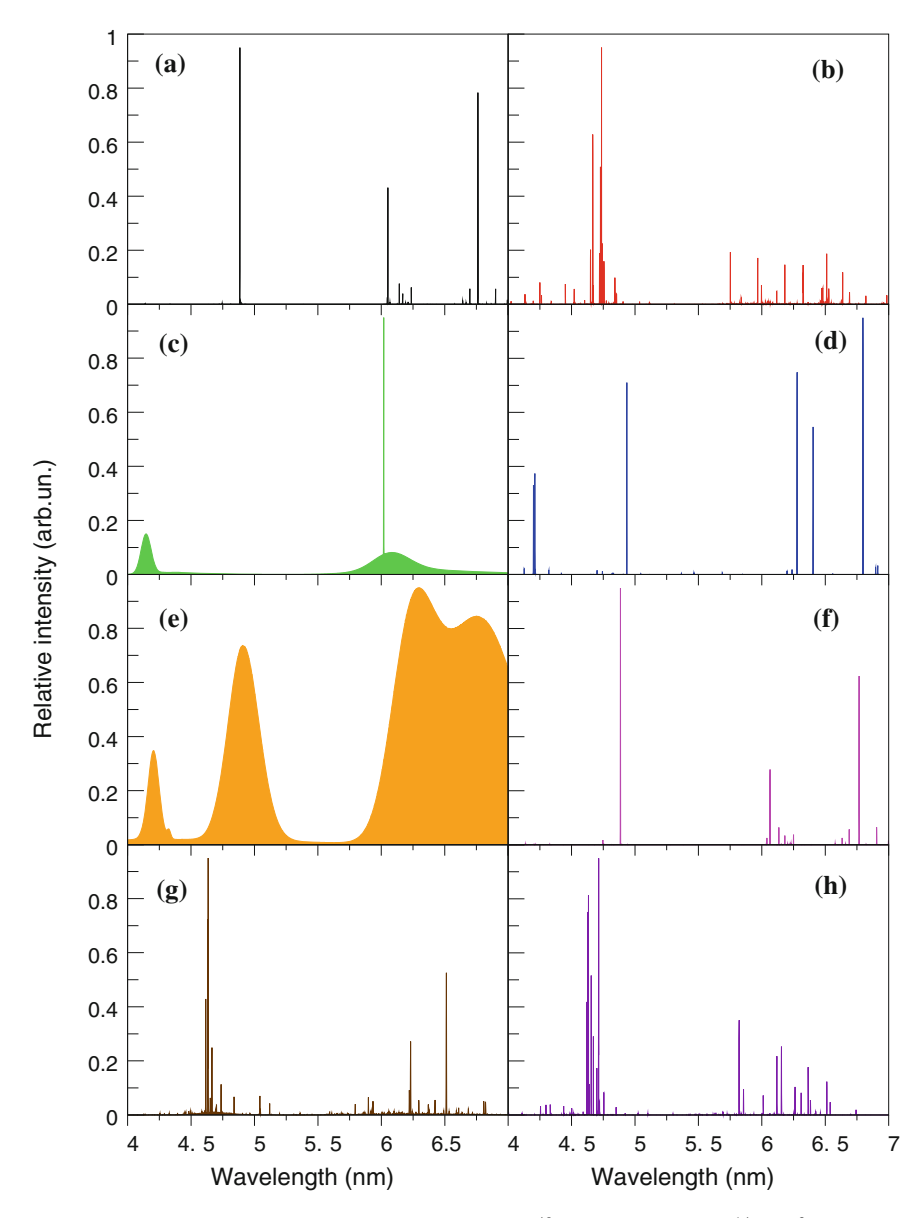


**Fig. 8.13** Calculated bound-bound spectra for Se-like  $W^{40+}$  at  $1800\,eV$  and  $10^{14}\,cm^{-3}$  (NLTE-8). Relativistic configuration codes: **a** and **f**, hydrogenic codes: **c**, **d**, and **e**; hybrid codes: **b** and **g**; averaged-atom code: **h** 

Moreover, a number of experimental groups provide their accurate data for code tests. Such encouraging interaction between experimentalists and modelers is one

of the most important developments that should significantly contribute to a better spectroscopic diagnostics of plasmas.

Although the idea of CR code comparisons emerged within the dense-plasma community, the test domain has swiftly extended to other plasmas including magnetic fusion and astrophysics. Moreover, such important effects as external radiation, opacity and non-Maxwellian distributions were regularly brought into comparisons. The variety of conditions that now need to be routinely addressed in laboratory and space plasmas together with ever more precise experimental techniques put new demands on coverage, quality and accuracy of CR modeling and related atomic data. These challenging requirements will give even stronger impetus to the ongoing efforts on validation and verification of collisional-radiative codes.

Acknowledgments The success of the NLTE Workshops is due to enthusiastic support of the participants and their inspiring feedback that was always instrumental in development of new code comparison methods. I am very thankful to all of them. In particular, it is my great pleasure to acknowledge Richard Lee (LLNL), Spiros Alexiou (University of Crete), Christopher Bowen (CEA), James Colgan (LANL), Hyun-Kyung Chung (LLNL/IAEA), Chris Fontes (LANL), Stephanie Hansen (LLNL/SNL), and Jesus Rubiano (University of Las Palmas de Gran Canaria) who had selflessly taken on themselves the duties of case development, session coordination, and general workshop organization. I also thank Evgeny Stambulchik (WIS) and Alexander Kramida (NIST) for valuable comments.

## References

- D.R. Bates, A.E. Kingston, R.W.P. McWhirter, Proc. R. Soc. London Ser. A 267, 297 (1962).
   Proc. R. Soc. London Ser. A 270, 155 (1962)
- H.R. Griem, Principles of Plasma Spectroscopy (Cambridge University Press, Cambridge, 1997)
- 3. J. Oxenius, Kinetic Theory of Particles and Photons (Springer, Berlin, 1986)
- 4. D. Salzmann, Atomic Physics in Hot Plasmas (Oxford University Press, Oxford, 1998)
- 5. T. Fujimoto, *Plasma Spectroscopy* (Clarendon Press, Oxford, 2004)
- 6. J.A.M. van der Mullen, Phys. Rep. **191**, 109 (1990)
- 7. D.E. Post, L.G. Volta, Phys. Today **58**, 35 (2005)
- Assessing the Reliability of Complex Models: Mathematical and Statistical Foundations of Verification, Validation, and Uncertainty Quantification, National Research Council report (The National Academies Press, Washington DC, 2012)
- 9. B.W. Boehm, in Euro IFIP 79: Proceedings of the European Conference on Applied Information Technology of the International Federation for Information Processing, ed. by P.A. Samet (North Holland, 1979), pp. 711–719
- 10. H.A. Scott, Preprint UCRL-99666 (1988)
- H.P. Summers, N.R. Badnell, M.G. O'Mullane, A.D. Whiteford, R. Bingham, B.J. Kellett, J. Lang, K.H. Behringer, U. Fantz, K.-D. Zastrow, S.D. Loch, M.S. Pindzola, D.C. Griffin, C.P. Ballance, Plasma Phys. Control. Fusion 44, B323 (2002)
- M.A. Bautista, V. Fivet, P. Quinet, J. Dunn, T.R. Gull, T.R. Kallman, C. Mendoza, Astrophys. J. 770, 15 (2014)
- 13. R. Wesson, D.J. Stock, P. Scicluna, Mon. Not. R. Astron. Soc. 422, 3516 (2012)
- C.P. Ballance, S.D. Loch, A.R. Foster, R.K. Smith, M.C. Witthoeft, T.R. Kallman, Fusion Sci. Technol. 63, 358 (2013)
- 15. Yu. Ralchenko, Y. Maron, J. Quant. Spectrosc. Radiat. Transf. 71, 609 (2001)

- 16. M.F. Gu, Can. J. Phys. **86**, 675 (2008)
- N.L. Johnson, S. Kotz, N. Balakrishnan, Continuous Univariate Distributions (Wiley, New York, 1994)
- 18. G. Marsaglia, T.A. Bray, SIAM Rev. 6, 260 (1964)
- 19. A. Rickert, J. Quant. Spectrosc. Radiat. Transf. 54, 325 (1995)
- 20. I.T. Iliev, B. Ciardi, M.A. Alvarez et al., Mon. Not. R. Astron. Soc. 371, 1057 (2006)
- 21. E. Stambulchik, High Energy Density Phys. 9, 528 (2013)
- 22. E. Stambulchik, A. Calisti, H.-K. Chung, M.Á. González, Atoms 2, 378 (2014)
- 23. R.W. Lee, J.K. Nash, Yu. Ralchenko, J. Quant. Spectrosc. Radiat. Transf. 58, 737 (1997)
- C. Bowen, A. Decoster, C.J. Fontes, K.B. Fournier, Yu. Ralchenko, J. Quant. Spectrosc. Radiat. Transf. 81, 737 (2003)
- 25. C. Bowen, R.W. Lee, Yu. Ralchenko, J. Quant. Spectrosc. Radiat. Transf. 99, 102 (2006)
- J.G. Rubiano, R. Florido, C. Bowen, R.W. Lee, Yu. Ralchenko, High Energy Density Phys. 3, 225 (2007)
- C.J. Fontes, J. Abdallah Jr, C. Bowen, R.W. Lee, Yu. Ralchenko, High Energy Density Phys. 5, 15 (2009)
- Yu. Ralchenko, J. Abdallah Jr., A. Bar-Shalom, et al., in: 16th International Conference on Atomic Processes in Plasmas, ed. by K.B. Fournier. AIP Proceedings, vol. 1161 (2009), p. 242
- 29. S.B. Hansen, G.S.J. Armstrong, S. Bastiani-Ceccotti et al., High Energy Density Phys. 9, 523 (2013)
- 30. H.K. Chung, C. Bowen, C.J. Fontes, S.B. Hansen, Yu. Ralchenko, High Energy Density Phys. 9, 645 (2013)
- 31. S. Mazevet, J. Abdallah Jr., J. Phys. B 39, 3419 (2006)
- 32. S.B. Hansen, J. Bauche, C. Bauche-Arnoult, M.F. Gu, High Energy Density Phys. 3, 109 (2007)
- 33. A. Burgess, Astrophys. J. **136**, 776 (1964)
- K.B. Fournier, M.J. May, D. Pacella, M. Finkenthal, B.C. Gregory, W.H. Goldstein, Nucl. Fusion 40, 847 (1999)
- A. Kramida, Yu. Ralchenko, J. Reader, NIST ASD Team, NIST Atomic Spectra Database (ver. 5.2). (National Institute of Standards and Technology, Gaithersburg, MD 2014), http://physics.nist.gov/asd Accessed 5 May 2015

A	Collisional double ionization, 21
Absorption coefficient, 97, 98, 120	Collisional excitation, 61, 64, 105, 167, 168,
Absorption lines, 163	174, 200
Abundances of elements, 154, 163, 174	Collisional ionization, 8, 62, 127, 135, 147,
Accretion disk, 156, 157, 159, 161, 170, 171	169, 170, 172, 184, 193, 194, 200,
Active galactic nuclei (AGN), 70, 156, 157,	201
161	Collisional-radiative modeling
Astrophysics, 70, 155, 160, 173, 207	large scale, 20
Auger electron, 71, 127, 129, 130	Collisionally dominated plasmas, 23, 26
Autoionization, 21, 28, 58, 63, 97, 108, 117,	Completeness of models
194, 200, 203	application-driven approaches, 9
Average atom, 13, 106, 116, 132	effect on charge state distribution, 66
	effect on radiative power loss, 190
	effective, 2, 4, 6
B	strict, 2, 3, 13
Balmer continuum, 164	Complex refractive index, 145
Bethe high-energy limit (electron-impact	Computational modeling, 78, 182
ionization), 29	Configuration interaction, 8, 12, 26, 27, 39,
Black holes, 156, 170	40, 172
Block tri-diagonal (BTD) matrix, 31	Configuration-average mode, 26, 32, 41
Boltzmann equilibrium, 160, 172	Continuum lowering, 3, 14, 65, 74, 75, 77,
Boundary conditions, 29, 162	see also Pressure ionization and ion-
Broad-lined region (BLR), 161	ization potential depression
	Coronal equilibrium, 19, 73, 105, 123, 181,
_	187
C	Coronal plasma, 23, 53
Charge exchange, 3, 5, 173, 174, 177, 184	Cosmic microwave background, 158, 160
Charge state distribution, 2, 4–6, 8, 10, 11,	Cosmic rays, 157, 158, 164
14, 23, 24, 37, 51–53, 57, 58, 64, 66,	
68, 69, 71, 73, 76, 77	
Charge-neutrality condition, 30, 31, 52	D
Chemical potential, 94, 111, 115, 138	Degeneracy, 92, 93, 95, 97
Close-coupling method, 18	Density diagnostics, 11, 177
Collision strength, 95, 96	Detailed balance principle, 184

Detailed configuration accounting (DCA),	G
11, 129, 150	Generalized minimum residual (GMR)
Detailed level accounting (DLA), 128	method, 32
Dielectronic capture, 5, 10, 11, 21, 108, 114,	Generalized rates, 139
117, 199–202	Grains, 153, 159, 163, 164
Dielectronic recombination	Griem boundary, 201, 203
effect on charge state distribution, 66	•
from inner-shell states, 25	
from multiply excited states, 5	Н
in coronal approximation, 35	Hartree-Fock method, 18
satellite lines, 10	Hartree-Fock-Slater method, 18
Dirac-Fock-Slater method, 18	Heating, photoelectric, 157
Discretization, 82	Heavy element formation, 159
Distorted-wave method, 18, 111	Helmholtz equation, 93
Doppler frequency shift, 10	
Dual methods, 41	High-density plasmas, 5
Buti memous, 11	Hollow ions, 56
	Hot electrons, 25, 28, 69, 75, 187
E	Hybrid methods, 40, 41
Effective temperature, 55, 67, 162	Hybrid-structure models, 12, 57
Electron-impact deexcitation, 199	Hydrodynamics, 14, 81, 84, 87, 104, 123,
Electron-impact excitation, 199	136, 146
Electron-impact excitation, 179 Electron-impact ionization, 21, 28	Hydrogen
Emission and absorption spectra, 6	Balmer lines, 155
Emission and absorption spectra, 6  Emission coefficient, 81, 82, 85, 86, 98, 100,	molecular, 155
102 Emission lines 0, 152, 156, 157, 166	
Emission lines, 9, 153, 156, 157, 166	I
Emissivity, 67, 75, 119, 120, 123, 124	Intensity, 60, 102, 114, 128, 130–132, 134,
Energy deposition, 144	139, 144, 148, 159, 160, 163
Energy states	Inter-galactic medium, 161
configuration averaged, 59	Interstellar medium, 156, 163
fine structure, 7	Ionization, 22, 26, 55–57, 63–65, 70, 72, 77,
ground, 7	83, 92, 97, 106, 111, 115, 117, 130,
high-n, 201	135, 137, 148, 162, 164, 167–170,
hybrid, 186	172, 173, 184, 187
in hydrogen-like ions, 3	Ionization potential depression, 3, 65, 77, 82,
inner-shell, 198	92, 104
metastable, 76	22, 101
multiply excited, 174	
singly excited, 10	K
superconfiguration, 41	
Equation of state, 6, 81	Kinetic Monte Carlo (KMC) method, 132
Equivalent two-level model, 167	Kirchoff's law, 86, 98
Expansion of the universe, 156, 157, 176	Kramers' high-energy limit(photoionization),
	29
F	
Fluorescence, 127, 138, 147, 150	L
Four-body recombination, 22	Laser-produced plasmas, 25, 53, 181
Fourier domain interferometry, 148	Layzer complexes
Free-free emission (bremsstrahlung), 97	statistical weight of, 24
Full configuration-interaction models, 40	Lighting systems, 21
Fully relativistic configuration-average	Linearization procedure, 144
models, 36	Lithography, 21, 181

Local thermodynamic equilibrium (LTE), 3, 19, 21, 35, 68, 74, 81, 105, 107, 160, 181	Populations of states, 31, 32, 34, 52, 171, 172, 184, 194, 198, 203 Pressure ionization, 3, 5, 6, 9, 14, 65, 121
Lyman continuum, 164	
M Magnetic reconnection, 157 Magnetohydrodynamic waves, 157	<b>Q</b> Quasar, 155–157, 159, 171
Maxwell-Boltzmann distribution, 140, 164 Mean (ion) charge, 19, 34, 141–144, 184 Metastable states, 7, 8, 10, 12, 39, 41 Micro-reversibility principle, 28 Mixed Unresolved Transition Array (MUTA) method, 41 Molecular clouds, 161 Monte-Carlo methods, 130	R Radiation transport, 78, 81–83, 86, 87, 89, 98, 100–103, 123, 124, 153 Radiation, ionizing, 70 Radiative decay spontaneous, 5, 21, 186, 199 stimulated, 21 Radiative power losses, 2, 76, 77, 190 Radiative recombination, 58, 61, 71, 139, 172, 194, 201
N Narrow-lined region (NLR), 161 Nebulae, 70, 154, 155, 163, 174 Neutron stars, 156 NLTE Code Comparison Workshops, 5, 22, 186 Non-Local Thermodynamic Equilibrium (NLTE), 57, 73	Rate equation, 1, 19, 29, 32, 52, 65, 87, 88, 127, 139, 178, 183, 184, 196  Reduced detailed configuration accounting (RDCA) method, 41  Relativistic subconfigurations, 8, 22, 41, 67, 186, 197, 198
O Occupation numbers, 28, 54–56, 105–108, 116, 120, 204 Opacity, 21, 52, 67, 82, 119, 123, 144, 145, 163, 172, 184, 186, 207 Optically-thick plasmas, 123	S Saha equation, 74, 83, 95 Screened hydrogenic models, 1, 6 Self-consistent field models, 14 Semi-relativistic configuration-average (SRCA) models, 26, 35, 36, 38, 41 Shell populations, 13, 203, 204 Shock ionization, 157 Single-configuration (SC, SCR, SCNR)
P Particle-conservation condition, 30, 52 Partition function, 12, 57, 83, 92, 93, 170 Photodissociation region, 164 Photoexcitation, 127, 130, 131, 134, 144, 196 Photoionization, 21, 60, 61, 70, 71, 97, 108, 117, 127–131, 134, 135, 137–139, 143, 144, 147, 154, 156, 157, 159, 163, 164, 167, 168, 172, 189, 190 Photoionized plasmas, 53 Planck function, 98, 99, 102, 156, 158 Plane-wave-Born method, 22 Planetary nebulae, 155 Polycyclic Aromatic Hydrocarbons (PAHs), 165, 176 Population flux, 147, 198, 199	models, 26 Solar convection zone, 21 Solar corona, 21, 184, 187 Source function, 87, 98, 101–103 Sparsity of a matrix, 32, 36 Specific heat, 87, 89–91, 101, 102 Spectral energy distribution, 156 Spectroscopy, integral field, 155 Spectroscopy, slit, 155 Spin-orbit-split array (SOSA), 130, 150 Stars, 154, 155, 159, 162, 163, 176 Statistical weights, 3, 6, 9, 12, 28, 55, 57, 68, 77, 107, 192, 199, 201 Steady-state solutions, 29 Stefan radiation-density constant, 160 Stellar envelopes, 21 Stewart-Pyatt model, 65, 92
2 op man on man, 111, 170, 177	5.0 art 1 jant 110001, 05, 72

Strict Thermodynamic Equilibrium(STE),	U
158	Uncertainty analysis, 182
Superconfigurations, 2, 3, 6, 11, 12, 24, 34, 41, 99, 186	Unresolved Transition Array (UTA) method, 38, 98
Supernovae, 21, 155–157	
Supershell notation, 23, 24, 33	
Surface brightness, 163	$\mathbf{V}$
Т	Validation and verification of models, 182, 183, 187
Temperature diagnostics, 205	
Three-body recombination, 6, 21, 28, 108,	
117, 121, 170, 172, 189	W
Time-dependent solutions, 29	White dwarf, 156
Transition, 2, 21, 25, 26, 28, 30, 32, 34, 36,	Wolf-Rayet stars, 155
38, 39, 51–53, 55, 58–61, 64, 67–70,	Wolf-Rayet stars, 133
72–76, 81, 83–88, 90, 91, 93–98, 100,	
106–108, 110, 111, 113, 117, 121,	
130, 133, 136, 164–168, 172, 174,	X
176, 181, 183, 194, 198–203, 205	X-ray free electron laser (XFEL), 65, 71, 196